BIOMACROMOLECULES UNDER HIGH HYDROSTATIC PRESSURE

A Dissertation

Presented to the Faculty of the Graduate School

of Cornell University

in Partial Fulfillment of the Requirements for the Degree of

Doctor of Philosophy

by

Nozomi Ando

January 2009

BIOMACROMOLECULES UNDER HIGH HYDROSTATIC PRESSURE

Nozomi Ando, Ph.D.

Cornell University 2009

Protein pressure denaturation cannot be explained by the classical thermodynamic model of protein denaturation derived from thermal denaturation studies. Recent studies imply that the mechanism of pressure denaturation is the penetration of water into the protein rather than the transfer of hydrophobic residues into water. To investigate water penetration and the volume change associated with pressure denaturation, we studied the solution behavior of four T4 lysozyme mutants having different cavity volumes at low and neutral pH up to a pressure of 400 MPa using small-angle X-ray scattering and fluorescence spectroscopy. At low pH, L99A T4 lysozyme expanded from a compact folded state to an extended but partially unfolded state. The denaturation volume change correlated positively with the total cavity volume, indicating that all of the major cavities are hydrated with pressure. At neutral pH, the pressure-denatured state is more compact than at low pH, and the small denaturation volume changes suggest that the preferential filling of large cavities is responsible for the compactness of the pressure-denatured state. These results confirm that pressure denaturation is characteristically distinct from thermal or chemical denaturation. In addition, pressure was investigated as a method to selectively measure the stability of tertiary contacts in hairpin ribozyme. Minimal hairpin ribozyme constructs were studied with the substrate or substrate analog using the base analog 2-aminpurine as a fluorescent reporter of local structural changes. Contrary to previous reports on another construct, it was found that the docked form was stable under pressure but that pressure may have an effect on the catalytic mechanism.

BIOGRAPHICAL SKETCH

Nozomi Ando received her B.S. in physics from M.I.T. in 2001. She joined the Gruner group upon arriving at Cornell University as a graduate student in physics. She will return to M.I.T. for her postdoc.

To my parents, Teiichi and Sumiko Ando.

ACKNOWLEDGEMENTS

This Ph.D. research could not have been possible without the support of many people. I am grateful to Prof. Sol Gruner for his guidance and for being a caring advisor. Many group members have contributed. I thank Martin Novak for machining the high-pressure SAXS cells and many other parts for my experiments, Dr. Mark Tate for many helpful discussions and training, Dr. Pascale Chenevier and Raphael Kapfer for help with high-pressure design and techniques, Dr. Gil Toombes for teaching me SAXS analysis and help with the pressure pump motor control, Buz Barstow for significant help with sample preparation, experiments, and critical reading of thesis and manuscript drafts, Dr. Marcus Collins for many helpful discussions regarding T4 lysozyme, and Lucas Koerner for critical reading of many thesis and manuscript drafts.

I have enjoyed my time at the Cornell High Energy Synchrotron Source (CHESS) and am thankful for CHESS staff scientists (Drs. Arthur Woll, Peter Busch, and Richard Gillilan), operators, and machinists. For their help with data acquisition at CHESS, I thank Buz Barstow, Yi-fan Chen, Fred Heberle, Raphael Kapfer, Dr. Chae Un Kim, Lucas Koerner, Darren Southworth, and Dr. Gil Toombes.

I consulted many people regarding the design of the high-pressure SAXS cell. I am grateful to Prof. Bill Bassett for providing and preparing diamonds, Dr. Chang-Sheng Zha (Carnegie Inst. of Washington) for help with preparing Bridgman window seals, Prof. Roland Winter (Univ. of Dortmund) for discussion of his high-pressure design, Dr. Testuro Fujisawa (RIKEN Harima Institute/SPring-8) for his insight, Special Metals Corp (Huntington, WV) for providing annealed Inconel 725 and age-hardening service, and the LASSP Machine Shop (Cornell) for providing EDM service.

I also thank the Protein Facility, Glass Shop, and the Microscopy and Imaging Facility at Cornell for their services, Prof. Héctor Abruña for letting me borrow equipment, and Prof. Manfred Lindau for letting me access his RNase-free lab area.

I enjoyed collaborations with many groups. At the Univ. of Oregon, I thank Prof. Brian Matthews for his collaboration with T4 lysozyme and for his insight, Andy Fields for expressing and purifying the mutants, and Dr. Walt Baase for many helpful discussions regarding T4 lysozyme and protein thermodynamics. At the Univ. of Rochester, I thank Prof. Joe Wedekind for his collaboration with hairpin ribozyme and many lively discussions, Jolanta Krusincka for preparing the samples, and Dr. Andy Torelli (currently at Cornell) for helpful discussions. At the Carnegie Institute of Washington, I thank Prof. Russell Hemley, Dr. Yufei Meng, and Dr. Felix Krasnicki for providing CVD diamonds as SAXS windows.

I am grateful to Prof. Lois Pollack and Dr. Jessica Lamb for helpful discussions on SAXS and ribozymes, Prof. Teiichi Ando (Northeastern Univ.) for helpful discussions regarding metals and thermodynamics, and Dr. Warren DeLano (Delano Scientific LLC) for providing a script for viewing molecular surfaces in PyMol.

Thank you committee members, Profs. Sol Gruner, Itai Cohen, Veit Elser, and Lois Pollack.

I will miss the members of the Gruner group - thank you for your friendship and inspiration. I won't forget the conversations, clovers, hand-made storage bench, field trips to mini-Gimme/Manndible and Wegmans, and many other great times.

Finally, I thank my parents, sister (Megumi), friends, and husband (Buz), for their encouragement.

TABLE OF CONTENTS

LIST OF TABLES

LIST OF FIGURES

LIST OF ABBREVIATIONS

→	mutation if in between two amino acids or nucleotides
2AP	2-aminopurine
2WJ	2-way helical junction
3WJ	3-way helical junction
4WJ	4-way helical junction
A, Ala	amino acid, alanine (in context of protein)
A	adenosine or adenine (in context of RNA)
A98L	the mutation or mutant containing alanine-98 to leucine substitution
cal	unit of energy, calorie, 4.184 joules
C, Cys	amino acid, cysteine (in context of protein)
C	cytidine or cytosine (in context of RNA)
C54T/C97A	the mutations, cysteine-54 to threonine, cysteine-97 to alanine
D	denatured state
CCD	charge-coupled device
CHESS	Cornell High Energy Synchrotron Source
DTT	dithiothreitol
DNA	deoxynucleic acid
E, Glu	glutamic acid
E108V	the mutation, glutamic acid-108 to valine
EDTA	ethylenediaminetetraacetic acid
EDM	electrical discharge machining
EOM	a SAXS analysis program, Ensemble Optimization Method
FTIR	Fourier transform infrared spectroscopy
G, Gly	amino acid, glycine (in context of protein)
G	guanosine or guanine (in context of RNA)
GASBOR	the name of a SAXS analysis program
GNOM	the name of a SAXS analysis program
H bond	hydrogen bond
HEWL	a protein, hen egg white lysozyme
HOMO	highest occupied molecular orbital
HPLC	high pressure liquid chromatography
IPTG	isopropyl-beta-D-thiogalactopyranoside
keV	unit of energy, kilo-electronvolts, $1.6022 \times 10^{?16}$ joules
L, Leu	amino acid, leucine
L99A	the mutation or mutant containing leucine-99 to alanine
L99G	the mutation or mutant containing leucine-99 to glycine
L99G/E108V	the mutant containing both L99A and E108V mutations

LB	Luria-Bertani broth, a type of bacterial growth medium
LBH	a variant of Luria-Bertani broth
LUMO	lowest unoccupied molecular orbital
M, mM, μM	units of concentration: molar, millimolar, micromolar
M, Met	amino acid, methionine
M9a	a type of bacterial growth medium
MPa	unit of pressure, megapascal, 0.1 MPa = 0.986 atm
MSMS	a molecular surface calculation program
N	native state
PAGE	polyacrylamide gel electrophoresis
PDB	Protein Data Bank
PIN diode	diode with intrinsic semiconductor layer between p- and n-type layers
PMT	photomultipler tube
psi	unit of pressure, pounds per square inch
RNA	ribonucleic acid
S9	nine-atom triethylene glycol linker
SAXS	small angle X-ray scattering
SAXS1, 2, 3	names of 3 high-pressure SAXS cells designed in this thesis
Se-Met	amino acid, selenomethionine-containing methione
Se-Met L99A	the mutant L99A with selenomethionine substituted for methionine
SNase	a protein, staphylococcal nuclease
sTRSV	satellite RNA of TRSV
SVD	singular value decomposition
T	transition state
T, Thr	amino acid, threonine
TEMED	tetramethylethylenediamine
Tris	tris(hydroxymethyl)aminomethane
TRSV	tobacco ringspot virus
U	uridine or uracil (in context of RNA)
UV	ultraviolet
U39C	a uridine-39 to cytidine mutation
V, Val	amino acid, valine
V149G	the mutation or mutant containing valine-149 to glycine
W, WAT	crystallographically identified water molecule
W, Trp	amino acid, tryptophan
WT*	cysteine-free (C54T/C97A) pseudo-wild-type of T4 lysozyme

LIST OF SYMBOLS

Å	Angstrom, a unit of length, 10^{-10} m
β_T	isothermal compressibility
$\Delta\beta_T$	change in isothermal compressibility due to denaturation
c	protein concentration
C_p	isobaric heat capacity
ΔC_p	change in isobaric heat capacity due to denaturation
D_{max}	maximum dimension of particle
$^\circ$	following number: degree, unit of angle; following thermodynamic variable: at standard conditions
$^\circ$C	unit of temperature, degree centigrade
e	charge of electron
E	electric field amplitude
E_0	incident electric field amplitude
E_{electron}, E_{protein}	electric field amplitude scattered from electron or protein
ϵ	molar extinction coefficient
f, f_D, f_N	mole fraction, denatured fraction, native fraction
$F[x]$	Fourier transform of variable, x
G	Gibbs' free energy
ΔG	change in free energy due to denaturation thermodynamic stability
ΔG°	thermodynamic stability at standard conditions
$\Delta\Delta G$	difference in thermodynamic stability between two protein mutants
G_D,G_N	free energy of denatured state, native state
H	enthalpy
ΔH	change in enthalpy due to denaturation
I	intensity
I_0	incident intensity
I_{electron}, I_{protein}	scattered intensity from electron or protein
I_A,I_A	absorbed intensity, fluorescence intensity
$I(q)$	buffer-substrated scattering profile, spherically averaged scattered intensity of protein
l	path length
λ	wavelength
$< \lambda >$	spectral center of mass
$< \lambda >_N$, $< \lambda >_D$	spectral center of mass of native or denatured states
k,$\vec{k}$	wavenumber, wavevector
K	unit of tempertature, Kelvins

K_T	isothermal compressibility factor
ΔK_T	change in isothermal compressibility factor due to denaturation
K_{eq}	equilibrium constant
m	mass of electron
μ	X-ray attenuation coefficient
N	number of data points
$\nu, < \nu >$	wavenumber, average wavenumber
ω	ratio of outer to inner diameter of tube
P, ΔP	pressure, change in pressure
P_m	midpoint of pressure denaturation
P_0	external pressure or reference pressure
$P(r)$	pair-distance distribution function
ϕ_F	fluorescence quantum yield
q	in context of X-ray scattering: momentum transfer; in context of thermodynamics, heat
R	gas constant, 83.1447 mL-bar/mole-K
R	in context of X-ray scattering: electron-detector distance; in context of high pressure seals, unsupported radius
r	in context of X-ray scattering: electron position or electron pair distance; in context of matrixes: rank
R^2	goodness of fit
$\vec{r}$	position of electron
r_e	radius of electron
R_c	material property, Rockwell hardness
R_g	radius of gyration
$\rho(\vec{r})$	electron density distribution
$\Delta\rho$	electron density contrast between protein and solvent
S	entropy
ΔS	change in entropy due to denaturation
σ	Poisson ratio
T	in context of thermodynamics: temperature; in context of high pressure seals, thickness
T_0	standard or reference temperature
T_S, T_H	temperature at which $T\Delta S = 0$, $\Delta H = 0$
2θ	scattering angle
U	internal energy
V	volume or in context of thermodynamics: partial molar volume
ΔV	volume change due to denaturation
ΔV°	volume change of denaturation at standard conditions
V_N, V_D	volume of native or denatured state
V_P	excluded volume of protein
w	external work
X	molal solubility [mole per kg water]
Y	yield strength
Z	atomic number

CHAPTER 1

INTRODUCTION

1.1 Overview

The relationship between the structure and thermodynamic stability of biological macromolecules is not fully understood as a function of pressure. The goal of this thesis is to provide further understanding of the mechanism of protein pressure denaturation and the effect of pressure on RNA structure. This chapter is largely devoted to introducing to the questions surrounding the pressure denaturation of proteins. To facilitate the discussion of this topic, the structure-stability relationship of proteins and the thermodynamics of two state denaturation are reviewed. The results obtained with the model protein, T4 lysozyme, are presented and discussed in Chapter 4. At the end of this chapter, the second topic investigated in this thesis, the effects of pressure on the tertiary structure of hairpin ribozyme, is briefly introduced, and the results are presented in Chapter 5. The study of these systems at high pressure necessitated the development of experimental techniques, namely high-pressure small-angle X-ray scattering and high-pressure fluorescence spectroscopy. The development and characterization of these techniques are described in Chapters 2 and 3. The final conclusions and suggested future experiments are outlined in Chapter 6.

1.2 The Pressure Denaturation of Proteins

The classical thermodynamic model of protein denaturation is founded upon the shared characteristics of thermal denaturation of proteins and temperature dependence of oil solubility in water. However, this model is not readily extended as a function of pressure. It has been observed that proteins denature at high pressure [17, 162, 52, 89], in other words, the pressure-denatured state of a protein is a lower volume state than the native state. The pressure dependence of oil solubility in water, however, fails to describe the volume change associated with the denaturation of proteins under pressure [162]. In recent years, studies have implicated the penetration of water into the hydrophobic core as the mechanism of pressure denaturation, a mechanism that is distinct from that of thermal denaturation [60]. In particular, the pressure-induced elimination of internal cavities in proteins is thought to be a significant contribution to the volume change associated with pressure denaturation [44, 115, 99]. This conclusion is supported by a high-pressure crystallography study of a cavity enlarged mutant of the globular protein T4 lysozyme [25]: It was shown by Collins, *et al.* that the cooperative water-filling of the enlarged hydrophobic cavity was favorable under pressure. To further understand the mechanism of pressure denaturation, this thesis reports on the investigation of the solution behavior of T4 lysozyme mutants with varying cavity volumes. Structural and thermodynamic characterization of the pressure-denatured states was performed with the complimentary methods of small-angle X-ray scattering and fluorescence spectroscopy. Correlating the pressure-denatured state with the known atomic structures of the native state provided insight into the mechanism of pressure denaturation.

1.2.1 Protein Structure and the Native State

Proteins perform many biological functions necessary for life. In this thesis, we consider the structure and denaturation thermodynamics of water-soluble globular proteins, such as enzymes and transporters, which occupy the aqueous intra- and extracellular fluid. In particular, the discussion will focus on the structure and free energy of small, monomeric globular proteins, including model proteins such as T4 lysozyme.

A protein molecule, after transcription and translation from its gene, is a linear polymer chain of amino acids with a specific sequence. During translation, the protein chain is synthesized from the formation of peptide bonds between amino acids by condensation reactions. The peptide linkages comprise the protein backbone, and the side chains are the chemical groups of the amino acids (or residues), of which there are twenty common types (Fig. 1.1 (a)). The sequence of the protein chain is called the *primary structure*. To achieve biological functionality, the protein folds into a compact and highly specific three-dimensional structure. A significant fraction of the protein backbone is organized into *secondary structures*, such as α-helices and β-sheets [111]. Secondary structures are formed by hydrogen bonding of the protein backbone in a regular pattern, and the side chains point away from these structural elements (Fig. 1.1 (b)). The side chain interactions become particularly important for the formation of the overall three-dimensional folded conformation or *tertiary structure* (Fig. 1.1 (c)). Although structural fluctuations are necessary for biological function, the final folded conformation is nearly unique and extremely well packed, typically containing packing defects, or internal cavities, that are in total less than 1% of the volume of a protein [115]. This density is comparable to an amino acid crystal, which is remarkable. For a protein that consists of a single globular unit or monomer, the tertiary structure is typically its folded or native state.

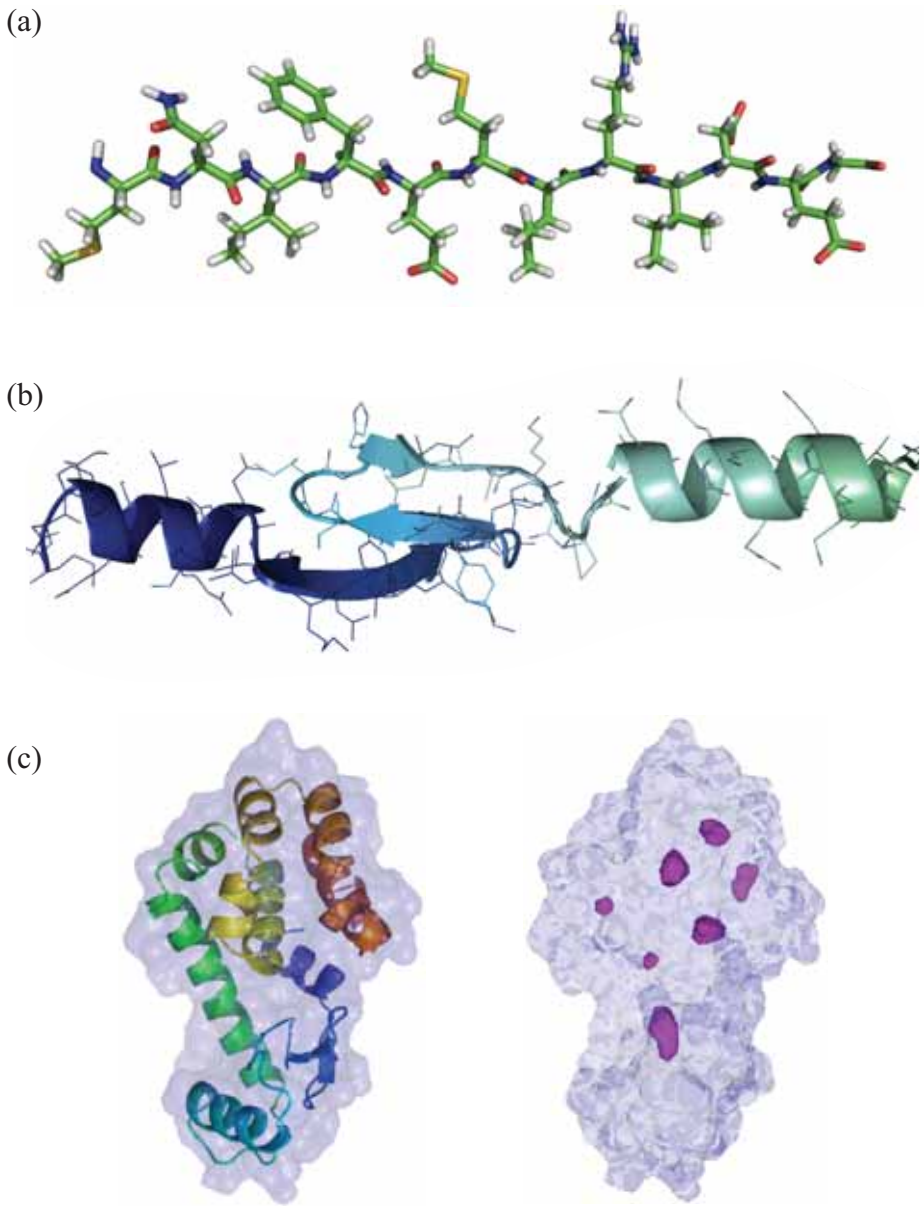

Figure 1.1: The native structure of a small, monomeric globular protein, T4 lysozyme. (a) The first 11 amino acids of the N-terminus of T4 lysozyme (from left to right). The zig-zagged protein backbone is comprised of peptide linkages, while the side chains are the chemical groups of the amino acids. (b) The first α-helix, a β-sheet, and the second α-helix of the N-terminus of T4 lysozyme (from left to right). (c) A cartoon representation of the overall three-dimensional structure of T4 lysozyme is shown on the left with an outline of the external surface. The internal cavities, or packing defects, that exist in this protein are shown on the right in magenta. Some of these cavities are occupied by internal water molecules.

1.2.2 Protein Folding and Denaturation

After translation, a protein must arrive at its biologically functional native state through a large conformational change, called folding. Many proteins, small ones in particular, can do so spontaneously without the aid of molecular chaperones [6, 42]. For such a protein, the native state is the most energetically favorable state under physiological conditions.

The reverse process in which the protein loses its native structure is called unfolding or denaturation. Protein denaturation can be observed in the kitchen when cooking protein-rich foods such as eggs. The opaque appearance of cooked egg white is due to the aggregation of thermally-denatured egg proteins. In the laboratory, denaturation is commonly promoted by exposing proteins to a non-physiological temperature, pressure, pH, or chemical composition of the solvent. Like folding, denaturation is thought to be a biologically important process [42, 29]. *In vivo*, the transport of proteins across the cell membrane requires denaturation [29]. Proteases, which are important agents for protein turnover in the cell, are also thought to act selectively on denatured proteins [29]. There also exists a class of water-soluble non-globular proteins known as intrinsically disordered proteins, which are normally denatured and only acquire structure when its biological function is switched on by binding a ligand [146].

The denatured state differs from the native state in that there is no defined structure. In other words, the denatured state is an ensemble of many conformations. The fully unfolded state of a protein is that which is an ensemble of random coil conformers. However, in recent years it has become clear that even under strong denaturing conditions, proteins retain some structure [29]. As a result, the nature of the denatured state also depends on the denaturant. For a particular protein, multiple denatured states can exist with various degrees of average backbone unfolding and hydration. Typically, the

greatest degree of backbone unfolding occurs by chemical denaturation, while changes in temperature, pressure, and pH yield more compact denatured states. Compact denatured states are often distinguished from fully unfolded states and classified as molten globule or partially unfolded states. In this thesis, however, the term "denatured" will be used to describe all non-native states. "Folded" and "native" will be used interchangeably. Intermediate states will not be discussed here as we will focus exclusively on two-state denaturation processes.

The relationship between the native and denatured states of a protein can be discussed in terms of its energy landscape. The energy landscape of a protein under physiological conditions can be visualized as a funnel with a deep minimum that corresponds to the native state. Minima at higher energy correspond to the various denatured states. Let us consider a cross section of this energy landscape along one reaction coordinate where reversible, two-state denaturation applies, e.g. between the native (N) and denatured (D) states, under a given set of experimental conditions (Fig. 1.2 (a)).

$$\mathrm{N} \rightleftharpoons \mathrm{D}$$

The two states are separated by a free energy barrier corresponding to the transition state (T) (Fig. 1.2). Because the transition state is unstable, the denaturation of small globular proteins is a first-order, i.e. cooperative, transition [29, 42]. The cooperativity is a feature that distinguishes protein folding from the coil-globule transitions of polypeptide chains with random sequences [81].

The energetic difference between the free energy minima corresponding to the native and denatured states determines the likelihood that a given protein is native or denatured. A protein is fully folded for a greater fraction of the time if this difference is greater. For the rest of the time, the protein is denatured, even under physiological conditions. Equivalently stated, both native and denatured populations exist in equilibrium under

any given set of conditions. By changing a parameter, such as temperature or pressure, the energy landscape is altered. Generally, as the temperature or pressure is raised above the physiological level, the energetic difference between the two states decrease until at one point it becomes zero where the two states are equally favorable and then switches sign when the denatured state becomes more favorable (Fig. 1.2 (b)-(c)).

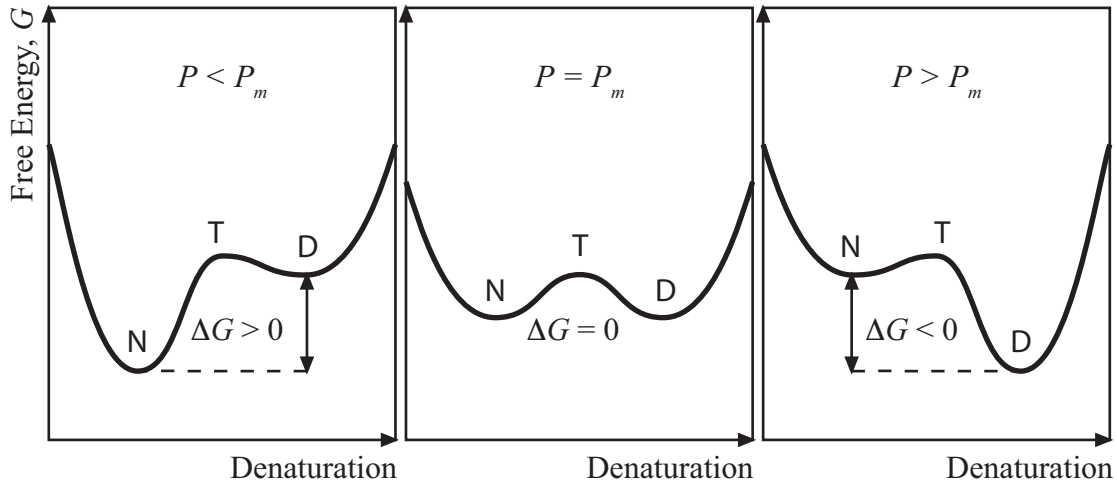

Figure 1.2: Illustration of the free energy landscape of two-state denaturation. A free energy barrier corresponding to the transition state (T) separates the native (N) and denatured (D) states. (a) At ambient pressure where the free energy difference between the native and denatures states, $\Delta G > 0$, the native state is more stable than the denatured state. (b) At the pressure midpoint, P_m where $\Delta G = 0$, both states are equally favorable. (c) Above P_m where $\Delta G < 0$, the denatured state is more favorable.

In an experiment where the average behavior of proteins in solution is measured, the energetic difference between the native and denatured state is called the *thermodynamic stability* [10, 120]. Conventionally, the thermodynamic stability of this system is defined as the difference between the partial molar Gibbs free energy of the denatured state (G_D) and native state (G_N) (Fig. 1.2).

$$\Delta G = G_D - G_N. \tag{1.1}$$

If the native and denatured states of the protein have characteristic signals, such as fluorescence spectra, the mole fraction of each species, f_N and f_D, can be determined experimentally. For ideal protein solutions, i.e. where the native and denatured proteins in solution are non-interacting, the equilibrium constant of protein denaturation, K_{eq}, is ratio of the denatured to native fractions at a given condition [112]. The thermodynamic stability as a function of temperature, T, or pressure, P, is thus expressed as

$$\Delta G(T,P) = -RT \ln K_{eq}(T,P) = -RT \ln \frac{f_D(T,P)}{f_N(T,P)}, \tag{1.2}$$

where R is the gas constant (83.1447 mL-bar/mol-K).

Although the native structure of a protein can be solved by X-ray crystallography or NMR, the energetic origins of the native structure and function are not yet fully understood [58]. Denaturation studies are thus often motivated by an interest in better understanding the native state. Measurement of the change in stability due to a mutation enables quantification of the contribution of specific interactions to the stability of the native structure [87]. Denaturation studies also provide insight into the structural characteristics of the denatured state, which cannot be solved by conventional 3-D structure determination methods, as well as the mechanism of denaturation.

1.2.3 Two-State Thermodynamics

Let us consider the thermodynamics of two state transitions, e.g. two-state protein denaturation, as a function of temperature, T, and pressure, P. Recall that the Gibbs free energy, G, and enthalpy, H, of a given state (native or denatured) in equilibrium are,

$$H = U + PV, \tag{1.3}$$

$$G = H - TS, \tag{1.4}$$

where U is the internal energy, V is the volume, and S is the entropy. The free energy differential, dG, and enthalpy differential, dH, is expressed as follows:

$$\begin{aligned} dH &= dU + PdV + VdP, \quad (1.5) \\ dG &= dH - TdS - SdT. \quad (1.6) \end{aligned}$$

Under reversible conditions, the internal energy differential is the sum of the differentials of heat, dq, and work applied to the system, $dw = -PdV$,

$$dU = dq + dw = TdS - PdV. \quad (1.7)$$

Therefore,

$$dG = VdP - SdT. \quad (1.8)$$

From Eqn. (1.8), we arrive at two Maxwell relations:

$$\begin{aligned} \left(\frac{\partial G}{\partial T}\right)_P &= -S, \\ \left(\frac{\partial G}{\partial P}\right)_T &= V. \quad (1.9) \end{aligned}$$

From (1.9) and the definitions of the isobaric (at constant pressure) heat capacity, C_p, the isothermal compressibility, β_T, and isothermal compressibility factor, K_T, we find that

$$\begin{aligned} \left(\frac{\partial^2 G}{\partial T^2}\right)_P &= -\left(\frac{\partial S}{\partial T}\right)_P = -\frac{1}{T}\left(\frac{\partial q}{\partial T}\right)_P = -\frac{1}{T}\left(\frac{\partial H}{\partial T}\right)_P \equiv -\frac{C_p}{T}, \\ \left(\frac{\partial^2 G}{\partial P^2}\right)_T &= \left(\frac{\partial V}{\partial P}\right)_T \equiv -\beta_T V = -K_T. \quad (1.10) \end{aligned}$$

We then expand the free energy with respect to T and P. The first fundamental theorem of calculus states that for a function, $df(x)/dx$, that is continuous in the interval $[x_0, x]$,

$$\int_{x_0}^{x} \frac{df(x)}{dx} dx = f(x) - f(x_0). \quad (1.11)$$

At constant pressure, the free energy as a function of temperature may therefore be written as the sum of the free energy at a reference temperature, T_0, and the change in free energy over the temperature interval, $T - T_0$. Applying Eqn. (1.11) twice and substituting (1.9) and (1.10),

$$G(T) = G(T_0) - S(T_0)(T - T_0) - \iint_{T_0}^{T} \frac{C_P}{T} dT. \tag{1.12}$$

Likewise, at constant temperature, the free energy with respect to a reference pressure, P_0, is

$$G(P) = G(P_0) + V(P_0)(P - P_0) - \iint_{P_0}^{P} K_T dP. \tag{1.13}$$

The free energy difference between two states, e.g. the native and denatured states of a protein (Eqn. (1.1)), is therefore expressed by the following equations.

$$\Delta G(T) = \Delta G(T_0) - \Delta S(T_0)(T - T_0) - \iint_{T_0}^{T} \frac{\Delta C_p}{T} dT, \tag{1.14}$$

$$\Delta G(P) = \Delta G(P_0) + \Delta V(P_0)(P - P_0) - \iint_{P_0}^{P} \Delta K_T dP. \tag{1.15}$$

where ΔS, ΔC_p, ΔV, and ΔK_T are the changes in entropy, isobaric heat capacity, volume, and isothermal compressibility factor accompanying denaturation. From (1.10), ΔC_p and ΔK_T can be related to ΔV, ΔS, and the enthalpy change, ΔH by the following:

$$\Delta C_p = \left(\frac{T \partial \Delta S}{\partial T} \right)_P = \left(\frac{\partial \Delta H}{\partial T} \right)_P, \tag{1.16}$$

$$\Delta K_T = -\left(\frac{\partial \Delta V}{\partial P} \right)_T. \tag{1.17}$$

1.2.4 Thermodynamic Model of Protein Denaturation

It is widely believed that the hydrophobic effect is the dominant driving force in protein folding. In this *liquid hydrocarbon compound transfer model* of proteins, denaturation is described as the transfer of hydrophobic residues from the hydrophobic core of

the molecule to the solvent [61, 62] (Fig. 1.3). Early X-ray crystallographic protein structures [103, 64] supported this model by revealing that hydrophobic residues are sequestered in the cores of the native structures of globular proteins. The liquid hydrocarbon compound transfer model originates from the similar thermodynamic features of the temperature dependence of oil solubility in water and the thermal denaturation of proteins. Fig. 1.4 (a) shows the temperature dependence of $\Delta G_{\text{oil-water}}$, the transfer energy of oil from its liquid phase to water, and the associated changes in enthalpic and entropic terms, $\Delta H_{\text{oil-water}}$ and $T\Delta S_{\text{oil-water}}$. The corresponding data for the thermal denaturation of a protein, ΔG_{den}, ΔH_{den}, and $T\Delta S_{\text{den}}$ are shown in Fig. 1.4 (b). In both cases, ΔG is large and positive around ambient temperature ($\approx 25\ ^{\circ}\text{C}$). The liquid hydrocarbon compound transfer model is further supported by measurement of the change in heat capacity, ΔC_p, for the thermal denaturation of proteins and oil dissolution in water. In both cases, ΔC_p was found to be large and positive [28]. This result is reflected in the curvature of ΔG and large positive slopes of ΔH and $T\Delta S$ in Fig. 1.4 (a)-(b) (refer to the relations (1.10) and (1.16)). A large and positive ΔC_p implies the existence of a temperature at which protein stability is maximized (Fig. 1.5). Thus, the temperature dependence of oil solubility in water successfully predicts the phenomenon of cold denaturation, i.e. the denaturation of proteins induced by lowering the temperature from ambient levels, further supporting the liquid hydrocarbon compound transfer model [110, 48, 94]. Because ΔC_p is a significant quantity in thermal denaturation, the thermal stability of proteins is thus commonly modeled by a second-order expansion of Eqn. (1.14).

$$\Delta G(T) = \Delta H(T_0) - T\Delta S(T_0) - \Delta C_p(T_0)\left[T_0 - T + T\ln\frac{T}{T_0}\right], \tag{1.18}$$

where Eqn. (1.3) has been substituted into $\Delta G(T_0)$.

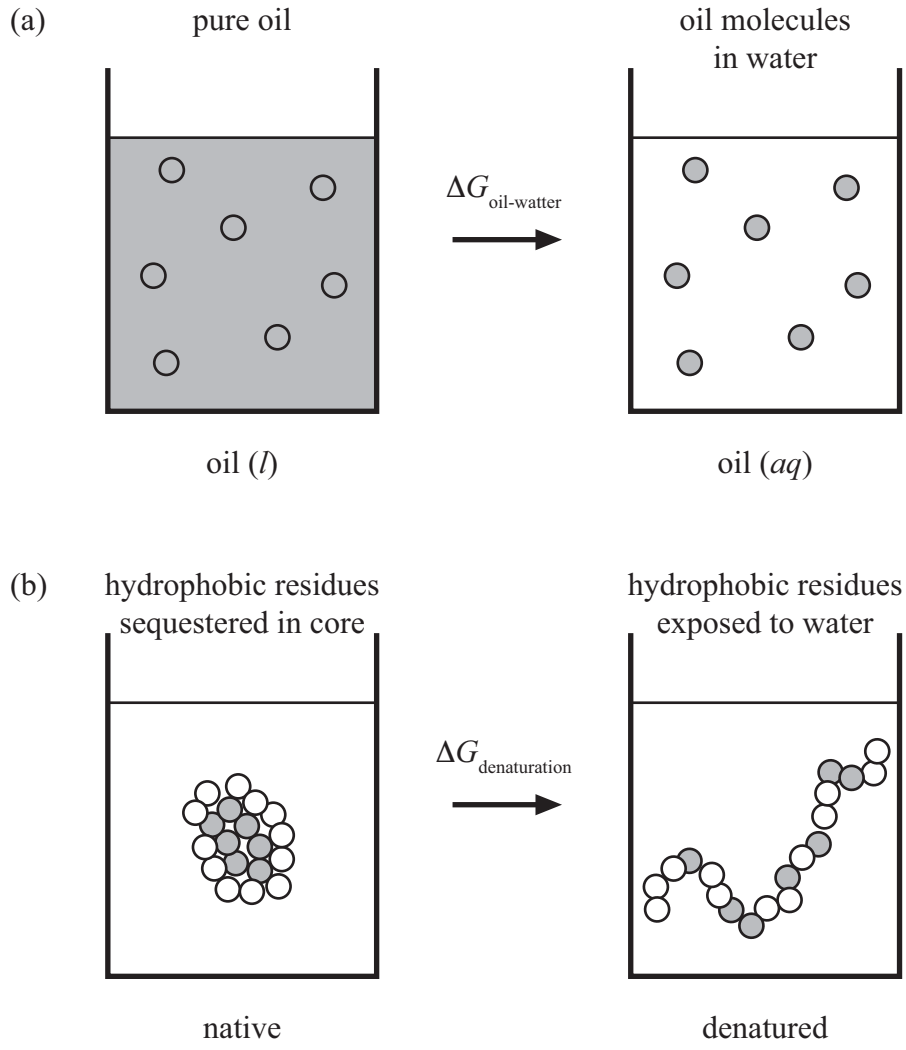

Figure 1.3: The liquid hydrocarbon transfer model of protein denaturation. Aqueous environments and hydrophilic residues are shown in white. Oily components such as hydrophobic molecules and residues are shown in gray. The circles represent single molecules or residues, not droplets. (a) The transfer of model hydrocarbon molecules from its liquid phase to water. (b) The denaturation of proteins. In this model, protein denaturation is described as the transfer of hydrophobic residues from the oily hydrophobic core to water in thermal denaturation.

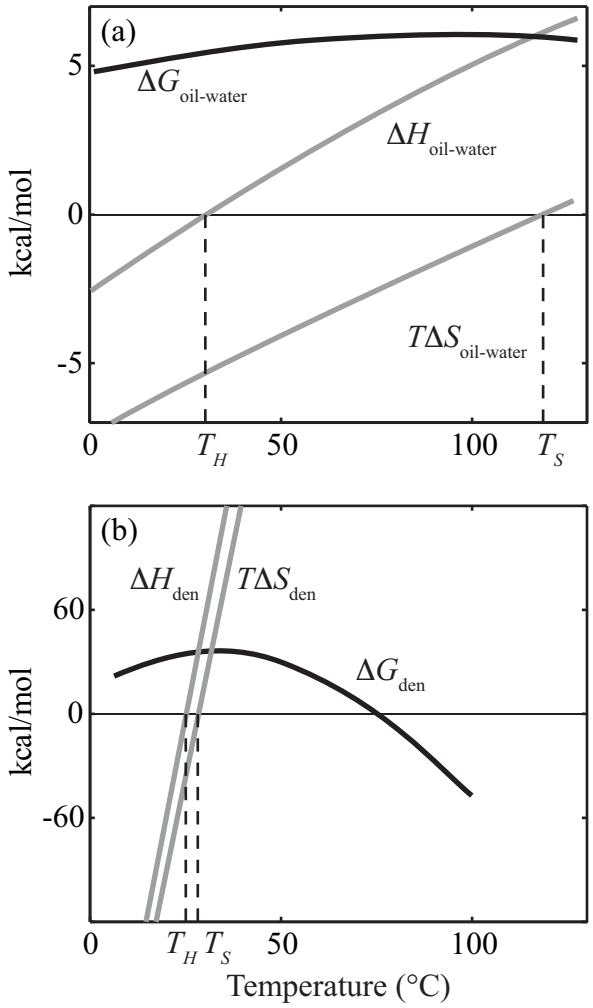

Figure 1.4: A comparison of the temperature dependence of oil solubility in water and the thermal denaturation of proteins (adapted from [77, 85, 128]. (a) The transfer energy of neopentane from its liquid phase to water, $\Delta G_{\text{oil-water}}$, and the associated changes in enthalpic and entropic terms, $\Delta H_{\text{oil-water}}$ and $T\Delta S_{\text{oil-water}}$. (b) The thermal stability of the protein myoglobin, ΔG_{den}, and the changes in enthalpic and entropic terms, ΔH_{den} and $T\Delta S_{\text{den}}$, associated with thermal denaturation. T_S is the temperature at which $T\Delta S = 0$ and T_H at which $\Delta H = 0$.

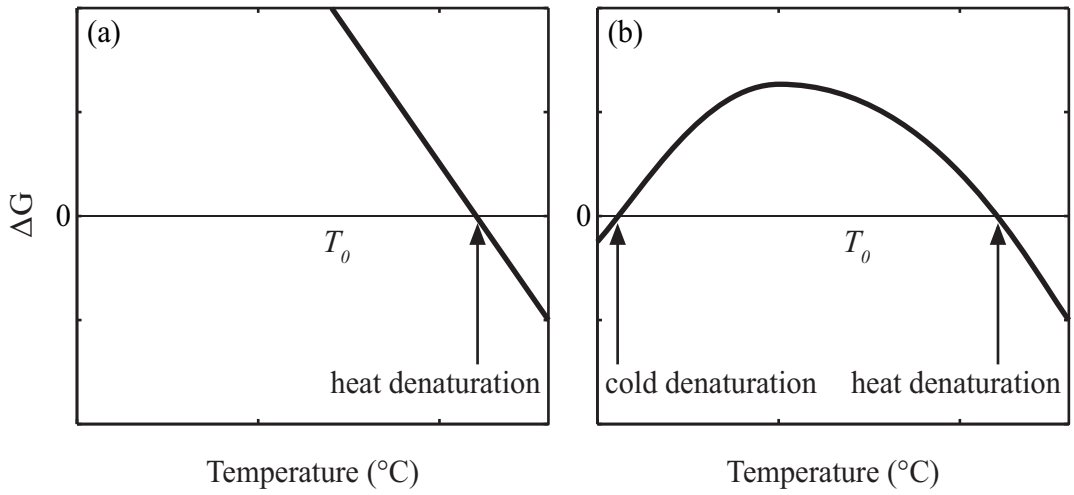

Figure 1.5: The stability, ΔG, of a protein that is native (folded) at ambient temperature, T_0, and exhibits two-state denaturation (native vs. denatured) as a function of temperature. (a) The change in heat capacity with denaturation is taken to be zero. The protein denatures at a high temperature, $> T_0$. (b) A large and positive heat capacity change is accounted for. Cold denaturation at a second temperature, $< T_0$, is predicted.

However, the liquid hydrocarbon compound transfer model alone cannot account for the subtle contributions of other interactions to the temperature dependence of the thermodynamic stability of proteins. The temperature dependence of oil solubility in water and the thermal denaturation of proteins are similar, but not equivalent. The transfer energy of oil in water is much smaller in magnitude per unit of nonpolar surface area compared with the thermal stabilities of proteins [128]. The entropic term $T\Delta S$ is also much closer in value to the enthalpic term ΔH in the case of proteins than in the oil-in-water system. This is reflected by the relationship of two temperatures, T_S and T_H, at which $T\Delta S = 0$ and $\Delta H = 0$. In the case of proteins, $T_S \approx T_H$, while $T_S >> T_H$ for oil in water (Fig. 1.4). A possible reason for these differences is that the polymeric nature of proteins is not accounted for in the liquid hydrocarbon compound transfer model; protein denaturation is accompanied by a gain in conformational entropy [128]. Measured values for the transfer free energies from oil-water partition experiments are

often used to predict or explain mutation-induced changes in the stability of a protein. It was demonstrated, however, that leucine-to-alanine substitutions at different buried sites of T4 lysozyme had context-dependent consequences to the thermal stability and that the context-dependent loss of van der Waals interactions was responsible for this [35]. More significantly, the liquid hydrocarbon transfer model fails completely as a thermodynamic model of protein denaturation with respect to pressure [162].

1.2.5 The Volume Properties of Proteins

While the temperature-dependence of oil solubility in water largely succeeds in describing major features of the thermal denaturation of proteins, under variable pressure, proteins display contrasting behavior to that of oil in water. The discussion of the relative pressure stability of two states necessitates the examination of the volume change from the initial state to the final state. It is well known that dissolving a solute in a solvent generally does not result in a final solution volume that is the sum of the components' initial volumes. The change in the volume of the solvent caused by dissolving a single solute molecule is known as the partial molar volume. In other words, the partial molar volume of a protein represents the hydrated volume of the protein.

As high pressure stabilizes low volume states, the transition from the initial to final state is favored if the change in partial molar volume is negative. The volume change from the native to pressure-denatured state of a protein, ΔV, is known as the volume change of unfolding or denaturation.

$$\Delta V = V_D - V_N, \tag{1.19}$$

where V_D and V_N are the partial molar volumes of the denatured and native states. If pressure denaturation is consistent with the transfer of hydrophobic residues from the

hydrophobic core to the surrounding water, the volume change of protein pressure denaturation should correlate with the volume change associated with the transfer of a model hydrophobic compound from its liquid phase to water. However, this is not the case.

The volume change associated with the transfer of a model hydrophobic compound from its liquid phase to water, $\Delta V_{\text{oil–water}}$, is determined from the partition of oil in its liquid and aqueous phases.

$$\text{oil}\,(l) \rightleftharpoons \text{oil}\,(aq)$$

Assuming an ideal solution, the equilibrium constant of this process is the ratio of the mole fractions of oil in water, f_{aq}, and of oil in its liquid phase, f_l. Since, the mole fraction of oil in its pure phase is 1, the free energy of transferring oil from pure oil to water is

$$\Delta G_{\text{oil–water}} = -RT \ln f_{aq}. \tag{1.20}$$

The change in ΔG at some pressure, P, relative to that ambient pressure, P_0, can be determined by the experimentally measurable molal solubility of oil in water, X.

$$\Delta G_{\text{oil–water}}(P) - \Delta G_{\text{oil–water}}(P_0) = -RT \ln \frac{f_{aq}(P)}{f_{aq}(P_0)} = -RT \ln(X/X_0), \tag{1.21}$$

where X_0 is the solubility at P_0. Fig. 1.6 (a) shows the pressure-dependence of this quantity for 4-octanone in water (data from [69]). Fig. 1.6 (b) shows the volume change associated with the transfer of a 4-octanone molecule to water determined from the slope of $-RT \ln(X/X_0)$ vs. P (refer to Eqn. (1.15)) [69]. The volume change of transferring 4-octanone was found to be pressure-dependent; it is large and negative at low pressure, becomes less negative at higher pressures, and finally becomes small and positive above the relatively low pressure of 150 MPa. Similar trends were observed for n-propyl benzene [163, 162]. Assuming 10 hydrophobic residues are exposed to solvent upon denaturation, the 4-octanone model predicts a volume change of denaturation that

is ≈ -600 Å^3 at ambient pressure and positive above 150 MPa. In other words, the liquid hydrocarbon compound transfer model predicts that pressure denaturation is very favorable at low pressure and becomes less favorable with increasing pressure. This may be more intuitively understood by inspection of Fig. 1.6 (a); this curve predicts that the protein stability will decrease with pressure relative to ambient levels below 150-200 MPa, and that the trend reverses above this pressure.

Proteins, however, display vastly different behavior. Proteins have been shown to denature with a pressure midpoint of several hundred megapascals with a volume change that is negative and small in magnitude, ≈ -30 to -300 Å^3, for proteins roughly 10,000 to 30,000 Å^3 in total volume [162, 115]. Refolding of pressure-denatured proteins at higher pressure has not been reported, consistent with volume changes of denaturation that are relatively pressure-independent. The pressure denaturation of proteins is thus well-modeled by a first-order expansion of ΔG (Eqn. (1.15)),

$$\Delta G(P) = \Delta G(P_0) + \Delta V(P_0)(P - P_0), \tag{1.22}$$

while the description pressure dependence of oil solubility requires at least two higher order terms (first and second derivatives of ΔV). The difference between the pressure dependence of oil-in-water and proteins may be in part due to the difference in compressibility of the native proteins and oil [128]. Proteins are highly incompressible - roughly a factor of 10 compared with oil at atmospheric pressure [52]. It should also be noted that the volume change of transferring hydrocarbons from its solid state into water is also pressure-dependent and therefore, unable to describe pressure denaturation of proteins [68].

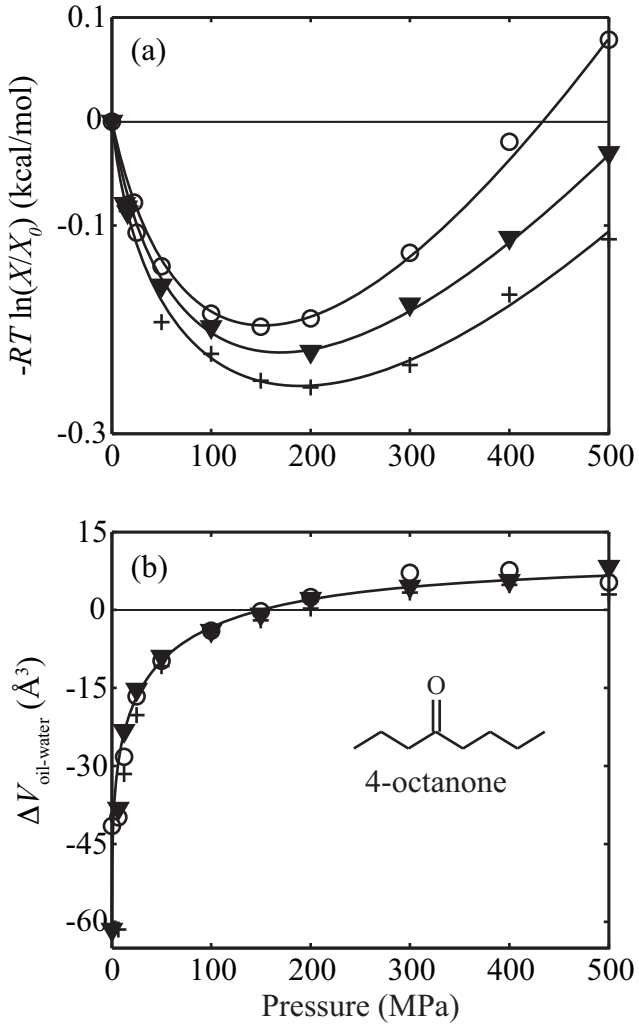

Figure 1.6: The pressure dependence of the 4-octanone solubility in water, X, in units of moles per kg water at 15 °C (○), 25 °C (▼), and 35 °C (+) (data from Kliman thesis [69]). (a) The free energy of transfer of oil from its liquid phase to water relative to the value at ambient pressure, P_0. A strong curvature is evident. (b) The volume change associated with the transfer of 4-octanone to water, $\Delta V_{\text{oil}-\text{water}}$. Trend lines were drawn as visual guides.

It is noted that Eqns. (1.18) and (1.22) are often written using the following notation.

$$\Delta G(T) = \Delta H^\circ - T\Delta S^\circ - \Delta C_p^\circ \left[T_0 - T + T \ln \frac{T}{T_0} \right] \quad (1.23)$$

$$\Delta G(P) = \Delta G^\circ + \Delta V^\circ (P - P_0) \quad (1.24)$$

The quantities ΔH°, ΔS°, and ΔC_p° are the enthalpy, entropy, and isobaric heat capacity changes measured at the reference temperature, T_0. Likewise, $\Delta G^\circ$and $\Delta V^\circ$are the stability and volume change measured at the reference pressure, P_0.

1.2.6 Water Penetration

Much of what is currently understood about pressure denaturation of proteins is derived from the extensive experimental and theoretical work on the globular protein staphylococcal nuclease (SNase) [44, 99, 101, 100, 122, 18, 149, 76, 156]. Small angle X-ay scattering (SAXS) and Fourier transform infrared spectroscopy (FTIR) indicated that the pressure-denatured state of SNase is structurally different from the thermally denatured state. The radius of gyration of the pressure-denatured SNase was found to be 35 Å while that of the thermally denatured SNase was 45 Å [101]. The pressure-denatured state was also found to retain more secondary structure [101, 100]. Tryptophan fluorescence measurements of SNase mutants with large-to-small amino acid substitutions at a buried site indicated that the volume change of denaturation is at least partially due to the hydration of internal packing defects [44]. These observations imply that the pressure denaturation of SNase, and other globular proteins, is achieved by a hydration mechanism that is distinct from thermal denaturation.

Molecular dynamics simulations by Hummer, *et al.* [60] provided a model of pressure denaturation that is distinct from thermal denaturation but remains consistent with the hydrophobic effect as the dominant force in protein folding. The simulations re-

vealed the existence of two free-energy minima for a pair of methane molecules in water under pressure. At low pressure, the methane pair prefers the dimer state but at higher pressure, increasingly favors a water-separated state. This result implies that the pressure denatured state of globular protein molecules is one in which water has penetrated the hydrophobic core of the molecule rather than one in which hydrophobic residues have been transferred into water. Such a model is consistent with the observed compactness of the pressure-denatured proteins and the dependence of volume change on internal packing defects. In a molecular dynamics simulation of the pressure denaturation of SNase, water penetration had to be initiated in order to induce denaturation within accessible timescales [99]. The denatured structures resulting from this simulation showed similarity to those experimentally characterized by small-angle neutron scattering.

The water penetration model of protein denaturation by pressure is further supported by high-pressure X-ray crystallographic and molecular dynamics experiments by Collins, *et al.* [25]. X-ray structures by Collins, *et al.* explicitly showed the progressive water filling of an enlarged hydrophobic cavity in the L99A mutant of the protein bacteriophage T4 lysozyme (Fig. 1.7). The wild-type T4 lysozyme shows no such filling of its corresponding, smaller cavity at pressures up to 200 MPa. Molecular dynamics simulations suggest that the cavity is cooperatively filled by four water molecules as the pressure applied to the molecule is increased.

In this thesis, we explore the following questions. What constitutes a pressure-denatured state? How does the volume change upon denaturation correlate with cavity volume? Can other hydration mechanisms be distinguished from cavity filling? Is pressure denaturation consistent with the water penetration model?

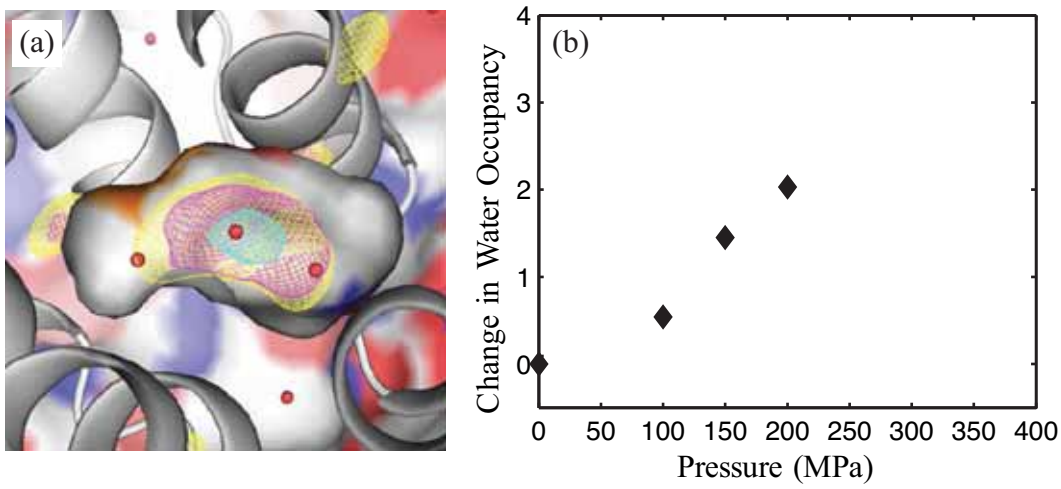

Figure 1.7: The pressure-induced water-filling of the large hydrophobic cavity in L99A T4 lysozyme was observed by high-pressure crystallography (figure and data reproduced from [25]). (a) The electron density of water at 1 atm (yellow mesh), 100 MPa (magenta), and 200 MPa (cyan) is shown superimposed over the cavity (white bubble). (b) The change in water occupancy of the large cavity determined by the integration of the electron density.

The solution behavior of L99A and three additional T4 lysozyme mutants with varying cavity volumes [86, 37, 158, 159, 80] were characterized using the complementary methods of high-pressure small-angle X-ray scattering (SAXS) and tryptophan fluorescence spectroscopy (see Chapter 4). Equipment and experimental methods for high-pressure SAXS [5] and fluorescence spectroscopy developed for this work are described in Chapters 2 and 3. SAXS is one of the few methods by which the global structure of proteins in solution, and particularly of denatured proteins, can be directly probed. In this thesis, SAXS was used to characterize the pressure-induced structural changes in L99A T4 lysozyme. Tryptophan fluorescence spectroscopy was utilized for the quantification of the native and denatured fractions of the proteins under various equilibrium conditions. Thermodynamic analysis was performed on tryptophan fluorescence data taken at various solvent conditions on all mutants. A fluorescence quenching study of a

seleno-methionine variant of L99A provided additional information on global structural changes due to high pressure. The results provide insight into the relationship between the thermodynamic and structural characteristics of T4 lysozyme and confirm that pressure denaturation is characteristically distinct from thermal and chemical denaturation. It is shown that the study of pressure effects provides further understanding of the energy landscape and the structure-stability relationship of proteins.

1.3 Other Biomacromolecules under Pressure

Later in the thesis, the effect of pressure on the relationship between structure, stability, and function of hairpin ribozyme is explored (see Chapter 5). Ribozymes are RNA molecules or regions of RNA that catalyze chemical reactions. Like proteins, ribozymes adopt three-dimensional structures that enable biological function. While denaturation thermodynamics provide into the energetic interactions responsible for the structural stability of proteins and ribozymes, thermal and chemical denaturation studies have shown that the folding pathways of ribozymes are not simple two-state transitions. Interpretation of the denaturation thermodynamics of hairpin ribozyme is therefore difficult. Using high-pressure fluorescence spectroscopy, high hydrostatic pressure was investigated as a method for selective measurement of the tertiary structure stability, i.e. free energy difference between the active and non-active forms, of hairpin ribozyme.

CHAPTER 2

HIGH-PRESSURE SMALL ANGLE X-RAY SCATTERING

2.1 Small-angle X-ray scattering of Proteins in Solution

Small-angle X-ray scattering (SAXS) is the product of interference between elastically scattered X-rays from individual electrons in the sample and is therefore, sensitive to the three-dimensional distribution of electrons. As protein samples for SAXS are in solution, structural information is spatially and rotationally averaged. Unlike X-ray diffraction from crystalline samples, SAXS yields only low-resolution structural information, such as the radii of gyration and envelope reconstructions of protein structures. However, SAXS can provide information on conformations that can only be populated in solution [79, 46, 132]. These structures include denatured protein ensembles and large macromolecular complexes. In this thesis, high-pressure SAXS was used to characterize the solution structure and pressure-denatured state of T4 lysozyme [5].

2.1.1 X-ray Scattering of Particles in Solution

In this thesis, we are concerned with protein SAXS under non-resonant conditions, i.e. at X-ray energies far from electron binding energies. Under such conditions, the X-ray scattering by an electron in a sample is weak and is independent of the atomic environment of the electron. Thus, all of the electrons in the sample contribute equally as scatterers. The interference of scattered X-rays from individual electrons gives rise to the scattering of a multielectron particle, such as a protein.

The scattering event of a single, free electron can be understood as an incident plane

wave applying an oscillating Lorentz force on the electron, causing it to emit a spherical wave (Fig. 2.1). The incident wave is described as a plane wave propagating along the z-direction with electric field amplitude, E_0 and wavevector, $\vec{k_0} = k_0\hat{z}$.

$$E_{\text{incident}} = E_0 e^{ik_0 z}. \tag{2.1}$$

The scattered wave is then described as a spherical wave with wavevector $\vec{k_r} = k_r\hat{R}$. As there is no energy loss in elastic scattering, $k_r = k_0 = 2\pi/\lambda$, where λ is the X-ray wavelength.

$$E_{\text{electron}} \propto E_0 \frac{e^{ik_r R}}{R}, \tag{2.2}$$

where R is the electron-detector distance.

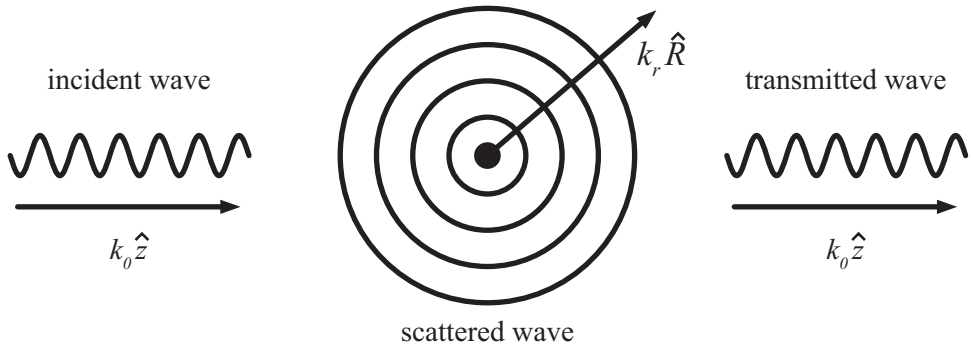

Figure 2.1: A plane wave traveling along $\hat{z}$ with wavelength $2\pi/k_0$ is incident on an electron (closed circle in center). Most of the wave is transmitted. A small fraction is scattered as a radially propagating spherical wave with wavelength $2\pi/k_r$.

The momentum transfer vector, $\vec{q} = \vec{k_r} - \vec{k_0}$, describes the change in direction of propagation due to scattering. The magnitude of the momentum transfer vector is given by

$$q = (4\pi/\lambda)\sin(\theta), \tag{2.3}$$

where 2θ is the scattering angle (Fig. 2.2). The scattering intensity at a distance R and angle 2θ from a single electron caused by an unpolarized incident wave is given by the Thomson scattering formula,

$$I_{\text{electron}} \propto |\vec{E}_{\text{electron}}|^2 = E_0^2 \cdot \frac{r_e^2}{R^2} \cdot \overbrace{\frac{1+\cos^2(2\theta)}{2}}^{\text{polarization factor}}, \tag{2.4}$$

where e and m are the electron charge and mass, and r_e is the classical electron radius. Note the R^{-2} dependence of the scattering intensity expected for a spherical wave (Eqn. (2.2)). In the small-angle regime, where θ is very small, $\cos(2\theta) \approx 1$, and hence, the polarization factor (the last factor in Eqn. (2.4)) is approximated as 1.

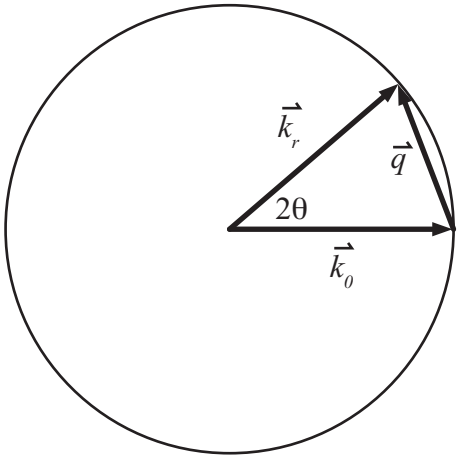

Figure 2.2: In the elastic scattering case, $\vec{k_r}$ and $\vec{k_0}$ lie on a sphere of radius $2\pi/\lambda = k_r = k_0$ (the Ewald sphere). The magnitude of $\vec{q}$ is dependent on the scattering angle, 2θ.

Let us now consider the scattering of many closely packed electrons, such as those in a protein molecule. Protein molecules are predominantly composed of low Z elements such as carbon, nitrogen, oxygen and sulfur. As typical X-ray energies are high when compared to the binding energies of electrons in low Z elements, all of the electrons in a protein molecule contribute equally as scatterers. An exception to this case is when the

X-ray energy is tuned to an absorption edge of an atom in the sample, causing a resonant scattering effect, not discussed further here. In the common case of non-resonant X-ray scattering from a protein molecule, waves scattered from individual electrons interfere (Fig. 2.3). The position of each electron, $\vec{r}$, determines the relative phase of the wave scattered by the electron, $-\vec{q}\cdot\vec{r}$ (Fig. 2.3); note that the dimension of $-\vec{q}\cdot\vec{r}$ is radians. Each electron emits a spherical wave,

$$E_{\text{electron}} \propto E_0 \frac{e^{ik_r R - \vec{q}\cdot\vec{r}}}{R}. \tag{2.5}$$

In the far-field approximation, the separation of the electrons in the protein is much smaller than the electron-detector distance, $\vec{R}$. In other words, $\vec{R}$ can be considered constant and parallel for all electrons. Thus, the total scattering amplitude from a protein can be determined by a sum over all of the electrons. Treating the electron density distribution, $\rho(\vec{r})$, as continuous, the scattering amplitude is determined by the integral over the protein molecule volume, V.

$$E_{\text{protein}} = \int_V E_{\text{electron}}\rho(\vec{r})dV \propto \frac{E_0}{R}e^{ik_r R}\int_V e^{-i\vec{q}\cdot\vec{r}}\rho(\vec{r})dV = \frac{E_0}{R}e^{ik_r R}F[\rho(\vec{r})], \tag{2.6}$$

where $F[\rho(\vec{r})]$ is the Fourier transform of the electron density distribution. The scattered intensity of a single protein is therefore, proportional to the square of the Fourier transform of the electron density distribution.

$$I_{\text{protein}} \propto |E_{\text{protein}}|^2 \propto |F[\rho(\vec{r})]|^2. \tag{2.7}$$

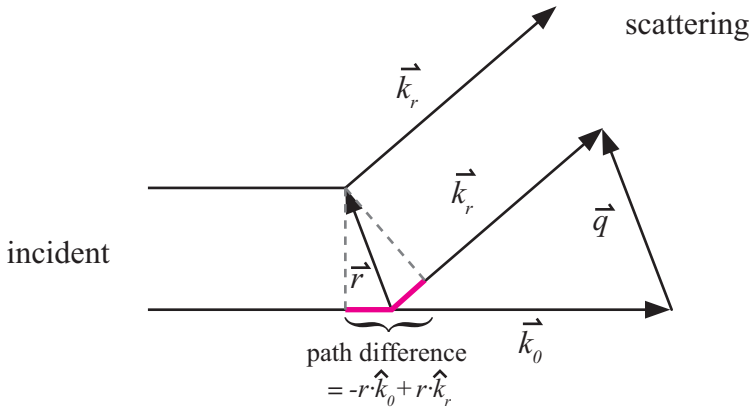

Figure 2.3: The path difference between the two scattered waves (shown in magenta) is $-\vec{r}\cdot(\vec{k_r}-\vec{k_0})$. The phase difference is thus $-\vec{q}\cdot\vec{r}$.

In a monodisperse protein solution, the protein and solvent molecules contribute to the X-ray scattering additively. In the case of a dilute solution where the protein molecules are non-interacting, unlike the case of a protein crystal, the molecules are randomly oriented. As a result, the observed X-ray scattering profile is spatially and rotationally averaged. The observed scattering profile, $I(q)$, is the rotationally averaged scattering intensity of a single protein [27, 46],

$$I(q) = \int 4\pi r^2 dr \tilde{\rho}^2(r) \frac{\sin(qr)}{qr} = 4\pi \int P(r) \frac{\sin(qr)}{qr} dr, \tag{2.8}$$

where r is the electron-pair distance, $\tilde{\rho}^2(r)$ is the autocorrelation function, and $P(r)$ is the one-dimensional electron pair-distance distribution function,

$$P(r) = r^2 \tilde{\rho}^2(r) \tag{2.9}$$

Equivalently stated, in protein solutions, the X-rays "see" the electron density of a single protein tumbling randomly as opposed to a three-dimensional electron density distribution with fixed orientation as is seen in a protein crystal. $P(r)$ is computed from the inverse transformation of $I(q)$ [46, 131].

$$P(r) = \frac{1}{2\pi^2} \int_0^\infty I(q) qr \sin(qr) dq, \tag{2.10}$$

2.1.2 Structural Information from SAXS

Experimentally, the scattering profile $I(q)$ is produced from two two-dimensional scattering images - one of the protein solution and another of the buffer taken under identical conditions. Fig. 2.4 shows the basic process of protein SAXS. Protein solution SAXS is typically performed at synchrotron X-ray sources. Single exposures in this thesis were approximately 1 - 10 s at the G1 station at the Cornell High Energy Synchrotron Source (CHESS) with a flux on the order of 10^{12} photon/s. On a rotating anode X-ray generator, the flux is approximately 10^{7} photon/s, requiring proportionally longer exposures. Once the scattering images of the protein solution and buffer are taken, the images are corrected, averaged, and integrated about the beam center producing two one-dimensional scattering profiles. The normalized buffer scattering, which includes parasitic scattering from the beamline components, is subtracted from that of the protein solution to produce the scattering profile of the protein. Detailed discussion of this process will be presented in later sections. Once $I(q)$ is obtained, shape and size information on the protein molecule can be deduced by various methods.

2.1.3 Guinier Analysis

The radius of gyration, R_g, of a protein molecule is a measure of its size and shape. The radius of gyration is the root-mean-square moment of charge of all of the electrons in a protein measured from the center of charge density. The radius of gyration is similar to the radius of inertia in mechanics, replacing mass with charge. R_g and the zero-angle scattering intensity, $I(0)$, of a protein from a monodisperse solution can be determined by fitting the low-q region of the scattering profile to a Guinier equation. The Guinier equation for scattering from a protein molecule approximates the low-q region of a scat-

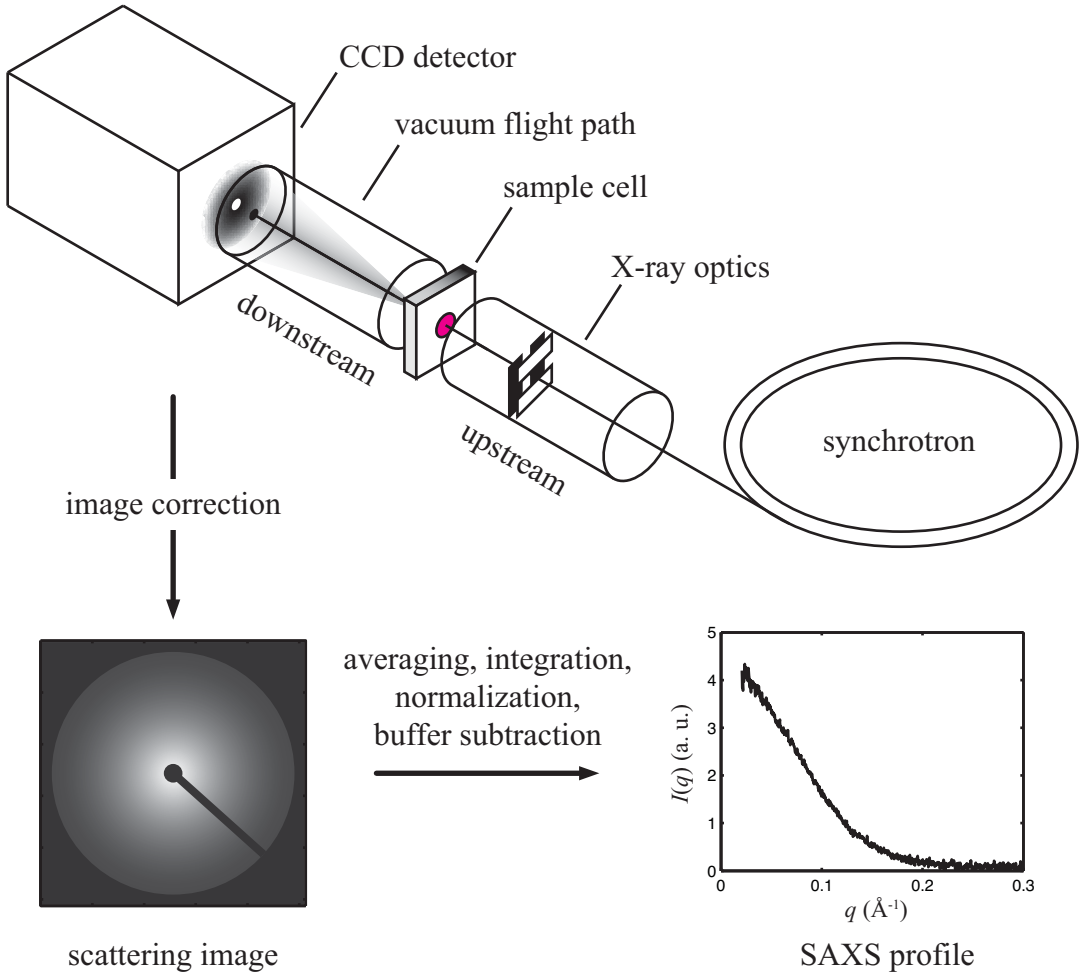

Figure 2.4: Protein solution SAXS at the synchrotron. X-ray optics are used to select a certain X-ray energy with a finite bandwidth, define the beam size and shape, and collimate the beam. Scattered X-rays pass through vacuum to minimize air scatter and 2D scattering image is taken by the detector. The direct beam is blocked by the beamstop, resulting in a shadow in the image. After treating the image, it is integrated about the beam center to produce 1D scattering profiles. The scattering profile of the protein, $I(q)$, is produced by subtracting the buffer scattering from that of the protein solution.

tering profile as Gaussian:

$$I(q) \approx I(0)\exp(-q^2R_g^2/3). \tag{2.11}$$

R_g and $I(0)$ are extracted from a linear fit to the Guinier plot, $\ln(I(q))$ vs. q, in the approximate region where the condition, $qR_g < 1.3$, holds [132] (Fig. 2.5).

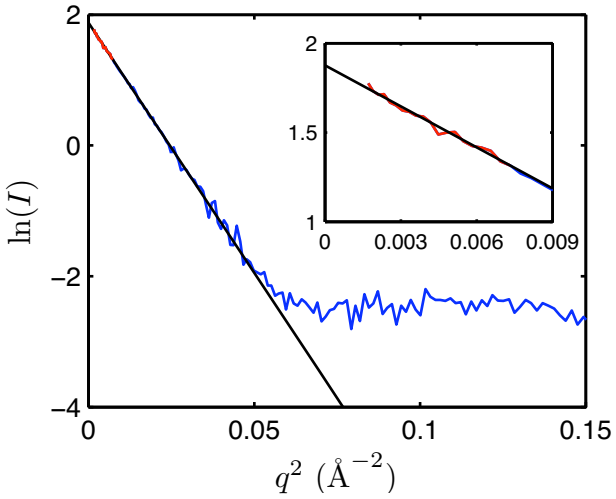

Figure 2.5: Guinier plot of hen egg white lysozyme (HEWL); the scattering profile distributed by Svergun, *et al.* in GNOM [73] is used here. The red portion of the curve is the Guinier region (zoomed in the inset). A linear fit to this region gives $R_g = 15.14$ Å^{-1} and $I(0) = 6.522$.

$I(0)$ is a function of the protein concentration, C, electron density contrast between the hydrated protein and solvent, $\Delta\rho$, the excluded volume of the protein, V_p, and the structure factor, $S(q)$, which is an interference factor dependent on inter-protein interactions.

$$I(0) = C \cdot S(0)(\Delta\rho \cdot V_P)^2. \tag{2.12}$$

Note that $\Delta\rho V_p$ is equivalent to the excess number of electrons in a protein relative to the background. Therefore, this quantity is also proportional to the protein molecular weight. Non-interacting solution conditions that satisfy $S(0) \approx 1$ are desirable for

Guinier analysis. Non-interaction between the protein molecules in a solution can be accomplished by modifying the solvent conditions (for example, the ionic strength or pH) and diluting the sample [46].

2.1.4 Kratky Plots

At higher q, the power-law dependence of the $I(q)$ decay provides information about the shape and in particular the degree of compaction of the protein [104, 105]. This power-law dependence is emphasized in the Kratky representation: $I(q)q^2$ vs. q. In the intermediate region, the scattering from a compact, folded protein falls off as $I(q) \propto q^{-4}$. The Kratky plot therefore exhibits a peak (see example in Fig. 2.6). The scattering from a coil-like protein falls off as $I(q) \propto q^{-2}$ in this regime, and thus, the Kratky plot exhibits a plateau. At higher q, i.e. smaller length scales, elements of the protein appear as a rigid rod and a $I(q) \propto q^{-1}$ dependence is observed.

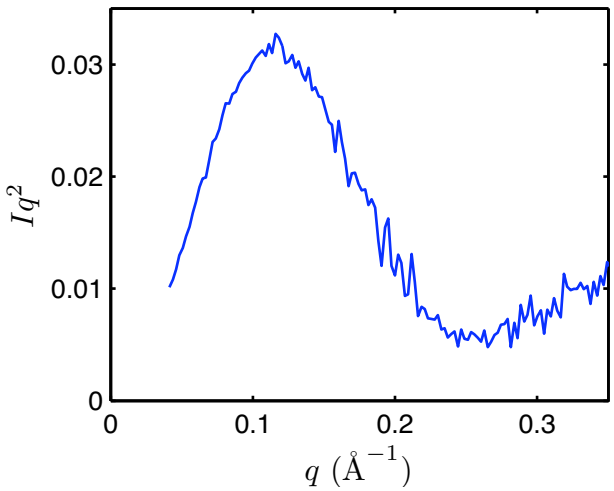

Figure 2.6: Kratky plot of HEWL (using scattering profile from [73]). The peak indicates that the protein is compact and folded.

2.1.5 Pair-Distance Distribution Analysis

The radius of gyration can also be determined from the pair-distance distribution function, $P(r)$ (see Eqn. (2.8)).

$$R_g^2 = \frac{\int_0^{D_{max}} P(r) r^2 dr}{2 \int_0^{D_{max}} P(r) dr}, \tag{2.13}$$

where D_{max} is the maximum size of the particle. The indirect Fourier transform method [46] is commonly used to calculate $P(r)$. In this method, an analytical $I(q)$ is produced by spline-fitting of the experimental curve. $P(r)$ is then calculated from the Fourier transform (Eqn. (2.10)). The program GNOM, which implements the indirect Fourier transform method [73] was used to calculate $P(r)$ in this thesis (see example in Fig. 2.7). The advantage to this method of obtaining R_g is that the entire scattering curve is used for analysis, rather than the only the low-q region. However, this method is also sensitive to termination effects, and particularly the quality of low-q data, which is affected by radiation damage and subtraction errors. As a result, D_{max}, where $P(r)$ approaches zero is often impossible to assign. In this thesis, this method was only applied to data where D_{max} could be unambiguously determined.

2.1.6 Envelope Reconstruction

Low-resolution models of protein structures can be reconstructed from SAXS data with a method similar to crystallographic refinement. In this thesis, an *ab initio* reconstruction program GASBOR was used [131] (Fig. 2.8). GASBOR uses simulated annealing to produce a chain-like assembly of dummy residues that best describe the experimental $I(q)$. A limitation of this program is that the user must specify number of residues per particle. For this reason, the GASBOR program is unable to accurately model solutions of protein molecules where multiple oligomerization states are present [141].

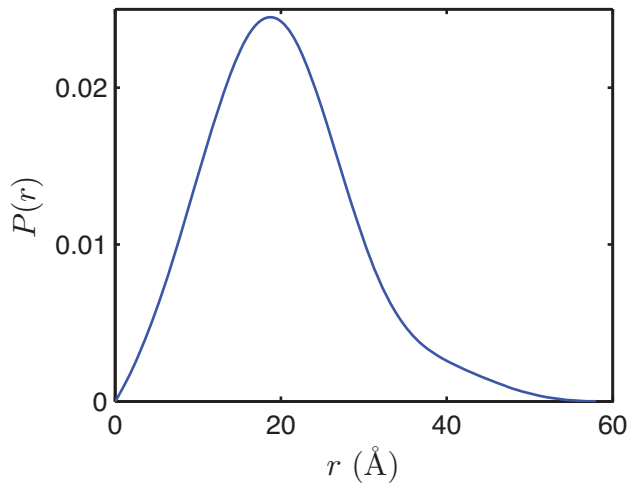

Figure 2.7: The pair-distance distribution function of HEWL (using scattering profile from [73]) generated with the program GNOM [73] using D_{max} = 58 Å. Eqn. (2.13) gives R_g = 15.63 Å^{-1} and $I(0)$ = 6.611, in good agreement with Guinier analysis (Fig. 2.5).

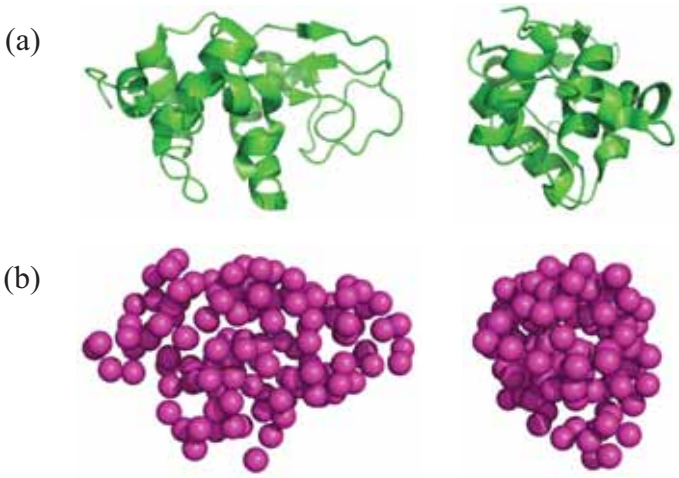

Figure 2.8: Envelope reconstruction of HEWL (using scattering profile from [73] in the region, $q < 0.31$ Å^{-1}). (a) Front and side view of HEWL crystal structure (Protein Data Bank accession code 2VB1). (b) Front and side view of low-resolution HEWL model generated form SAXS data with the program GASBOR [131].

2.1.7 Ensemble Models of Unfolded Proteins

For unfolded proteins that do not have unique structures, an ensemble of extended models may be fit to the experimental $I(q)$. In this thesis, the Ensemble Optimization Method (EOM) package developed for modeling flexible proteins in solution [13] was used for this purpose. EOM generates a large pool of randomly generated conformations available for a polypeptide of a certain sequence [12] from which an optimization algorithm selects the subset that best fits the experimental scattering profile. It was demonstrated that the size distributions of both compact and extended test ensembles could be successfully identified from a starting pool of randomly generated conformations by this method [13].

2.2 Principles of High-Pressure SAXS Design

As high-pressure SAXS cells are not commercially available, it was necessary to design and fabricate our own cell[1]. For solution SAXS studies of protein conformational changes under pressure, the sample must be contained in a cell that withstands pressures of several hundred megapascals while allowing sufficient transmission of the weak scattering signal from proteins in solution. As background subtraction is necessary, it is also critical to reproduce the sample path length, the parasitic scattering from the windows, and the internal pressure and temperature of the cell. In these regards, the diamond anvil cell [43] and the cylindrical beryllium cell [74] are inappropriate for protein solution SAXS (Fig. 2.9). Diamond anvil cells lack fine control of the sample path length and internal pressure in the pressure range used in this thesis: from 0.1 to 400 MPa. Diamond anvils are also quite thick (approximately 2 mm), corresponding to an X-ray

[1] Much of the information in this chapter on the design of high-pressure SAXS cells has been published [5]. Reproduced with permission of the International Union of Crystallography (http://journals.iucr.org/).

attenuation of 96% through two windows at 10 keV. Geometric considerations prevent the simultaneous optimization of the maximum operating pressure and transmission of the beryllium cell. A window geometry that has been effective for high-pressure SAXS is one in which flat windows are secured against flat, metal apertures with Bridgman unsupported area seals and will be discussed in a following section.

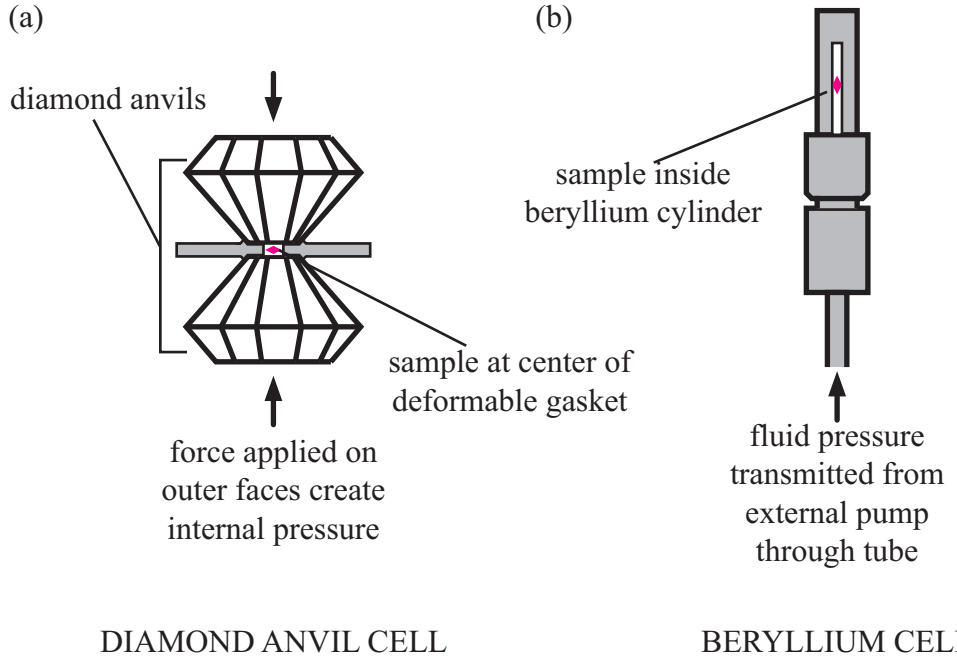

Figure 2.9: Two types of high-pressure X-ray diffraction cells (sample shown in magenta). Neither of these window geometries are appropriate for solution SAXS of proteins. (a) Diamond anvil cell. (b) Cylindrical beryllium cell.

Three high-pressure SAXS cells with Bridgman-type diamond windows were designed for this thesis and characterized for equilibrium solution studies of proteins at pressures up to 400 MPa with 8 - 12 keV X-rays (Fig. 2.10). The two first-generation cells, SAXS1 and SAXS2, were based on the design of Pressl, *et al.* [109], utilizing industry standard cone-seal connections at the window ports. Unlike the Pressl cell, which incorporates polyimide-coated beryllium windows and a built-in downstream window

aperture, the first-generation cells were fitted with diamond windows mounted on removable window holders (Fig. 2.11). The diamond windows were preferable to beryllium as they are non-hazardous and optically transparent. Removable window holders enabled polishing of the window-mounting surfaces, which is critical for preparing Bridgman window seals. These two design features were carried over to the second-generation cell, SAXS3.

Figure 2.10: Three high-pressure SAXS cells designed for this thesis. The first-generation cells, SAXS1 and SAXS2, utilized cone seals for the window holders. The second-generation cell, SAXS3, features a corrosion-resistant Inconel body, window-retaining caps and robust seals for the window holders, enabling sample loading from the window port.

The first-generation cells presented four major concerns regarding the design of high-pressure SAXS cells: the corrosion resistance of the cell parts, the high-pressure seals for the window holders, the method of window retention and low-pressure seals, and finally, the method of sample loading and isolation. These concerns were addressed

in the second-generation cell, SAXS3. The cell body of SAXS3 was based on that of Woenckhaus, *et al.* [157] by incorporation of Bridgman-type O-ring seals at the window ports and a window-retaining cap for low-pressure sealing. Disposable inner cells were incorporated to address sample handling concerns. The experimental SAXS data presented in Chapter 4 of this thesis were collected with the second-generation cell.

2.2.1 Design Requirements for SAXS

Protein solution SAXS requires careful subtraction of the background scattering before data analysis, and therefore two measurements are taken at each sample condition. Achieving a satisfactory background subtraction requires the minimization of parasitic scattering from the system and reproducibility of the sample conditions including the X-ray path length, pressure and temperature. Samples are commonly contained in transmission-style cells with a fixed path length, and the window materials are chosen carefully. Windows benefit from being as thin and uniform as possible to optimize the X-ray transmission while minimizing the parasitic scattering, so as to maximize the reproducibility of the scattering signal from the sample. Typical SAXS windows include low-Z materials such as beryllium and diamond, thin polymer films such as mylar and polyimide, and thin sheets of mica. The scattering signal is optimized when the sample path length is approximately equal to the X-ray attenuation length. The X-ray transmission, I/I_0, through a material of thickness, x, and energy-dependent X-ray attenuation coefficient, μ can be determined with the following relation.

$$\frac{I}{I_0} = e^{-\mu x}. \tag{2.14}$$

The attenuation, or $1/e$, length is thus $1/\mu$. For aqueous solutions, the attenuation length is 1 - 3 mm for 8 - 12 keV X-rays.

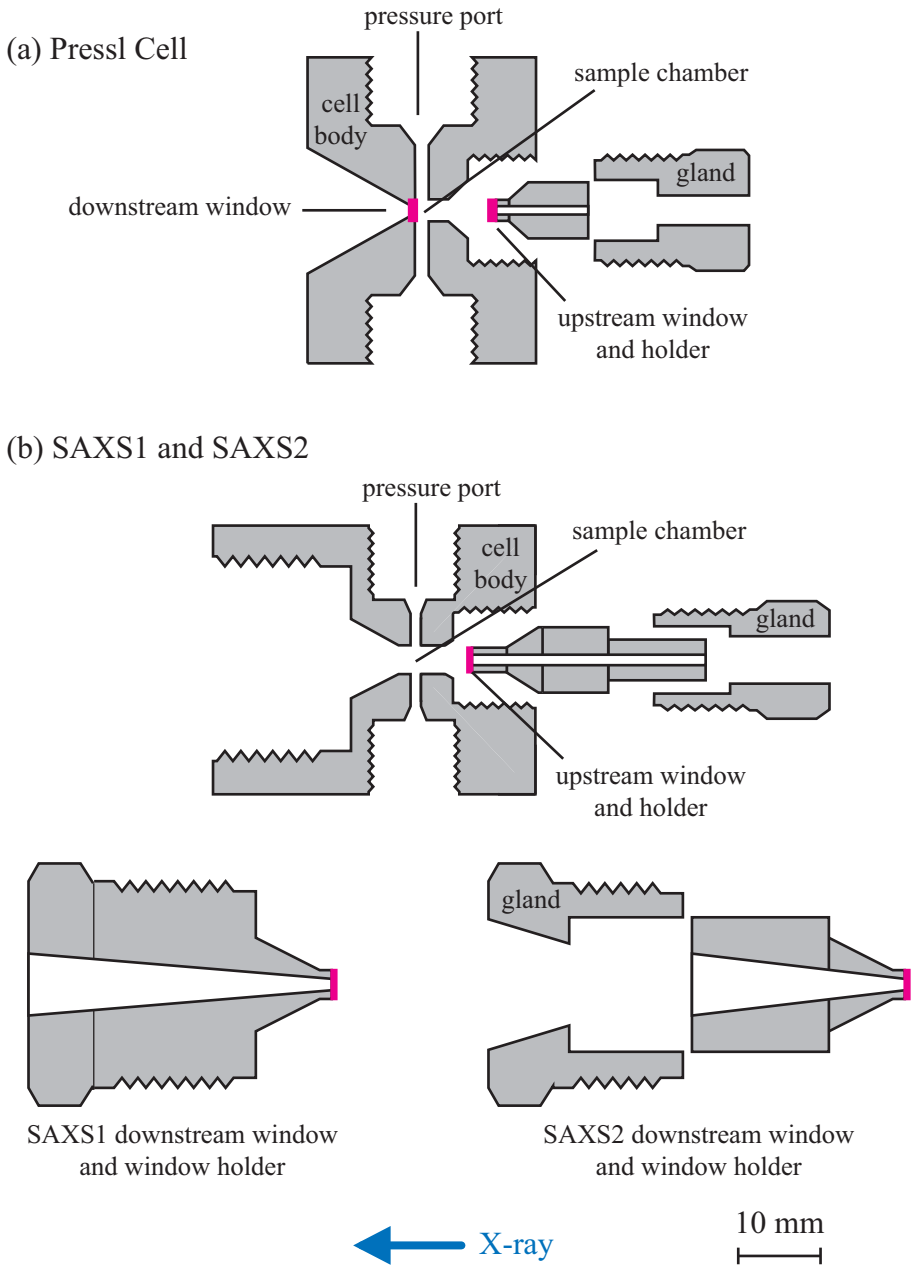

Figure 2.11: Design of first-generation high-pressure SAXS cells. (a) Pressl cell [109]. (b) SAXS1. (c) SAXS2. Samples were loaded via the pressure feed in all cells. Beryllium windows (magenta) were used in the Pressl cell, while SAXS1 and SAXS2 featured diamond windows (magenta).

The length scales of the samples must also be considered. The momentum transfer, q, is a function of X-ray wavelength, λ, and the scattering angle, 2θ. At a fixed X-ray wavelength, the resolution limit or maximum q that can be collected unobstructed from a sample cell is determined by the window thickness, window aperture, and irradiated sample volume [109], while the minimum accessible q is often determined by the parasitic scattering of the system. For many SAXS experiments, low q data is essential for data analysis. Guinier analysis is particularly demanding as the q range over which a Guinier fit is valid moves to lower q with increasing protein size.

2.2.2 Material Selection

The material selection for a high-pressure SAXS cell is based on chemical properties, yield strength, and X-ray transmission. The body of a high-pressure cell must be made of corrosion-resistant, high strength material. Corrosion is detrimental to high-pressure seals, which depend upon good contact (Fig. 2.12 (a)) and contaminates the surrounding fluid. Although the cell bodies of SAXS1 an SAXS2 were made from stainless steel 316, corrosion was a common problem. In these first-generation cells, the samples, which were often saline and acidic, were in direct contact with the cell parts. Additionally, some forms of corrosion are worsened at high pressure [5]. Stress-corrosion cracking can compromise pressure vessels [129]. In the presence of other metals, galvanic corrosion occurred at high pressure in the first-generation cells even in the absence of electrolytes (Fig. 2.12 (b)).

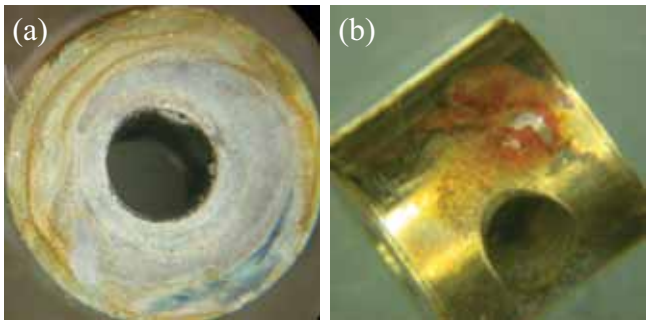

Figure 2.12: Corrosion observed in the first-generation cells compromised seals and contaminated samples. (a) Corrosion of the window-mounting surface of a window holder caused Bridgman window seals to fail. (b) High-pressure galvanic corrosion was promoted in the presence of a brass spacer used to reduce sample volumes in SAXS2.

As the cell body is typically made by drilling a cylindrical bore in a solid piece of metal, the required yield strength can be estimated by the following relation for the elastic limit of a cylindrical vessel under pressure [129].

$$\Delta P = \frac{Y}{\sqrt{3}}(1 - \omega^2), \tag{2.15}$$

where ΔP is the pressure differential across the wall at which the cylinder will yield, Y is the yield strength of the material, and ω is the ratio of the outer to inner wall diameters. Alloys commonly used for high-pressure applications include stainless steels 316 and 304 and nickel-chromium alloys [157, 5]. Relevant properties of the materials considered for this thesis are presented in Table 2.1. For SAXS3, age-hardened Inconel 725 was selected for its superior strength and corrosion resistance.

For high-pressure applications, strong low-Z materials such as beryllium and diamond are typically used as X-ray windows. A comparison of the transmission of 10 keV X-rays as a function of window thickness is shown for several materials in Fig. 2.13 (refer to Eqn. 2.14). While beryllium is more transparent to X-rays than diamond, the latter was preferred in this work to avoid the hazards of beryllium oxide dust. Diamond is also

convenient for its chemical inertness and transparency to a wide radiation spectrum, enabling visual inspection of samples and the use of non-X-ray probes. A crucial step in the selection of SAXS windows is the characterization of the parasitic scattering. In the case of diamond, nitrogen impurities can cause strong parasitic scattering [125, 124] that can dominate the signal at low scattering angles, complicating background subtraction from the collected data.

Table 2.1: Material comparison of alloys and window materials

Alloy	Yield Strength (MPa)	Poisson Ratio
Stainless steel 316[a]	552	
Inconel 725 (annealed form)[b]	427	-
Inconel 725 (age-hardened form)[b]	1029	-
Diamond[c]	750	0.1
Beryllium[d]	430	0.07
Sapphire[e]	200	0.27

[a]Data from Larry Loper, High Pressure Equipment Co., Erie, PA (private communication). This is a stronger form of SS316 than commonly available. [b]Data from Special Metals Corp., Huntingon, WV. The R_c hardness of the annealed form is ≈ 5, while for the age-hardend form it is ≈ 36. [d]Data from [41].

Finally, the materials chosen for the SAXS cell should not interact with the sample. In addition to chemical resistance, the hydrophobicity and charge of the materials that contact the sample should be considered when dealing with highly charged or aggregating systems.

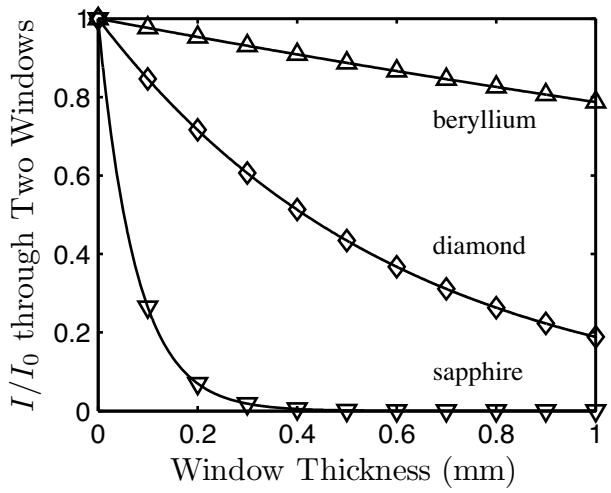

Figure 2.13: Material comparison of the transmission of 10 keV X-rays through two windows: beryllium (triangle), diamond (diamond), sapphire (inverted triangle). Diamonds of 0.5 mm thickness were used as windows in this thesis.

2.2.3 High-Pressure Seals

Seals at an interface rely on contact pressure at the interface that is greater than the internal pressure contained in a vessel. Two types of seals that are particularly useful in designing cells rated to several hundred megapascals are the cone seal and the Bridgman unsupported area seal. The cone seal is a simple and reliable industry standard seal used for connecting high-pressure plumbing [129]. It is therefore convenient for building the pressure network between the pressure pump and the high-pressure cell. In a cone seal connection, the mating parts have slightly differing cone angles, such that a seal pressure is created at the line of contact (see Fig. 2.14 (a)). Ideally the cone angle of the male piece is 1 - 2° smaller than that of the female [129]. Cone-seal parts are available commercially in various sizes, shapes, and pressure ratings. In this thesis, 60,000 psi (400 MPa) grade connections made of stainless steel 316 (High Pressure Equipment Co., Erie, PA) were used. 1/8" (3.18 mm) cone-seal connections can be made

with little torque (8.5 N-m), and are therefore convenient where minimal disturbance of the apparatus and repeated assembly-disassembly are necessary. A disadvantage of 1/8" connections is that they can easily become untorqued. This can be a problem if there are 1/8" connections in a rigid series; torquing one connection may loosen a 1/8" connection. Standard 1/4" (6.35 mm) connections are optimal for rigid connections. Generally, cone seals become deformed after repeated use and must be periodically replaced.

Cone seals are not suitable for sealing precision parts that need to be frequently disassembled. This was found to be the case in the first-generation cell where the cone seals used for sealing the window holders in the cell body. As cone seals rely on jamming the mating parts, the cone-seals on the window holders were prone to deformation. As a result, the sample path length was not constant, which is a requirement for solution SAXS. Deformation of the coned window holders also propagated to the window-mounting surface, causing poor contact with the diamond windows.

The second type of high-pressure seal was more suited for precision cell parts. This seal utilizes Bridgman's principle of unsupported area to create a seal pressure exceeding that of the contained pressure. In a Bridgman seal, the contact area between the two surfaces forming a seal, a, is smaller than the area in contact with the internal pressure of a vessel, A. The seal pressure is therefore the internal pressure multiplied by A/a. An anti-extrusion ring can operate on this principle in order to seal a clearance between mating high-pressure parts [34] (Fig. 2.14 (c)). This principle is also used to seal flat windows against apertures [107] (Fig. 2.14 (b)). In the latter case, the elastic limit of the window can be estimated using the following equation for an unclamped circular plate against a circular aperture [57].

$$P_{max} = \frac{8}{3}\left(\frac{T}{R}\right)^2 \frac{Y}{3+\sigma}, \tag{2.16}$$

where the yield pressure, $P_{\max}$, is determined by the window thickness, T, radius of the unsupported hole, R, yield strength of the window, Y, and the Poisson ratio of the window, σ. Experimentally, it has been shown that the effectiveness of a Bridgman window seal is also dependent on the relative sizes of the window and the aperture; the diameter of the window should not exceed approximately 2.77 times that of the unsupported aperture [123]. As the Bridgman seal depends on a pressure differential, it improves with increasing pressure. At low pressure, however, the Bridgman seal must be assisted by another mechanism, such as an O-ring seal.

Bridgman window seals were implemented in the first-generation cells to seal the diamond windows at high pressure. The diamond windows were fixed on the window-mounting surfaces by small amounts of glue applied around the perimeter of the windows. This method of window retention served to assist the Bridgman seals at low pressures. However, while the greatest success was achieved with high-strength epoxies that cured at room temperature (Stycast 2850 FT/Cat 11 LV, Cat 24 LV), the gluing method was not effective or reliable. In particular, the glue was weak to temperature variation due to different thermal expansion coefficients of the glue and mating materials. A failed bond was also difficult to repair during a synchrotron experiment. The window-mounting surface required refinishing after each failure, and the glue curing times were long. To circumvent the use of glues, a brass spacer with a rubber O-ring on either side was used inside the cell to apply pressure against the two windows. Although the use of a spacer improved the low-pressure seals, it complicated experiments by creating more small spaced in the cell that were harder to fill with sample and clean. A reliable low-pressure seal was therefore a major design criterion of the second-generation cell.

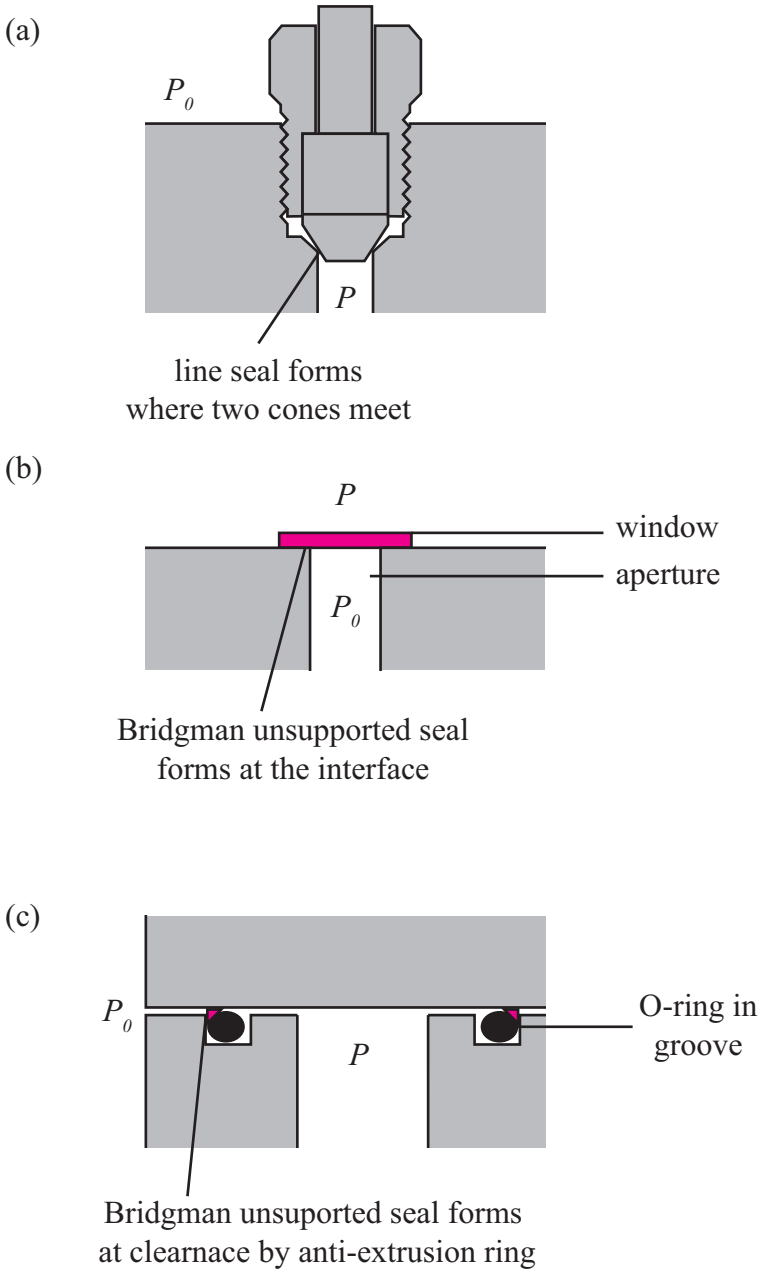

Figure 2.14: Two types of high-pressure seals, where P is the internal pressure of the high-pressure container and P_0 is the external pressure; $P >> P_0$. (a) A cone seal connection is made between mating parts with a 1 - 2° difference in cone angles. Bridgmans principle of unsupported area can be used (b) to seal a flat window against an aperture and (c) to seal a clearance between mating parts. It is important that the volume of the O-ring slightly exceed that of the groove into which it fits.

A high-pressure seal not used in thesis but worth mentioning is the O-ring seal with an angled seat [144]. This seal only requires finger tightening and has been used successfully to 200 MPa in the cylindrical beryllium cell [145, 24]. Future incorporation of this seal in the high-pressure SAXS system, such as in the high-pressure reservoir, may be useful. However, the seal must be incorporated such that loosening of the connection is prevented.

2.2.4 Sample Isolation

An important but often overlooked feature of a high-pressure cell is the method of sample isolation. Generally, pressure is generated by an external fluid or gas pump, necessitating a means for separating the sample from the pressurizing medium. One method is to inject the sample directly into the sample chamber of the high-pressure cell, then closing the chamber with a piston that separates the sample and pressurizing medium [96]. This method was implemented in the first-generation cells for two obvious advantages; additional parasitic scattering from an internal cell is eliminated and the cell windows do not have to be disassembled to load samples. However, this method also presented major difficulties. As the sample must occupy small spaces in the sample chamber, cleaning was difficult without disassembling the cell. The use of a brass spacer to reduce sample volumes also created additional small spaces that could not be easily wetted, further complicating sample filling, cleaning, and removal of air bubbles. Without proper removal of air bubbles, the sample-isolation piston can push into beam path under pressure (Fig. 2.15). Another drawback of this method is that biological buffers, which are often highly saline, alkaline or acidic, are very corrosive to metal chambers at high pressure (Fig. 2.12).

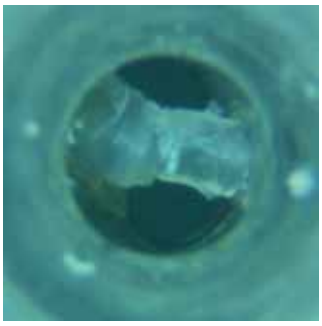

Figure 2.15: Viewing into the cell through a window port: trapped air bubbles in the sample chamber caused the silicone rubber sample-isolation piston to push into the sample chamber under pressure.

Alternatively, the sample can be encapsulated in an internal cell with a piston or a soft membrane that isolates the sample while transmitting the pressure [33, 109]. The use of an internal cell allows for minimizing the sample volume and facilitating sample changes. However, such an internal cell must function well as a SAXS cell on its own. In other words, the path length and parasitic scattering must be reproducible.

2.3 Second-Generation High-Pressure SAXS Cell

The second-generation cell, SAXS3, was optimized for use up to 400 MPa in liquid pressure and 8 -12 keV X-rays with emphasis on the ease of use. Particular attention was paid to the design of Woenckhaus, *et al.* [157], which featured Poulter-type window assemblies composed of flat diamonds glued then secured against the apertures with window-retaining screw caps (Fig. 2.18 (a)). In the Woenckhaus design, the window holders were sealed in the cell with Viton O-rings, which were replaced after each experiment: no anti-extrusion rings were used (Prof. Roland Winter, private communication). Samples were loaded directly into the Woenckhaus cell.

The SAXS3 design added window-retaining caps and O-ring seals assisted by anti-extrusion rings to the Woenckhaus design. Unlike the Woenckhaus cell, samples were encapsulated in disposable plastic sample cells with a defined path length and reproducible parasitic scattering. These inner cells facilitated rapid sample changes and eliminated the need for cleaning. A schematic is shown in Fig. A.2 (Appendix). All of the experimental SAXS data presented in Chapter 4 of this thesis were taken with this cell.

2.3.1 Preparation of Bridgman Window Seals

The common feature of the first- and second-generation cells is the use of Bridgman seals to seal diamond windows against metal apertures. Good contact is necessary for an effective Bridgman window seal. To achieve this, the window-mounting surface must be polished to a good flatness and mirror finish. It is therefore necessary that the window holder be removable from the cell body. The window-mounting surface was first made flat with sand paper (401Q 1200 grit; 3M, St. Paul, MN) and then polished to a mirror finish using 0.5 - 1 μm diamond lapping films (PSI-1601D-6, PSI-1601D-6 A, PSI-16.5D-6A; Precision Surfaces International, Houston, TX) wetted with distilled water (Fig. 2.16). This procedure proved more effective than diamond grit slurries and diamond lapping paste at preserving the flatness around the window aperture. Custom-fabricated brass polishing jigs were used to hold the window holder perpendicular to the lapping surface. When polishing, the window holder was allowed to glide over the wet film in a figure of eight motion; no downward force was applied by the hand. The flatness of the surface may be checked during the lapping process by observing the reflection of straight edges; the grid cover on the overhead fluorescent lights is useful for this (Fig. 2.16). The lapping surfaces were cleaned and replaced frequently to prevent loose particles from scratching the window holder surface. The window holders were

also periodically rinsed with water. After radial scratches near the aperture are removed, the mounting surfaces were rinsed in water, briefly dipped in a sonication bath, and wiped with dust-free solvent, such as HPLC-grade acetone or ethanol, before drying in the vacuum oven. Corrosion occurred when the parts were left unattended in wet or humid conditions; this was also true for the highly corrosion-resistant Inconel 725HS alloy.

Natural diamonds recycled from diamond anvil cells were used as windows. Flat diamonds with the faces normal to the [100] axis were prepared by grinding above and below the anvil girdles to a final thickness of 500 to 560 μm with a parallelism of only a few milliradians (provided by Prof. Bill Bassett, Cornell University). The diamonds were cleaned by sonication in HPLC-grade acetone or ethanol and wiped with lens paper to remove dust particles.

Once good contact was established between the window and the window holder (Fig. 2.17), the window was secured in place. The method by which the windows were fixed against the aperture was one of the significant differences between first- and second-generation cells and will therefore be discussed in the following sections.

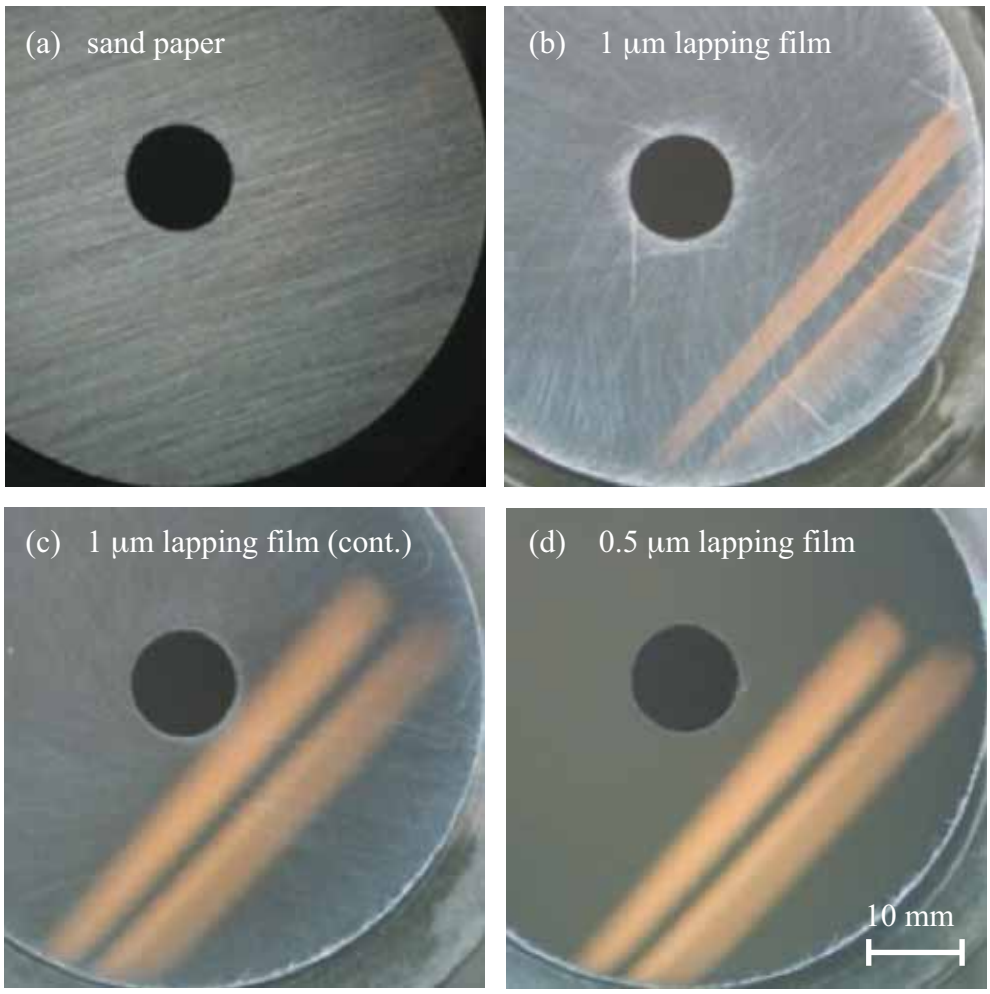

Figure 2.16: Preparation of window mounting surface for Bridgman seal. The window-mounting surface was first made flat with (a) sand paper and then polished to a mirror finish using (b) - (d) 0.5 - 1 μm diamond lapping films wetted with distilled water. Radial scratches near the aperture must be removed to prevent leaks at high-pressure. The overhead fluorescent lights are reflected on the surface.

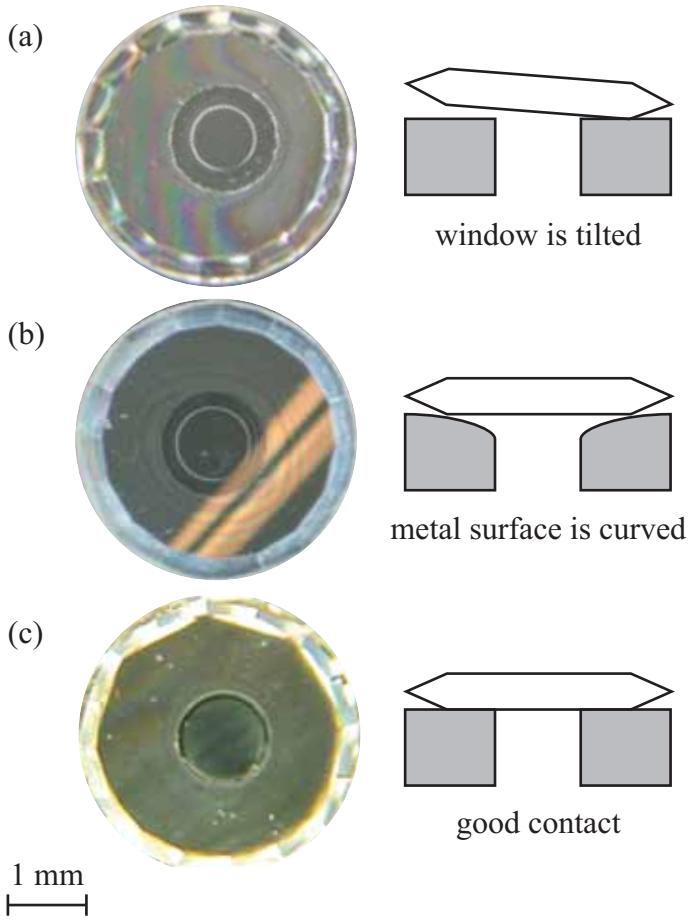

Figure 2.17: 3.3 mm diameter diamond windows on metal window holders with 1.2 mm diameter apertures. The interface is wetted with acetone or ethanol. Interference fringes enable the evaluation of the contact between the window and window-mounting surface [123]. (a) The window is tilted with respect to the mounting surface, likely because of trapped dust particles. (b) The surface is curved near the aperture due to loose particles tending to accumulate near the aperture during polishing. (c) A very broad interference fringe is observed, indicating that the contact is very good, particular near the aperture.

2.3.2 Cell Body, Window-Holders, and Low-Pressure Seals

The cell body, window holders, and window-retaining screw caps of SAXS3 were machined from Inconel 725 alloy (Special Metals Corp., Huntington, WV). Inconel 725 was chosen for its strength and resistance to corrosion and stress-corrosion cracking. Prior to machining, the stock alloy was annealed by heating at 1010 °C for one hour in a pre-heated furnace followed by cooling in air. The initial annealing step rendered the alloy sufficiently soft for machining (Table 2.1). Inconel 725 is also a "tough" material even in its annealed form and can only be cut very slowly. Following machining, the cell components were age-hardened to their final strength by heating for 8 hours at 760 °C in a pre-heated furnace after which the temperature was lowered to 650 °C at 140 °C per hour. The components were then held at 650 °C for 8 hours, and finally allowed to air-cool. All heat treatments were performed in air with no effort made to provide a protective atmosphere. A 25 μm thick oxide layer is formed by this process. Two identical window holders were fabricated with a 1.2 mm diameter aperture with a 30° full angle conical opening formed by electrical discharge machining (EDM). As described in the previous section (2.3.1), natural diamonds were used as windows and fitted against the polished surface of the window holders. Once good contact between the diamond and window holder was established, the diamonds were fixed in place with window-retaining screw caps.

The assembled window holders are plugged into the window ports of the cell body in a transmission orientation such that the distance between the window caps is approximately 2.3 mm. The distance between the diamond faces is 3.1 mm. The seal between the window holder and cell body is created by an O-ring assisted by a brass anti-extrusion ring. With the anti-extrusion ring, a Viton O-ring (2-113 75D Viton; MARCO Rubber & Plastic Products Inc., N. Andover, MA) can be used reliably to

400 MPa at room temperature and does not require replacement during the course of a typical synchrotron experiment. Without anti-extrusion rings, the O-ring seals were only effective up to 200 MPa. The window holders are torqued into the window ports with a stainless steel closure nut and a brass jam washer in between. The compression of the jam washer corrects for slight differences in the parallelism of the closure nut and window holder; the stiffness of the age-hardened form of Inconel 725 is less forgiving of such differences in parallelism. The threads of the closure nuts are protected with a thin layer of molybdenum grease. The required closure torque of the closure nut is 120 N-m.

The cell has two 1/4" (6.35 mm) cone-seal connections with 1 mm diameter channels that lead to the central chamber. One connection is used as the pressure feed, while the other may be used for another purpose such as a temperature probe. A 1/4" (6.35 mm) male to 1/8" (3.18 mm) female adapter (HM4HF2; High Pressure Equipment Co., Erie, PA) is used to protect the pressure feed from frequent connections and releases. The high-pressure cell is connected to an external pump (Cat. No. 37-6.75-60; High Pressure Equipment Co., Erie, PA) with 1/8" (3.18 mm) pressure tubing through a custom-built stainless steel high-pressure reservoir described in Sec. 2.3.4. Only a small torque of 8.5 N-m is required to fasten the 1/8" pressure tubing to the high-pressure cell, allowing the connection to be made on the beamline. To prevent corrosion of the high-pressure cell, it is never kept filled with water or under pressure when not in use. The cell is disassembled and dried in a vacuum oven prior to storage.

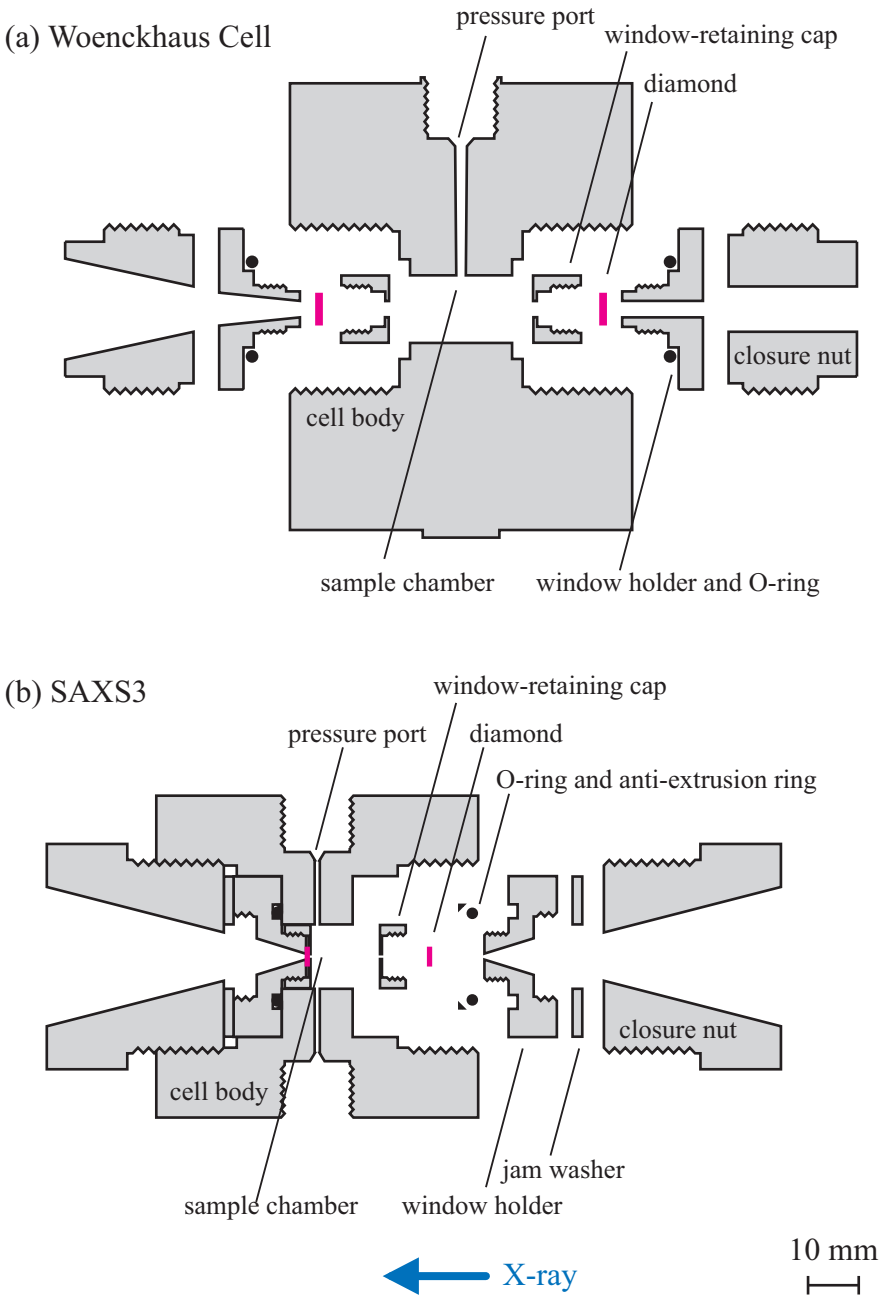

Figure 2.18: (a) Woenckhaus cell (Woenckhaus, 2000) and (b) second-generation cell, SAXS3 [5]. Unlike the Woenckhaus cell, SAXS features O-ring seals assisted by anti-extrusion rings, jam washers, and windows made from natural diamonds. Samples were loaded via a pressure port in Woenckhaus cell and a window port in SAXS3. A schematic is shown in Fig. A.2 (Appendix).

2.3.3 Sample Isolation Loading, and Ambient-Pressure SAXS

Isolation of the sample from the pressurizing medium was accomplished with a disposable internal sample cell (Fig. 2.19). The inner cell serves multiple purposes: minimizing the sample volume, facilitating sample changes, providing temporary storage, and functioning outside the high-pressure cell for ambient-pressure SAXS measurements.

The sample cell is composed of thin polymer film windows glued on the faces of 12.65 mm diameter, 2 mm thick discs. The laminate body has a 2.5 mm diameter hole through the center, which acts as the sample chamber and a narrow sample-loading channel that spans the edge of the body and the central hole. Acetal homopolymer discs cut on a lathe were used for early experiments with SAXS3; a 1 mm diameter sample loading channel was drilled into the side of each disc. Later, these were replaced by custom-fabricated laser-cut acrylic laminates with a 1.2×1.0 mm sample-loading channel (ALine Inc, Redondo Beach, CA). The laminates are constructed from cast acrylic sheets joined by 0.002" thick pressure-adhesive film (467MP; 3M, St. Paul, MN). Cast acrylic was chosen for its thickness tolerance and bio-compatibility.

To complete the construction of a sample cell, 7.5 μm Kapton windows (Spectromembrane No. 3022; Chemplex Industries) were stretched flat and glued onto each face with cyanoacrylate glue. Pressure-adhesive film (467MP; 3M, St. Paul, MN) was not strong enough to maintain the flatness of the films under pressure. With the acetal homopolymer cells, both disc faces were wiped over a gluing pad made from several sheets of tissue paper (Kimwipes; Kimtech Science) wetted with a low-viscosity cyanoacrylate glue (Loctite 420, 3M). The disc was then immediately sandwiched between two polymer film windows stretched over supports (Cat. No. 1060; Chemplex, Palm City, FL) and allowed to dry. Each cell was examined under the microscope to filter out those with glue smeared into the X-ray window area. Finally, the excess window

material was trimmed from the cell.

Due to the specific interactions of cyanoacrylate and acetal homopolymer, very little time was allowed to complete this step, and wetting with faces with the correct amount of glue was difficult. Humidity was also a large determinant of the curing times. The use of acrylic laminate discs greatly facilitated the gluing process, and the success rate increased from roughly 60 to 95%. A thin layer of cyanoacrylate glue (Brush-on Super-glue; Loctite, Rocky Hill, CT) was applied on each laminate. After wiping the excess to prevent the glue from wetting the central hole through which the X-rays will pass, the sticky face was placed on a polymer film window that was stretched flat over a support (Cat. No. 1060; Chemplex, Palm City, FL). There is sufficient time, e.g. up to 30 seconds, to perform this step successfully. Once a face is glued, the cell is allowed to cure for several hours, and the process is repeated for the other face before the excess window material is trimmed.

The completed sample cell has two flat windows, and the path length is determined by the thickness of the laminate body. Samples are loaded into the central chamber of the sample cell from the side channel using a syringe needle and plugged with vacuum grease (High Vacuum Grease; Dow Corning, Midland, MI) (Fig. 2.19 (c)). The sliding grease plug acts as a pressure-transmitting piston to prevent the formation of a pressure differential across the windows and thus allows the maintenance of a constant sample path length under pressure. The space in the loading channel also acts as a sample reservoir to account for volume reduction under pressure. A minimum sample volume of approximately 12 μL is required to prevent the grease plug from entering the sample chamber at 400 MPa. The loaded sample cell is placed into the high-pressure cell through a window port. The sample cell fits snugly in the high-pressure cell, assuring alignment of the sample with the diamond windows. Side grooves facilitate removal of

the sample cell from of the high-pressure cell with tweezers.

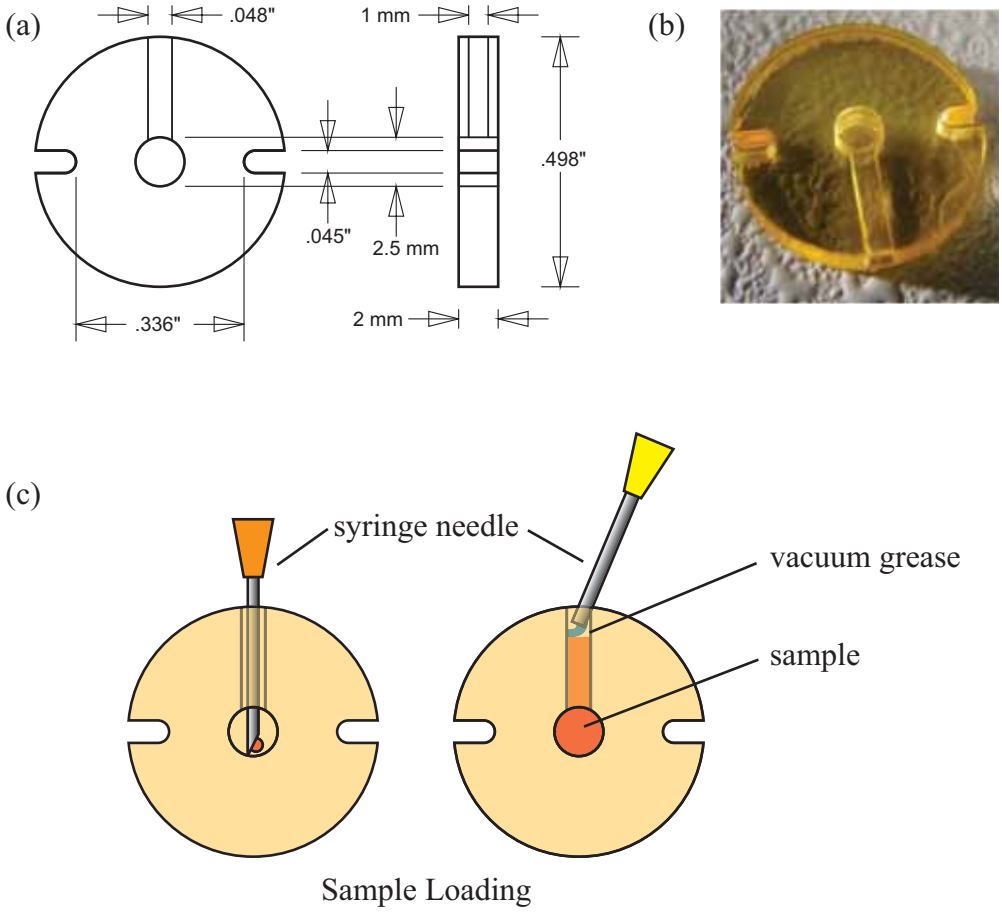

Figure 2.19: Sample isolation was accomplished with a disposable inner cell. (a) Dimensions of cell body made of acrylic laminate. (b) Acrylic cell with polyimide windows glued on both faces. (c) The sample is loaded with a syringe, such that the sample wets the bottom of the sample chamber before the loading channel. The sample chamber and loading channel are filled, leaving approximately 2 mm of empty space in the channel. Vacuum grease is filled into the remaining space as a sliding plug separating the sample from the pressurizing medium.

2.3.4 High-Pressure Reservoir and Network

The pressure network consists of a liquid high-pressure pump, low-pressure reservoir, high-pressure reservoir, pressure transducers and valves (Fig. 2.20 (a)). All experimental data were collected with a 60,000 psi (400 MPa) grade high-pressure pump (Cat. No. 37-6.75-60; High Pressure Equipment Co., Erie, PA) fitted with a custom motor control shown in Fig. 2.20. The motor control circuit is shown in Fig. A.1 (Appendix).

The high-pressure reservoir is a crucial element of the pressure network. The pressure network is filled with an inert fluid, Fluorinert (FC-77; 3M, St. Paul, MN), as the pressurizing medium to prevent corrosion. As Fluorinert scatters X-rays, distilled water is used as the pressurizing medium in the cell. To separate the two fluids, a high-pressure reservoir with an internal piston is necessary. In early experiments, a commercially available 9/16" (14.29 mm) cone-seal tube (High Pressure Equipment Co., Erie, PA) with a custom-fabricated nylon piston was used as the reservoir. However, the inner bore of these tubes was not uniform, especially near the cone seals, which become deformed when torqued. To address this, a stainless steel cylindrical reservoir was designed (Fig. 2.20 (b), schematic in Fig. A.3 (Appendix)) with a snugly fitting brass piston with two rubber O-rings. The bore and piston are coated with vacuum grease lubricant. To prevent corrosion, liquid is never left inside for long periods. The grease coating also appears to assist in preventing corrosion; grease coating is not recommended inside the high-pressure SAXS cell as grease scattering will contaminate the X-ray scattering signal from the sample. The inner bore of the reservoir and the piston becomes deformed over time due to pressure and requires refinishing or replacement. The seal at the closure nut is the least robust in the whole pressure system and would benefit from reexamination for future experiments.

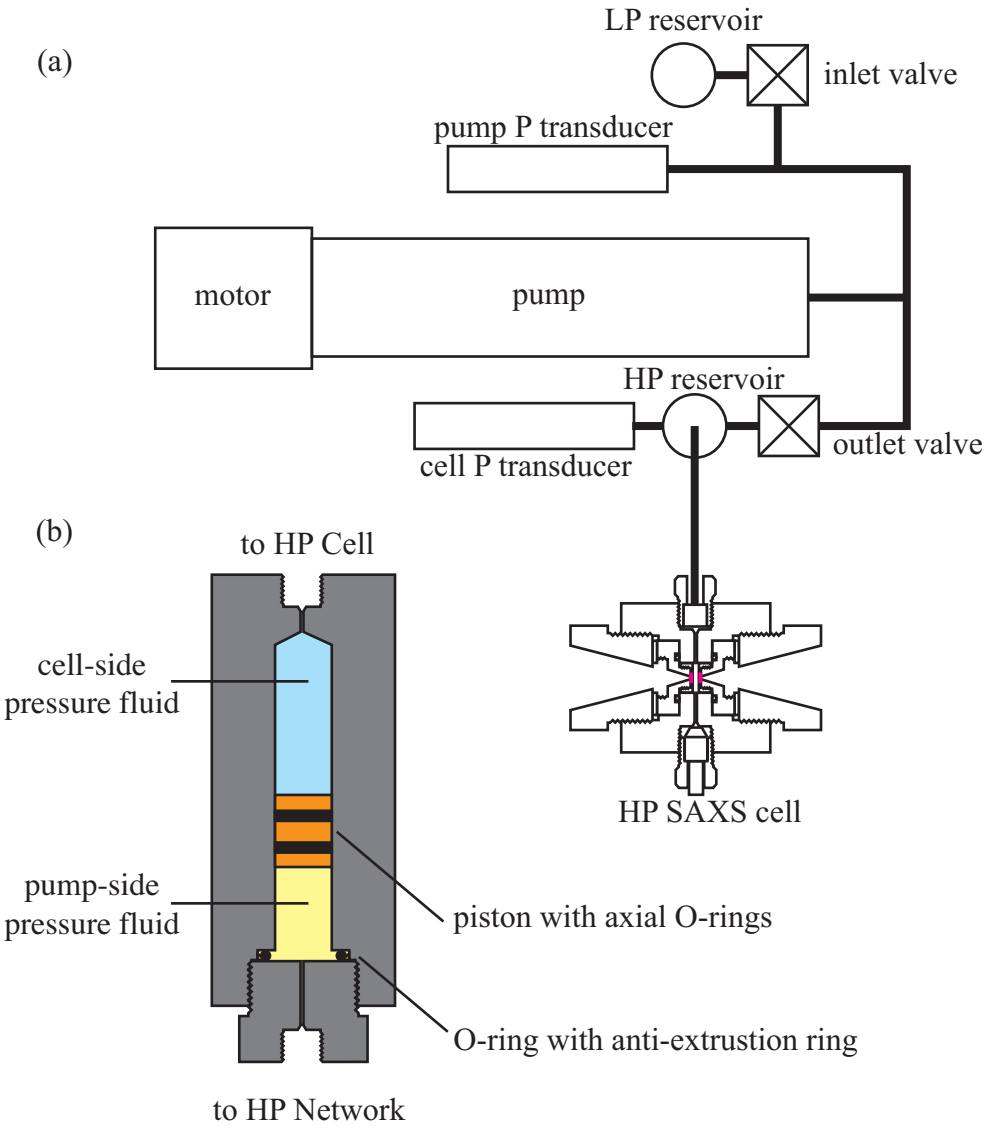

Figure 2.20: (a) Layout of the pressure network. The low-pressure reservoir containing Fluorinert at ambient pressure, supplies the pump side of the network and is isolated by the inlet valve. (b) The high-pressure reservoir is held vertically separating Fluorinert and water, the pressurizing medium in the high-pressure cell. A schematic is shown in Fig. A.3 (Appendix). The two pressure transducers measure the pressure on the pump and cell sides of the network separated by the outlet valve.

2.3.5 Experimental Protocols

All of the SAXS data presented in this thesis were collected at the Cornell High Energy Synchrotron Source (CHESS) G1 Station. The basic layout of the beam line is shown in Fig. 2.21. Upstream of the sample cell, an X-ray beam is defined by several sets of helium-enclosed slits in order of upstream to downstream. The beam is roughly defined and centered through the slits using the upstream ion counters. Following this, the PIN-diode beamstop and the vacuum flight path, evacuated to < 30 mtorr, are positioned downstream of the sample cell and aligned with respect to the beam. The beam line components are positioned as closely together as possible to minimize air scattering. After positioning the components, the sample cell is temporarily removed from the sample stage. The PIN-diode beamstop, which is used to block the non-scattered beam from the detector while recording the transmitted intensity, is first aligned with the beam. The beamstop is made of a silicon PIN diode (Silonex solderable photodiode, SLSD-71N4, Allied Electronics; cut to size with diamond saw) with lacquered copper wires soldered to the two electrodes. The diode is embedded with the front face exposed into a milled groove in a small piece of lead and secured with epoxy. The beamstop can be roughly aligned by visually inspecting its position with respect to the slits and through use of an ion chamber downstream of the beamstop. Once the beam hits the beamstop, the PIN diode reading allows more precise alignment of the beamstop.

The detector can then be positioned behind the vacuum flightpath and used to take images. The detector is placed as closely as possible to the beamstop to prevent shadows created by air scattering. The horizontal and vertical positions of the detector are refined by taking a series of images. The slit positions are also further refined by taking images and observing the parasitic scattering area near the beamstop (Fig. 2.22). To record the detector zero offset, a region of the detector face is masked with lead tape. Finally, the

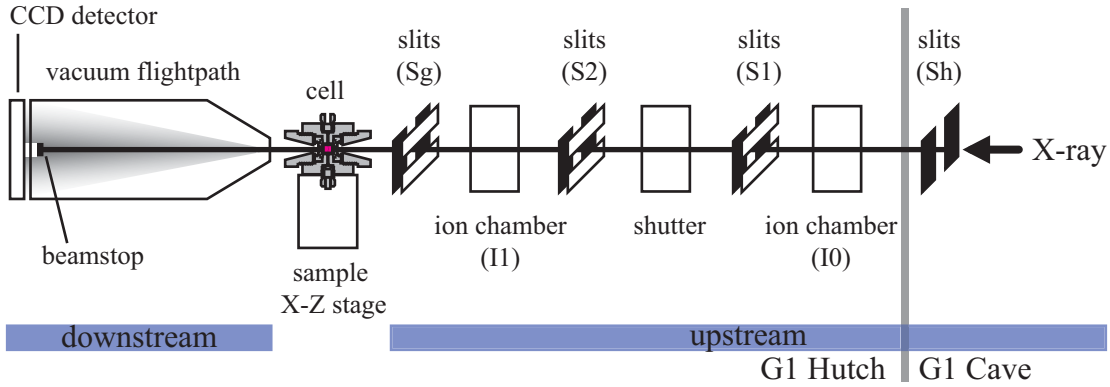

Figure 2.21: SAXS beamline layout at G1 Station. X-rays generated by a wiggler feed though focusing optics and a monochromator in the G1 cave. Upon entering the G1 hutch, the beam size and collimation are adjusted by helium-enclosed slits (high precision, rough vacuum compatible motorized slits, Advanced Design Consulting USA, Inc.) before transmission through the sample cell. The beam intensity is monitored by ion chambers and a PIN-diode beamstop. The scattered and transmitted X-rays pass through a vacuum flight path before reaching a 2D CCD detector.

sample cell is mounted on the motorized sample X-Z translation stage and aligned with respect to the cell. Photosensitive paper (commonly known as "burn tape") can be used for rough alignment. For fine alignment, the cell aperture is centered with respect to the beam by using the beamstop reading.

For the experimental SAXS results presented in this thesis, a custom 1024 x 1024 CCD detector (similar to that described in [135]) was used. Lead tape was used to cover a 20 to 30 pixel wide vertical strip along one edge of the detector face allowing measurement of the average zero-offset of every row of pixels. Following row-by-row zero-offset subtraction, each SAXS image was treated with distortion and intensity correction, dark current subtraction, and shadow masking. The dark current was recorded before each set of exposures with identical exposure times. Masking may be performed

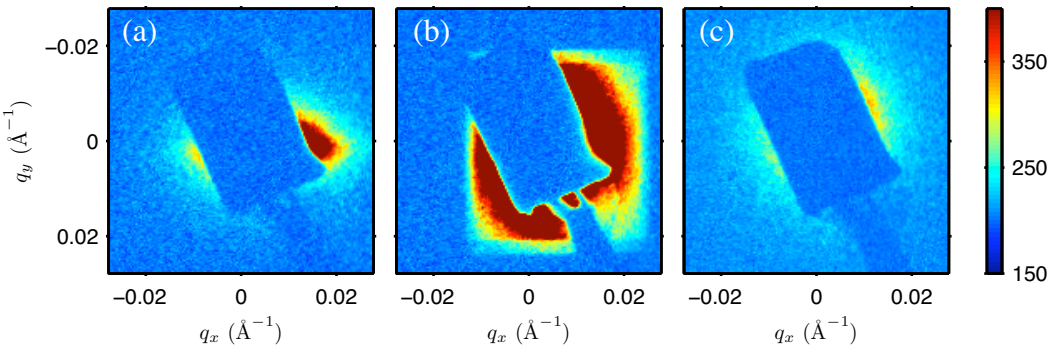

Figure 2.22: Slit scatter. (a) 0.1 second image taken after roughly alignment of beamstop with X-ray beam. Beam is scattering on guard slits. (b) 0.1 second image taken with guard slits open, strong slit scattering from upstream focusing slits is visible. (c) 1.0 second image taken after removing slit scatter. The shadow of the PIN beamstop is clearly shown.

with a SAXS image converted to a high-contrast (black and white) image (Fig. 2.23 (b)), or with a manually-defined shape. Diffraction from a SAXS calibrant is used to locate the beam center and convert from image pixel number to q. Silver behenate with a lamellar spacing of 58.376 Å [59, 15] was used in thesis (Fig. 2.23 (c)).

As the scattering of proteins in solution is symmetrical about the beam axis, the corrected detector images were azimuthally integrated about the beam center and normalized by a PIN diode reading to produce a 1-D scattering profile, $I(q)$ vs. q. The corresponding buffer profile was subtracted from that of the protein solution without any additional scaling. Accurate subtractions are crucial for protein solution SAXS, and therefore the reproducibility and linear response of the PIN-diode should be checked by recording multiple exposures at various times and with different durations. Biological samples are also prone to radiation damage. Radiation damaged samples tend to aggregate, affecting the low-q region of $I(q)$. The exposure limit of a sample depends upon numerous factors including the sample and solvent conditions. Multiple, short

exposures are recommended rather than single, long exposures in order to identify the exposure limit of a sample. Each exposure is integrated and compared. In cases where exposure-dependent changes were undetected in the scattering profiles, the images were averaged to reduce noise. A large source of noise often referred to as "zingers" that are recorded in CCD detector images is the radioactive impurities in the fiber optic taper, and therefore the zinger frequency is dependent on the detector. De-zingering can be performed during image averaging [8]. With the detector used for this thesis, zingers were infrequent, and therefore, de-zingering was unnecessary. Data treatment and analysis were performed with a suite of custom programs written in C and Matlab (The Mathworks, Natick, MA)

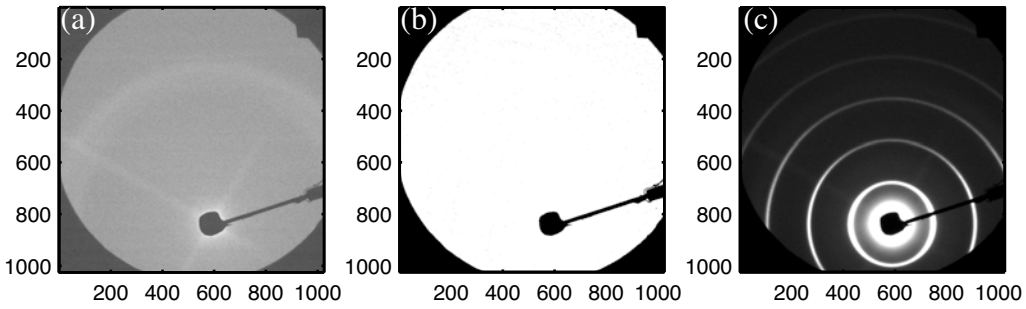

Figure 2.23: Calibration and masking of shadows in scattering images. (a) A SAXS image through an empty high-pressure cell. The cross-shaped scattering is from the diamond window, and the ring is from polyimide film. (b) A high-contrast version of (a) was used as an integration mask. (c) A diffraction image of a SAXS calibrant, silver behenate.

2.3.6 Background Scattering: Diamond Windows

Natural diamonds often contain more nitrogen impurities than type IIa synthetic diamonds, and thus exhibit greater parasitic scattering. However, it was found that even a strongly scattering diamond can perform satisfactorily if it displays reproducibility and has very little stress-induced variability in parasitic scattering. The parasitic scattering from diamond windows depended strongly upon the particular diamond and the location through which the beam travels. Three diamonds selected as high-pressure windows were each mounted in a window holder and compared. Diamond 1 (Fig. 2.24 (a), (c)) showed very little scattering around the beamstop, while diamond 2 (Fig. 2.24 (b), (c)) exhibited intense and azimuthally asymmetric scattering. The integrated SAXS profiles of all three diamonds at ambient pressure are compared to the system scattering in Fig. 2.24 (c).

The intensity of the diamond scattering was also pressure-dependent, and the magnitude of the changes were found to vary depending upon the diamond. Two of the diamonds, diamond 1 which showed the least scattering and diamond 2 which scattered the most, showed little variation with pressure (Fig. 2.25 (a)). In comparison, diamond 3 with intermediate scattering intensity showed significant changes in low-q scattering below 100 MPa (Fig. 2.25 (b)), making reliable background subtractions difficult. All high-pressure SAXS measurements on proteins were therefore performed with the first pair. Since diamond 2 had asymmetric scattering, this window was fixed during the course of an experiment to yield reproducible background scattering, Sample cells were loaded by removing the window containing diamond 1.

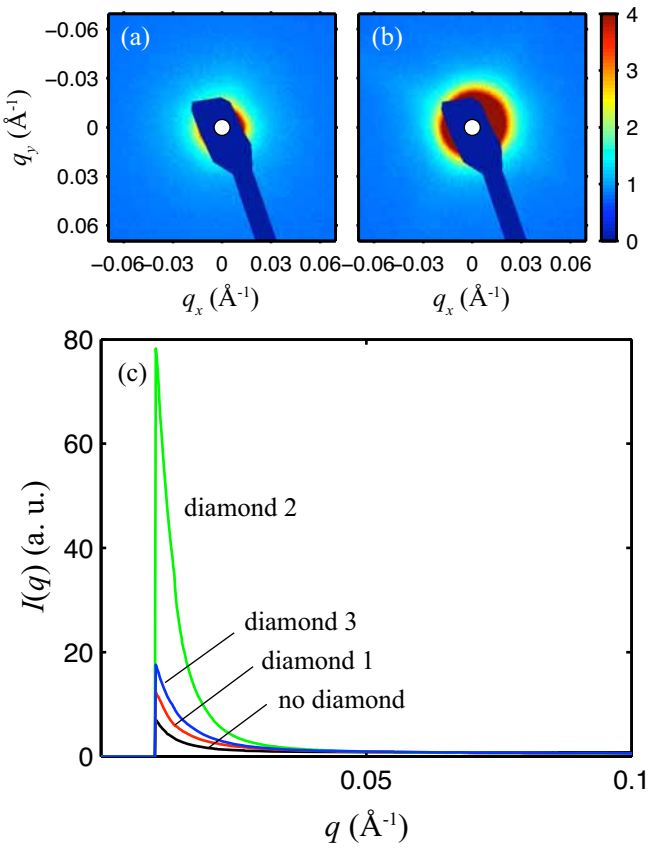

Figure 2.24: Comparison of the parasitic scattering from three natural diamond windows. (a) SAXS image of diamond 1 shows little scattering around the beamstop which is shown in dark blue with the beam center marked with a (white) circle. (b) SAXS image of diamond 2 shows intense azimuthally asymmetric scattering near the beamstop. (c) Transmission-normalized 1-D scattering profiles of the system (black, bottom curve), diamond 1 (red curve), diamond 2 (green curve), and diamond 3 (blue curve).

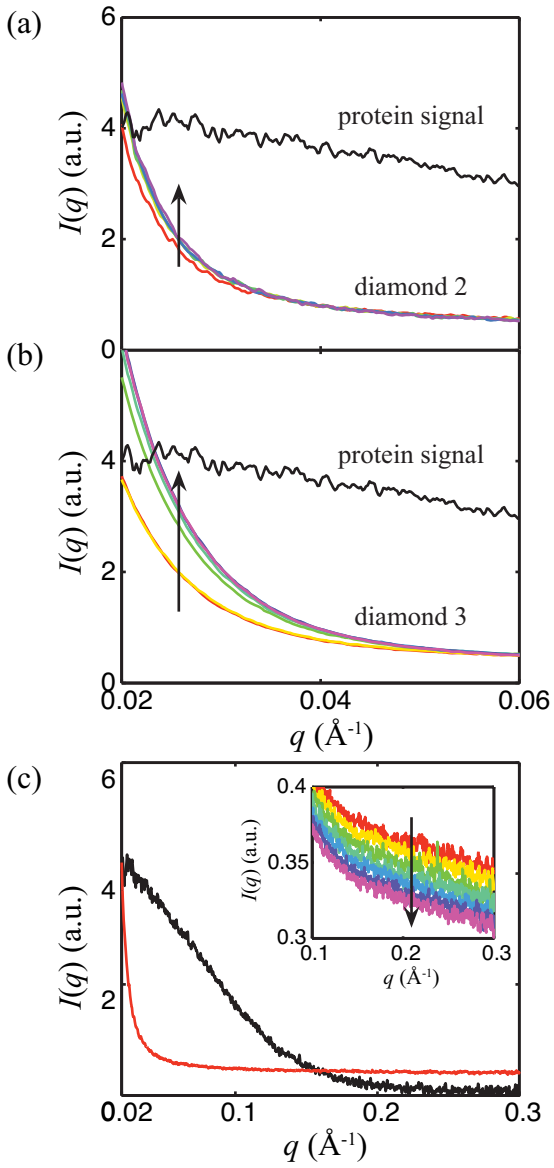

Figure 2.25: Comparison of diamond scatter as a function of pressure (28 MPa to 300 MPa in direction of arrow). Diamond 1 was used as the downstream window in both cases. The buffer-subtracted protein signal is shown in black. (a) Diamond 2 as the upstream window. The inner cell contained 50 mM glycine, 100 mM NaCl buffer, pH 3.0. The variation in the diamond scattering was small relative to protein signal. (b) Diamond 3 as upstream window. The inner cell contained water. The variation in diamond scattering was large relative to the protein signal. (c) Comparison of diamond scattering (red) and buffer-subtracted protein signal (black) at 28 MPa. Inset: The high-q region of the scattering profile decreases with pressure due to reduced X-ray transmission.

The high-q region of the diamond SAXS profiles was comparatively featureless, but the intensity decreased with pressure reflecting the reduction in transmission due to the increased water density and deflection of the windows (Fig. 2.25 (b), inset). As the high-q region can contain information about the shape of proteins, protein and buffer measurements were taken at the same pressure before subtraction.

CHAPTER 3

HIGH-PRESSURE FLUORESCENCE SPECTROSCOPY

3.1 Fluorescence Spectroscopy of Proteins and RNA

Conventional fluorescence spectroscopy is primarily concerned with the interaction of light with the valence electrons responsible for molecular structures, i.e. the electrons in the partially filled outer shells of the individual atoms of the molecule. These electrons are promoted to higher energy levels by the absorption of photons and return to the ground state via various pathways. One of these pathways is by the emission of fluorescence radiation. As fluorescence spectroscopy is a probe of molecular electronic structure, it is sensitive to structural and environmental changes of the sample, and can therefore be used to monitor conformational changes of proteins and RNA. In this thesis, high-pressure steady-state UV fluorescence spectroscopy was employed as a structural probe as a complement to high-pressure SAXS.

3.1.1 Molecular Electronic Structure and Transitions

Fluorescence spectroscopy is a form of electronic spectroscopy - the study of transitions between the electronic states of a chromophore [143, 121, 142, 3, 75]. In the case of molecular chromophores, the electronic states are determined by the occupancy of molecular orbitals (i.e. the electronic configuration) and the spin state of the occupant electrons. The occupants of molecular orbitals are the valence electrons of the constituent atoms in a molecule. The valence electrons and the lowest energy molecular orbitals are responsible for the covalent bonds in molecules.

A σ-bond is formed by the overlap of two atomic orbitals, such as *s* orbitals, that is cylindrically symmetrical about the axis joining the nuclei of two atoms. The electron pair participating in a σ-bond is localized on the internuclear axis and therefore tightly bound to the molecule. Promoting one of these electrons to a higher molecular orbital requires a large energy. Absorption of light in the vacuum-UV region (40-190 nm or 6.5 - 30 eV) is typically required. The σ-bonds make up the lowest energy molecular orbitals (called σ-orbitals) of a molecule. The electronic transitions of σ-electrons are not studied in conventional fluorescence spectroscopy.

The π-bond, is formed by the overlap of two atomic orbitals, such as *p* orbitals, that are perpendicular to the axis joining the two nuclei. As the π-electrons are not localized in the internuclear axis, these electrons are less tightly bound to the parent nuclei than σ-electrons. As a result, when multiple atoms joined by σ-bonds also form π-bonds, the π-electrons are distributed among all of the atoms. Molecules with such delocalized electrons are often called aromatic. An example of such a molecule is the six-carbon ring, benzene. The degree of delocalization of such electrons depends on the size of the aromatic molecule. Delocalized π-electrons can be excited by the absorption of UV radiation for small aromatic molecules such as benzene and by lower energy radiation for larger aromatic molecules such as the chromophore from the *Aequorea* Green Fluorescent Protein [121, 140]. The π-orbitals typically make up the next lowest set of molecular orbitals.

Organic molecules with certain atoms (such as nitrogen, oxygen, and halogens) also contain lone pair valence electrons. These electrons do not participate in a covalent bond but fully occupy a molecular orbital referred to as a nonbonding or *n* orbital. As these electrons do not participate in bonding, *n* orbitals often lie higher in energy than π orbitals.

Anti-bonding orbitals lie higher in energy than σ, π, and n orbitals. Anti-bonding orbitals with σ geometry are known as σ*-orbitals, while π*-orbitals are those with π geometry. As the electrons are on average farther apart in π*-orbitals than σ*-orbitals, π*-orbitals lie lower in energy.

The electronic state of a molecule is dependent upon the distribution of valence electrons among the molecular orbitals. In the ground state, all of the bonding and nonbonding (if any exist) molecular orbitals are doubly occupied (with the exception of free radicals, which we do not discuss here). All of the anti-bonding orbitals in a molecule are unoccupied. The electrons pairs have opposite spin, as necessitated by the Pauli exclusion principle. The ground state is therefore a singlet state, i.e. with a net spin of zero, denoted as S_0. In the first excited state, one electron of the electron pair in the highest occupied molecular orbital (HOMO) is promoted to the lowest unoccupied molecular orbital (LUMO), which is typically a π*-orbital. For an organic molecule with a heteroatom, the HOMO is often an n orbital, while for others the HOMO is typically a π-orbital. The second excited state is the electronic configuration resulting from the molecular orbital transition with the second smallest energy gap, and so on. The energy level of the excited state is also dependent upon the spin state of the unpaired electrons. If the unpaired electrons retain opposite spin, the excited state is a singlet state. If the electrons become unpaired (antiparallel), the excited state is a triplet state, i.e. a three-fold degenerate state with a net spin of 1. As the electrons are on average physically farther apart in a triplet state, resulting in less charge repulsion, a triplet state is generally lower in energy than a singlet state. Excited singlet states will be denoted S_1, S_2, and so on; excited triplet states will be denoted T_1, T_2, etc. Each electronic state has vibrational substructure. See Fig. 3.1 for a graphical representation of the electronic states of a molecule.

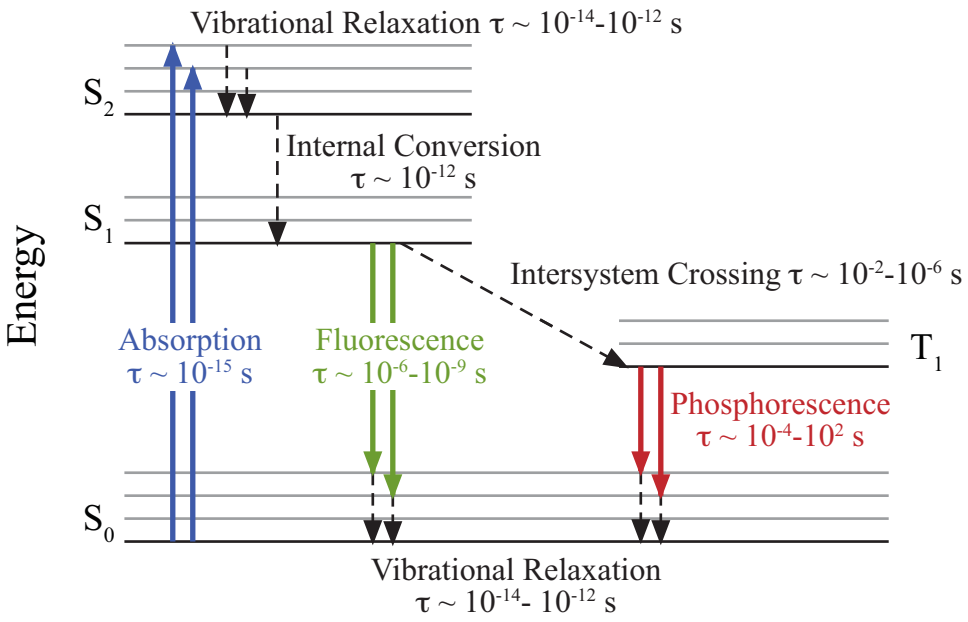

Figure 3.1: Electronic states and transitions of a chromophore. Following rapid absorption of a photon, the chromophore relaxes to the ground by radiationless processes (shown as dotted arrows) and by emission of fluorescence or phosphorescence. Values of lifetimes were from [3, 75, 22, 121].

A transition between two electronic states can be induced by the absorption or emission of radiation, or it can be radiationless. Excitation of a chromophore is achieved by the absorption of light. During absorption, an electron is promoted typically from a low vibrational mode in S_0 to one of the vibrational modes in an excited singlet state. The absorption spectrum of the molecule therefore represents the vibrational substructure of the excited states. As already mentioned, excitation leads to a change in electron configuration. Such a change can cause the nuclei to move and therefore change the electronic states of the chromophore. However, because an electronic transition by light absorption is rapid, on the order of 10^{-15} s, there is insufficient time for the nuclei to move from their equilibrium positions. As a result, the electronic states of the excited chromophore can be represented by those of the ground state chromophore. This simplification is

known as the Franck-Condon principle [22, 75, 121].

Following absorption of a photon, the chromophore relaxes to the ground state via various pathways. As thermal relaxation is rapid, the molecule quickly reaches the lowest vibrational mode of the excited electronic state (e.g. S_2 in Fig. 3.1). If this state spatially overlaps with a higher vibrational mode of a lower electronic state (i.e. the orbitals overlap and have the same energy), interval conversion to the lower electronic state follows rapidly. Both thermal relaxation and internal conversion are radiationless transitions. Internal conversion usually repeats until the molecule reaches the lowest vibrational mode of S_1. The energy gap between S_1 and S_0 is usually too great for internal conversion to occur. At this point, the molecule may relax further by intersystem crossing to the T_1 triplet state which is often lower lying than the S_1 state. However, in most cases the excited singlet will relax directly to S_0 by the emission of radiation. This radiation is fluorescence (Fig. 3.1). Although the lifetime of the lowest excited singlet state is long compared with thermal relaxation, the actual transition to the ground state is as rapid as absorption (10^{-15} s). Therefore the molecule usually does not have time to thermally relax and reaches a high vibrational mode of S_0. Following this, the molecule proceeds to thermally relax. The fluorescence spectrum therefore represents the vibrational substructure of the ground state and is often a mirror image of the absorption spectrum (Fig. 3.2). In the event that intersystem crossing proceeds, the triplet state will also relax to the ground by emitting radiation; this radiation is known as phosphorescence (Fig. 3.1). As the excited electron must flip spins, the lifetime of a triplet state is usually much longer than that of a singlet state. This long decay lifetime is the reason for the long glow that is characteristic of phosphorescence (e.g. “glow in the dark”).

It is well known that the fluorescence spectrum of a chromophore is centered at lower energies than the absorption spectrum. One of the reasons for this shift in energy

between absorption and fluorescence emission is thermal relaxation. As mentioned, fluorescence emission typically occurs from the lowest vibrational mode of the first excited state to high vibrational modes of the ground state, while absorption occurs from the lowest vibrational mode of the ground state. Because of this, the same fluorescence spectrum can be obtained by excitation at different energies (assuming one type of chromophore is selectively excited in this energy range). Another significant contribution to the red shift is solvent relaxation. Typically, the excited state has a larger dipole moment than the ground state. As a result, the energy level of the excited state is dependent on the polarity of the surrounding solvent. As solvent relaxation occurs in $10^{-11} - 10^{-10}$ s (much faster than fluorescence lifetimes), solvent dipoles can reorient with the excited molecule and lower the energy of the excited state. The effect of solvent relaxation on lowering the excited state energy is greater for polar solvents such as water. Therefore, the radiation emitted from a solvent-relaxed excited state is further red-shifted from the absorption spectrum.

Further discussion of molecular electronic structure and transitions can be found in [143, 121, 142, 3, 75].

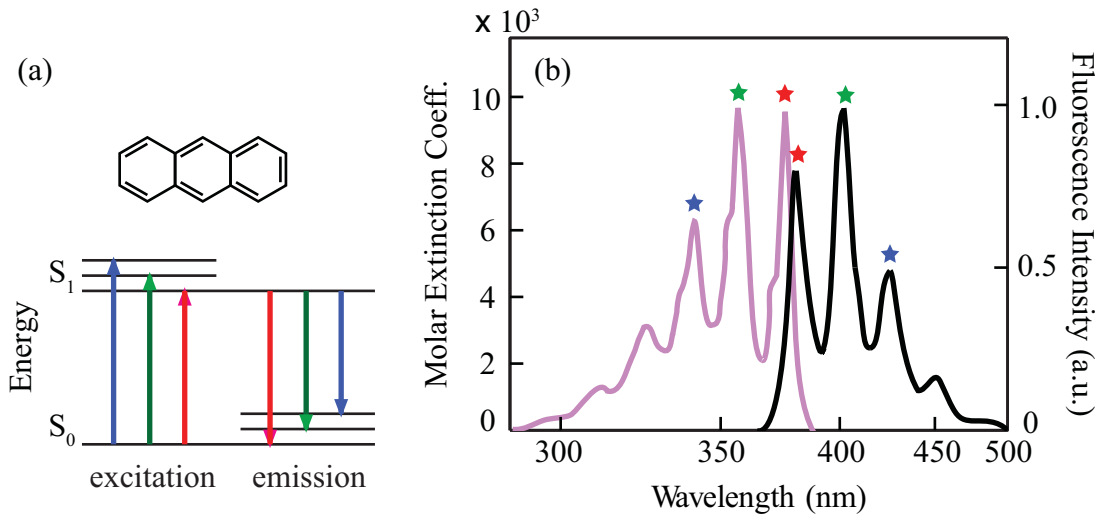

Figure 3.2: The absorption and emission spectra of anthracene. (a) The chemical structure and illustration of the energy levels of anthracene. (b) Excitation (pink) and emission (black) spectra. The transitions are labeled by color. Blue corresponds to the 0-2 transition, green corresponds to the 0-1 transition, and red corresponds to the 0-0 transition, where the numbers represent the vibrational state of S_0 and S_1.

3.1.2 Fluorescence Spectroscopy of Solution Samples

Given a collimated excitation beam with incident intensity, I_0, the fraction of the beam that is absorbed by a homogeneous sample with molar extinction coefficient of ϵ, molar concentration c, and a path length of l can be written as,

$$\frac{I_A}{I_0} = 1 - 10^{-\epsilon c l}, \tag{3.1}$$

where the second term is the transmitted fraction. Note that by convention, transmission in spectroscopy is defined by a power of 10 rather than an exponential. Expansion of the exponential term as a power series yields,

$$\frac{I_A}{I_0} = \sum_{n=1}^{\infty} -\frac{(-2.3\epsilon c l)^n}{n!} \tag{3.2}$$

At conditions where ϵc is small, the absorbed fraction is approximately linear with path length. This is known as the Beer-Lambert Law:

$$\frac{I_A}{I_0} \approx 2.3\epsilon cl. \tag{3.3}$$

It is useful to prepare samples under these conditions as this enables the normalization of spectra with sample concentration and path length. An isosbestic point in a set of spectra signifying a two-state process also requires that the spectral intensity is linear with concentration. For samples with overlapping absorption and fluorescence spectra, these conditions also minimize the re-absorption of fluorescence, which can cause an apparent red-shift of the fluorescence spectrum. The fraction of excited molecules that relax to the ground state by emitting fluorescence is called the fluorescence quantum yield, ϕ_F. The ratio of fluorescence to incident beam intensity at small ϵc values is thus,

$$\frac{I_F}{I_0} \approx 2.3\phi_F\epsilon cl. \tag{3.4}$$

Generally, ϕ_F is also very small. Therefore, the detectable fluorescence signals are very dim compared with the incident and transmitted excitation beams. Fluorescence is also subject to quenching, a decrease in fluorescence intensities. Causes include energy transfer to molecular oxygen dissolved in the solvent and collisional quenching, which is dependent of temperature and pressure. Additionally, fluorescence emission is omni-directional, and typically, only a small solid angle of the total emission is collected. To maximize fluorescence detection and minimize detection of transmitted and scattered light, the emission is often collected off-axis from the incident beam, typically at right angles.

Samples for fluorescence spectroscopy experiments are prepared at concentrations where Eqn. (3.3) is satisfied while maximizing the signal-to-background. To minimize unwanted fluorescence background and scattering, samples are often filtered to

remove aggregates and dust particles (this may be especially necessary when rehydrating lyophilized samples). The background should ideally be identical to the solvent in the sample solution (typically an aqueous buffer for biological studies) and contain as few chromophores as possible. A single excitation wavelength (with a finite bandwidth) is chosen to selectively excite one type of chromophore and to minimize the overlap of scattered light with the fluorescence spectrum. For ambient pressure measurements, solution samples are often contained in a 10 mm path length square cuvette with quartz windows on all four sides. Sample concentrations are often on the order of a few μM or less.

A typical layout for solution fluorescence spectroscopy consists of a light source at a single excitation wavelength, sample, and detector in an L-shaped format. In later sections, two setups used in this thesis will be described.

3.1.3 Tryptophan Fluorescence

Three aromatic amino acids typically contribute to the intrinsic fluorescence of most proteins: phenylalanine, tyrosine, and tryptophan. The absorption and fluorescence spectra of these amino acids are shown in Fig. 3.3. Phenylalanine contains a phenyl group (consisting of a benzene ring), the smallest aromatic group among those contained by the three amino acids. For this reason it is not surprising that the absorption spectrum of phenyalanine is bluest of the three amino acids. Tyrosine contains a phenol group (a benzene ring with a hydroxyl group), while tryptophan contains the largest aromatic group, an indole. The indole consists of two aromatic rings as well as a nitrogen. The highest degree of electron delocalization and the influence of nonbonding orbitals are expected for tryptophan. Accordingly, tryptophan absorption is the furthest to the red

of the three amino acids. At the absorption maximum of tryptophan (280 nm), tyrosine is also excited. Hence, selective excitation of tryptophan is often performed at 295 nm (Fig. 3.3).

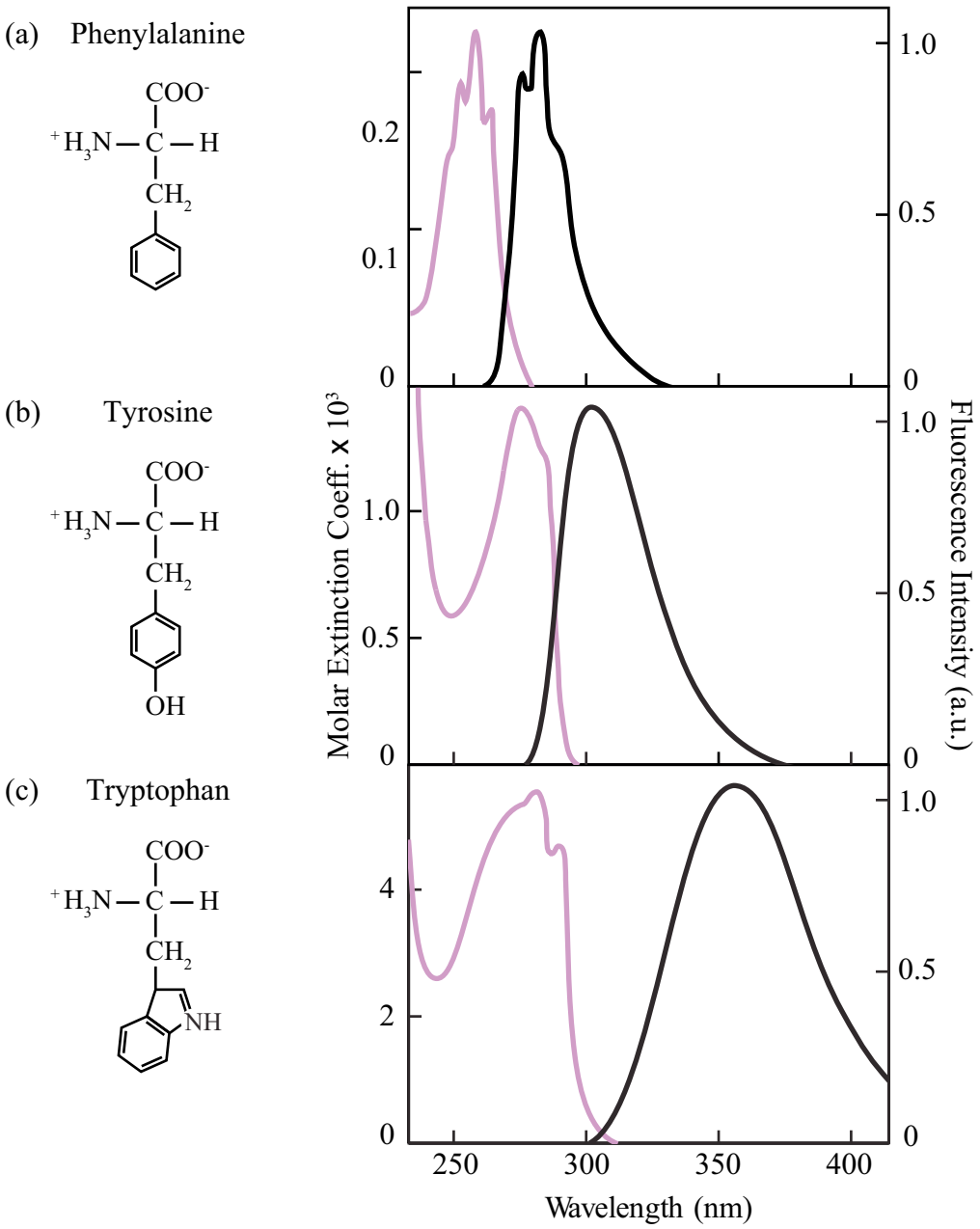

Figure 3.3: The chemical structures and absorption and emission spectra of the aromatic amino acids (adapted from [75]). (a) Phenylalanine. (b) Tyrosine. (c) Tryptophan.

Of the three aromatic amino acids, tryptophan displays the greatest solvent sensitivity in its fluorescence spectrum [75, 22]. For this reason tryptophan has been employed most widely for protein fluorescence studies. The two lowest excited singlet states of tryptophan are called ^1L_a and ^1L_b. These two excited states have dipole moments that are nearly perpendicular to one other (Fig. 3.4 (a)). In nonpolar environments, ^1L_b is the lowest excited state and dominates tryptophan fluorescence. The fluorescence spectrum of ^1L_b is highly structured. ^1L_a has a large dipole moment involving the nitrogen in the indole ring (Fig. 3.4 (a)). As the -NH group is hydrogen-bondable, ^1L_a can be stabilized by solvent relaxation in polar environments. This stabilization forms the basis for the red shift of tryptophan fluorescence with solvent polarity. The fluorescence spectra of indole in various cyclohexane-ethanol solutions are shown in Fig. 3.4 (b). As the polarity of the solution increases, the structured spectrum of the ^1L_b state becomes dominated by the solvent-dependent ^1L_a state. Similarly, the intrinsic fluorescence of proteins containing tryptophan can vary greatly depending on the location of the residue inside the protein molecule. Tryptophan is deeply buried in the hydrophobic core of apoazurin while completely solvent-exposed in glucagon (Fig. 3.4 (c)). The same principles allow one to monitor the change in solvent exposure of buried tryptophans caused by conformational changes of protein molecules due to denaturation. The quantum yield of tryptophan also varies with its location. Dissolved in water, the quantum yield is apprximately 0.12.

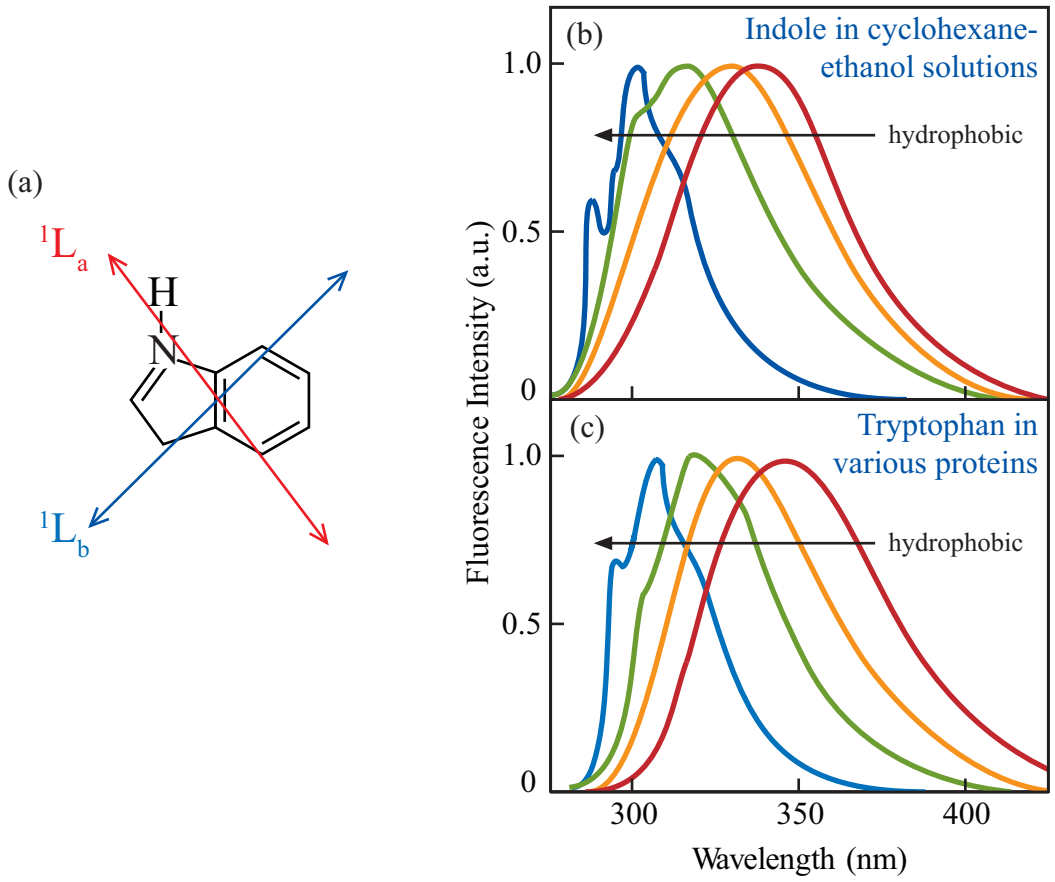

Figure 3.4: The solvent dependence of tryptophan fluorescence [adapted from [75]]. (a) The dipole moments of the two lowest excited states of the indole group. (b) Indole spectra in cyclohexane-ethanol solutions: from left to right, 0%, 1%, 5%, and 100% ethanol. (c) Tryptophan fluorescence of several folded proteins: from left to right, apoazurin Pfl, ribonuclease T_1, stapphyloccocal nuclease, and glucagon.

3.1.4 RNA Fluorescence

Unlike proteins, naturally occurring nucleic acids do not exhibit intrinsic fluorescence. Although the nucleotides that make up DNA and RNA contain aromatic bases, the fluorescence signal from these bases are very weak. The quantum yields of nucleic acids are on the order of 10^{-5} to 10^{-4}. Therefore, fluorescent dyes and nucleotide analogs

are commonly used to probe conformational changes of nucleic acids with fluorescence spectroscopy. 2-aminopurine (2AP) is a fluorescent analog of adenine that can be incorporated into DNA or RNA chains. The quantum yield of free 2AP is very high, ≈ 0.68 in water. As its absorption band lies at longer wavelengths than naturally occurring bases, it can be selectively excited. 2AP is especially useful as a conformational probe of nucleic acids as its fluorescence signal is highly sensitive to base interactions - particularly, base stacking. Incorporation of 2AP into an RNA chain reduces the quantum yield by a factor of 20 to 100, while incorporation into a double-stranded (helical) RNA reduces the yield by another factor of 3 to 10 [153]. 2AP fluorescence is thus a useful probe for changes in local base interactions resulting from RNA conformational changes [152].

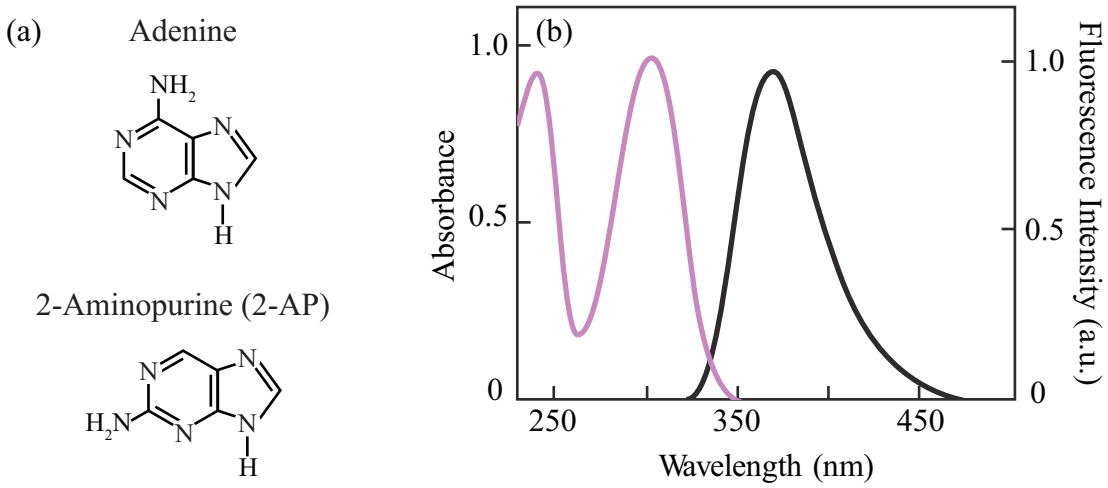

Figure 3.5: Fluorescence of 2-aminopurine (2AP) in water [adapted from [153]]. (a) The chemical structures of adenine and its fluorescent analogue, 2AP (b). The absorption (pink) and fluorescnce (black) spectra of 2AP

3.2 High-Pressure Fluorescence Spectroscopy

An important design requirement for a high-pressure fluorescence cell is transparency, and particularly, UV transparency. This criterion must be satisfied by every component along the excitation and emision beam paths, including windows, internal sample cells, and pressure medium not only to maximize the transmission of fluorescence signals, but also to prevent background fluorescence and scattering.

3.2.1 High-Pressure Cell

A commercially available high-pressure fluorescence cell (HP Cell 3rd Version, ISS, Champagne, IL) was purchased (Fig. 3.6, 3.7). This cell, based on the design of Paladini, *et al.* [98, 97], features a large stainless alloy body and three large Poulter-type windows [107]. The cell body is roughly cubic, 91.3 mm in each dimension, and features four 22 mm diameter bores that are perpendicular to each other. Three of these bores lie in the horizontal plane in a T-format geometry and function as window ports. The sample is loaded from the top via the fourth, vertical bore.

Two sets of 19 mm diameter windows can be fitted: 8.5 mm thick quartz windows, which can hold pressures up to 300 MPa and 6.4 mm thick sapphire windows, which are less UV transparent but can hold up to 400 MPa. As very few materials are both transparent in the far UV (wavelengths below 300 nm) and strong enough to hold high pressure, the choice of economical high-pressure fluorescence window materials is limited to quartz and sapphire. The windows are placed onto threaded metal window holders with 10 mm diameter apertures and fixed in place by anodized metal screw caps to form Bridgman seals (Fig. 3.7 (b)). The assembled windows are torqued into the

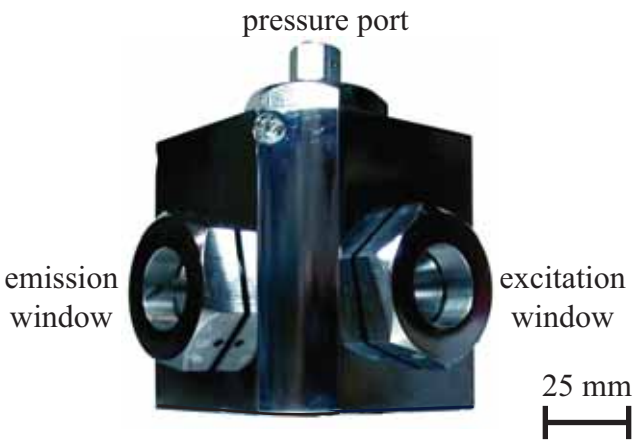

Figure 3.6: Photo of high-pressure fluorescence cell (ISS).

window ports. The sample chamber is closed by a closure nut with a 1/4" (6.35 mm) cone seal connection and a small channel for pressure transmission. A 1/8"(3.18 mm) high-pressure tube (HF2; High Pressure Equipment Co., Erie, PA) is connected to the pressure port via a 1/8"-to-1/4" cone seal coupling (HM4HF2; High Pressure Equipment Co., Erie, PA). High-pressure seals are formed at the mating surfaces of the threaded closures and the cell by hard plastic rings that extrude into the tolerance (Fig. 3.7 (b)). A high-pressure reservoir (described in the previous chapter) is used to separate the pressure-transmitting fluids in the pump and high-pressure cell.

3.2.2 Sample Isolation and Pressure-Transmitting Fluid

As in high-pressure SAXS, high-pressure fluorescence samples required sample isolation from the surrounding pressurizing medium. Several fluids were investigated for use as the pressure medium in the high-pressure cell (Fig. 3.8 (a)). Water exhibits the least background fluorescence. The spectrum of water is featureless except for a small Raman peak around 330 nm (at 290-295 nm excitation). ISS recommends spectroscopy-grade

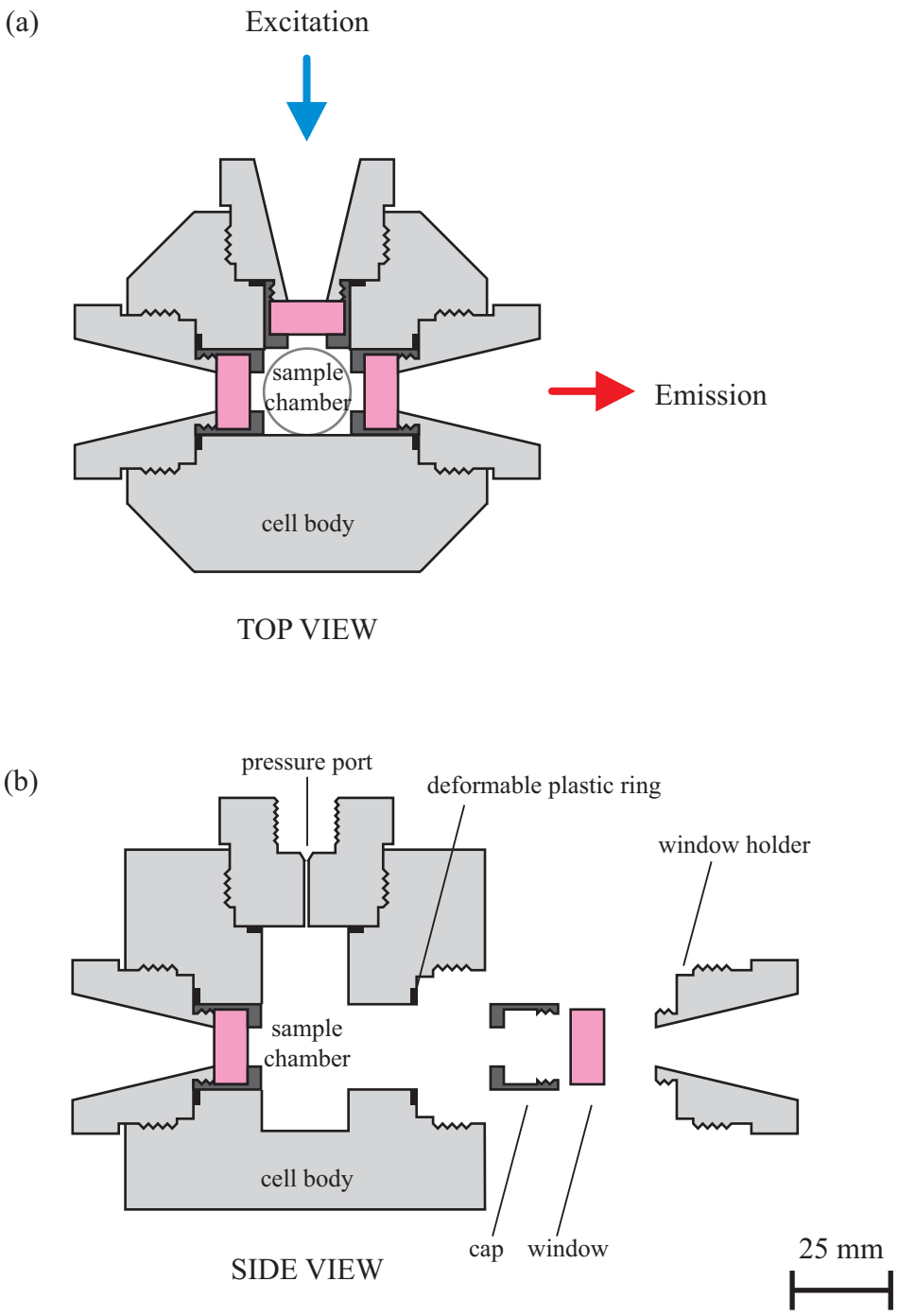

Figure 3.7: Cross-sectional views of high-pressure fluorescence cell (ISS) (a) Top view. (b) Side view. The sample-filled inner cell (described in following section) is placed in the sample chamber.

ethanol as the pressure medium. Although in principle, all components along the excitation and emission beam paths should be free of spectroscopic contaminants, we found maintaining solvent purity in a high-pressure system to be difficult and costly. Many high-pressure components, such as pistons and threads, must be coated with grease that can easily contaminate the ethanol. For this reason, frequent exchanges of ethanol were required (once every few pressure cycles). Approximately 30 mL of solvent is required to fill the high-pressure fluorescence cell and reservoir. As non-denatured (pure) ethanol is expensive, regular isopropanol was used as an inexpensive alternative. We found that the background fluorescence from regular isopropanol was not worse than that of spectroscopic-grade ethanol, most likely due to the difficulty in controlling small levels of contaminants that easily dissolve in these solvents. Fluorinert (3M) was also investigated as it is the pressure medium in the high-pressure pump. Using a single pressure medium for the entire system eliminates the need for a high-pressure reservoir, which is the least robust component. Fluorinert can also be left inside high-pressure components without concern for corrosion. Although Fluorinert was found to transmit UV at ambient pressure, we found that it becomes cloudy above 150 MPa (Fig. 3.8 (b)), which caused a decrease in UV transmission and an increase in scattering. The kinetics of this clouding effect were quite slow in both pressure directions.

The quartz internal cell provided by ISS for sample isolation was found to be inadequate for our needs. This cell is bottle-shaped with a 9 mm path length cylindrical bottom and a 3 mm inner diameter neck. A hard plastic cap made from a Teflon resin was used to close this cell. Pressure transmission to the sample was achieved by the cap sliding down the neck (much like a piston). However, due to the space constraints created by beam position in the high-pressure cell, the cap could only slide a few millimeters before hitting the bottle shoulder at the base of the neck. As the cap itself was not very compressible under pressure, the sliding motion was not sufficient to trans-

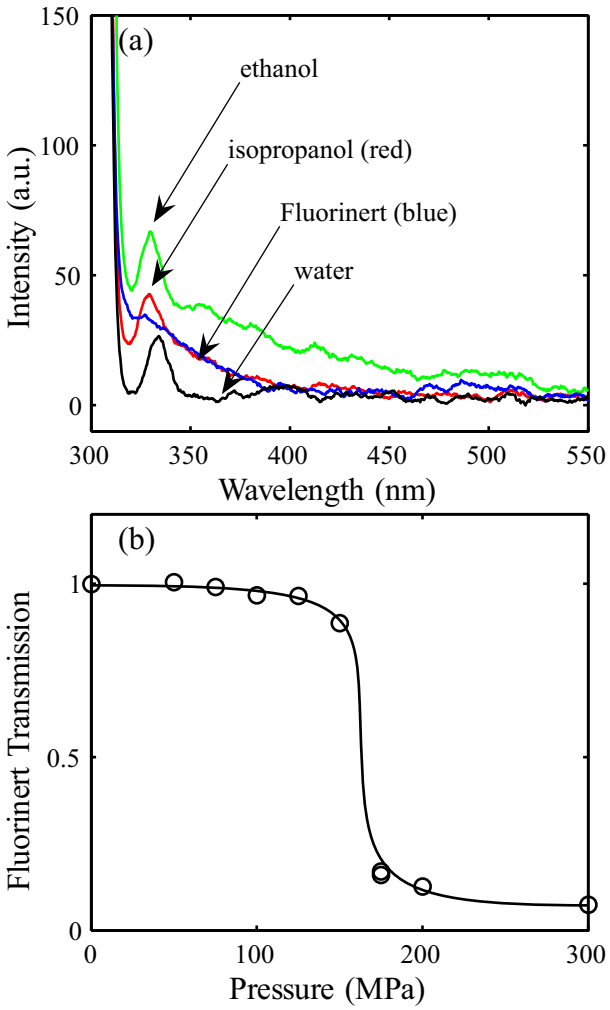

Figure 3.8: Fluorescence of various pressure-transmitting fluids. (a) The spectra of water, spectroscopy-grade ethanol, and isopropanol feature a Raman scattering peak around 330 nm. In terms of minimizing background fluorescence, spectroscopy-grade ethanol did not perform better than regular isopropanol, most likely due to the difficulty in controlling small levels of contamination. (b) The transmission (normalized by the ambient pressure value) through Fluorinert was pressure-dependent. Above 150 MPa, Fluorinert becomes cloudy. Note that the kinetics are slow (minutes) and data were not collected at full equilibrium conditions.

mit high pressure to the sample. Consequently, this internal cell frequently shattered at pressures above ≈ 250 MPa. This cell was also not optimized to minimize background fluorescence and scattering.

A custom internal cell was designed to minimize scattering and background fluorescence and to perform reliably at pressures up to 400 MPa (Fig. 3.9). The internal cuvette was constructed by fusing a 10 mm path length square quartz cell (Cat. No. CQ110; VitroCom, Mountain Lakes, NJ, USA) and a short 3 mm inner diameter quartz tube (Cornell Glass Shop). A soft bulb made from polyolefin heat shrink tubing (Cat. No. 03F3745; Newark Electronics, Chicago, IL, USA) was used as the closure with a deformable pressure-transmitting membrane. To make the bulb, one end of the heat shrink tubing was allowed to fully shrink under the heat of a heat gun or soldering iron. The other end was crimped and melted together with a pair of pliers heated over a flame. The internal cuvette is aligned in the high-pressure cell with a two-piece Delrin cuvette holder (Fig. 3.9). One corner of the cuvette is marked with a smooth scratch enabling reproducible orientation in the bottom piece of the holder. The top piece functions as a spacer to minimize the volume of pressure fluid required in the high-pressure cell. The large flat windows of the square cuvette minimize scattering of the incident beam, while the window holder blocks any background fluorescence from the pressure-transmitting fluid from reaching the emission collection window.

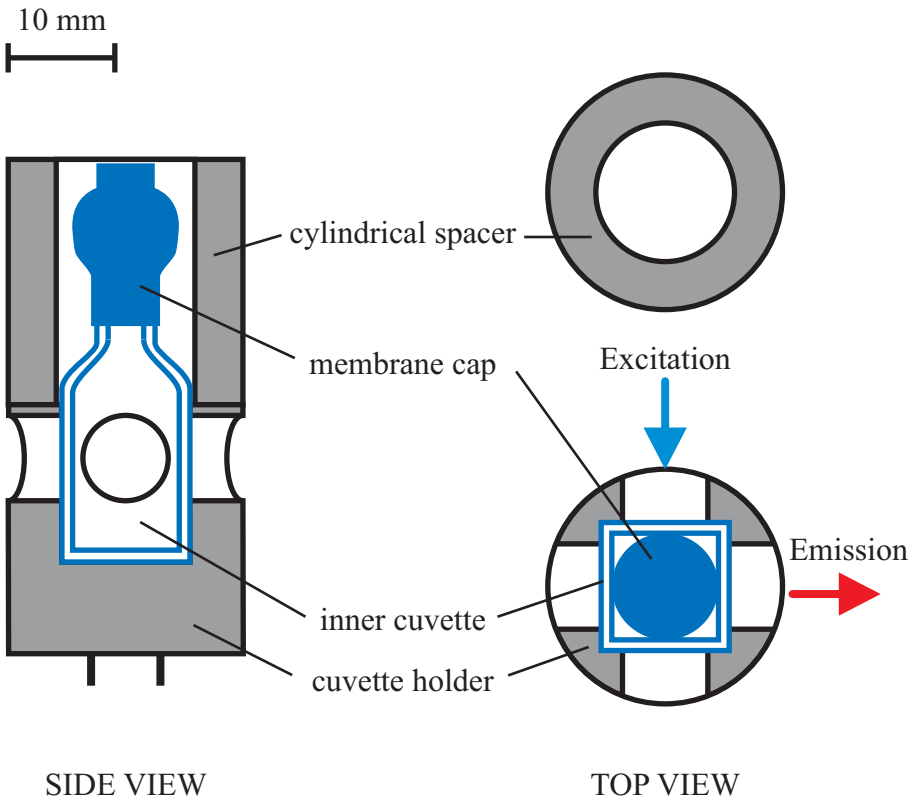

Figure 3.9: Internal sample cell. (a) Top view. (b) Side view. The cuvette body is made of quartz, the cuvette holder is made of black delrin, and the membrane cap is made of polyolefin heat-shrink tubing. Two metal pins in the bottom of the cuvette holder fit into alignment holes in the high-pressure fluorescence cell.

3.2.3 Experimental Protocols

Prior to each set of experiments, the high-pressure reservoir is cleaned, refilled, and tested for pressure leaks. After disconnecting the reservoir from the pressure network, it is opened and the piston is removed. The O-rings are removed from the piston, and the reservoir and piston are cleaned with detergent and rinsed with tap water and isopropanol before drying completely in the vacuum oven. Detergent is necessary for removal of oil-based contaminants. Fig. 3.10 (a) shows the fluorescence of unwashed machining oil

dissolved in the isopropanol dominating the sample fluorescence. Upon drying, a thin layer of vacuum grease is applied to the inner walls of the high-pressure using the piston as applicator. The piston is then removed and a fresh set of O-rings is installed. The cell-side opening of the high-pressure reservoir is closed with a 1/8" (6.35 mm) plug (hand tight) and the reservoir is filled with fresh isopropanol. After inserting the piston, the reservoir is flipped upside down and the 1/8"plug is loosened to allow trapped air and excess isopropanol to flow out as the piston is inserted completely. A fresh O-ring is inserted below the closure nut before torquing. The assembled reservoir is connected to the pressure network, and the 1/8" (6.35 mm) plug is torqued for pressure testing. After confirming that the reservoir does not leak more than 5-10 psi/min at 300 MPa, the reservoir is ready for experiments.

Contaminants can also be introduced into samples during preparation. After buffers were titrated to the appropriate pH, they were filtered into sterile bottles through 0.22 μm cellulose acetate lters by aspiration (Catalog Number 431175; Corning Inc, Corning NY, USA). Sample dialysis is performed several times at 4 °C to exchange the storage buffer with the experimental buffer. No spectroscopically observable contaminants were detected in the buffer after filtration and the final dialysis; the buffer spectrum was nearly identical to that of pure water (Fig. 3.10 (b)). Although sample aggregates and dust could be removed with small-volume-retention syringe filters after dialysis, it was found that low levels of spectroscopically observable contaminants were deposited by the syringe filters themselves (Fig. 3.10 (b), Whatman Anotop 10 Plus, Puradisc 13). The amount of contaminants leached from the syringe filters could not be controlled because they were dependent on the filter and amount of pressure applied during the filtration process. Samples were thus unfiltered after dialysis.

The buffer spectra varied very little with pressure relative to the protein and RNA

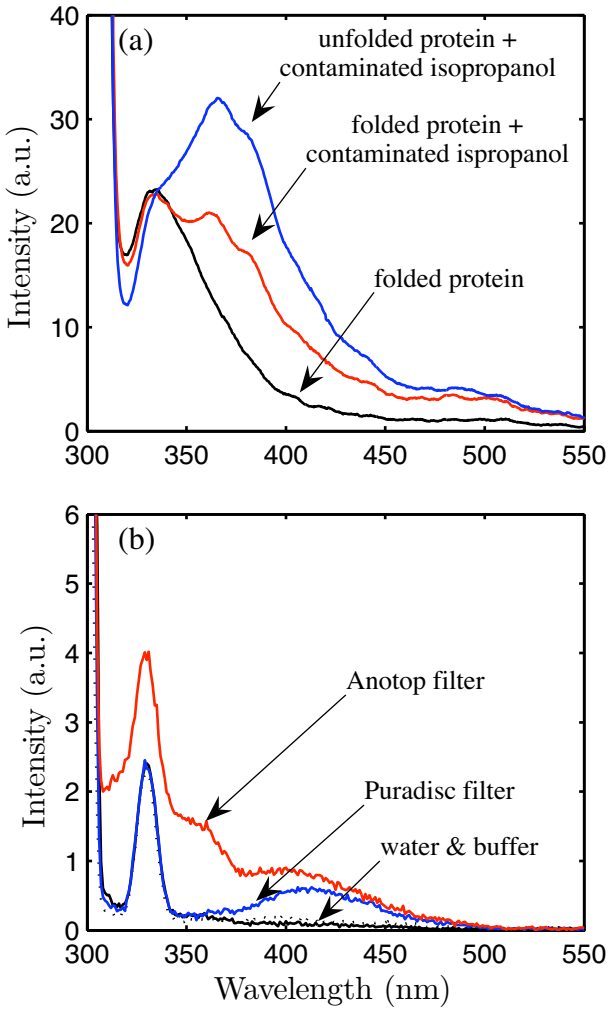

Figure 3.10: Contamination of fluorescence spectra. (a) Contamination of pressure-transmitting fluid with machining oil: spectra of protein (0.05 g/L L99A T4 lysozyme pH 3.5) in internal cuvette without pressure fluid (black) and surrounded by contaminated isopropanol (red, blue). Protein was folded at ambient pressure (red) and unfolded at high pressure (blue). (b) Contamination of buffer with syringe filters (contained in internal cuvette and surrounded by clean isopropanol). Spectra of water and buffer are nearly identical. The contamination caused by the Anotop 10 Plus filter (Whatman) was roughly 7% of the protein signal at 356 nm. Another Whatman filter (13 mm Puradisc) also caused contamination but to a lesser degree. The peak at 330 nm is the Raman peak of water.

signal (Fig. 3.11). As a typical experiment required roughly 10 hours for collection of sample spectra alone, only one or two buffer spectra were collected in later experiments. At the start of an experiment, a buffer spectrum was collected at ambient pressure to check for contaminants. The pressure was then increased to 50 MPa to prime the system. By doing so, the isopropanol in the high-pressure cell and reservoir is allowed to equilibrate. As the high-pressure cell is stored dry between experiments, it is prone to forming small air bubbles when it is refilled with isopropanol. Pressurizing to 50 MPa collapses air bubbles in small spaces and facilitate wetting of these surfacing. After equilibrating at 50 MPa, a buffer spectrum is collected. This spectrum is used for buffer subtraction of sample spectra taken on the same day.

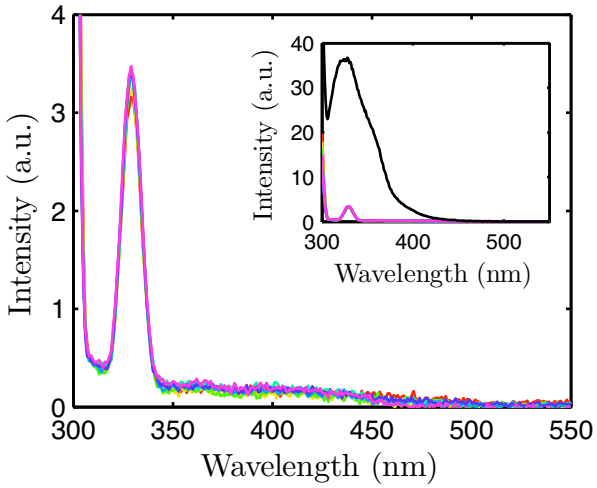

Figure 3.11: Background fluorescence under pressure. The fluorescence signal of buffer (50 mM glycine, 20 mM NaCl pH 3.0) is pressure-independent between 0.1 - 300 MPa. The spectra are featureless except for a small Raman peak around 330 nm. Inset: a comparison of the buffer spectra with 0.05 g/L L99A T4 lysozyme in the same buffer.

.

3.3 Spectrometers

Two spectrometers were used for the majority of spectroscopy experiments presented in this thesis. Preliminary characterization of L99A and wild-type T4 lysozyme was performed with a fiber-optic spectrometer (Ocean Optics). All of the fluorescence data presented in Chapters 4 and 5 were collected with a scanning spectrometer (ISS).

3.3.1 Fiber-Optic Spectrometer

Preliminary experiments on T4 lysozyme were performed with a fiber-optic spectrometer (USB2000, Ocean Optics) (Fig. 3.12). Emitted radiation was fed into the compact instrument via an optic fiber. An internal diffraction grating disperses the 200 - 850 nm range of the collected emission onto a 2048-pixel CCD detector, providing 0.3 nm/pixel resolution. The USB2000 was configured with a large slit size (200 μm $\times$ 600 μm) and the diffraction grating most effective in the far UV (Grating #1, Ocean Optics) in order to maximize collection of the relatively weak fluorescence signals. The CCD detector was also coupled with a collection lens to focus dispersed light onto the pixels. The pixels were calibrated with a high-pressure mercury lamp with known fluorescence lines. The intensity at each pixel was corrected with scale factor determined by a blackbody source with a known spectrum.

As tryptophan exhibits low quantum yields, a powerful UV source was necessary as the excitation source. A polymer curing lamp (UVEXS 110 Series Spot Curing System) was found to be suitable for this purpose. The UVEXS lamp is a medium-pressure mercury lamp optimized for UV-A (315-400 nm) output. The lamp spectrum is structured but continuously spans 280 - 740 nm; it is very broad compared with the lines usually

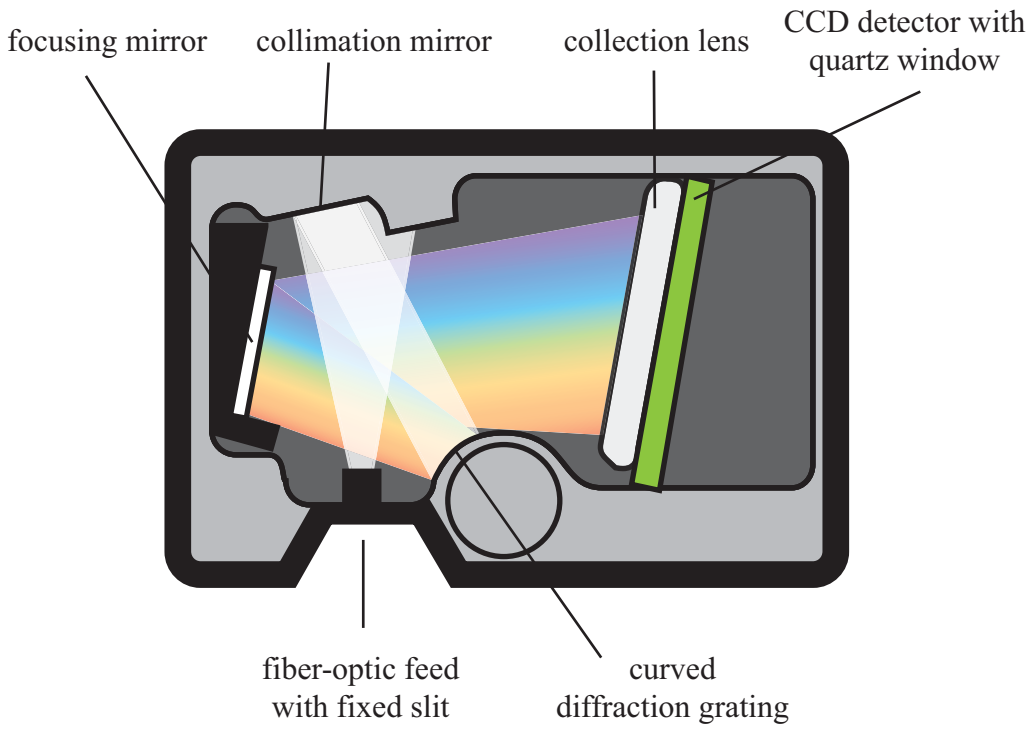

Figure 3.12: USB2000 fiber optic spectrometer (Ocean Optics). The emission radiation is fed into the instrument via the fiber-optic feed. After collimation, the light dispersed with a diffraction grating onto CCD detector, which records the intensity at 0.3 nm/pixel resolution. The device is connected to a PC via a USB cable.

seen in high-pressure mercury lamp spectra. The lamp light is focused with an internal mirror in the lamp housing into an 8 mm diameter fluid optic wand. Selective excitation of tryptophan was possible by coupling the wand output with two 289 nm bandpass filters (Andover). Each filter has a 12% transmission at 290 nm. The filtered light was fed directly into one of the windows of the high-pressure cell. Right angle emission was focused into a UV-grade 600 μm quartz optic fiber (Ocean Optics) with a lens (74-UV, Ocean Optics) and fed into the spectrometer.

The strengths of the USB2000 include speed, portability, and customizability. Although the CCD detector is not as sensitive as the photomultiplier tubes (PMT) used

in conventional spectrometers, as an entire spectrum is collected in a single electronic readout, data collection is much faster and sample exposure to radiation is minimized. A tryptophan fluorescence spectrum that takes 4 minutes to collect on a scanning spectrometer can be collected in 30 seconds on the USB2000. The USB2000 is also robust as there are no moving parts. A major disadvantage of the fiber-fed spectrometer system was the light source, which was not wavelength tunable. The power output of the UVEXS source was also variable over the course of a several hour experiment.

3.3.2 Scanning Spectrometer

All fluorescence data presented in Chapters 4 and 5 were collected on Chronos (ISS), a scanning spectrometer featuring a compact xenon arc lamp coupled to a monochromator and an monochromator-coupled emission photomultiplier tube (PMT) at right angles (Fig. 3.13). The PMT functions by converting light into current and amplifying it. The excitation and emission bandwidths are set by slits that are inserted in the beam path. A beam splitter reflects part of the excitation beam to the reference channel where the beam intensity is monitored by the reference channel. The reference sample, a saturated rhodamine B ethanol solution, converts light within 220-600 nm to fluorescence with a nearly constant quantum yield and emission maximum. The peak intensity of this reference sample is therefore directly proportional to the incident flux. This information is used to normalize the sample and buffer spectra. The shape of the emission spectrum is corrected by a blackbody calibration. As UV radiation can create ozone from oxygen in the air, the spectrometer is flushed with nitrogen and the lamp is ventilated.

Tryptophan fluorescence was performed by excitation at 295 nm with a bandwidth of 8 nm to minimize tyrosine excitation and collection of emission from 310 to 550

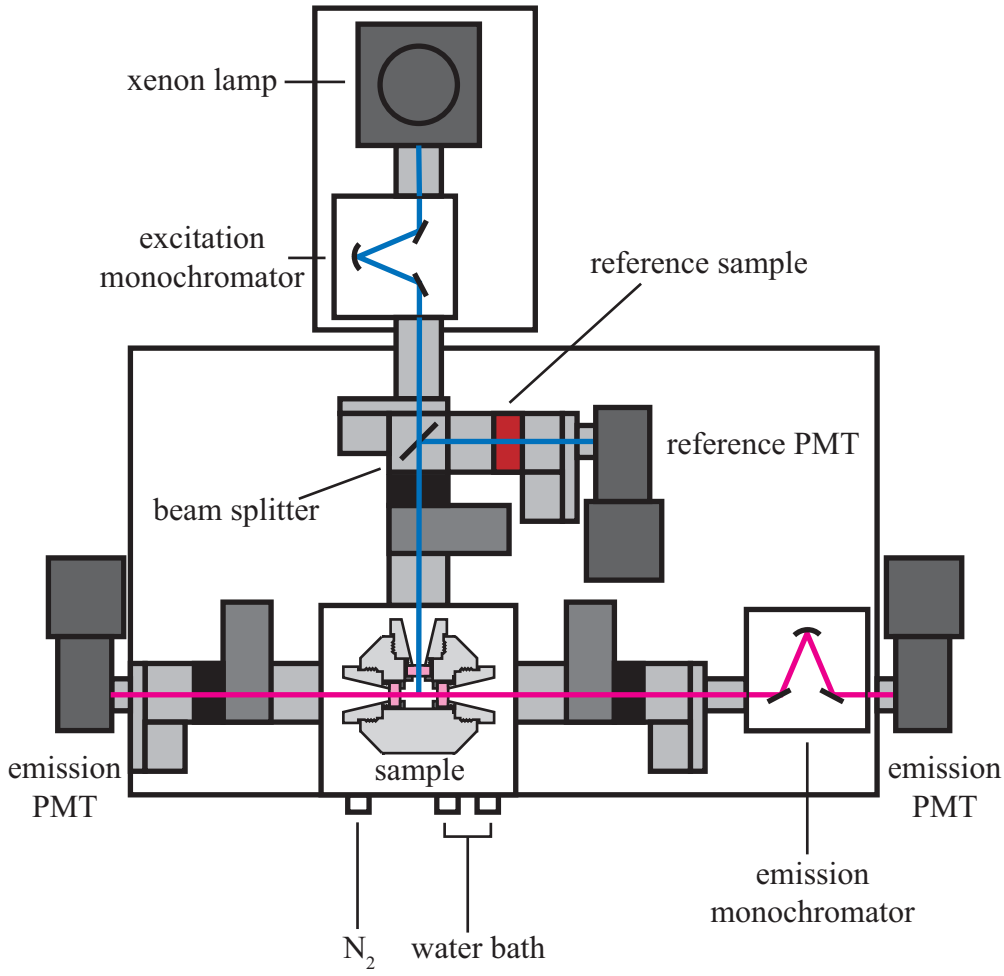

Figure 3.13: Chronos scanning fluorimeter (ISS). A monochromator-coupled xenon lamp was used as the excitation source. Emission was collected at 90° with a monochromator-coupled PMT. The reference PMT monitored the beam intensity via a reference sample. Water bath connections on the sample compartment enable thermal regulation. At low temperature, the gas connection can be used to flush the sample compartment with nitrogen in order to prevent condensation on the windows. Filters and polarizers can be fitted in this instrument but were not used for this thesis.

nm with a bandwidth of 4 nm. 2AP fluorescence was excited at 312 nm with a 4 nm bandwidth, and emission was collected from 320-500 nm. The lamp current was set to 18 A in both experiments. Temperature variation experiments at ambient pressure were performed in a standard 10 mm path length quartz cuvette (Two-Cuvette Sample Compartment; ISS, Champaign, IL, USA), while pressure variation experiments were performed in the high-pressure fluorescence cell (HP Cell; ISS, Champaign, IL, USA) with the custom internal cell. The temperature was controlled by a water bath (Neslab, Thermo Scientic, Waltham, MA, USA) via the water bath connections on the sample compartment (Fig. 3.13).

CHAPTER 4

STRUCTURAL AND THERMODYNAMIC CHARACTERIZATION OF T4 LYSOZYME MUTANTS AND THE CONTRIBUTION OF INTERNAL CAVITIES TO PRESSURE DENATURATION

4.1 Introduction

The characterization of non-native states stabilized under a variety of conditions is important towards understanding how proteins fold into their biologically functional, native structures [29]. It is widely believed that the dominant driving force in protein folding is the hydrophobic effect and that denaturation can be described as the transfer of hydrophobic residues to water. Although the hydrophobic compound transfer model [61, 62, 28, 94] largely succeeds in explaining the thermodynamic stability of proteins as a function of temperature, it does not explain denaturation with pressure [162]. In particular, this model fails to explain the magnitude and pressure dependence of the volume difference between the native and denatured states. Recent simulation studies and experimental work suggest that this failure is due to fundamental differences between the temperature- and pressure-denatured states of a protein [25, 44, 101, 60, 99, 26]. These studies suggest that unlike thermally and chemically denatured states, the pressure-denatured state is one in which water penetration into the protein is favorable, and that a significant contribution to the volume reduction with pressure is the hydration of internal cavities or packing defects.

The literature raises specific questions that require further study. Is pressure denaturation consistent with the water penetration model? How does the volume change upon denaturation correlate with cavity volume? Can other hydration mechanisms be distinguished from cavity filling? What constitutes a pressure-denatured state? We attempt

to answer these questions by characterizing the pressure-denatured states of several mutants of the protein T4 lysozyme with varying cavity sizes.[1]

4.1.1 T4 Lysozyme

T4 lysozyme is a small globular protein, 164 amino acid residues in length, with a molecular weight of 18.6 kDa (Fig. 4.1) [86].

In vivo, T4 lysozyme is expressed by the bacteriophage T4, a virus that infects the *E. coli* bacteria, to aid in the release of replicated phages. Lysozymes are a family of enzymes that catalyze cleavage of peptidoglycans that make up bacterial walls. T4 lysozyme should not be confused with hen egg white lysozyme, another well characterized protein, as they differ vastly in structure and sequence [88]. *In vitro*, T4 lysozyme has been studied extensively as a model protein for structure-stability studies. Owing to its high helical content and the three tryptophans in the C-terminal lobe (Fig. 4.1), T4 lysozyme is suitable for denaturation studies probed by circular dichroism and fluorescence spectroscopy [31]. T4 lysozyme and its mutants have also been shown to form large high quality protein crystals, typically diffracting to < 2.0 Å resolution. Over 300 X-ray structures of T4 lysozyme mutants have been deposited in the Protein Data Bank (PDB), and the thermal stabilities of many of these mutants have been measured [87].

Recently, the pressure-induced water filling of an enlarged hydrophobic cavity in the L99A mutant of the pseudo-wild-type T4 lysozyme (Fig. 4.2 (b), cavity 6) was observed by X-ray crystallography [25]. Molecular dynamics simulations suggested that

[1] The results of this chapter have been published in [4]. Reproduced in part with permission from Ando, N., Barstow, B., Baase, W. A., Fields, A., Matthews, B. W., and Gruner, S. M. (2008). *Biochemsitry*, **47**, 11097-1110. Copyright 2008 American Chemical Society.

four water molecules cooperatively fill this cavity as the applied hydrostatic pressure is increased [25]. No water molecules were observed in the corresponding cavity of the pseudo-wild-type, WT* (Fig. 4.2 (a), cavity 6) [25].

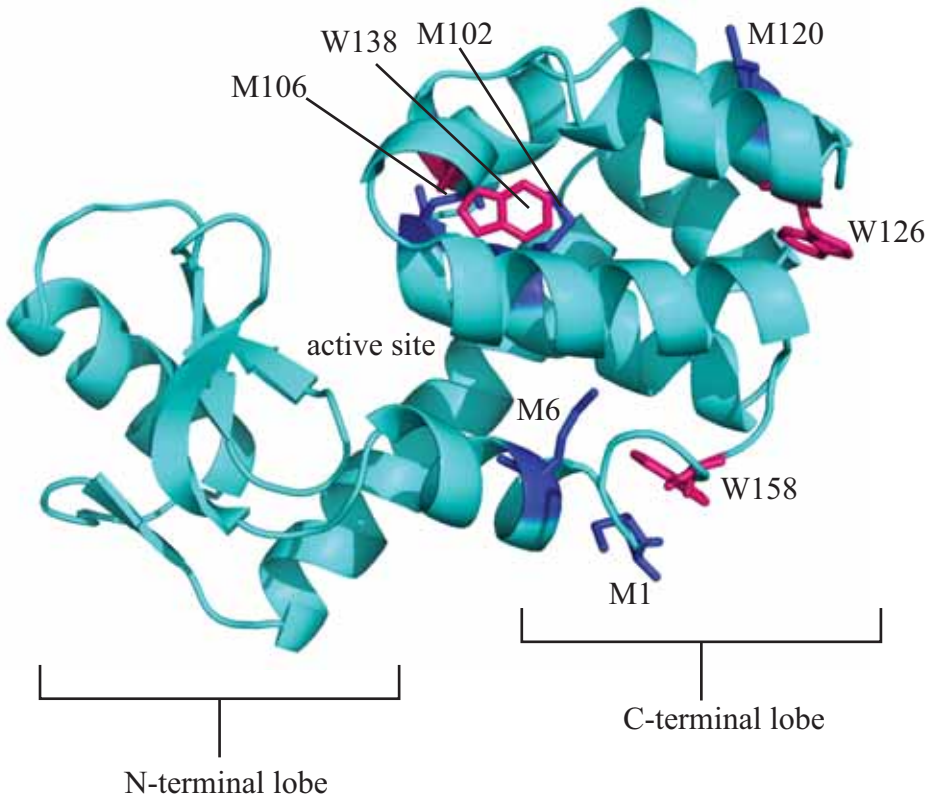

Figure 4.1: T4 lysozyme structure. The active site is in the cleft between the N-termal and C-terminal lobes. In the C-terminal lobe, there are three tryptophan residues (W126, W138, W158; shown in magenta) and five methione residues (M1, M6, M102, M106, and M120; shown in dark blue).

In this thesis, the solution behavior of L99A and three additional T4 lysozyme mutants (Fig. 4.2) were compared using high-pressure SAXS and tryptophan fluorescence spectroscopy. The three additional mutants were identified from approximately 300 T4 lysozyme mutants available as satisfying the criteria of having similar thermal stabilities as L99A, approximately 5 kcal/mol less than that of WT* [87, 37, 158, 159, 80], yet hav-

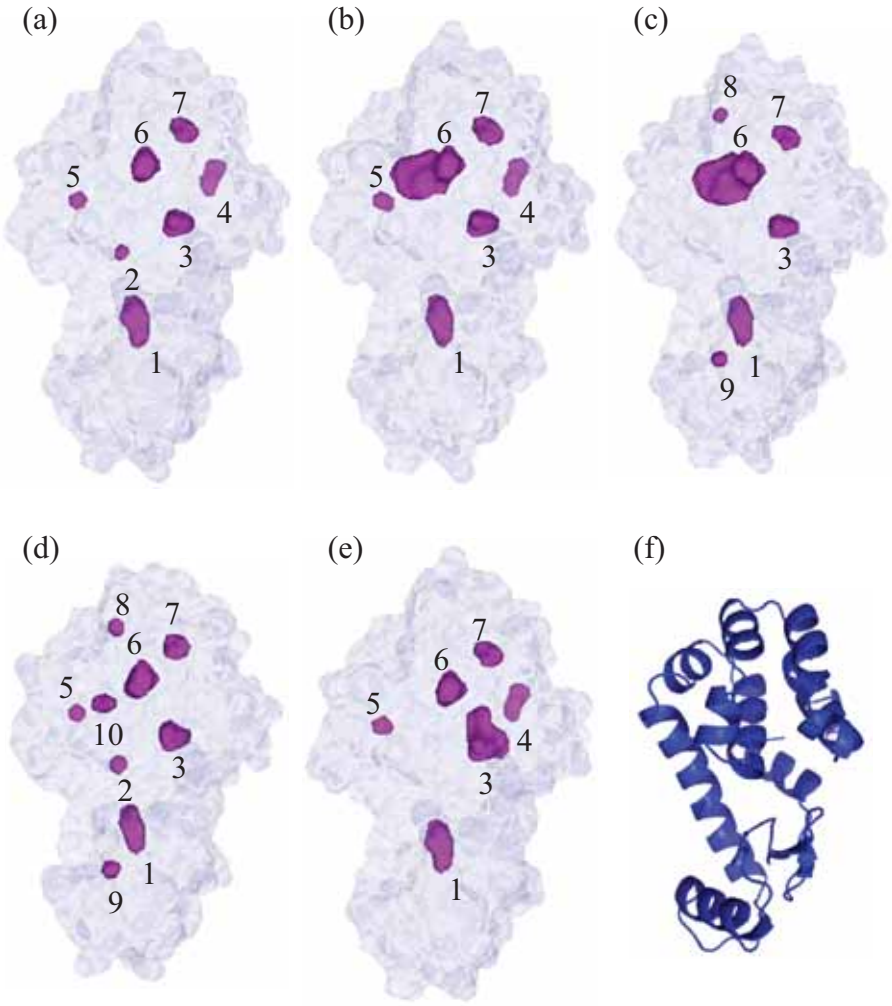

Figure 4.2: T4 lysozyme mutants shown from the same perspective. The external surface and buried cavities (shown in magenta) of (a) WT* (PDB code: 1L63), (b) L99A (1L90), (c) L99G/E108V (1QUH), (d) A98L (1QS5), and (e) V149G (1G0P) identified with a 1.2 Å probe in MSMS [119] with all internal solvent molecules removed (described in later sections). Cavities are identified by numbers 1 - 10 (refer to Table 4.1). (f) Cartoon representation of WT* T4 lysozyme. The C-terminal lobe is on the top side.

ing differing internal cavity volumes. These features were important for this study in order observe complete denaturation transitions of all the mutants under identical solvent conditions and to determine the effect of internal cavity volume on the volume change of pressure denaturation. Two of the investigated mutants, L99A and L99G/E108V, are structurally very similar to WT* except for differing volumes of the hydrophobic cavities at the mutation site where the 99th residue, leucine, L, has been replaced by alanine, A, or glycine, G [37, 158]. The V149G mutation enlarges an existing solvent-bound polar cavity at the mutation site [159]. A98L is destabilized relative to WT* by a strain-inducing small-to-large amino acid substitution [80]. As described in this chapter, small angle X-ray scattering (SAXS) was used to characterize the pressure-induced change in radius of gyration and overall shape of L99A T4 lysozyme. Thermodynamic analysis was performed on tryptophan fluorescence data taken at various solvent conditions on all mutants. A fluorescence quenching study of a seleno-methionine variant of L99A provided additional information on global structural changes due to high pressure. The thermal denaturation of T4 lysozyme has been extensively characterized at pH 3.0 [37, 158, 80, 10], and therefore this pH was chosen as a major test condition for this work. For direct comparison with high-pressure crystallography results of Collins, *et al.* [25], characterizations were also made at pH 7.0.

4.2 Mutant and Buffer Preparation

In this work, the cysteine-free pseudo-wild-type, C54T/C97A T4 Lysozyme [86] is referred to as WT*. All mutants used in this study contain the mutations C54T and C97A. The mutants were prepared by our collaborators, Prof. Brian Matthews and co-workers (Univ. of Oregon) using the following protocols.

The L99A, L99G/E108V, and A98L mutants were expressed and purified by a modified version of the protocol described by Poteete, *et al.* [106]. *E. coli* strain RR1 containing lysozyme-producing plasmids were streaked from frozen cultures onto modified LB-agar plates (modified Luria-Bertani broth: 12 g tryptone, 10 g NaCl, 1 g glucose and 5 g yeast extract per liter of broth) containing 100 μg/mL ampicillin. Single colonies were used to inoculate 100 mL cultures of LBH broth (10 g tryptone, 5 g NaCl, 1 ml of 1 N NaOH and 5 g yeast extract per liter of broth) containing 200 μg/mL ampicillin, and were incubated overnight at 32 °C. The 100 mL culture was diluted into four 1 L cultures of LBH broth in Fernbach flasks with aeration. Protein expression was induced by an IPTG concentration of 180 mg/L of culture when the culture optical density reached 0.6. After 90 minutes the cultures were centrifuged to pellet the cells. The bacterial pellets were resuspended in 100 mL of 50 mM tris/tris-HCl, pH 7.5, 10 mM Na_3HEDTA, 0.1% triton X-100 buffer with 1 protease inhibitor tablet (Complete Mini, EDTA-free Protease Inhibitor Cocktail Tablets, Roche Applied Science, Indianapolis, IN, USA). The viscosity due to the bacterial genomic DNA was reduced by DNase I treatment, sonication or the use of a French press. The products from the DNase I treatment were removed by dialysis (Spectra/Por 10 kDa MWCO, Spectrum Laboratories, Inc., Rancho Dominguez, CA, USA). The dialyzed solution was then loaded onto a 2.5 × 5 cm CM-sepharose column, pre-equilibrated with 50 mM Tris-HCl, 1 mM sodium EDTA, pH 7.25 and gradient eluted using a 0 to 0.3 M NaCl gradient in the same buffer. Proteins were dialyzed into 0.025 M $NaPO_4$, pH 5.8, then concentrated using SP sephadex and stepped off with 0.55 M NaCl, 0.1 M $NaPO_4$, 1 mM sodium EDTA, 0.01% sodium azide, pH 6.6, and stored in the same buffer [106].

The V149G mutant was isolated using a modified version of the inclusion body protocol described by Vetter, *et al.* [148]. Protein expression was induced at 37 °C. Following expression, the culture was pelleted by centrifugation at 4,700 × g. The

bacterial pellet was resuspended in a buffer composed of 50 mM Tris-HCl, 10 mM sodium EDTA, pH 8.0 plus 1 protease inhibitor tablet (Roche) and then sonicated. The resuspended mixture was then centrifuged for 30 minutes at 27,200 × g to pellet the cellular debris. The pellet was resuspended in 50 mM Tris-HCI, 10 mM sodium EDTA, 50 mM NaCl, 1 mM phenyl methane sulfonyl fluoride, 2.5 mM benzamide, 0.1 mM DTT, pH 8.0 [148]. One tenth of the volume of the resuspension buffer of 2% Triton X-100 in 50 mM Tris, 10 M sodium EDTA, pH 8.0 was added to the resuspended bacterial pellet solution [148]. The suspension was stirred overnight at 4 °C, and then centrifuged at 27,200 × g for 30 minutes. Ten volumes of 2.5% octyl-β-D-glucopyranoside in 50 mM Tris, 10 mM sodium EDTA, pH 8.0, per apparent volume of pellet were added and the suspension was stirred at 4 °C for 4 hours. Following centrifugation at 27,200 × g for 30 minutes, the pellet was washed with double-deionized water. The pellet was then suspended in freshly made 4 M urea (unbuffered, pH 6 to 7). The pH of the urea solution was lowered to 3 - 3.5 by the addition of 10 mM glycine, 2 N phosphoric acid, then mixed well for several minutes, and centrifuged at 12,000 × g for 15 minutes. The supernatant, containing the protein, was dialyzed against a 50 mM citrate, 10% glycerol, pH 3.0 buffer at 4 °C overnight, and then dialyzed against a 50 mM citric acid buffer, 10% glycerol, pH adjusted to 5.5 using NaOH at 4 °C for 8 - 16 hours. The solution was centrifuged at 12,000 × g for 25 minutes. The procedure yields at least 40 mg of protein, estimated to be approximately 99% pure.

A seleno-methionine containing variant of the L99A mutant (Se-Met L99A) was prepared in a methionine deficient, seleno-methionine rich growth medium using an adaptation of the procedure by Van Duyne, *et al.* [147]. Frozen stocks of E. coli strain RR1 [93] containing an L99A expressing plasmid were streaked onto modified LB-ampicillin agar plates and grown overnight. Single colonies were used to inoculate 200 mL modified LB cultures containing 200 μg/mL ampicillin. The 200 mL cultures

were grown for approximately 8 hours at 37 °C. Each 200 mL culture was used to inoculate a 1.25 L culture of M9a media (7 g $Na_2HPO_4 \cdot 7H_2O$, 3 g KH_2PO_4, 1 g NH_4Cl, 0.5 g NaCl mixed with one liter of water and autoclaved, followed by sterile addition of 10 mL 20% glucose, 0.4 mL 0.25 M $CaCl_2$, 1 mL 1 M $MgSO_4$, and 2 mL 0.5 mg/mL thiamine). Each 1.25 L culture was shaken at 250 rpm at 37 °C overnight. The next day, each 1.25 L culture was transferred to a 4 °C cold room for 30 minutes. Methionine biosynthesis was halted by adding 50 mL of M9a media containing an amino acid mixture of 100 mg lysine hydrochloride, 100 mg threonine, 100 mg phenylalanine, 50 mg leucine, 50 mg isoleucine and 50 mg valine to each 1.25 L culture. The 1.3 L cultures were shaken at 30 °C for approximately 30 minutes at 150 rpm. Next 50 mg/L of L-(+)-selenomethionine (Anatrace, Maunee, OH) was added and protein expression was induced by addition of 45 mg of IPTG per 1.3 L culture. Induction was allowed to proceed for 4 hours.

Following protein expression the cell cultures were pelleted at 5,000 $\times$ g for 10 minutes. The cell pellet was resuspended in 50 mM NaCl, 50 mM Tris pH 7.5 buffer with 15 mM methionine to prevent oxidation, and lysed by sonication for 7 minutes. The cellular debris was pelleted by centrifugation at 17,000 $\times$ g for 20 minutes. The supernatant was loaded onto a column containing a 2.5 cm bed of CM sepharose. This procedure yields approximately 70 mg of Se-Met L99A per 4 L of culture.

High concentration buffers with low volume changes of ionization were chosen to stabilize the pH as a function of pressure [95, 63]. At pH 3.0, 50 mM glycine buffer (Cat. 17-1323-01; GE Healthcare Bio-Sciences Corp., Piscataway, NJ, USA) and at pH 7.0, 50 mM Tris-HCl buffer (T-3253; Sigma, St. Louis, MO, USA) were used, unless otherwise noted. The NaCl (Cat. 7581; Mallinckrodt Baker, Phillipsburg, NJ, USA) concentrations used were 20 and 100 mM. Buffers were sterilized with 0.22 μm

cellulose acetate filters (Catalog Number 431175; Corning Inc, Corning NY, USA), stored at 4 °C, and used within two weeks of preparation.

4.3 Cavity Volume Calculation and Visualization

The volumes contained by the external protein surface and the volumes of internal cavities present in the crystallographically determined atomic structures of the T4 lysozyme mutants were calculated to determine if a correlation exists between the volume changes of denaturation extracted from thermodynamic analysis and the volume of buried cavities. Cavity calculations were performed on the atomic structures of L99A (Protein Data Bank accession code 1L90), L99G/E108V (1QUH), A98L (1QS5), V149G (1G0P), and WT* (1L63). An additional atomic structure of WT* was provided by Marcus Collins (private communication). Cavities were identified using the program MSMS [119] with a 1.2 Å probe. MSMS implements a rolling probe to determine reduced surfaces, from which the solvent excluded surface can be computed.

Two sets of molecular surfaces were produced for each structure. In the first set of calculations, all crystallographically determined solvent particles were manually removed from the PDB atomic coordinate files prior to analysis to eliminate false surface cavities caused by surface water, and to enable detection of hydrated internal cavities. The external surface and six to nine cavities were identified for each mutant (Fig. 4.2). In the second set, internal water molecules were retained in the atomic coordinate files to determine changes in cavity size due to hydration. The identified molecular surfaces were viewed using the program PyMol (Delano Scientific LLC, Palo Alto, CA, USA) with a script provided by Warren DeLano (private communication).

Four water molecules, WAT 171, 179, 175, and 208, are considered conserved in-

ternal solvent molecules in T4 lysozyme [160]. WAT 213 was also observed within the external surface of all mutants. WAT 175 was found either in a solvent-exposed pocket on the surface or within the external surface. As WAT 175 was considered to fully occupy its cavity, its exact location did not contribute to the total cavity volume. Both L99G/E108V and V149G structures contain two additional poorly ordered water molecules in their respective mutation-enlarged cavities. The L99G/E108V structure contains WAT 401 and 402 in the hydrophobic cavity near the L99G mutation (Fig. 4.2 (c), cavity 6). The V149G mutation enlarges the polar cavity binding WAT 208 (Fig. 4.2 (d), cavity 3) and introduces WAT 323 (alternative site 423) and 324. Molecular surfaces that intersected or were located outside the external surface were not considered internal cavities. For comparison, a second crystal structure of WT* (provided by Marcus Collins, private communication) was also analyzed. The variability of individual cavity volumes in the two WT* structures was within 5.4 $Å^3$ (3% of the total cavity volume of WT*). Table 4.1 summarizes the results.

Table 4.1: Cavity Volumes (Å^3) of T4 lysozyme Mutants.

#	WT* (1L63)	WT*[a]	L99A (1L90)	L99G/E108V (1QUH)	A98L (1QS5)	V149G (1G0P)	Comments
0	21044.0	21113.6	21103.3	20866.9	20919.7	21312.7	External Surface
1	50.3 (0)	44.9 (0)	51.9 (0)	47.5 (0)	46.8 (0)	49.2 (0)	WAT 171, 179
2	4.6	-	-	-	10.4	-	-
3	25.3 (0)	22.2 (0)	27.6 (0)	23.6 (0)	37.8 (0)	106.3 (0)[b]	WAT 208, Trp138
4	25.8 (0)	29.3 (4.2)	26.7 (0)	-	-	27.5 (0)	WAT 175
5	7.1	11.9	9.2	-	7.7	9.6	-
6	39.2	39.1	161.1	222.5 (87.2)[c]	53.7	40.7	-
7	24.6	23.9	28.9	24.3	24.3	25.0	Trp126
8	-	-	-	5.0 (0)	7.1 (0)	-	WAT 213
9	-	-	-	5.5	8.5	-	-
10	-	-	-	-	12.1	-	-

Volumes of molecular surfaces found with crystallographic solvent molecules removed from structures. In parentheses: volumes of solvent-containing cavities determined with crystallographic solvent molecules kept in structures. Surfaces found to intersect with the external surface of the protein are not shown. [a]Structure provided by Marcus Collins (private communication). [b]Contained WAT-323 (alternative site 423) and 324 according to the crystal structure. [c]Contained WAT-401 and 402.

4.4 High-Pressure Small Angle X-ray Scattering

Small-angle X-ray scattering (SAXS) is sensitive to electron density distributions with inhomogeneities on the length scales of 10 to 100 Å and thereby provides structural information for proteins in solution. SAXS was used to characterize the solution structure and the pressure-denatured state of T4 lysozyme at pH 3.0.

4.4.1 Methods

SAXS samples were prepared up to 48 hours in advance of experiments by dialyzing against buffers in micro-dialysis buttons (Cat. HR3-362; Hampton Research, Aliso Viejo, CA, USA) closed with a 10 kDa molecular weight cut-off dialysis membrane (Cat. 68100; Pierce Biotech, Rockford, IL, USA). Protein solution concentrations were adjusted to 4 to 25 g/L by UV absorption measurement (Nanodrop ND1000; Nanodrop Technologies, Wilmington, DE, USA) and centrifugal re-concentration when necessary (Microcon YM-10 centrifugal concentrator; Millipore, Billerica, MA, USA). The final dialysate solutions were used for sample dilutions and background scattering measurements. Samples were stored at 4 °C or on ice. Experiments were performed at room temperature.

X-ray experiments were performed at the G1 station at the Cornell High Energy Synchrotron Source (CHESS, Cornell University, Ithaca, NY, USA). Data were collected over several synchrotron runs with an X-ray flux of 10^{12} photons/s to within a factor of two. Scattering images were recorded on a home-built 1024×1024 pixel CCD detector, and the transmission intensity was measured with a home-made PIN diode beamstop.

Ambient-pressure measurements were made with the internal sample cells (ALine

Inc., Redondo Beach, CA, USA) with 7.5 μm Kapton film windows (Spectromembrane No. 3022; Chemplex Industries, Palm City, FL, USA) described in Chapter 2, used separately from the high-pressure cell. Multiple sample cells were mounted side-by-side in a card-shaped brass holder with 1.2 mm apertures. Each sample cell was reused for alternating buffer and protein measurements. A 10 keV 300 μm $\times$ 300 μm beam and a 1.25 m vacuum flight path were used.

High-pressure SAXS measurements were performed with the custom high-pressure SAXS cell, SAXS3, described in Chapter 2 with samples isolated in the internal sample cells. The protein solution and corresponding buffer were filled in separate internal sample cells up to a few hours in advance of each experiment and stored at 4 °C or kept on ice until measurement. As the sample cell path length varies slightly from piece to piece, the sample cells were individually measured with a caliper and matched to within 10 μm. After loading a sample cell, the high-pressure cell was fixed tightly in a copper water-bath controlled thermostating jacket on an X-Z translation stage with the windows normal to the beam. The sample was aligned by centering the aperture with an attenuated beam before measurement of a new sample and was periodically checked for drift in beam position. The cell position relative to the beam did not vary more than 30 μm between sample and buffer exposures. This was sufficient to reproduce the parasitic scattering from the cell. The sample was allowed to equilibrate for 10 to 60 minutes at each pressure. Buffer scattering was measured at each pressure. The high-pressure pump and the pressure network were positioned next to the beam line. A long flexible 1/8" cone-seal tube (High Pressure Equipment Co, Erie, PA) was used to connect the cell to the pressure pump via the fluid-separating reservoir described in Chapter 2. A 12 keV 250 μm $\times$ 250 μm beam and a 1.25 m vacuum flight path were used.

Data treatment and acquisition methods were described in detail in Chapter 2. Protein scattering profiles, $I(q)$, were produced by subtracting buffer scattering from that of the protein solution. The momentum transfer, q, is defined as Equation (2.3). The radius of gyration, R_g, and zero-angle scattering intensity, $I(0)$, were determined from Guinier analysis (Equation (2.11)) and pair-distance distribution analysis (Equation (2.13)). The pair-distance distribution function, $P(r)$, was calculated with program GNOM, which implements the indirect Fourier transform method [46, 73] using the experimental $I(q)$ as the input. Low-resolution models of protein structures were generated from the $I(q)$ fit produced by GNOM using the ab initio reconstruction program GASBOR [131]. The scattering profile of the denatured state was also analyzed with the Ensemble Optimization Method (EOM) package developed for modeling flexible proteins in solution [13].

4.4.2 Ambient Pressure SAXS Results

The performance of the sample cells and experimental conditions appropriate for SAXS studies of T4 lysozyme at pH 3.0 were first investigated at ambient pressure, separately from the high-pressure cell. SAXS profiles of the same buffer in two separate sample cells with matched path lengths were nearly identical in the q range investigated. Typical results are shown in Fig. 4.3 (a). The reproducibility of the parasitic scattering from the sample cells supports the use of separate cells for protein solution and its corresponding buffer. Because of the reproducible parasitic scattering from the sample cells, background subtraction was also straightforward and did not require scaling other than transmission-normalization. Fig. 4.3 (b) shows typical data taken from L99A T4 lysozyme (the protein solution scattering is the black curve, and the background scattering is the red curve). The parasitic scattering from the low q region subtracts well from the protein solution, yielding a Guinier plot (Fig. 4.3 inset) that is linear to very low

q. Buffer subtraction is also challenging at high q where the scattering intensities are very low. A common problem that is seen with SAXS is buffer subtraction that yields zero or negative scattering intensities at high q, but under the conditions used for our measurements, this was not a problem with these sample cells.

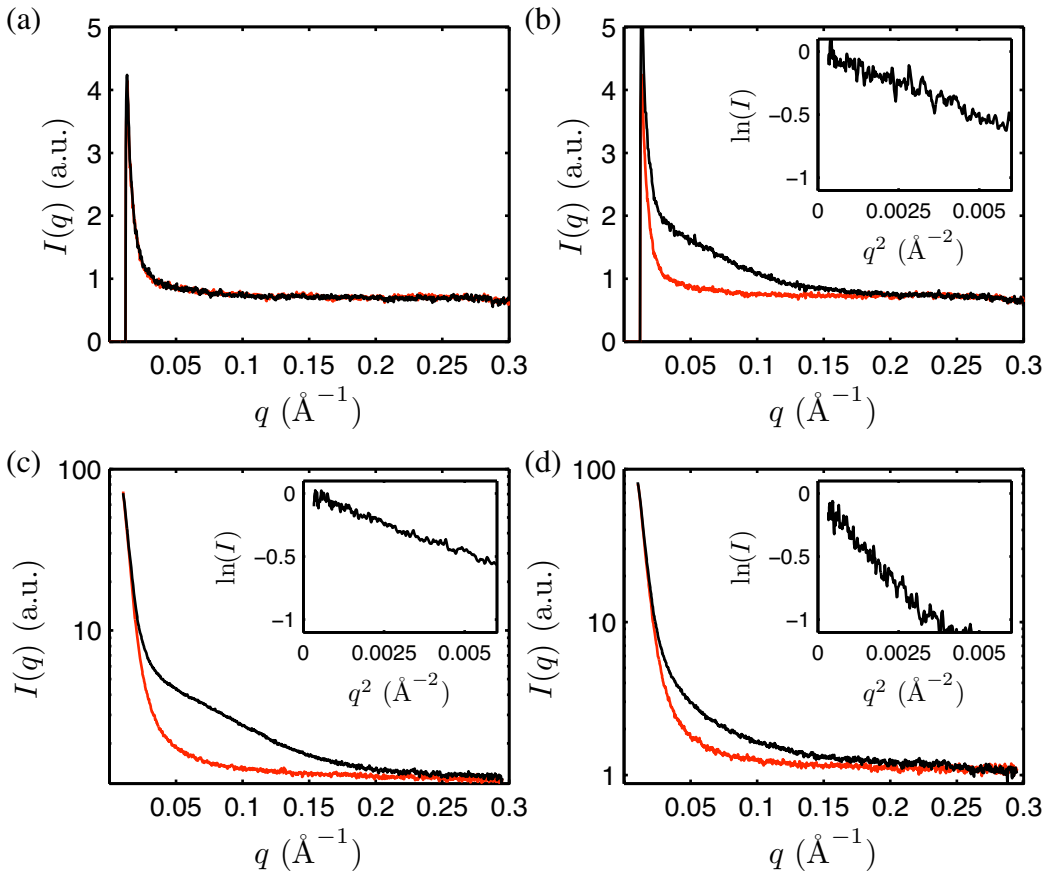

Figure 4.3: Buffer subtraction of transmission-normalized scattering profiles. (a) Buffer scattering at ambient pressure from two different acrylic sample cells (black and red) collected separately from SAXS3 is nearly indistinguishable. Scattering from L99A T4 lysozyme (black) and buffer (red) collected at (b) ambient pressure in acrylic sample cell separately from SAXS3, (c) 28 MPa in acrylic cell loaded in SAXS3, and (d) 300 MPa in acrylic cell loaded in SAXS3. Insets show Guinier plots of subtracted scattering intensity.

In order to extract structural information from SAXS profiles, interaction-free solvent conditions, $S(q) \approx 1$ (Equation (2.12)), are desirable. The low q region of protein scattering profiles is particularly sensitive to inter-particle interactions, such as charge repulsion, volume exclusion, and aggregation and therefore depends on solvent conditions including protein concentration, pH, salt concentration, and radiation damage.

As the isoelectric point of T4 lysozyme is near pH 10 [10], at pH 3.0 where the SAXS measurements were made, T4 lysozyme is highly positively charged. Inter-particle charge repulsion results in a dip at low q corresponding to a zero-angle structure factor, $S(0) < 1$. This can be observed in the scattering profile of 10 mg/mL WT* T4 lysozyme at pH 3.0 in the absence of NaCl (Fig. 4.4, red curve). Accordingly, the Guinier region Fig. 4.4 inset) is not linear, and the R_g cannot be extracted unambiguously. The effect of inter-particle charge repulsion was alleviated by the introduction of counter ions (Fig. 4.4, blue curve). The appropriate NaCl concentration was dependent on the protein concentration. To fine tune the appropriate NaCl concentration, protein solutions without NaCl were mixed with those at 150 mM NaCl in various proportions. The scattering profile of 4 mg/mL L99A T4 lysozyme, 50 mM glycine 50 mM NaCl pH 3.0 (Fig. 4.3 (b)) was measured under conditions that minimize inter-particle charge repulsion. A Guinier fit (Equation (2.11)), of this data over $q = 0.024 - 0.076 \text{Å}^{-1}$ gave a radius of gyration, R_g, of 16.5 ± 0.3 Å, in agreement with that calculated from the crystal structure of a folded T4 lysozyme monomer, 16.4 Å.

As with other X-ray techniques, radiation damage is ultimately the limiting factor in solution SAXS studies of biological materials. The extent of radiation damage depends upon the sample and the experimental conditions, including solvent conditions and X-ray energy. Radiation damage usually results in the aggregation of protein. The aggregates, being larger in size than the undamaged proteins, scatter at lower q. If they

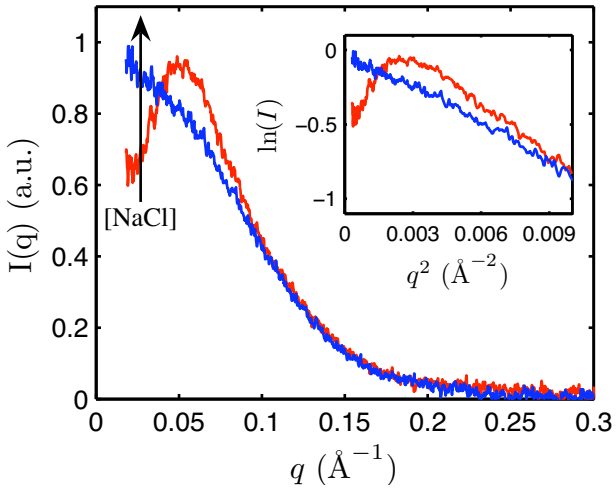

Figure 4.4: Effect of NaCl on the scattering profiles of T4 lysozyme at pH 3. Shown are ambient pressure profiles of 10 mg/mL WT* in pH 3.0 50 mM glycine buffers without NaCl (red) and with 100 mM NaCl (blue). Charge repulsion is strong without NaCl, resulting in a low q dip. Guinier analysis is not possible due to nonlinearity (red curve, inset). Addition of NaCl minimizes this effect and results in a more linear Guinier region (blue curve, inset).

are detectable, i.e. not blocked by the beamstop, the presence of aggregates is reflected by an upturn at low q in the Guinier plot.

In the case of T4 lysozyme at pH 3.0, susceptibility to the radiation damage-induced aggregation was dependent upon the concentration of counter ions (Fig. 4.5). Samples with less NaCl in the buffer tolerated greater exposure times before radiation damage was detectable. This is expected as T4 lysozyme is highly charged at this pH. We have also observed that multiple short exposures can be less damaging than one long exposure and that pauses between exposures can in some cases recover the undamaged scattering profile. We believe that these are related to the diffusion rate of the aggregates. Radiation damage can be suppressed to a certain extent by the choice of X-ray energy. By tuning beam transmission through the samples, we can optimize the balance between radiation damage and the scattering signal from the proteins. The total exposure times before

radiation damage irreversibly distorted the scattering profiles of T4 lysozyme were on order of 10 to 100 seconds with 10^{12} photons/s 10 - 12 keV X-rays.

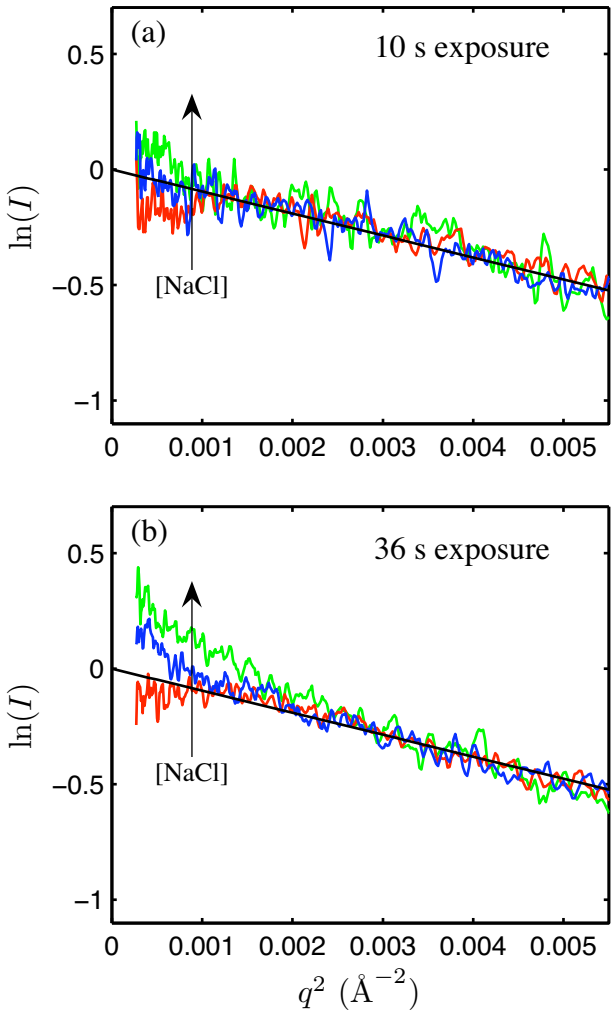

Figure 4.5: Radiation damage of 4 mg/mL L99A in pH 3.0 50 mM glycine at 1 atm after a total X-ray exposure of (a) 10 s and (b) 36 s at 10 keV, 10^{12} photon/s. After 10 s, aggregation is not detected in L99A at 50 mM NaCl (blue). The Guinier fit (black line) yields a R_g of 16.9 Å, in good agreement with that of the crystal structure. L99A at 100 mM NaCl (green) shows a slight indication of aggregation. After 36 s, L99A at 50 (blue) and 100 mM (green) NaCl show radiation damage, indicated by a higher slope at very low q. L99A without NaCl (red) exhibits charge repulsion but no aggregation at these exposures.

4.4.3 High-Pressure SAXS Results

High-pressure SAXS samples were prepared at the interaction-free solvent conditions identified at ambient pressure. The performance of the high-pressure SAXS cell was demonstrated by buffer subtraction of data taken on L99A T4 lysozyme (Fig. 4.3). Reproducible alignment of the high-pressure cell with respect to the X-ray beam between protein solution and buffer scattering measurements enabled subtraction of the strong parasitic scattering from the diamond windows to a minimum q value of around 0.024 Å^{-1} at all pressures. The buffer-subtracted scattering profiles and corresponding Guinier plots of WT* and L99A T4 lysozyme taken at 28 to 300 MPa are shown in Fig. 4.6. In this pressure range, the size and shape of the WT* do not change, reflected by the unchanging shape of $I(q)$ and slope of the Guinier plots (Fig. 4.6 (a)). By contrast, scattering of L99A moved to lower q with pressure and the slope of the Guinier plots increased, corresponding to a change in shape and increase in size (Fig. 4.6 (b)).

Guinier analysis (Equation (2.11)) was performed on the low q region of the SAXS profiles. At 28 MPa, L99A T4 lysozyme was still mostly folded (Fig. 4.3 (c) and Fig. 4.6 (a), red curve). The radius of gyration obtained by a Guinier fit over $q = 0.024 - 0.076\text{Å}^{-1}$ was 17.1 ± 0.1 Å, approximately that measured at ambient pressure. As the applied pressure was increased, the radius of gyration increased to 31.6 ± 1.7Å (determined over $q = 0.024 - 0.038\text{Å}^{-1}$) at 300 MPa (Fig. 4.3 (d) and Fig. 4.6 (a), violet curve). The results of Guinier fits to the data are shown in Fig. 4.7. As the radius of gyration as determined by Guinier analysis is only accurate for homogeneous samples, we do not place strong meaning on the specific value of R_g at intermediate pressures where L99A was a mixture of folded and denatured forms.

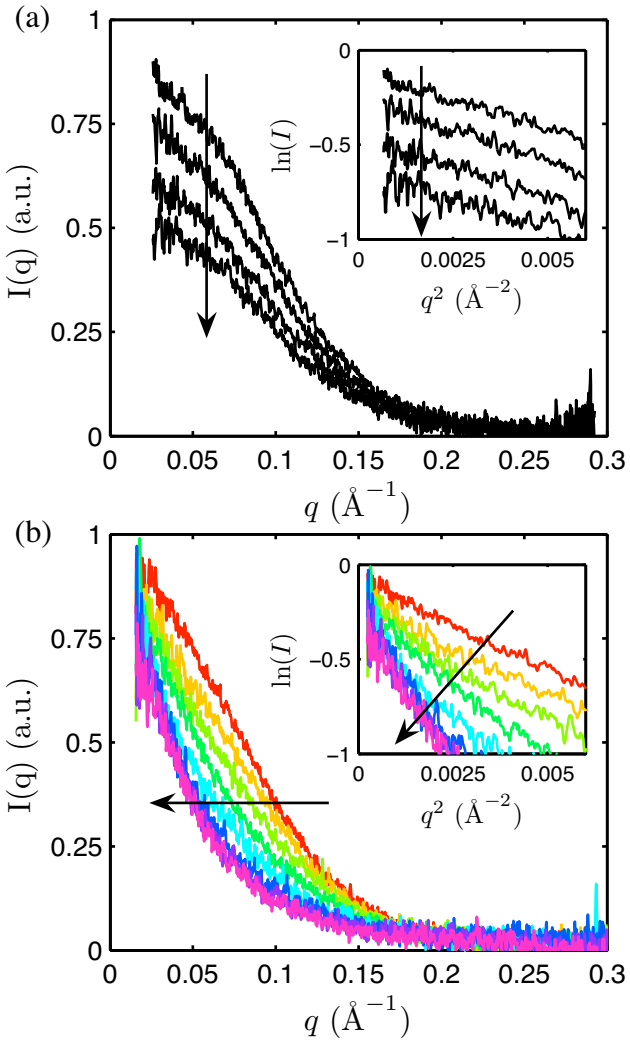

Figure 4.6: Buffer-subtracted scattering profiles of WT* and L99A T4 lysozyme at pressures ranging from 28 to 300 MPa (arrows indicates increase in pressure), pH 3.0. (a) 16 mg/mL WT* in pH 3.0 50 mM glycine 150 mM NaCl. R_g does not depend on pressure as indicated by the unchanging slope of the Guinier plot (inset). (b) 10 mg/mL L99A in pH 3.0 50 mM glycine 100 mM NaCl. Due to the exposure limit set by radiation damage, the data presented here were taken on two aliquots of the same sample. The Guinier plot shows an increase in slope with pressure, indicating an increase in R_g (inset).

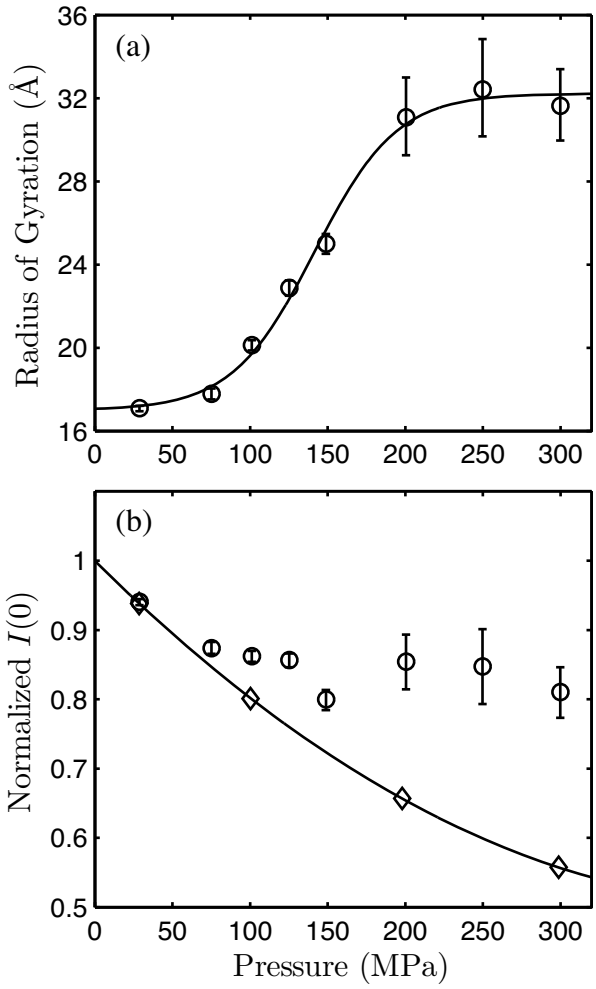

Figure 4.7: Results of Guinier analysis of profiles presented in Fig. 4.6. (a) Radius of gyration, R_g, as a function of pressure for 10 mg/mL L99A in pH 3.0 50 mM glycine 100 mM NaCl at room temperature. R_g was determined by a Guinier fit to the $qR_g < 1.3$ region of scattering profiles taken at each pressure. The error bars are larger at high pressure because only one exposure was taken at each pressure. At lower pressure, the sample was less susceptible to radiation damage-induced aggregation and multiple exposures were taken at each pressure, which enabled averaging of images. A two-state thermodynamic fit is shown (solid line) to guide the eye. (b) The zero-angle scattering intensity of L99A (circle) and the WT* (diamond), measured at 16 mg/mL in 50 mM glycine 150 mM NaCl, at pH 3.0. WT* does not denature below 300 MPa.

At high pressure, several factors conspire to make accurate measurements of the radius of gyration more difficult. As a protein unfolds, it expands, and the scattering profile shifts to lower q where the parasitic scattering is worse, making background subtraction more challenging (Fig. 4.3 (d)). In cases such as these, it becomes even more critical that the background scattering remain reproducible. Guinier analysis was relatively straightforward for L99A T4 lysozyme at high pressure because of the relative compactness of the unfolded state at pH 3.0. The R_g of the pressure-denatured state was quite small in comparison to 40.7 Å, the predicted radius of gyration of a fully unfolded polypeptide of the same length [71, 72].

A second reason for the increased difficulty of background subtraction at high pressure is specific to high pressure, and is caused by the decreasing protein-solvent electron density contrast. As the compressibility of water is roughly one order of magnitude greater than that of protein molecules [52], the electron density contrast decreases with increasing pressure. This can be demonstrated with WT* T4 lysozyme, which did not unfold below 400 MPa at pH 3.0. Although the radius of gyration of WT* T4 lysozyme did not change appreciably, as can be seen by the unchanging slope of the Guinier plots (Fig. 4.6 inset), the scattering intensity at zero q decreased with pressure (Fig. 4.7 (b)). The zero-angle scattering intensity, $I(0)$, is a function of the electron density contrast between the hydrated protein and solvent, the excluded volume of the protein, molecular weight, and inter-protein interactions (Equation (2.12)). Confidence in the background subtraction was obtained by thoroughly checking the reproducibility of the parasitic scattering and repeating the protein SAXS measurements.

Relative to WT*, L99A shows an increase in $I(0)$ centered about the pressure midpoint of denaturation (Fig. 4.7 (b)). A similar trend was observed with the pressure denaturation of SNase studied by small-angle neutron scattering [99]. As L99A is highly

charged at pH 3.0 and sensitive to the ionic strength, we attribute the increase in $I(0)$ to changes in hydration or protein interactions that accompany denaturation [7, 23, 134]. Although $I(0)$ is also a function of the protein volume, the volume changes due to denaturation are on the order of 1% of the volume of the protein and therefore do not significantly affect $I(0)$.

Shape information can be inferred from the one-dimensional pair-distance distributions (Eqn. (2.13)) and Kratky plots, $I(q)q^2$ vs. q. Pair-distance distribution functions of L99A T4 lysozyme were computed using GNOM [73] from data taken at 28 and 300 MPa with a maximum particle size, D_{max}, of 54 and 134 Å, respectively (Fig. 4.8 (a)). Radii of gyration determined from the pair distance distribution functions were 17.0 and 34.5 Å, in good agreement to the Guinier fits. The shape of the pair-distance distribution function at low pressure is nearly symmetrical and bell-shaped indicating that T4 lysozyme is globular. At 300 MPa, the $P(r)$ is asymmetric and lean towards lower r, suggesting that the protein is elongated. The maximum at small r corresponds to a cross-sectional radius of an elongated particle [132]. The small shoulders at high r suggest residual structure. Kratky plots of L99A T4 lysozyme are shown in the inset of Fig. 4.8 (b). Krakty plots emphasize the $I(q)$ decay in the intermediate q region, which is sensitive to the shape of the protein [105]. The 28 MPa profile shows a peak around 0.1 $Å^{-1}$, indicating that L99A is compact and globular at this pressure. Increasing the pressure 300 MPa greatly reduces the peak, indicating that L99A is extended. No additional peak forms at lower q, indicating that L99A is largely monomeric at high pressure.

For further structural characterization, low-resolution three-dimensional models of L99A were produced using the *ab initio* reconstruction program GASBOR [131] and the denatured ensemble was modeled with the Ensemble Optimization Method (EOM)

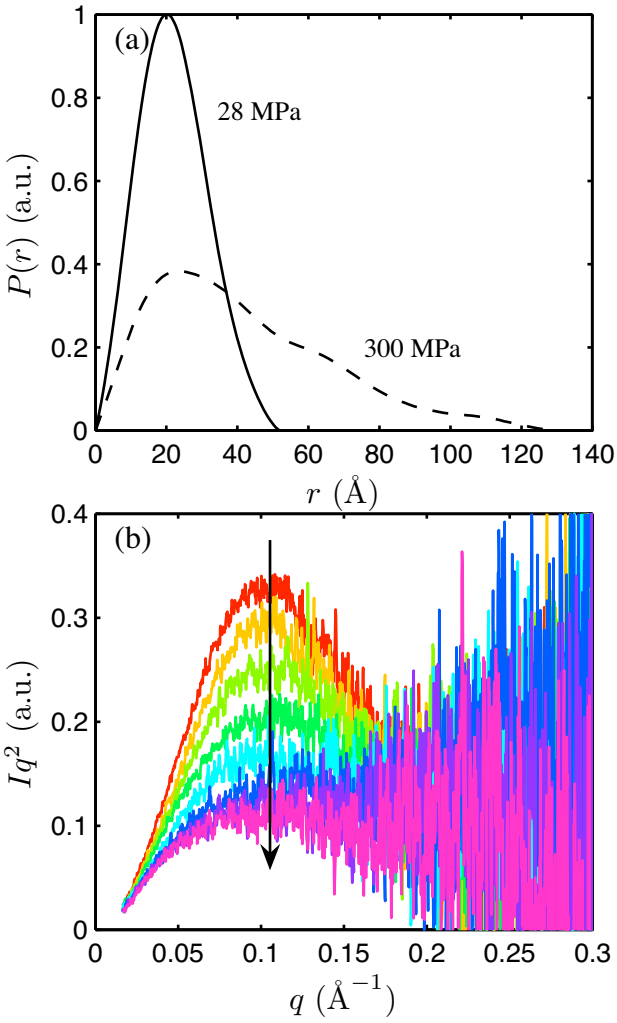

Figure 4.8: The shape of L99A T4 lysozyme in pH 3.0 50 mM 100 mM NaCl. (a) Pair distance distribution functions of native (28 MPa, solid line) and denatured (300 MPa, dotted line) L99A obtained with GNOM [73]. The change in shape and peak location of $P(r)$ suggests that L99A is globular at low pressure and extended with residual structure at high pressure. (b) Kratky representation of L99A scattering from 28 MPa - 300 MPa (arrow indicates increase in pressure). The reduction in the peak indicates a loss in compactness with pressure.

package [13]. Five GASBOR reconstructions were performed on the small X-ray scattering data taken at 28 and 300 MPa on the assumption that L99A is a monomer at both pressures. The results of this reconstruction are shown in Fig. 4.9. The low-pressure reconstructions resembled the crystal structure of L99A in exterior shape and size. The high-pressure reconstructions do not represent actual structures found in solution, as the denatured state is an ensemble without a unique conformation, but rather, they are models that closely match the experimental scattering profile. While the low-pressure structures are compact, the high-pressure reconstructions are noticeably more extended.

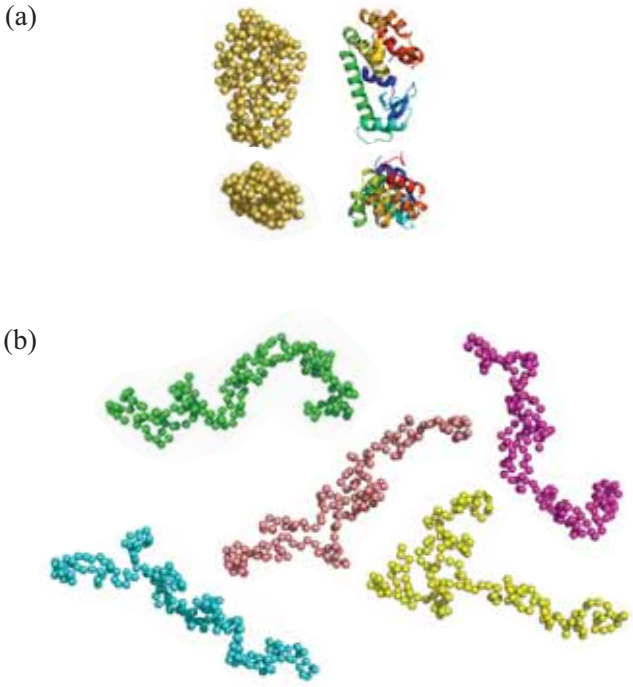

Figure 4.9: Low-resolution three-dimensional models of L99A T4 lysozyme at pH 3.0 50 mM glycine 100 mM NaCl. (a) Side and top views of the crystal structure of L99A (right) and a representative low-resolution structure at 28 MPa obtained with GASBOR [131] (left) show good agreement. (b) GASBOR models that fit well to 300 MPa data were extended.

The small angle X-ray scattering profile taken at 300 MPa was also examined with EOM. EOM generates a large pool of randomly generated conformations available for a polypeptide of a certain sequence [12] from which an optimization algorithm is used to select the subset that best fits the experimental scattering profile. Two starting pools were generated. The first contained 10,000 random coil conformations with an average R_g of 38.0 Å, and the second contained 10,000 unfolded conformations with residual structure with an average R_g of 29.7 Å. The ensemble selected from the pool with residual structure had an average R_g of 31.2 Å, in agreement with Guinier analysis, and better described our experimental data than the selected random coil ensemble, which had an average R_g of 36.1 Å (Fig. 4.10).

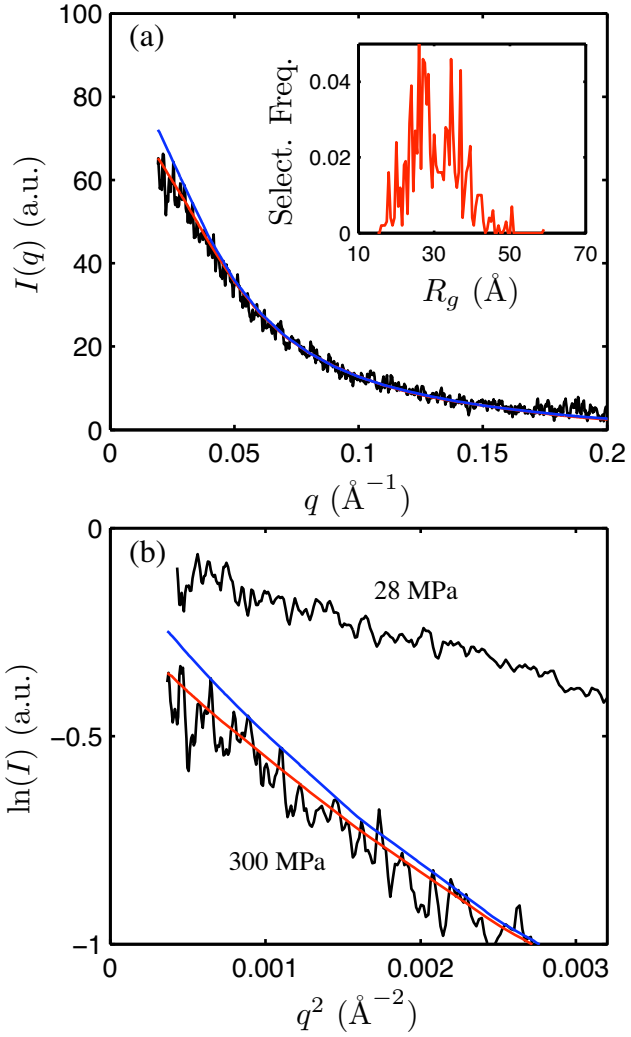

Figure 4.10: Ensemble model of the pressure-denatured state of L99A T4 lysozyme at pH 3.0. (a) The scattering profile of 10 mg/mL L99A in pH 3.0 50 mM glycine 100 mM NaCl at 300 MPa (black) was examined with EOM [13]. An ensemble of unfolded conformers with residual structure (red scattering profile) better described the experimental data compared to an ensemble of random coil conformers (blue scattering profile). Inset: the distribution of R_g in the selected subset of the first ensemble. (b) Guinier plots of the experimental data (black) and the EOM results.

4.5 High-Pressure Fluorescence Spectroscopy

The fluorescence of tryptophan is sensitive to the polarity of its local environment and can be used to monitor protein conformation changes. Both the solvent and protein contribute to environmental polarity, such that protein denaturation is generally accompanied by a red-shift in tryptophan fluorescence [150]. Tryptophan fluorescence measurements were made on the T4 lysozyme mutants at pH 3.0 and 7.0.

4.5.1 Methods

Samples for tryptophan fluorescence spectroscopy were prepared up to 48 hours in advance of experiments by dialyzing 100 - 200 μL protein solutions in micro-dialysis floats (Cat. PI-69560; Thermo Scientific Pierce Slide-A-Lyzer, Thermo Fisher Scientific, Waltham, MA, USA). The dialyzed protein solutions were further diluted to a final volume of 2.4 - 2.5 mL, resulting in protein concentrations of < 3 μM.

High-pressure fluorescence measurements were performed with the commercial cell and custom internal cuvette described in Chapter 3. The pressurizing medium in the high-pressure cell, isopropanol, was separated from the pressurizing medium (Fluorinert FC-77; 3M, St. Paul, MN, USA) in the high-pressure pump (Cat. No. 37-6.75-60; High Pressure Equipment Co., Erie, PA, USA) by a piston in a home-built stainless steel high-pressure reservoir. Data were collected with a scanning spectrometer (Chronos, ISS, Champaign, IL) using Vinci software (ISS, Champaign, IL, USA) for instrument control and data acquisition. Samples were excited at 295 nm with a bandwidth of 8 nm to minimize tyrosine excitation, and emission from 310 to 550 nm was collected at 90° with a bandwidth of 4 nm. Protein solutions were equilibrated at each pressure for 20 to

90 minutes. Buffer reference spectra were pressure independent and featureless, with the exception of a small pressure independent water Raman peak around 330 nm (Fig. 3.11). For this reason only one representative reference spectrum was taken at 50 MPa for each protein sample. Sample temperature was maintained with a water circulation pump (Neslab, Thermo Scientific, Waltham, MA, USA).

Data were analyzed with MATLAB (The MathWorks, Natick, MA, USA). The collected emission spectra were background-subtracted. Intensity corrections were performed with calibration data collected by ISS (Champaign, IL, USA) with 4 nm excitation and emission bandwidths. To monitor the red-shift of tryptophan, the center of spectral mass, $< \lambda >$, of each spectrum was calculated in the region 310 to 550 nm with the following equation [126].

$$< \nu >= \sum_{i=1}^{N} \nu_i I_i \, / \, \sum_{i=1}^{N} I_i \tag{4.1}$$

where I_i is the fluorescence intensity at the wavenumber, ν_i, and N is the number of data points collected in the spectrum. The weighted average $< \nu >$ was then converted to wavelength, $< \lambda >$.

4.5.2 Thermodynamic Model

For two-state denaturation, the thermodynamic stability of the protein is ΔG, the free energy difference between the native (N) and denatured (D) states (Equation(1.1)). Assuming that the protein solution is an ideal solution, ΔG at a given pressure can be expressed as a function of the observable quantity, the center of spectral mass, $< \lambda >$ (refer to Equation (1.2)).

$$\Delta G(T,P) = -RT \ln K_{eq}(T,P) = -RT \ln \frac{< \lambda > - < \lambda >_N}{< \lambda >_D - < \lambda >}, \tag{4.2}$$

where K_{eq} is the equilibrium constant, R is the gas constant (83.1447 mL-bar/mol-K), T is the experimental temperature, and $< \lambda >_N$ and $< \lambda >_D$ are the spectral centers of mass of the native and denatured states. $< \lambda >_N$ and $< \lambda >_D$ were inferred by fitting experimental data.

The dominant contribution to the pressure-induced change in protein stability is the volume change [115, 122]. Thus, using a first-order expansion of ΔG with pressure (Equation (1.24)), we arrive at the following model to model the pressure denaturation of T4 lysozyme:

$$< \lambda >= \frac{< \lambda >_N + < \lambda >_D \exp\{-[\Delta G^\circ + \Delta V^\circ (P - P_0)]\}}{1 + \exp\{-[\Delta G^\circ + \Delta V^\circ (P - P_0)]\}}, \tag{4.3}$$

where $< \lambda >_N$, $< \lambda >_D$, ΔG°, and $\Delta V^\circ$are free parameters, and P_0 is the standard pressure, 1 atm, and T is the experimental temperature.

4.5.3 Singular Value Decomposition

Singular value decomposition (SVD) can be used to support the use of a two-state thermodynamic model by determining the number of significant independent basis vectors whose linear combinations represent the data. SVD can be considered a method to extract eigenvectors and eigenvalues from general matrices.

Recall that the eigenvectors of a matrix $\tilde{A}$ (tildes denote matrices), $\vec{x}$, are vectors that do not rotate when multiplied by A.

$$\tilde{A}\vec{x} = \lambda\vec{x}, \tag{4.4}$$

where λ is the eigenvalue, a scalar. Equivalently, if $\tilde{S}$ is an orthogonal matrix of eigenvectors of $\tilde{A}$,

$$\tilde{A}\tilde{S} = \tilde{S}\,\tilde{\Lambda}, \tag{4.5}$$

where $\tilde{\Lambda}$ is a diagonal matrix of the eigenvalues.

Suppose we have a general $m \times n$ matrix, $\tilde{A}$, that cannot be diagonalized by a single orthogonal matrix, $\tilde{S}$. Instead, we look for an orthogonal matrix, $\tilde{V}$ that when rotated by $\tilde{A}$ produces an orthogonal matrix, $\tilde{U}$. Then,

$$\tilde{A}\tilde{V} = \tilde{U}\tilde{\Sigma}, \tag{4.6}$$

where $\tilde{\Sigma}$ is a diagonal matrix of singular values. The columns of $\tilde{U}$ are the singular vectors. Note that when $\tilde{V} = \tilde{U}$, they are equivalent to the eigenvector matrix, $\tilde{S}$, and $\tilde{\Sigma}$ becomes the eigenvalue matrix, $\tilde{\Lambda}$. To find $\tilde{V}$ and $\tilde{U}$, we apply the orthogonality relations, $\tilde{V}^T = \tilde{V}^{-1}$ and $\tilde{U}^T = \tilde{U}^{-1}$. Then,

$$\tilde{A}^T\tilde{A} = \tilde{V}\tilde{\Sigma}^T\tilde{U}^T\tilde{U}\tilde{\Sigma}\tilde{V}^T = \tilde{V}\tilde{\Sigma}^T\tilde{\Sigma}V^T \tag{4.7}$$

$$\tilde{A}\tilde{A}^T = \tilde{U}\tilde{\Sigma}\tilde{V}^T\tilde{V}\tilde{\Sigma}^T\tilde{U}^T = \tilde{U}\tilde{\Sigma}\tilde{\Sigma}^T\tilde{U} \tag{4.8}$$

In other words,

$$(\widetilde{A^TA})\tilde{V} = \tilde{V}(\widetilde{\Sigma^T\Sigma}) \tag{4.9}$$

$$(\widetilde{AA^T})\tilde{U} = \tilde{U}(\widetilde{\Sigma\Sigma^T}). \tag{4.10}$$

The columns of $\tilde{V}$ are the eigenvectors of the matrix $\widetilde{A^TA}$ and those of $\tilde{U}$ are the eigenvectors of $\widetilde{AA^T}$. The diagonals of the matrix, $\widetilde{\Sigma^T\Sigma} = \widetilde{\Sigma\Sigma}^T$, (the squares of the singular values) are the eigenvalues. For further information, refer to [130].

We are concerned with matrices, $\tilde{A}$, where the rank, r, i.e. the number of singular vectors that span the column space of $\tilde{A}$, is less than n, the number of columns of $\tilde{A}$. Suppose $\tilde{A}$ is a matrix of data, where the columns are the intensities of fluorescence spectra collected at the same wavelength values at n pressures, $P_1, P_2, .., P_n$.

$$\tilde{A} = [I(P_1)I(P_2)...I(P_n)]\,. \tag{4.11}$$

The goal of SVD analysis is to determine r and the r singular vectors (referred to as SVD states from here on) and corresponding linear combination coefficients that describe our data, $\tilde{A}$.

From Equation (4.6), we know that $\tilde{A}$ can be deconstructed as follow.

$$\tilde{A} = \tilde{U}\tilde{\Sigma}\tilde{V}^T. \tag{4.12}$$

The first r columns of $\tilde{U}$ are the orthogonal SVD states that span $\tilde{A}$. The first r rows of the matrix product, $\tilde{W} = \tilde{\Sigma}\tilde{V}^T$, are the linear combination coefficients for the SVD states. In other words, for real data, we are interested in determining the value of r where the product of the first r rows of $\tilde{U}$ and the first r rows of $\tilde{W}$ is approximately $\tilde{A}$ and the difference is within experimental noise [99].

4.5.4 Thermodynamic Analysis of Fluorescence Measurements

Fluorescence measurements were made on L99G, L99G/E108V, A98L, V149G, and WT* at pH 3.0. In the range of 16 - 25 °C, the experimental temperature had the effect of shifting the pressure midpoint of denaturation without changing the volume change of denaturation (Fig. 4.11). The temperature was therefore set to 16 °C, where the denatured fractions of the least stable mutants, L99G/E108V and V149G were nearly zero at ambient pressure.

All samples exhibited two-state behavior (native versus denatured) under pressure, consistent with observations made in other denaturation studies [102, 32]. The peak intensities of the mutants were normalized to that of WT*, which did not denature under our conditions, to correct for pressure-induced changes in fluorescence quenching and solvent transmission. An isosbestic point was evident in the pressure-corrected spectra

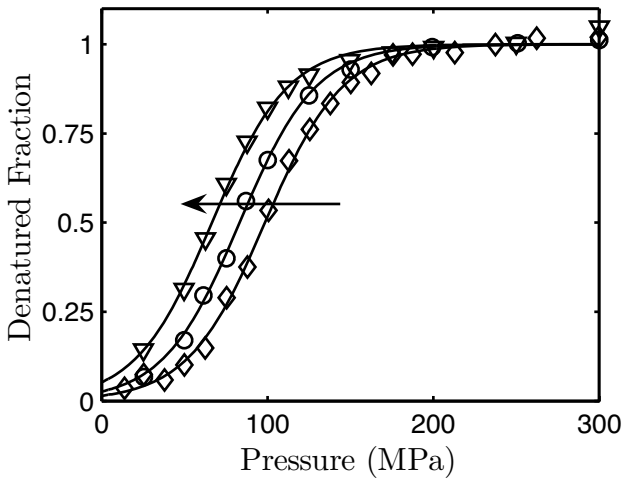

Figure 4.11: Effect of temperature on pressure stability on filtered L99A in pH 3.0 50 mM glycine 20 mM NaCl at 16 (diamond), 22 (circle), and 25 (inverted triangle) °C. Increasing the temperature (direction of arrow) shifts the denaturation curve to lower pressure without changing its shape, corresponding to a change in ΔG° of -0.3 kcal/mol from 16 to 22 °C and -0.4 kcal/mol from 22 to 25 °C. The volume change, ΔV° remained the same to within experimental error.

of each denaturation series (Fig. 4.12 (a)), indicative of two-state denaturation; note that the wavelength at which the isosbestic point appears depends on the pressure stability of the sample. SVD analysis determined that the data could be adequately described as linear combinations of two independent SVD states (an example is shown in Fig. 4.12). For each data set, denaturation curves reconstructed from the two significant SVD states fit the experimental spectra with a goodness of fit parameter, $R^2 \geq 0.9986$. The reversibility calculated from the center of spectral mass upon decompression to ambient pressure was 80-93%. The low end of this range applied to samples maintained at high pressure for several hours. The effects of non-reversibility were apparent only at low pressure, and therefore, low-pressure data were collected first in order of increasing pressure.

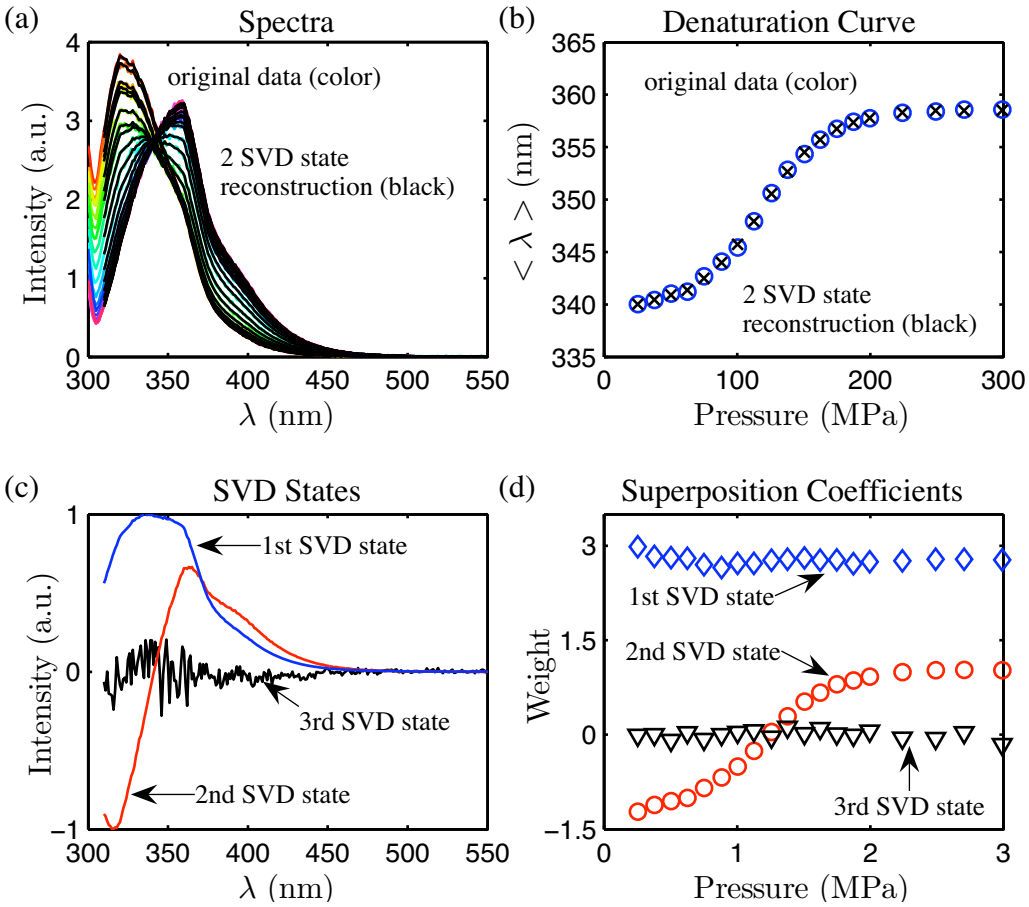

Figure 4.12: SVD analysis of L99G/E108V in pH 3.0 50 mM glycine 100 mM NaCl. The region close to the scattering peak (≈ 300 nm) was not included in this analysis. (a) The spectra reconstructed from the two major SVD states (black) is nearly identical to the original experimental spectra. (b) The denaturation curves derived from both sets of spectra are nearly identical. (c) - (d) The first three SVD states in order of significance and the superposition coefficients. The first SVD state is largely responsible for the overall intensity of a spectrum. The second SVD state, which has a node, is responsible for the peak shift with pressure. Note that the coefficients for the second SVD state switches sign. The third SVD state does not have a distinct shape, nor does it constitute a significant part of the original data (the superposition coefficients are nearly zero at all pressures). It is likely that the third SVD state arises from small errors in the subtraction of the water Raman peak at ≈ 330 nm.

The centers of spectral mass of all mutants showed sigmoidal dependence on pressure, indicative of conformational changes (Fig. 4.13), while that of WT* did not change up to 300 MPa (not shown). The results of the thermodynamic analysis performed on the pressure-induced change in the center of spectral mass are summarized in Table 4.2. The thermodynamic model (Equation 4.2) described our data well, yielding goodness of fit parameters, $R^2 \geq 0.9990$. The centers of spectral mass of the native and denatured states were similar for L99A and L99G/E108V at each solvent condition. This observation is consistent with the structural similarity of L99A and L99G/E108V compared with the other two mutants. The steepness of the denaturation curves is a function of the magnitude of the volume change of denaturation, ΔV°, while the pressure at which the transition begins is indicative of the stability at ambient pressure, ΔG°. At pH 3.0, A98L and V149G exhibited similar volume changes although V149G was less stable, denaturing at a lower pressure. Compared to A98L and V149G, L99A and L99G/E108V showed large volume changes. The magnitude of ΔV° was also dependent on the ionic strength of the solvent. An increase from 20 to 100 mM NaCl resulted in a reduction by approximately 25 Å^3 in the magnitudes of ΔV° for all mutants. At both NaCl concentrations, the volume change of L99G/E108V was roughly 50 Å^3 greater than that of L99A.

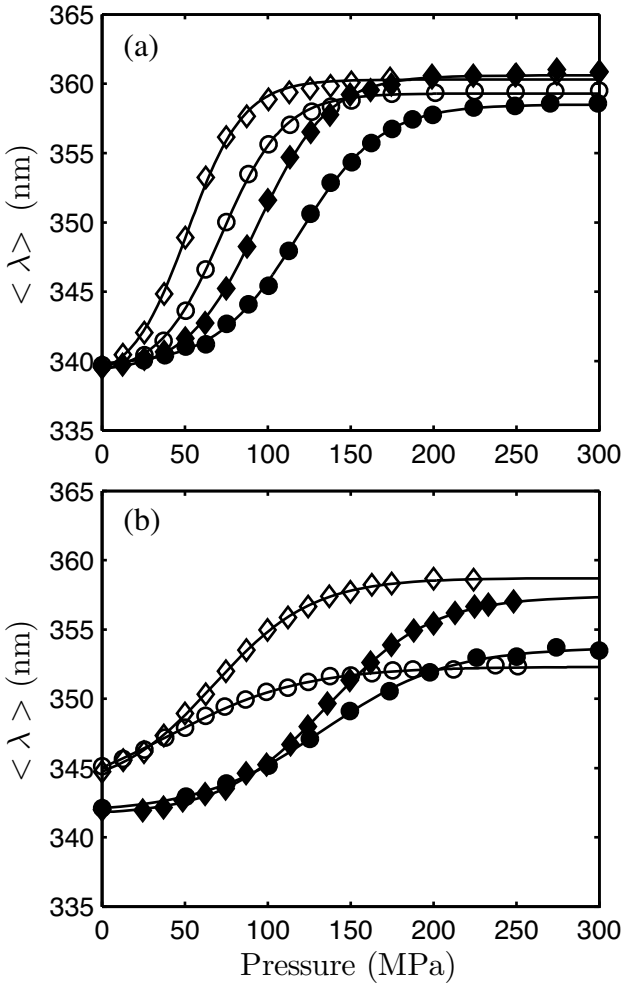

Figure 4.13: Pressure denaturation of T4 lysozyme mutants in pH 3.0 50 mM glycine 20 mM NaCl (diamond) and 100 mM NaCl (circle) buffers monitored at 16 °C by tryptophan fluorescence spectroscopy. (a) L99G/E108V (open) and L99A (closed). (b) V149G (open) and A98L (closed).

For direct comparison with the room-temperature high-pressure crystal structures of L99A and WT* acquired by Collins, *et al.* [24], fluorescence measurements were also made at pH 7.0, 24 °C. L99G/E108V was also studied because of its structural similarity to L99A. We observed sigmoidal transitions for L99A and L99G/E108V as a function of pressure, while no transition was detected for WT* up to 350 MPa (Fig. 4.14). The denaturation curves of the two mutants are similarly shaped with a gradual transition except that of L99G/E108V is shifted by about 65 MPa to a lower pressure with respect to that of L99A. Compared to the values at pH 3.0, the volume changes of denaturation at pH 7.0 were similar and small in magnitude (approximately -100 $Å^3$). The results of thermodynamic fits are given in Table 4.2.

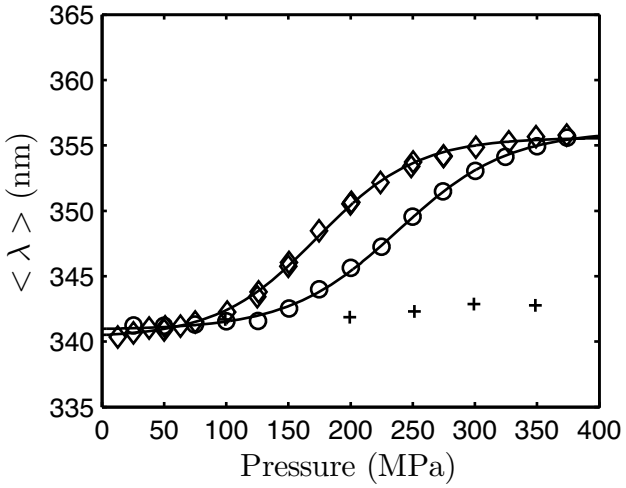

Figure 4.14: Pressure denaturation of L99G/E108V (diamond), L99A (circle), and WT* (plus) T4 lysozyme in pH 7.0 50 mM Tris HCl 20 mM NaCl buffer monitored at 24 °C by tryptophan fluorescence spectroscopy.

Table 4.2: Thermodynamic Quantities Calculated from a Two-state Denaturation Model.

Sample	Condition	$<\lambda>_N$(nm)a	$<\lambda>_D$(nm)a	$\Delta G°$(kcal/mol)	$\Delta V°$(Å^3)	P_m (MPa)[b]
pH 3.0, 16 °C						
L99G/E108V	20 mM NaCl	338.4 ± 1.0	360.3 ± 0.3	1.75 ± 0.24	-235.8 ± 25.5	51.7
	100 mM NaC	339.0 ± 0.5	359.3 ± 0.2	2.21 ± 0.17	-212.8 ± 13.8	72.3
L99A	20 mM NaCl	339.2 ± 0.4	360.6 ± 0.2	2.54 ± 0.15	-187.3 ± 10.0	94.5
	100 mM NaCl	339.7 ± 0.2	358.5 ± 0.2	2.75 ± 0.14	-161.4 ± 7.5	118.7
A98L	20 mM NaCl	341.6 ± 0.2	357.4 ± 0.3	2.49 ± 0.13	-127.2 ± 6.8	136.0
	100 mM NaCl	341.8 ± 0.4	353.7 ± 0.2	2.07 ± 0.22	-107.7 ± 10.0	133.7
V149G	20 mM NaCl	343.3 ± 0.4	358.7 ± 0.2	1.30 ± 0.10	-134.1 ± 7.3	67.4
	100 mM NaCl	342.4 ± 1.0	352.3 ± 0.2	0.58 ± 0.17	-99.2 ± 10.0	40.8
pH 7.0, 24 °C						
L99G/E108V	20 mM NaCl	340.3 ± 0.2	355.6 ± 0.3	2.56 ± 0.17	-102.8 ± 7.0	172.8
L99A	20 mM NaCl	340.9 ± 0.2	356.1 ± 0.5	3.19 ± 0.26	-93.1 ± 8.2	238.1

Results of fitting Equation 4.2 to data. [a]Subscripts N and D refer to the native and denatured states, respectively. [b]P_m is the midpoint pressure of denaturation.

4.5.5 Ligand-Binding in the Cavity

T4 lysozyme mutants with large engineered hydrophobic cavities such as that in L99A are also known to bind hydrophobic molecules such as benzene [36, 91]. In the case of L99A T4 lysozyme, benzene binding in the mutation-enlarged cavity (Fig. 4.2 (b), cavity 6) has been observed by crystallography (PDB 1L83) with only modest structural changes to the protein backbone [36]. The presence of a benzene molecule in this enlarged cavity essentially restores the original cavity size of WT* and partially compensates for the loss in thermal stability caused by the L99A mutation [91]. As the loss in thermal stability caused by L99A has been attributed to a loss in van der Waals interactions [37], the effect of benzene binding can be thought of regaining these stabilizing interactions.

We have shown that at pH 3.0, WT* T4 lysozyme is too stable to denature at pressures below 400 MPa (Fig. 4.6). Because the cavities in WT* are small, this result strongly supports the hypothesis that the pressure stability of proteins and the magnitude of ΔV°, the volume change of pressure denaturation, are dependent on the ability of water to fill cavities. To test this further, we investigated whether plugging a cavity with benzene affects pressure denaturation. Measurement of the pressure stability of a benzene-bound protein is complicated by several factors. As discussed in Chapter 1, the partition of model hydrophobic compounds in its liquid phase and in water is known to be highly pressure-dependent. The effect of this pressure-dependence on pressure denaturation is unknown. Additionally, benzene binding is expected to increase the pressure stability and decrease the magnitude of the denaturation volume change. Observation of the complete denaturation curve may be limited by the pressure range of our apparatus. Furthermore, the material used to fabricate soft cap of the internal sample cell was not chosen for containment of non-aqueous solvents. Finally, benzene fluorescence may

overlap that of tryptophan. Although further refinement of these experimental parameters remains for future experiments, preliminary results could be obtained.

In order to maximize the observable portion of the denaturation curve, L99G/E108V - one of the least stable T4 lysozyme mutants - was chosen for this experiment, and the temperature was raised from 16 to 25 °C. Benzene binding has been observed for this mutant in the mutation-enlarged cavity (Fig. 4.2 (c), cavity 6), which is the largest in size of all the mutants studied here [158]. It was shown earlier that temperature changes in this range shift the stability without affecting the volume change (Fig. 4.11). A solution of L99G/E108V in 50 mM glycine 20 mM NaCl 7 mM benzene pH 3.0 and the corresponding blank solution were prepared by introducing benzene to the samples and vigorously shaking. The background fluorescence was first measured to determine if tryptophan could be selectively excited with minimal contributions from benzene fluorescence. Excitation at 295 nm was found to be sufficient. A comparison of L99G/E108V denaturation without benzene taken at 16 °C and without benzene at 25 °C is presented in Fig. 4.15. Measurements of equilibrium points were complicated by slow kinetics and the pressure limit of our apparatus. The sample was equilibrated for 30 - 120 min at each pressure. Nonetheless, it is clear that benzene has a dramatic effect on the pressure denaturation of L99G/E108V. The slope of the denaturation transition decreases considerably. According to SVD analysis, two SVD states are sufficient to describe these spectra. Assuming two-state denaturation, this result indicates that the magnitude of ΔV° is considerably reduced by benzene binding. Although there are too few data points for our thermodynamic model (Equation 4.2), fitting gives us an estimate for ΔV° of -41 ±13 to -89 ±65 Å^3. These values are very small compared to $\Delta V^\circ = -235 \pm 25.5$ Å^3 for L99G/E108V without benzene.

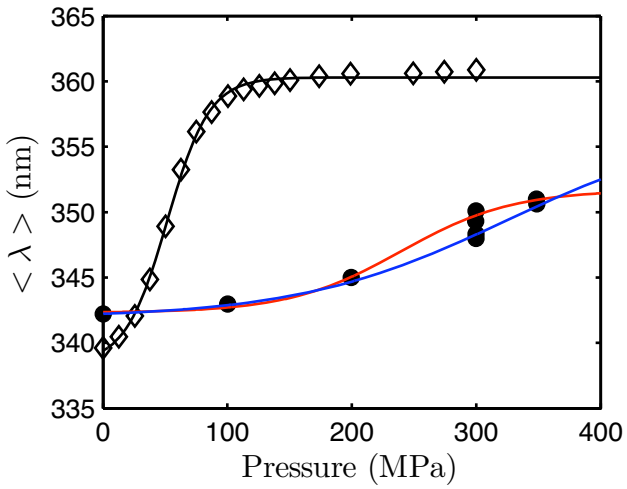

Figure 4.15: Effect of benzene binding of large cavity in L99G/E108V on pressure denaturation. Shown are the denaturation curved of L99G/E108V in pH 3.0 20 mM NaCl at 16 °C (diamond) and in pH 3.0 20 mM NaCl 7 mM benzene at 25 °C (circle). The solid curves are thermodynamic fits. Slow kinetics prevented from achieving equilibrium. A thermodynamic fit through the bottom two points at 300MPa (blue curve) gives a minimum estimate of ΔV° = -41 ±13 Å^3 ($< \lambda >_D$ was estimated as the value measured without benzene). A fit through the top two points at 300 MPa (taken an hour after the bottom two points) gives an upper estimate of -89 ±65 Å^3 (red curve). The volume of a benzene molecule in its liquid phase is 147 Å^3.

It was mentioned in Chapter 3 that the use of syringe filters (Anotop 10 Plus, Whatman) in the preparation of fluorescence samples introduced spectroscopically detectable contaminants in the solution. It was shown that they can have large effects on the pressure behavior of T4 lysozyme (Fig. 4.16). At both pH 3.0 and 7.0, the contaminants changed the values of $< \lambda >_N$ and $< \lambda >_D$. Although the thermodynamic values, ΔG° and ΔV°, remained the same at pH 3.0 to within experimental error, at pH 7.0, the presence of the contaminants had a large effect. The S shape of the transition was lost, resulting in a significant decrease in the magnitude of ΔV° from -102.8 ± 7.0 Å^3 to -34.8 ± 15.1 Å^3. While the contaminants remain unidentified it is possible the reason for this decrease is due to contaminants binding with protein cavities under certain sol-

vent conditions. At the very least, this result underscores the need to maintain solvent purity in pressure denaturation studies of cavity mutants.

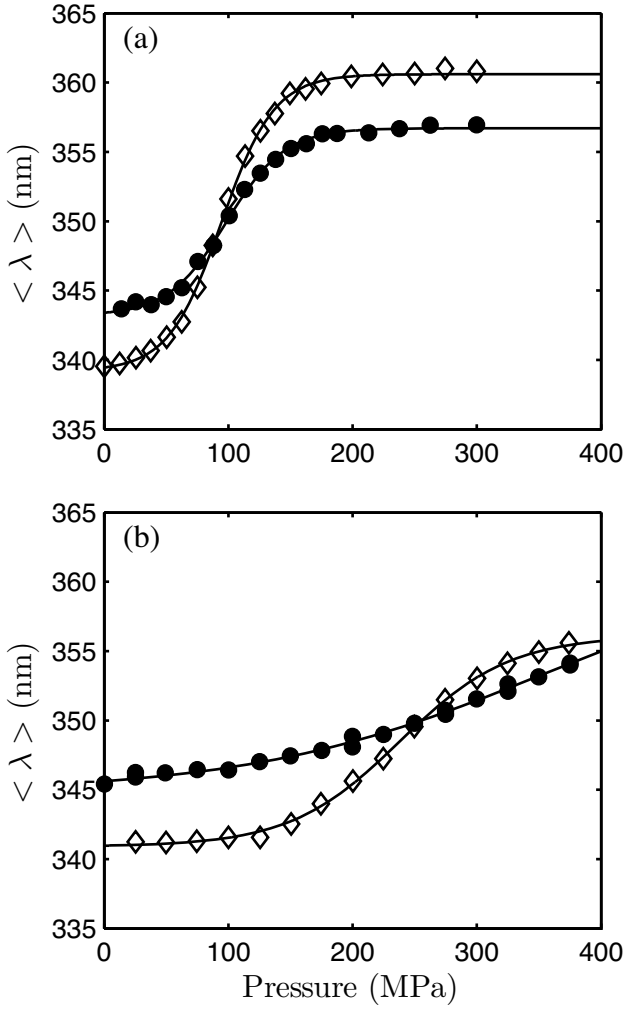

Figure 4.16: The effect of solvent contamination by a syringe filter (Anotop 10 Plus, Whatman) on pressure denaturation. (a) L99A 50 mM glycine 20 mM NaCl, pH 3.0, 16 °C unfiltered (diamond) and filtered (closed circle). The change in ΔV° due to the filter was 187.3 ± 10.0 Å^3 to −170.7 ± 16.3 Å^3; no change to within error (b) L99A 50 mM Tris HCl 20 mM NaCl, pH 7.0, 25 °C unfiltered (diamond) and filtered (closed circle). The change in ΔV° due to the filter was −102.8 ± 7.0 Å^3 to −34.8 ± 15.1 Å^3.

4.5.6 Structural Information from Fluorescence Quenching

Additional information on global conformational changes was derived from fluorescence quenching measurements. T4 lysozyme has five methionine residues in close proximity to the three tryptophan residues present in the C-terminal lobe (Fig. 4.1). The sulfur atom in methionine quenches tryptophan emission and provides a probe of the methionine-tryptophan separation. Denaturation of T4 lysozyme is usually accompanied by an increase in emission intensity [32], consistent with an increased methionine-tryptophan distance. In the seleno-methionine variant of L99A (Se-Met L99A), the methionines are replaced with seleno-methionines. As selenium and sulfur have differing quenching strengths a comparison of L99A and Se-Met L99A yields additional information on the spatial compactness of the unfolded state of L99A [160].

Tryptophan fluorescence measurements were made on Se-Met L99A in pH 3.0, 50 mM glycine, 20 mM NaCl and pH 7.0, 50 mM tris, 20 mM NaCl buffers and compared to those of L99A under the same conditions. The intensity increase accompanying denaturation was more pronounced for Se-Met L99A than for L99A, consistent with the stronger quenching ability of selenium (Fig. 4.17). Fig. 4.18 (a) shows that at each pressure, the centers of spectral mass were similar for L99A and Se-Met L99A in the same solvent, indicating that these two mutants are structurally similar at any given pressure and that the introduction of seleno-methionines does not significantly distort the shape of the fluorescence spectra or change the denaturation behavior.

Pressure-induced changes to the fluorescence yield of tryptophan or transmission through the solvent were factored out in the ratio of the emission intensities of L99A and Se-Met-L99A, I_{L99A} and $I_{Se-MetL99A}$, at the same pressure. The ratios were calculated as

follows at each pressure

$$\left\langle \frac{I_{Se-MetL99A}}{I_{L99A}} \right\rangle = \frac{1}{N} \sum_{i=1}^{N} \frac{I_{Se-MetL99A}(\lambda_i)}{I_{L99A}(\lambda_i)}. \tag{4.13}$$

The sum was taken over points in the wavelength range 310-400 nm where the fluorescence signal is strong. N is the number of ratios in the sum (91, in this case). Fig. 4.18 (b) shows a comparison of these ratios at pH 3.0, 50 mM glycine, 20 mM NaCl and pH 7.0, 50 mM Tris, 20 mM NaCl as a function of denatured fraction. They are normalized at 0.1 MPa. We see that as denaturation progresses, the ratio is greater at pH 3.0 than at pH 7.0. This result suggests that the denatured state at pH 7.0 is more compact than at pH 3.0.

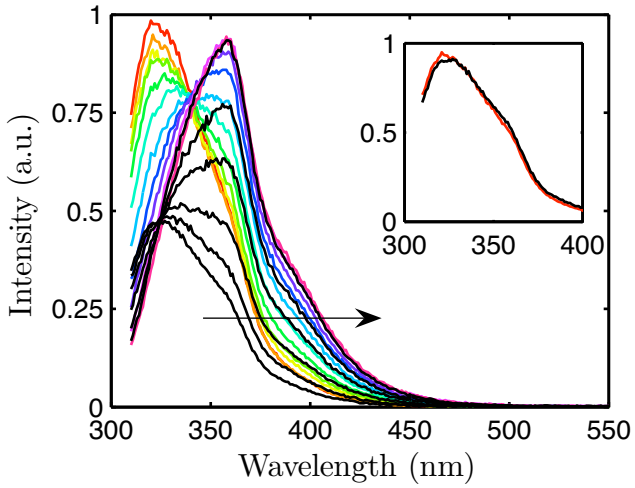

Figure 4.17: Tryptophan uorescence spectra of L99A (color) and Se-Met L99A (black) in 50 mM glycine 20 mM NaCl pH 3.0 16 °C with increasing pressure (direction indicated by arrow). The emission intensities were normalized at high pressure (200 MPa) to emphasize the pressure-induced intensity increase of Se-Met L99A compared with L99A. Inset: Spectra of L99A (red) and Se-Met L99A (black) at low pressure (25 MPa) scaled by a constant factor.

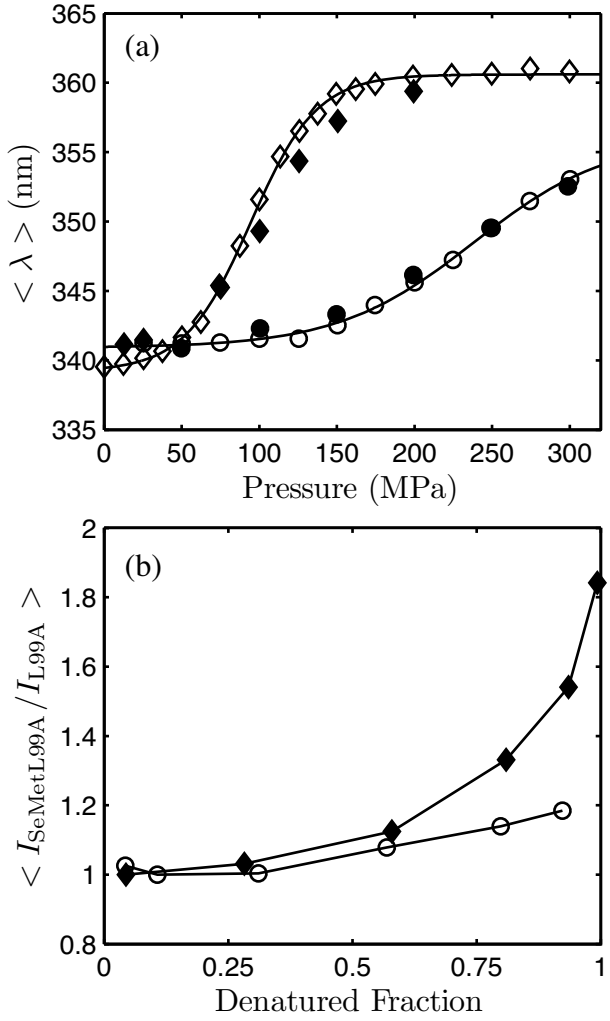

Figure 4.18: Pressure denaturation of L99A and Se-Met L99A in 50 mM glycine 20 mM NaCl pH 3.0 16 °C and 50 mM Tris HCl 20 mM NaCl pH 7.0 24 °C. (a) Centers of spectral mass of L99A (open) and Se-Met L99A (closed) at pH 3.0 (diamond) and pH 7.0 (circle). L99A and Se-Met L99A show similar denaturation curves, indicative of structural similarity at each pressure. (b) Normalized intensity ratios of Se-Met L99A and L99A emission at pH 3.0 (closed diamond) and pH 7.0 (open circle). At pH 7.0, the ratio shows little change with pressure, while at pH 3.0, there is a large increase. This indicates a greater separation between tryptophan and seleno-methionine residues in the denatured state at pH 3.0 compared with pH 7.0, suggesting that the pH 3.0 denatured state is more unfolded than at pH 7.0.

4.6 Discussion

4.6.1 Structural Characterization of Solution States

The low-resolution solution structures of native L99A T4 lysozyme at pH 3.0 obtained from SAXS showed good agreement with the crystal structure solved at neutral pH. This supports the reasonable assumption that the shapes and sizes of the internal cavities in the crystal structure are representative of the solution structure. For the pressure-denatured state of L99A at pH 3.0, SAXS results suggest that the average overall conformation is extended while local regions may have residual structure. The radius of gyration of the pressure-denatured state was smaller than that predicted for the chemically-denatured state [71, 72], consistent with the view that the widely accepted model of protein denaturation, i.e. the transfer of core residues to water, does not appropriately describe pressure denaturation. Fluorescence quenching measurements suggest that the pressure-denatured state of L99A at pH 7.0 is even more compact than at pH 3.0.

4.6.2 Unfolding at pH 3.0

The volume change accompanying denaturation is contributed by volume changes of the protein atoms, the solvent-excluded cavities, and the hydration of solvent-exposed residues. As the atoms are the least compressible component, it is thought that the major contributions to the volume change of denaturation are the elimination of solvent-excluded cavities and the hydration of solvent-exposed residues [115, 52]. Around charged residues, electrostriction of water molecules is known to occur [115]. However, the volume properties associated with the hydration of hydrophobic residues are still under investigation, particularly with respect to pressure [115, 26, 67, 50]. It is

therefore difficult to probe the contributions of the hydration changes. By comparing mutants with various volumes of internal cavities, however, we can investigate how these volumes correlate with the volume change of denaturation.

Our experiment with benzene-bound L99G/E108V at pH 3.0 suggests that cavity hydration is a major component of ΔV°. According to X-ray crystallography [158], benzene binds exclusively in cavity 6 (Fig. 4.2 (c)) in the L99G/E108V mutant. If hydration of this cavity contributes to the magnitude of ΔV°, we expect a reduction in the magnitude that is comparable to the volume of a benzene molecule. The volume of a benzene molecule in bulk, calculated from its density and molecular weight, is roughly 147 Å^3. This volume is comparable to the observed reduction in $|\Delta V^\circ|$ of 146 ± 28.6 to 194 ± 69.8 Å^3 caused by benzene-binding. This result suggests that a correlation between ΔV° and the cavity volumes can be expected.

To quantify cavity volumes, structural changes caused by a mutation must be identified, and the solvent occupancy of each cavity must be quantified. In a manner similar to the estimation of a mutation-induced change in stability ($\Delta\Delta G$) by solvent transfer free energies, the change in cavity volume as a result of a single buried mutation can as a first approximation be estimated as the difference between the van der Waals volumes of the exchanged side chains. This analysis has been performed on staphylococcal nuclease and ribonuclease A mutants to predict the mutation-induced change in cavity volumes [44, 139]. Particularly in the case of large-to-small amino acid substitutions in staphylococcal nuclease, the cavity volumes predicted by this method successfully correlated with the ΔV° of pressure denaturation, lending support to the hypothesis that internal hydration of cavities is implicated in pressure denaturation. However, in both studies, atomic resolution structures were not available for most of the mutants to support the assumption that the structural changes were localized at the mutation sites.

The same side-chain volume analysis, when applied to T4 lysozyme, fails to predict mutation-induced changes in cavity volumes that correlate with ΔV°. Using the side chain volumes of Leu, Ala, Val, and Gly reported by Richards, *et al.* [113] and the experimental ΔV° of L99A at pH 3.0, 50 mM glycine, 20 mM NaCl as a reference, ΔV° was predicted for L99G/E108V, A98L, and V149G [44]. Note that the mutation, E108V, was not included in this analysis because the 108th residue is on the surface of the protein. We therefore do not expect differences in the hydration of Glu (E) and Val (V), to contribute differently to the volume change of denaturation. The predicted results in Table 4.3 show in particular, the failure to account for the observed behavior of A98L and V149G. The $\Delta V^\circ$of V149G was predicted to be as large in magnitude as L99A, while that of A98L was predicted to be very small in magnitude, roughly half of the experimentally observed value.

Table 4.3: Denaturation volume changes predicted by side-chain volumes.

	$\Delta V^\circ_{predict}$ (Å^3)	$\delta\Delta V$ (Å^3)
L99G/E108V	206.2 ± 10.0	29.6 ± 26.9
A98L	73.1 ± 10.0	54.1 ± 12.1
V149G	187.1 ± 10.0	-53.0 ± 12.4

The experimental denaturation volume change, ΔV°, of L99A at pH 3.0 20 mM NaCl was used as a reference. $\delta\Delta V = \Delta V^\circ_{experiment} - \Delta V^\circ_{predict}$. Volume changes of other mutants were predicted with van der Waals volumes of side-chains [113] of exchanged amino acids

The failure of this method to estimate mutation-induced changes in cavity volumes is not surprising. Previous crystallographic studies of T4 lysozyme have also shown that structural changes due to a mutation cannot be easily predicted. At some buried sites,

a large-to-small amino acid substitution in T4 lysozyme created or enlarged a cavity, while at other sites, a similar mutation caused a rearrangement of the protein that filled the cavity [35]. Moreover, for mutations that permitted the creation or enlargement of cavities, the new cavity volume could not be simply predicted by a side-chain analysis using the WT* structure and the van der Waals volumes of the exchanged amino acids. In the case of L99A, the change in cavity size is slightly smaller than expected. An extreme case was L99G T4 lysozyme. Unlike L99A, the L99G mutation exposes the large cavity to the solvent. A second mutation, E108V, far from the cavity and on the surface of the protein was required to close the opening of the molecules surface created by the L99G mutation [158]. The structural changes caused by a small-to-large amino acid substitution such as A98L are less predictable [80].

Crystal structures of T4 lysozyme were thus necessary to quantify cavity volumes. The internal cavities of the mutants identified with a 1.2 Å radius radius rolling probe [119] (refer to Sect. 4.3) are shown in Fig. 4.2 (a)-(e), and the corresponding volumes are presented in Table 4.1. An inspection of the crystal structures explains the large discrepancies between the experimental ΔV° and that predicted by side-chain volume analysis for A98L and V149G (Table 4.3). The A98L mutation does not fill the cavity at the mutation site, but instead, causes the strain-induced formation of several small cavities throughout the protein (Fig. 4.2 (d)). Therefore the total cavity volume is greater than that predicted by side-chain volume analysis. In the case of V149G, the mutation not only enlarges a cavity (Fig. 4.2 (e)) but this cavity accommodates two additional solvent-binding sites. Thus, the effective volume of this cavity is likely smaller than that predicted by side-chain volume analysis.

The volume of a single water molecule in bulk is approximately 30 Å^3, which is roughly the size of a small cavity in T4 lysozyme. Therefore, the solvent occupancy of

each cavity can have large effects on its effective volume. Cavity 1 (Fig. 4.2, Table 4.1) is a conserved solvent-binding site in T4 lysozyme [161] and contains WAT 171 and 179. Similarly, cavity 3 binds another conserved internal water molecule, WAT 208. Cavities 4 and 8 contain WAT 175 and 213, respectively. Crystal structures enable the identification of internal water molecules that otherwise may not be identified. However, the average occupancy of internal water is not easily determined by conventional model-based crystallographic refinement methods [56]. WAT 171, 175, 179, and 208 have been observed in a large number of mutant structures solved over many independent experiments, and several of these water molecules show evidence of hydrogen bonding stabilization [161]. WAT 213 was also observed in all of the mutants studied in this work. We therefore made the reasonable assumption that these water molecules have full occupancy in all of the studied mutants.

The occupancies of poorly ordered water molecules introduced by the V149G and L99G/E108V mutations were more difficult to assign. In the crystal structures, the enlarged cavity at the V149G mutation site (Fig. 4.2 (e), cavity 3) contains two additional water molecules (WAT 323 and 324) in addition to WAT 208, while that of L99G/E108V (Fig. 4.2 (c), cavity 6) contains WAT 401 and 402. We first assume that both of these cavities are fully occupied. Under this assumption, however, no correlation is apparent in the relationship between ΔV° at pH 3.0 with the calculated total cavity volumes (Fig. 4.19). As discussed earlier, the ΔV° of V149G predicted by side-chain volume analysis was much larger than the experimentally determined value because solvent binding of the mutation-enlarged cavity was not accounted for. As this mutation site is the location of the only buried polar network in T4 lysozyme [159], we believe that it is reasonable that WAT 323 and 324 occupy this cavity at least partially under the solvent conditions used in this study. This may explain why the tryptophan fluorescence spectrum of V149G in its folded state was the most red-shifted of all the mutants (Fig. 4.13).

It is possible that the tryptophan residue lining this polar cavity (Trp 138) reports the increased hydration of V149G.

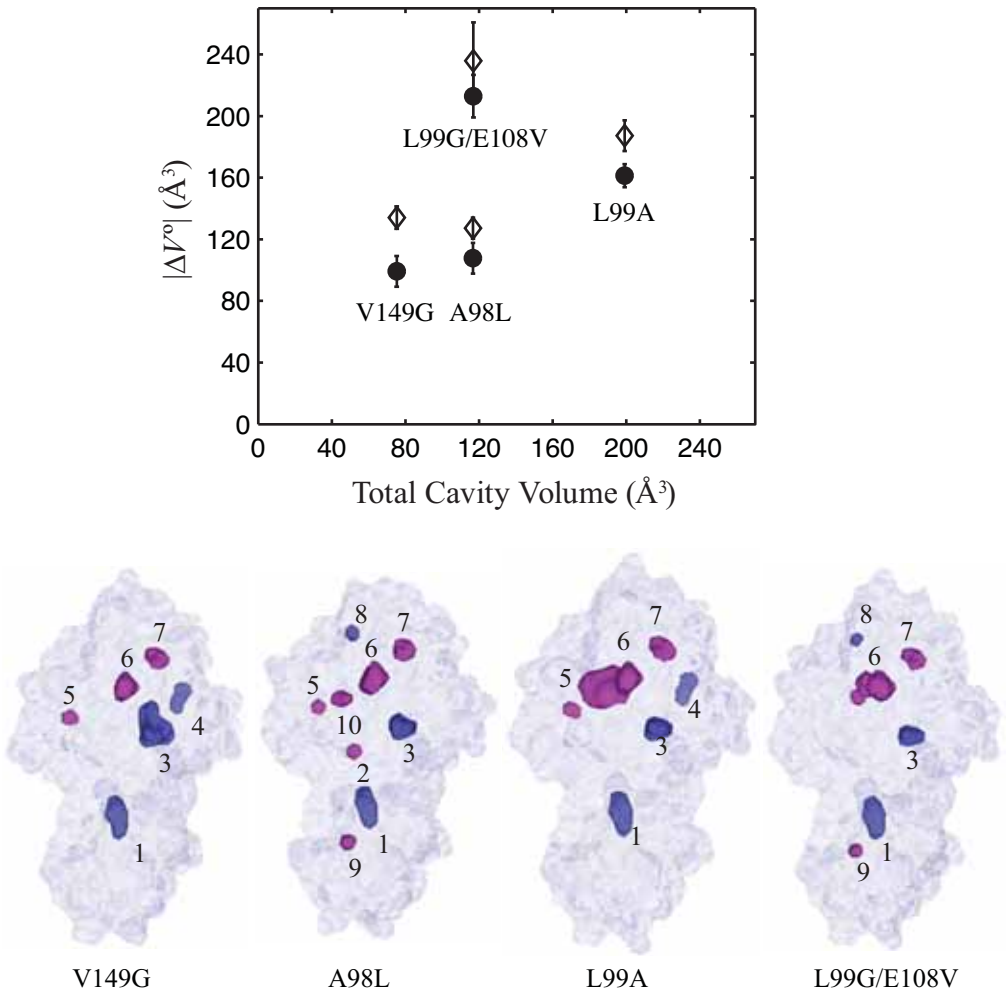

Figure 4.19: The volume changes of denaturation (see Table 4.2) of L99G/E108V, L99A, V149G, and A98L T4 lysozyme in pH 3.0 buffer, 16 °C at 20 mM NaCl (closed circle, top plot) and 100 mM NaCl (open diamond, top plot) compared to the total cavity volumes calculated from crystal structures assuming full occupancy of all internal solvent molecules. No correlation is apparent. Bottom: cavities assumed to be fully occupied are shown in dark blue while unoccupied volumes are in magenta.

In contrast, we speculate that the enlarged hydrophobic cavity in L99G/E108V is empty at pH 3.0. The enlarged cavity of L99A is believed to be empty [25, 37], and

the crystal structures of L99G/E108V and L99A are very similar except for the differing volumes of the enlarged cavities [158]. At pH 3.0, the magnitude of the volume change upon pressure denaturation was roughly 50 $Å^3$ greater for L99G/E108V compared to L99A. This value is similar to the difference in volumes of the enlarged cavities (Fig. 4.2 (b)-(c), cavity 6) in their empty states (61.4 $Å^3$), which are the dominant contributors to the total cavity volumes of the two mutants. This suggests that the occupancies of the two cavities are similar at pH 3.0. The large reduction in volume change observed with benzene-bound L99G/E108V is also consistent with the large hydrophobic cavity being empty in the native state at this pH. The total cavity volumes were recalculated with the new assumption that the enlarged cavity in L99G/E108V is empty and that all other crystallographically determined solvent-binding sites are fully occupied. A correlation between denaturation volume changes and total cavity volume is now observed (Fig. 4.20). The proportionality of the two quantities suggests that all the cavities are hydrated under pressure denaturation at this pH. The slope of the linear fits was dependent on the probe size used to calculate the cavity volumes. Using a 1.4 Å probe gave a smaller slope as fewer small cavities could be detected, reducing the estimated total cavity volume of small cavity mutants by a greater fraction than that of the large cavity mutants.

The magnitude of the volume change of denaturation was also dependent on the ionic strength, reflected by the ≈ 40 $Å^3$ change in vertical positions of linear fits in Fig. 4.20. We consider two possible mechanisms of hydration changes around solvent-exposed residues to explain this ionic strength dependence. At pH 3.0, T4 lysozyme is highly positively charged. Most of the charged residues are on the surface of T4 lysozyme, and no change in the hydration of these residues is expected from denaturation. However, there are several buried and semi-buried salt bridges in T4 lysozyme. Crystal structures of T4 lysozyme solved at various ionic strengths demonstrate that a change in ionic

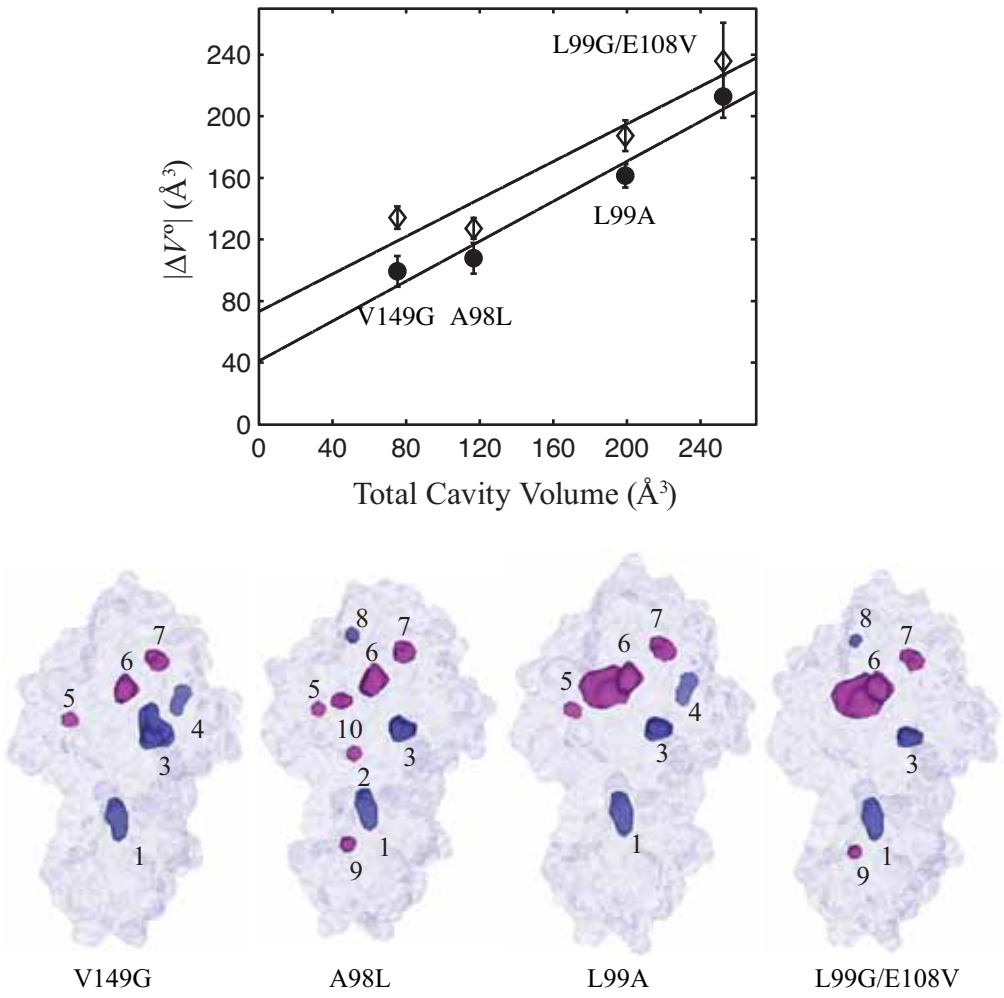

Figure 4.20: The volume changes of denaturation (see Table 4.2) of L99G/E108V, L99A, V149G, and A98L T4 lysozyme in pH 3.0 buffer, 16 °C at 20 mM NaCl (closed circle, top plot) and 100 mM NaCl (open diamond, top plot) compared to the total cavity volumes calculated from crystal structures assuming cavity 6 of L99G/E108V to be empty and full occupancy of all other internal solvent molecules. A positive correlation is seen. Bottom: cavities assumed to be fully occupied are shown in dark blue while unoccupied volumes are in magenta.

strength does not affect buried salt bridges in the native state [11]. These salt bridges are likely exposed in the pressure-denatured state, and the presence of counter ions around the dissociated salt pairs would reduce the effect of electrostriction on the denaturation volume change. The presence of counter ions may also affect the compactness of the denatured state, and thus change the number of solvent-exposed residues. Refolding of an acid-denatured protein has been observed at high anion concentrations [47]. This is thought to be due to reduced charge repulsions in the protein. A similar behavior can be expected to occur to T4 lysozyme at pH 3.0. This may be the basis for the apparent blue-shift in the tryptophan fluorescence of the denatured state with increased NaCl concentration. Regardless of mechanism, our data indicate that under the conditions investigated at low pH, all of the internal cavities are hydrated while the ionic strength of the solvent affects the volume contribution of hydration around solvent-exposed residues.

4.6.3 Cavity Filling at pH 7.0

Fluorescence measurements were made at pH 7.0, 24 °C as a direct comparison to the high-pressure, room-temperature crystal structures of L99A and WT* T4 lysozyme [25]. According to the high-pressure crystal structures acquired by Collins, *et al.*, cooperative water filling of the large hydrophobic cavity in L99A (Fig. 4.2 (b), cavity 6) is favorable under pressure even without unfolding [25]. We emphasize that in the crystal state, large conformational changes such as unfolding do not occur. Only the large cavity of L99A showed increased internal electron density with pressure (PDB structures 2B6T, 2B6W, 2B6X, 2B6Y, 2B6Z, 2B70, 2B72, 2B73, 2B74, 2B75). No other pressure-induced changes in internal hydration were observed in the crystal structures. WT*, which has a smaller corresponding cavity (Fig. 4.2 (a), cavity 6), showed no water filling up to 200 MPa (PDB structures 2OE4, 2OE7 are at 100 MPa; 2OE9, 2OEA at

200 MPa). Molecular dynamics simulations performed on the high-pressure structures of L99A suggested cooperative filling of four water molecules in the large cavity [25].

In solution, L99A underwent a pressure-induced change in fluorescence corresponding to a denaturation volume change of $\Delta V^{\circ} = -93.4 \pm 8.2$ Å^3, nearly a factor of two smaller than at pH 3.0, with a pressure midpoint of roughly 240 MPa. Structural information obtained from comparative fluorescence quenching of L99A and Se-Met L99A indicated that the pressure-denatured state of L99A at pH 7.0 is even more compact than that at pH 3.0. While our methods do not provide direct evidence of preferential water filling of the large cavity in L99A in solution at this pH, we explored this is as a possible mechanism to explain the small volume change and compactness of the denatured state. Assuming that the volume change of transferring each water molecule from the bulk to the large cavity is 30 Å^3, this mechanism would suggest that in solution, the large cavity is filled by three water molecules (93.4 Å^3 $\approx 3 \times 30$Å^3). This is in reasonable agreement to the predictions made by the MD simulations [25]. For comparison with the change in water occupancy of the large cavity determined experimentally by integrated electron densities in the crystal structures [25], the centers of spectral mass of L99A were converted to change in water occupancy under the assumption that under pressure, the large cavity is filled by three water molecules (Fig. 4.21). A two-state thermodynamic fit to the converted fluorescence data with a fixed volume change of three bulk water molecules shows good agreement with the crystallographic results. This suggests that preferential water filling of the large cavity is a plausible mechanism to explain the small volume change and size of the denatured state at this pH.

As a comparison to L99A, fluorescence measurements were also made on the structurally similar mutant, L99G/E108V. Although the large cavity of L99G/E108V is approximately 61 Å^3 greater in volume than the corresponding cavity in L99A, the de-

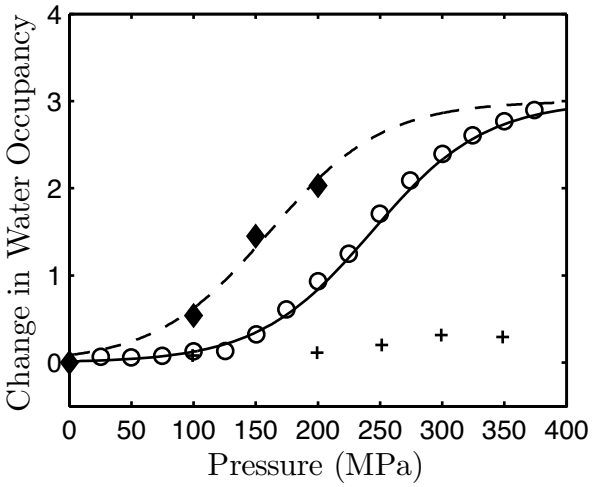

Figure 4.21: Comparison of change in water occupancy of L99A at neutral pH determined by X-ray crystallography (diamond, reprinted with permission from Collins, *et al.* [25]) and fluorescence spectroscopy (circle). A two-state (0 or 3 water molecules) thermodynamic fit to the data is shown on each data set with a fixed volume change of 90 Å^3 (volume of three water molecules in bulk). The fit to the crystallography data is shifted to lower pressure by 82 MPa relative to the fluorescence data. This stability difference may be due to subtle differences between structure and dynamics of the T4 lysozyme molecule in solution and in the crystal. The change in water occupancy of WT* determined by fluorescence is shown for reference (cross).

naturation volume changes were the same to within error (approximately 10 Å^3). As mentioned earlier, the crystal structure of L99G/E108V shows two poorly ordered water molecules in the large cavity (WAT 401 and 402). We interpret this to mean that at neutral pH, where the crystal structure was solved, the large cavity of L99G/E108V is partially filled with a maximum occupancy of two water molecules. By taking two water molecules into consideration, the difference in volume changes of cavity-filling for L99A and L99G/E108V can be as small as 1 Å^3 (61 Å^3 $\approx$ 2 x 30 Å^3).

One of the paradoxes of pressure denaturation has been the small magnitudes of observed volume changes. It has been thought that a positive volume contribution must

exist, possibly due to the hydration of hydrophobic residues [115]. While this is plausible, it cannot be assumed that all the existing cavities and packing defects of a protein are hydrated or eliminated with the application of pressure. The high-pressure crystallography study of L99A showed that water penetration of the large cavity and not other, smaller cavities in the native structure of L99A was possible in part due to the cooperativity [25]. Only the hydrophobic cavity large enough to accommodate multiple waters interacting with hydrogen bonds was filled in the folded structure.

4.7 Conclusions

Our results imply the existence of multiple pressure-denatured states of the T4 lysozyme family with differing levels of internal hydration and unfolding that were dependent on the solvent conditions and particularly pH. The results were thus consistent with water penetration of the protein rather than transfer of hydrophobic residues from the core of the protein to the water as the mechanism of pressure denaturation. At pH 3.0, the pressure-denatured state was extended but more compact than the predicted size of a chemically denatured protein of the same length [71, 72]. We were able to relate the volume change of denaturation to cavity volume and hydration changes by comparing multiple mutants of T4 lysozyme with known crystal structures and varying the ionic strength of the solvent. The magnitudes of the volume changes of denaturation for L99A, L99G/E108V, A98L, and V149G T4 lysozyme positively correlated with the total cavity volume, while the binding of benzene in the large cavity of L99G/E108V caused a reduction in volume change by an amount comparable to the volume of a benzene molecule. These results suggest that at pH 3.0, all the cavities were hydrated in the pressure-denatured state. Increasing the ionic strength reduced the magnitude of the volume change likely as a result of counter ion interactions with salt pairs exposed

in the denatured state. At pH 7.0, the denaturation thermodynamics of L99A in solution was in good agreement with the preferential cavity filling observed by high-pressure crystallography and MD simulations [25]. The pressure-denatured state at pH 7.0 was more compact in size than at pH. 3.0. These results suggest that at pH 7.0, not all the cavities are filled.

We showed that the problem of pressure denaturation not only requires understanding of the change in water occupancy as a function of pressure, but also in the volume properties of the protein and interacting waters. The availability of crystal structures was necessary for the quantification of cavity volumes and solvent occupancy of the T4 lysozyme mutants investigated in our work. However, we recognize that a crystal structure represents a static picture of the average conformation of a protein under a specific condition. As a protein is a fluctuating system, the cavities and internal solvent molecules are not static. The calculation of a cavity volume from an atomic structure also depends on the probe size and the van der Waals radii of the amino acids used for identifying molecular surfaces. For the T4 lysozyme mutants used in this study, a 1.2 Å probe was preferred over a 1.4 Å probe. Small cavities that were found in all mutants by a 1.2 Å probe were not consistently identified with a 1.4 Å probe. The magnitudes of the experimentally observed volume changes of denaturation were roughly the size of several water molecules. The interpretation of volume changes from native structures, therefore, requires certainty in the occupancy of internal water molecules in the native state and its dependence on the solvent condition.

In this work, we investigated the contribution of cavity volumes and electrostriction to the volume change of pressure denaturation. The volume properties of hydration waters, particularly around hydrophobic residues as a function of pressure, remain to be established. Finally, it was assumed in this study that the volume change accompanying

denaturation was pressure-independent because the magnitude and sign of isothermal compressibility change with denaturation, i.e. the pressure dependence of the denaturation volume change, are still under debate. Direct measurements of the isothermal compressibility change associated with pressure denaturation have not yet been made [136]. With the exception of the study by Seemann, *et al.* [122], the isothermal compressibility change has only been determined from fitting a thermodynamic model with a second-order expansion of ΔG to denaturation data [136]. It is noted that the sign of the isothermal compressibility is defined inconsistently in the literature, causing confusion on the sign of the second-order term of ΔG [115, 136, 52, 108, 127, 89]. A second-order fit also increases the number of free fitting parameters such that over-fitting of data is also a concern. Further investigations of the pressure-dependence of the volume change accompanying denaturation are suggested.

The magnitude of the volume change accompanying pressure denaturation of a protein is generally less than 1% of the protein volume and on the order of several bulk water molecules in volume. Our results support the growing view that the pressure-denatured state of a protein is one in which the penetration by a few water molecules is favored and emphasizes the importance of the role of water in protein folding and biological processes.

CHAPTER 5

PRESSURE EFFECTS ON THE TERTIARY STRUCTURE AND FUNCTION OF HAIRPIN RIBOZYME

5.1 Introduction

Ribozymes are RNA molecules or regions of RNA that catalyze chemical reactions. Like proteins, ribozymes adopt specific tertiary structures that are biologically active. Typically, a large fraction of the ribozyme structure is double-stranded and participates in a form of secondary structure, such as double-stranded helices consisting of hydrogen-bonded base pairs and loops consisting of unpaired bases (Figure 5.1). Tertiary contacts between secondary structural elements give rise to the compact, active form of the ribozyme. Likewise, the ribozyme can adopt extended, non-active configurations by removal of these tertiary contacts. This conformational change is analogous to the unfolding of proteins. In this thesis, we are interested in the free energy difference between the active and non-active forms, i.e. the stability of the tertiary contacts.

As in the case of proteins, unfolding thermodynamics provide insight into the energetic interactions responsible for the structural stability of ribozymes. However, thermal and chemical denaturation studies have shown that in contrast to proteins, the folding pathways of ribozymes are not simple two-state transitions. Instead, the tertiary structure unfolding (the removal of tertiary contacts) of ribozymes often overlap with secondary structure melting (the dissociation of double-stranded regions). Selective extraction of the tertiary structure stability can therefore be diffcult [70]. This has been the case for hairpin ribozyme derived from the tobacco ringspot nepovirus (TRSV)[1].

[1]The genus of nepoviruses, or nematode-transmitted polyhedral viruses, belongs to the family Comoviridae. Visible symptoms include ringspots on leaves, stunted growth, necrosis, and death [1].

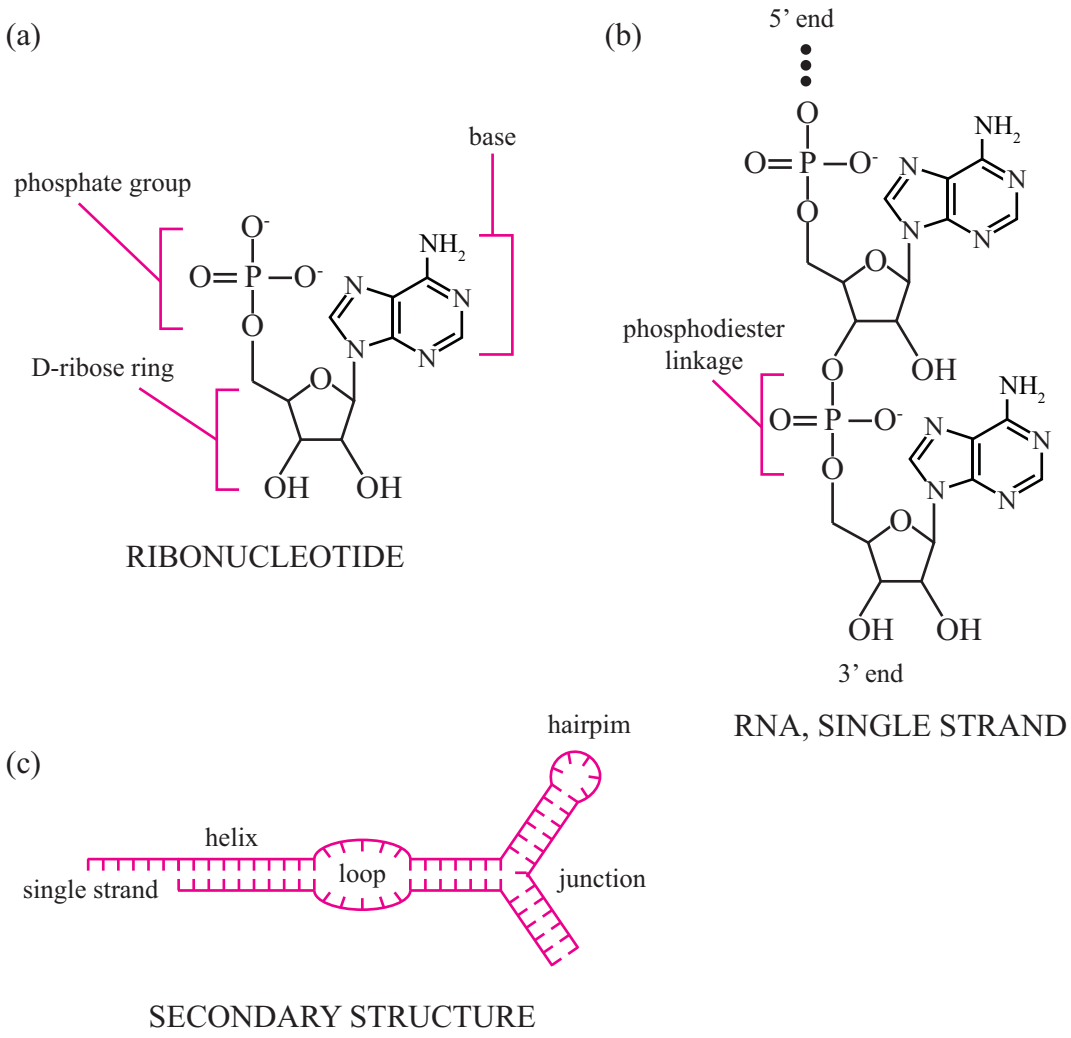

Figure 5.1: Structure of RNA. (a) The ribonucleotide is the building block of RNA. It consists of a D-ribose ring, a phosphate group, and a base (adenine shown here). Bases include adenine (A), guanine (G), cytosine (C), and uracil (U). (b) A single strand of RNA consists of ribonucleotides in phosphodiester linkages. Like a protein molecule, a single RNA strand has a distinct polarity: it has a 3' and 5' end. (c) The secondary structure of RNA is determined by the base interactions (bases are illustrated as short lines). Double stranded regions where bases in different strands or different regions of a single strand are paired by hydrogen bonding are helices. Double stranded regions that do not base pair are loops. A single strand can fold upon itself by forming a hairpin. Double stranded regions can branch at junctions. In a canonical Watson-Crick pairing, A pairs with U, and G pairs with C, but non-canonical pairs can occur as well.

Selective extraction of tertiary structure stability of hairpin ribozyme has been attempted by varying the solvent conditions [70]. Changing the counter ion content of the solvent can to a certain extent shift the secondary structure melting and tertiary structure unfolding transitions with respect to one another. In particular, lowering the magnesium concentration shifts the tertiary structure transition to lower temperatures than secondary structure melting. However, even at a low magnesium concentration of 1 mM where the tertiary structure of hairpin ribozyme was significantly destabilized, the two transitions were shown to overlap [70] (Fig. 5.2). To deconvolve the two transitions under these transitions, Klostermeier, *et al.* required two probes: FRET (Fluorescence Resonance Energy Transfer) to monitor the tertiary structure and UV absorption spectroscopy to monitor the secondary structure. Due to to complex behavior of hairpin ribozymes, thermodynamic studies remain limited and difficult to interpret.

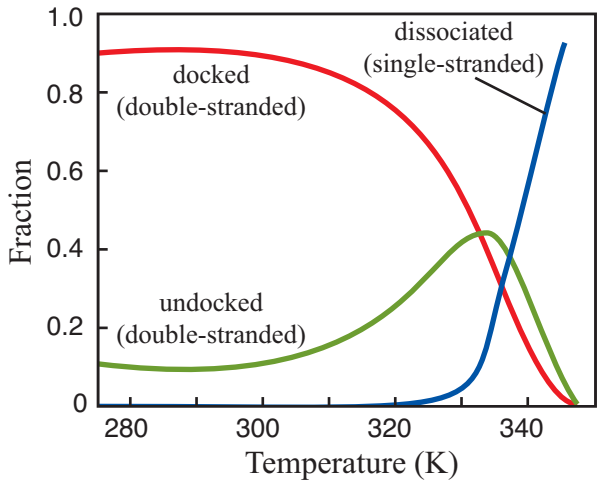

Figure 5.2: Tertiary structure unfolding (undocking) and secondary structure melting (dissociation) transitions as a function of temperature for a 4-way helical junction construct of hairpin ribozyme (adapted from Klostermeier, *et al.* [70]). The undocking (loss of tertiary contacts) and dissociation (loss of secondary structure) transitions overlap.

In this study, hydrostatic pressure was investigated as a method for selective measurement of the tertiary structure stability of a hinged hairpin ribozyme construct derived from TRSV. Although very few studies of nucleic acids under pressure exist in the current literature, we hypothesized that pressure is a unique variable to investigate. According to the phase diagram of DNA helix-coil transitions (secondary structure melting of DNA helices) produced by Dubins, *et al.*, pressure has a very different effect on secondary structure than temperature [30, 84]. While the DNA helix is only stable within a closed temperature range, Dubins, *et al.* demonstrated that the effects of pressure could be destabilizing, stabilizing, or none depending on the thermal stability of the helix. For helices with secondary structure melting temperatures of approximately 50°C and above, pressure had no effect or a stabilizing effect. The melting temperature of even a very unstable hairpin ribozyme mutant is very high; Klostermeier, *et al.* reported values of 48°C and above for a series of mutants [70]. We therefore speculated that the secondary structure of hairpin ribozyme would remain stable at high pressure. It was also recently shown that the cleavage activity of hairpin ribozyme was significantly reduced with the application of pressures up to 200 MPa [137, 55]. This reduction in activity was attributed to pressure-induced tertiary undocking. However, this hypothesis was inferred from cleavage assays; no structural evidence was provided. In order to understand the effect of pressure on the conformation of hairpin ribozyme, we studied two mutants labeled with 2-aminopurine (2AP, Fig. 3.5) using high-pressure fluorescence spectroscopy.

5.1.1 The Hairpin Ribozyme

The hairpin ribozyme is a catalytic RNA motif found in the satellite RNAs of plant viruses. The hairpin ribozyme is considered an RNA motif, as it is a region contained

within a longer RNA strand that acts catalytically *in cis*, i.e. intramolecularly, when it obtains a characteristic tertiary fold. As is the case with proteins, because of the tertiary fold, the catalytic region of RNA may be non-contiguous in sequence.

The first hairpin ribozyme to be identified was found in the negative-polarity (-) strand, running 3' to 5', of the 359-nucleotide satellite RNA associated with the tobacco ringspot nepovirus (TRSV). Satellite viruses and RNAs are often associated with plant RNA viruses. While the plant virus does not require the presence of satellite RNAs, the satellites are dependent upon co-infection with the plant virus for replication. Satellite viruses are those that encode their own coat protein, while satellite RNAs rely on the plant virus for encapsidation and replication. Infection with satellites modulates the symptoms induced by the plant virus, ranging from amelioration to severe exacerbation [114]. Co-infection of TRSV with the satellite RNA (sTRSV) leads to the reduction in TRSV yield and milder symptoms of TRSV infection [20].

During rolling-circle replication of the satellite RNA (sTRSV), linear multimeric (-) strands are synthesized using the pathogenic circular form of the (+) strand as a template, and vice versa [133]. Both (+) and (-) strands of sTRSV incorporate a catalytic RNA motif that when folded, cleaves the multimeric strands into monomers. For sTRSV, the catalytic RNA motif in the (-) strand is the hairpin ribozyme, while that in the (+) strand is the hammerhead ribozyme. The two ribozymes perform the same reaction, i.e. site-specific phosphodiester bond cleavage that forms 5'-hydroxyl and 2',3'-cyclic phosphate termini (Fig. 5.3) via different strategies. It is interesting to note that the same reaction is also performed by the protein, ribonuclease A, although the hairpin does not perform the second cyclic-phospate hydrolysis [40]. The cleavage reaction of the hairpin ribozyme is also highly reversible [53, 54]. The reverse reaction, ligation, converts the cleaved monomeric strands into circular forms.

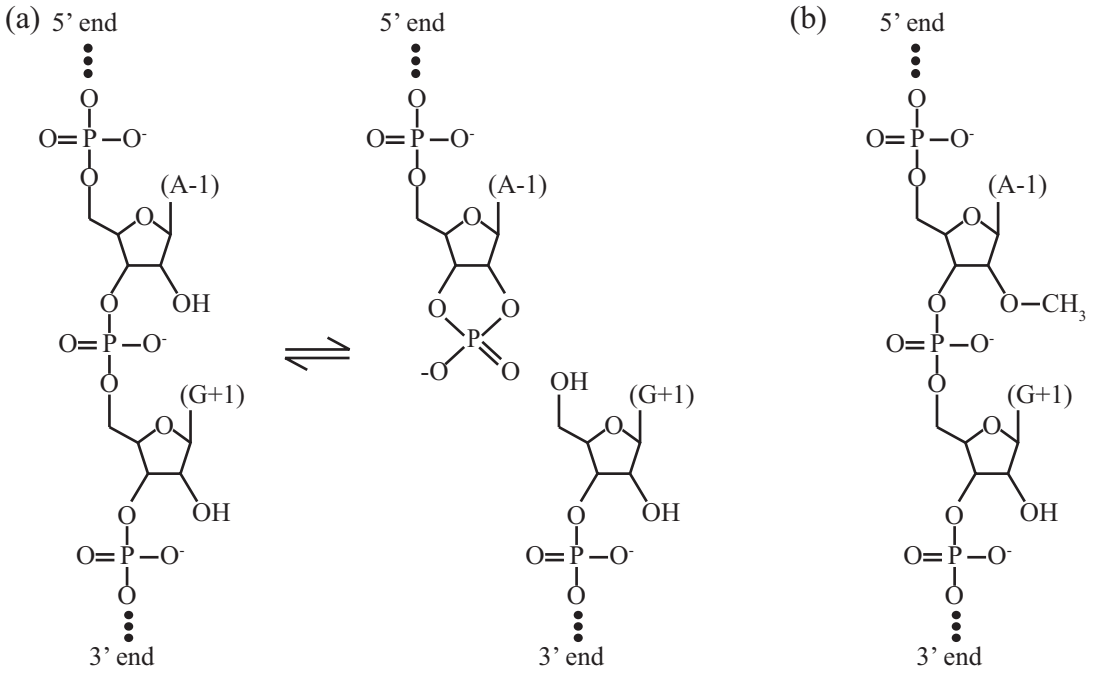

Figure 5.3: (a) The reaction catalyzed by hairpin ribozyme at a specific phosphodiester bond. Cleavage is the forward reaction (left to right) and ligation is the reverse. (b) Cleavage is prevented by a 2'O-methyl group replacement in the A-1 ribonucleotide.

In vivo, the hairpin ribozyme is a small region in the (-) sTRSV strand consisting of two helix-loop-helix domains that are part of a 4-way helical junction (Fig. 5.4 (a)). Only a small fraction of the sTRSV sequence and the preservation of two helix-loop-helix domains, containing loops A and B, are essential for the formation of an active hairpin ribozyme [14, 20]. Truncation of the (-) sTRSV strand to produce smaller constructs is therefore possible for use in *in vitro* studies. The hairpin ribozyme can also be studied *in trans*, i.e. reconstituted as a functional structure from separate strands, enabling the use of external strands as substrates and substrate analogs. These so-called minimal constructs may preserve the naturally occurring 4-way helical junction (4WJ) or be further minimized as 3-way or 2-way helical junctions (3WJ, 2WJ) and *trans*-acting hinged structures [83] (Fig. 5.4 (b)-(c)).

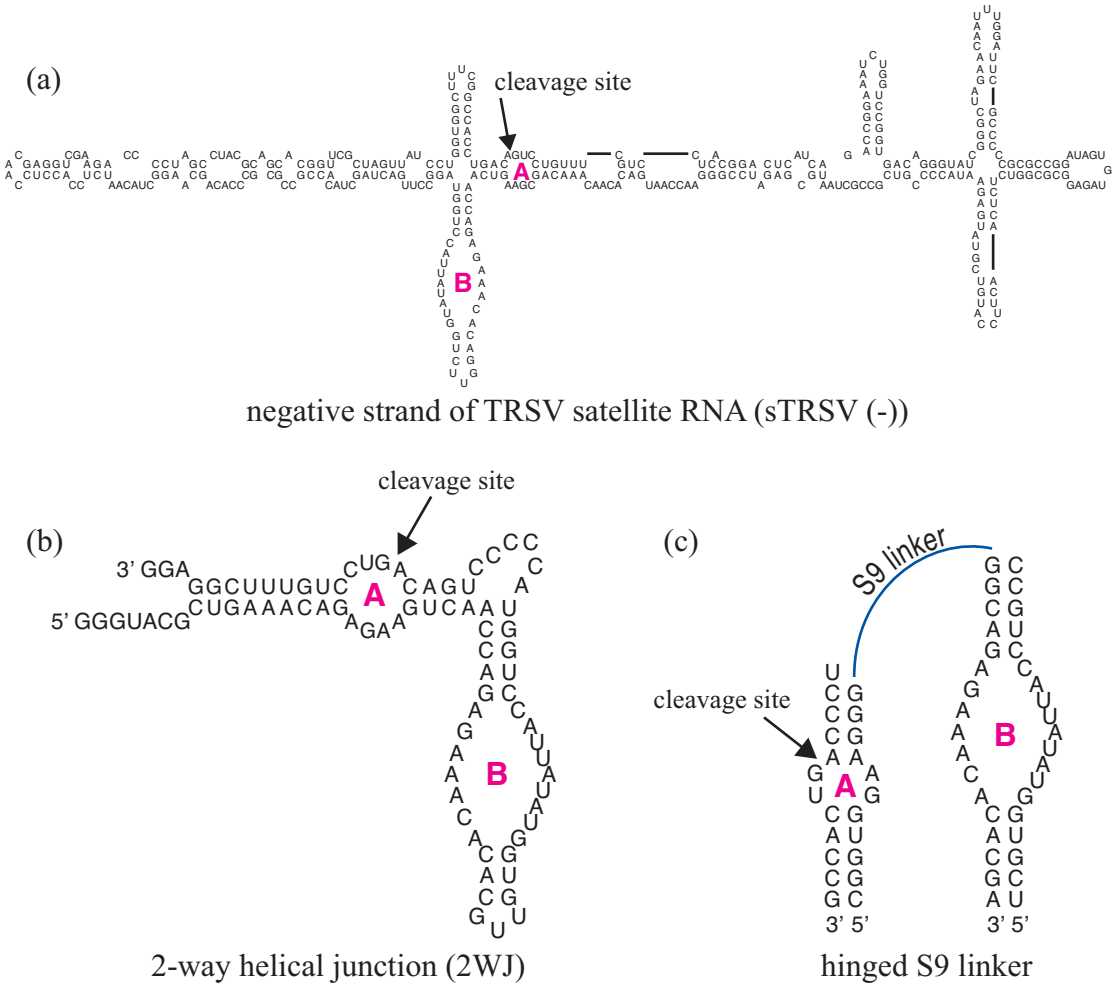

Figure 5.4: The secondary structures of (a) the negative-polarity strand of the satellite RNA associated with the tobacco ringspot virus (hairpin ribozyme motif is colored), which features a 4-way helical junction, (b) a minimal construct with a 2-way helical junction [137], and (c) a hinged construct with a nine-atom triethylene glycol linker (S9) [83]. The active conformation where loop A and B are docked is promoted by the addition of Mg^{2+}. The cleavage site is indicated by an arrow.

The catalytically active docked state (similar to the folded state of proteins) is formed by the two helix-loop-helix domains coming together like a hairpin (Fig. 5.4, 5.5) to interact in a ribose zipper: a tertiary structural motif in ribozymes where there are consecutive hydrogen bonds between inter- or intra-chain ribose 2'-hydroxyl groups. The active site of the ribozyme is formed between the docked loops (A and B). In solution conditions where the secondary structures of the ribozyme are intact, the docked and undocked fractions exist in equilibrium [152]. The tertiary structure stability is the difference in free energy, G, between these two states:

$$\Delta G = G_{undocked} - G_{docked} \tag{5.1}$$

The docked state is favored by the addition of Mg^{2+}, although divalent metal ions are not required for catalysis [51, 90].

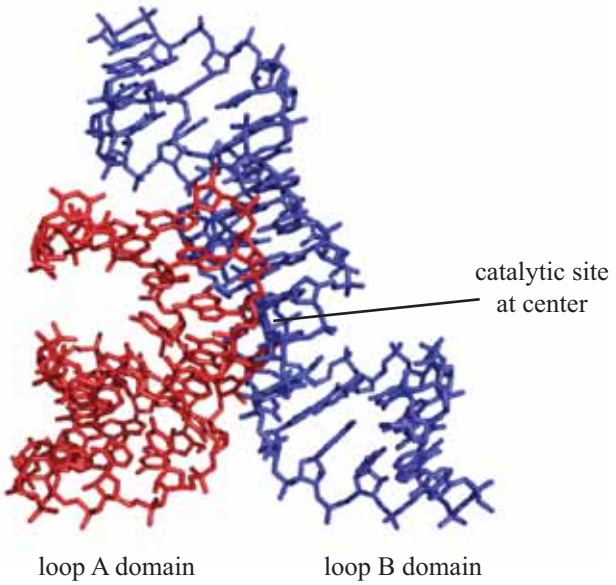

Figure 5.5: The three-dimensional structure of the docked hinged hairpin ribozyme (PDB 2NPY, secondary structure in Fig. 5.4 (c)). Loops A and B of the two helix-loop-helix domains form the catalytic site.

The hinged hairpin ribozyme construct used in this thesis consists of three RNA strands (Fig. 5.6): (i) a 13-mer[2] substrate or substrate analog, (ii) a 29-mer with a nine-atom triethylene glycol linker (S9) at A14 [83], and (iii) a 19-mer with a gain-of-function U39C[3] mutation that prevents conformational heterogeneity in the S-turn [2]. The S9 linked 29-mer associates with the 13-mer on one end and the 19-mer on the other to form a hairpin with two helix-loop-helix domains. Docking was initiated by the addition of Mg^{2+}. Upon docking, the ribozyme performs cleavage on the phosphodiester bond between the G+1[4] guanosine and A-1 adenosine in loop A. In order to measure the free energy change of undocking, cleavage must be prevented. This is possible by the use of a substrate analog where the 2'-hydroxyl nucleophile on A-1 is replaced by a 2'O-methyl group (Fig. 5.3 (b)).

Two 2AP mutants were investigated with high-pressure fluorescence spectroscopy; 2AP is a fluorescent base analog that when incorporated in RNA can report local conformational changes [153] (Section 3.1.4). In one mutant, 2AP was substituted for U+2 in loop A (U+2→2AP[5]) and in the other, 2AP was substituted for A38 in loop B (A38→2AP) (Fig. 5.6).

[2]The term, "N-mer" refers to an RNA strand with N ribonucleotides.

[3]The notation "U39C" denotes a substitution of uracil at position 39 by a cytosine

[4]Note that by convention, the nucleotides on the substrate strand are numbered relative to the bond that is cleaved; A-1 refers to the adenosine adjacent to the cleavage site on the 5' side, and G+1 refers to the guanosine adjacent to the cleavage site on the 3' side.

[5]The notation "X→2AP" denotes 2AP substitution at nucleotide X.

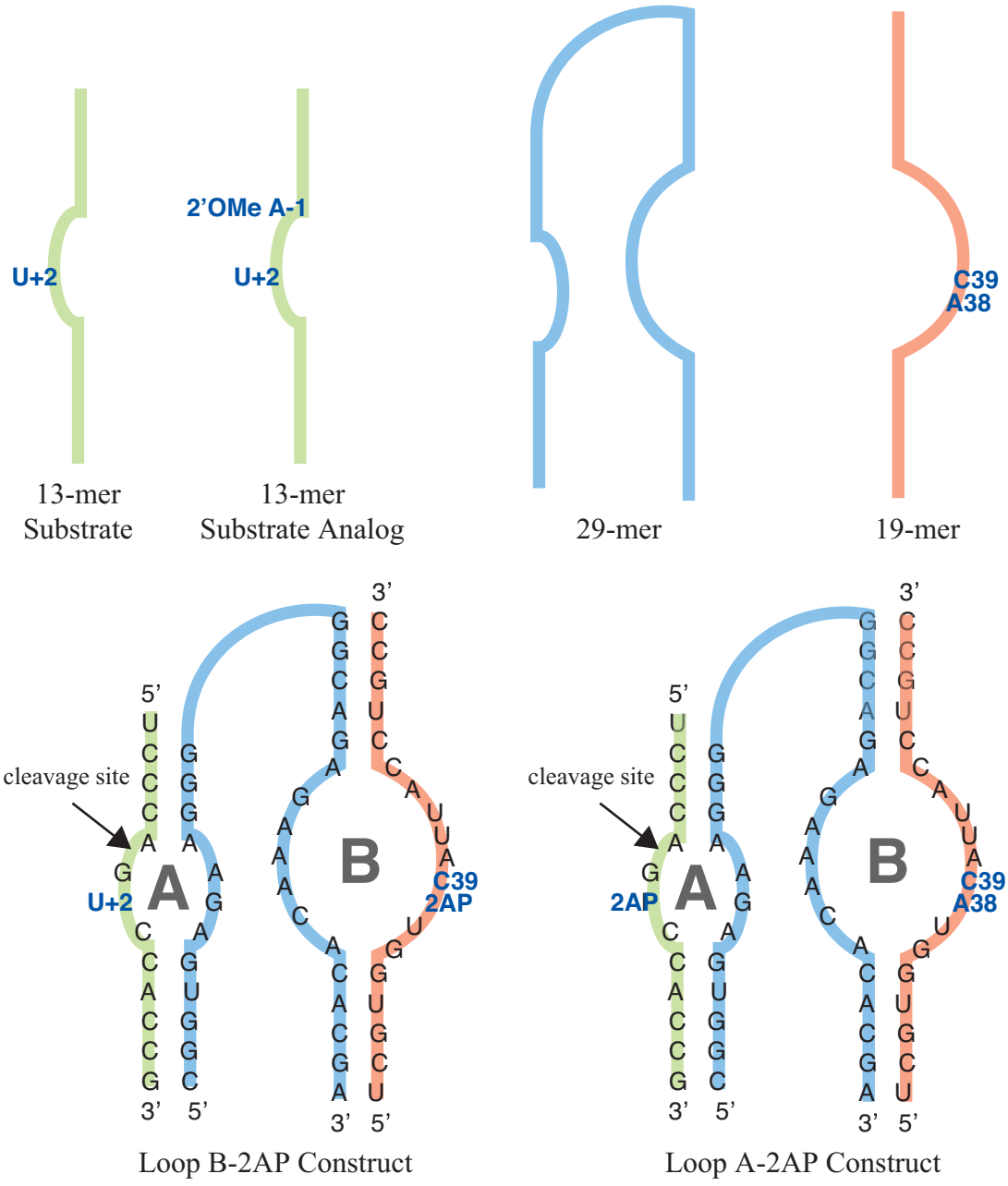

Figure 5.6: Illustrations of samples. The hinged hairpin ribozyme consists of three strands: 13-mer substrate or substrate analog, 29-mer, and 19-mer with a U39C mutation. The Loop B-2AP construct contained the substitution A38→2AP in loop B. The Loop A-2AP construct contained the substitution U+2→2AP in loop A. The cleavage site is indicated by an arrow. Note that the substrate analog is cleavage-protected by a 2'O-methyl substitution at A-1.

5.2 High Pressure Fluorescence Spectroscopy

The fluorescence intensity of 2AP is highly sensitive to the quenching caused by base stacking, i.e. the stacking of two adjacent bases in an RNA strand [153]. Therefore, when incorporated into an RNA strand, 2AP is sensitive to local structural changes that affect base stacking interactions. Steady-state fluorescence spectroscopy was used to investigate the effects of pressure on the structure of two 2AP mutants of hairpin ribozyme.

5.2.1 Methods

2AP was substituted in two different locations of the hinged hairpin ribozyme construct (Fig. 5.6). The "loop B-2AP construct" refers to samples with 2AP incorporated in loop B at the A38 site on the 19-mer strand. The "loop A-2AP construct" incorporated 2AP in loop A at the U+2 site on the 13-mer substrate or substrate analog.

The hairpin ribozyme constructs were prepared by Jolanta Krucinska (Wedekind lab, Univ. of Rochester, NY). The RNA strands were obtained from Dharmacon Inc. (Lafayette, CO, USA). Subsequently, the strands were deprotected in 2'-deprotection buffer (0.1 M Acetic acid, adjusted to pH 3.8 with TEMED), purified with HPLC, and desalted on a C18 or G-50 Sephadex column according to protocols described in [155]. After desalting, the RNA samples were lyophilized. The lyophilized RNAs were then dissolved in 10 mM Na Cacodylate buffer pH 6.0 to a final concentration of 1 mM. Samples with multiple strands were prepared by incubating 30 μL of each strand (1 mM concentration) together for 30 min and diluted to 5 - 6 μM in 50 mM Tris pH 7.5 buffer.

For each construct, docking was promoted by the presence of 12 mM Mg^{2+} in a

1:1:1 mixture of the three strands. The Mg^{2+} concentration was adjusted slowly by introducing 0.25 - 0.5 M $MgCl_2$ stock solution into the sample one drop at a time along with frequent vortexing. The docked form of the loop B-2AP construct was equilibrated at room temperature for > 24 hours prior to experiments. The docked form of the loop A-2AP construct was prepared by the addition of $MgCl_2$ 10 min prior to the first fluorescence measurement. In order to study the effect of pressure on the undocked form of hairpin ribozyme, two types of control experiments where docking was prevented were performed for each construct. In the first type, the 1:1:1 mixture of the three strands was examined in the absence of $MgCl_2$. In the second type of control experiment, the construct was examined without the substrate or substrate analog.

The effects of temperature and pressure on free 2AP (A3509-100MG, Sigma) were also investigated as a control. As 2AP is not easily soluble in aqueous solutions, 6 μM 2AP solution was prepared by dissolving 2AP in 50 mM Tris pH 7.5 buffer at 60 °C under sonication.

The samples were excited at 312 nm, and the emission was collected at 90° to the excitation beam in a scanning fluorimeter (described in Section 3.3.2). The peak fluorescence intensity of 2AP was determined from a quadratic fit to the 355-371 nm region of the emission spectrum. Temperature variation experiments at ambient pressure were performed in a standard 10 mm path length quartz cuvette (Two-Cuvette Sample Compartment; ISS, Champaign, IL, USA), while pressure variation experiments at a fixed temperature were performed in a high-pressure fluorescence cell with an internal quartz cell (described in Section 3.2). Pressure was generated with a motor-controlled liquid pump (Cat. No. 37-6.75-60; High Pressure Equipment Co., Erie, PA, USA) using protocols described in Section 3.2. The temperature was controlled by a water bath (Neslab, Thermo Scientific, Waltham, MA, USA). Samples were equilibrated at each pressure

or temperature for 3 to 90 minutes. Data were analyzed with MATLAB (The MathWorks, Natick, MA, USA). The collected emission spectra were background-subtracted and intensity corrected.

Intensity corrections were performed with calibration data collected with 4 nm excitation and emission bandwidths by ISS (Champaign, IL, USA). For each construct, the spectra were normalized by the peak intensity of the Mg^{2+}-free control sample at ambient conditions and by sample concentration; sample dilution due to the addition of stock $MgCl_2$ solution was accounted for. Note that ambient conditions refer to 25 °C (thermostated by the water bath), 1 atm.

5.2.2 Control Experiments

The temperature and pressure effects on free 2AP were first investigated. The peak intensity of free 2AP was sensitive to temperature, showing an approximately 30% reduction in peak intensity over a temperature range of 20 to 70 °C, in agreement with the observations by Ward, *et al.* [153] (Fig. 5.7 (a)). By comparison, the peak intensity of free 2AP was insensitive to pressure (Fig. 5.7 (b)). While the primary peak remained constant with pressure, the secondary peak, or shoulder, increased slightly. The relative heights of the two peaks did not change with temperature variation. The secondary peak may be due to wavelength-dependent emission detection caused by beam path optics that was not fully corrected by the calibration data used in our analysis. Nonetheless, a change in spectral shape with pressure is significant. The effect of $MgCl_2$ concentration on free 2AP fluorescence was not measured.

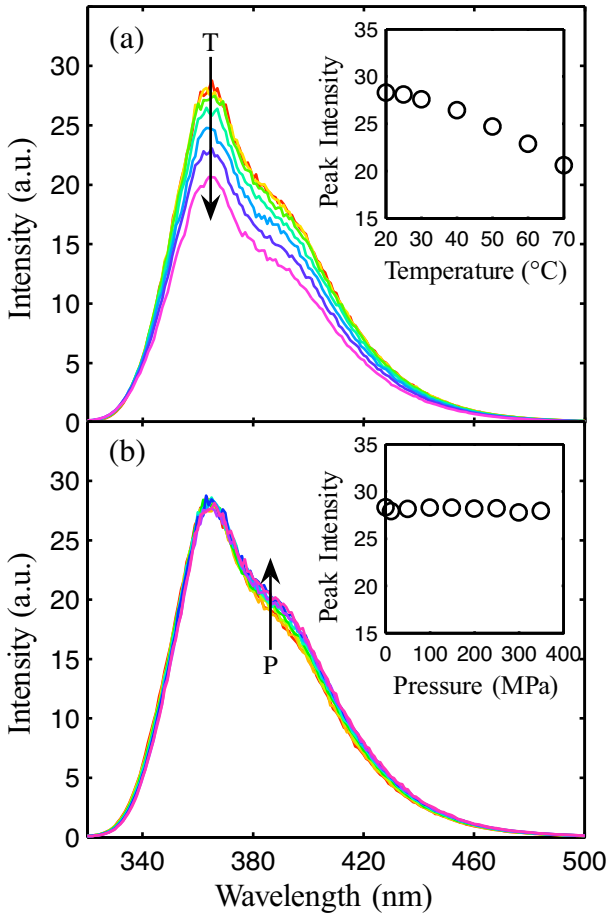

Figure 5.7: Pressure and thermal effects on free 2-aminopurine (2AP) in 50 mM Tris pH 7.5. (a) Thermal quenching causes the fluorescence intensity to decrease at ambient pressure (arrow indicates increasing temperature). (b) The peak intensity is insensitive to pressure at 25 °C, but the secondary peak (shoulder) increases slightly (arrow indicates increasing pressure).

In the next set of controls, the 2AP-incorporated strand (Fig. 5.6: U+2→2AP 13-mer or A38→2AP 19-mer) was studied in isolation from the other strands. The peak intensity of 2AP in a strand was roughly 3.6% of the peak intensity of free 2AP at 0 mM $MgCl_2$ under ambient conditions. Addition of $MgCl_2$ to the isolated 2AP-incorporated strand caused a decrease in peak intensity (Fig. 5.8 (a)).

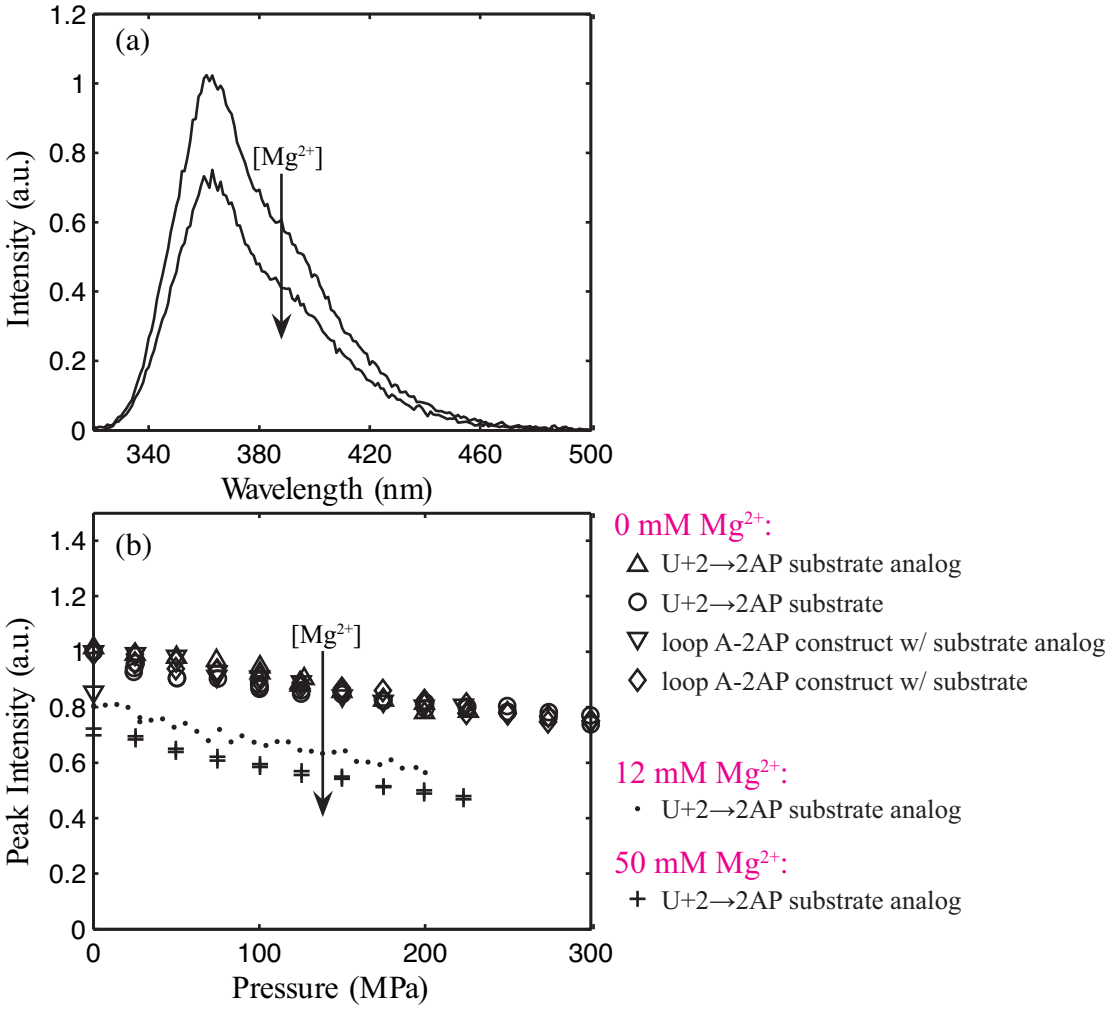

Figure 5.8: Pressure effects on 2AP-incorporated control samples (docking cannot occur). (a) The fluorescence spectra of the U+2→2AP substrate analog at 0 mM $MgCl_2$ (top) and 50 mM $MgCl_2$ (bottom). (b) All control samples at 0 mM $MgCl_2$ showed similar pressure dependence (upper band of data points). The pressure dependence of the U+2→2AP substrate analog at 12 mM $MgCl_2$ (dot) and 50 mM $MgCl_2$ (plus) is also shown.

Unlike free 2AP, the fluorescence intensity from 2AP-labeled strands decreases approximately linearly with pressure (Fig. 5.8 (b)). This reduction in intensity is likely to be due to pressure-induced compression of the hairpin ribozyme that brings the 2AP in closer proximity to neighboring bases. As a comparison, the effect of temperature on an isolated 2AP-incorporated strand in the presence of $MgCl_2$ is shown in Fig. 5.9.

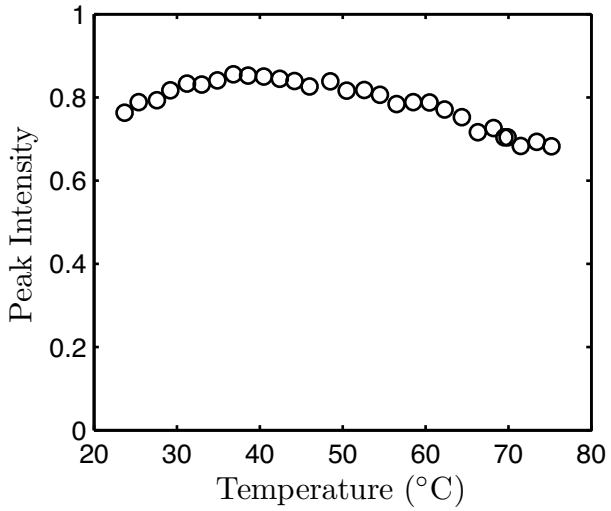

Figure 5.9: Thermal effects on a 2AP-incorporated control sample. Shown is the peak intensity of the U+2→2AP substrate analog at 12 mM $MgCl_2$, ambient pressure.

Under Mg^{2+}-free conditions, the peak intensities and their pressure dependence of the complete three-strand mixture and that of isolated 2AP-incoporated strands were similar (Fig. 5.8 (b)). As a change in the peak 2AP fluorescence intensity is expected if strand association occurs, the results suggest that the three strands in the complete mixture are dissociated in the absence of Mg^{2+}.

5.2.3 Pressure Effects on the Loop B-2AP Construct

The loop B-2AP construct contained the substitution, A38→2AP, in loop B (Fig. 5.6). Docking of the loop B-2AP construct with the substrate analog was induced by increasing the $MgCl_2$ concentration to 12 mM. Docking was accompanied by an approximate 2.4-fold increase in 2AP fluorescence under ambient conditions, indicating the occurrence of a structural change in the construct (Fig. 5.10 (a)). These results suggest that 2AP at the A38 site is sensitive to local structural change caused by $MgCl_2$. However, the addition of $MgCl_2$ to the same construct lacking the 13-mer substrate analog yielded a similar response at ambient pressure (Fig. 5.10 (a)). The response of 2AP fluorescence to pressure in this construct was also similar with and without the substrate analog (Fig. 5.10 (b)). As docking requires the presence of the substrate or substrate analog, the Mg^{2+}-induced structural change detected by A38→2AP cannot be attributed to docking.

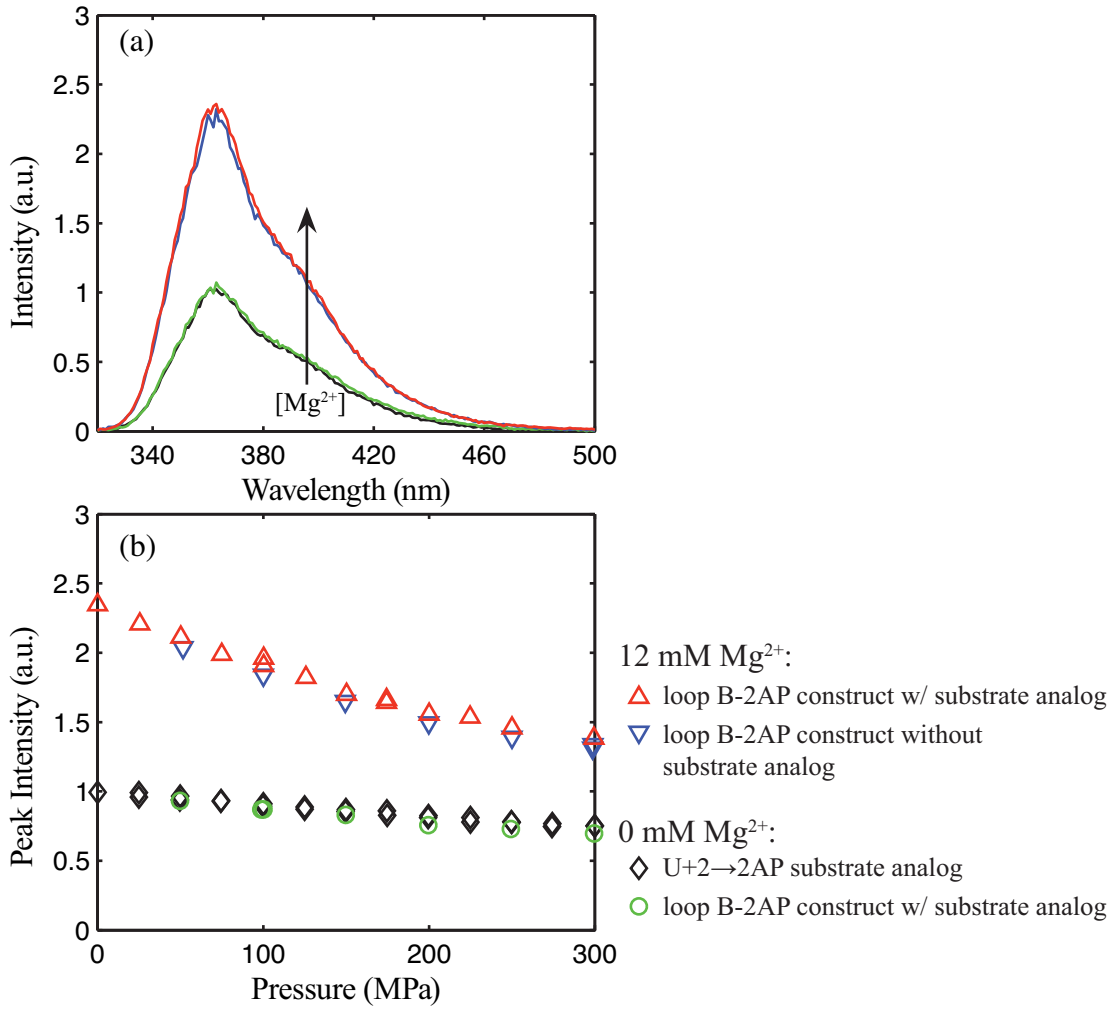

Figure 5.10: Pressure effects on the loop B-2AP construct. (a) Fluorescence spectra under ambient conditions of the U+2→2AP substrate (black) and the loop B-2AP construct with a substrate analog at 0 mM $MgCl_2$ (green) and the complete loop B-2AP construct with (red) and without the substrate analog (blue) at 12 mM $MgCl_2$. (b) The pressure dependence of the peak fluorescence intensity.

5.2.4 Pressure Effects on the Loop A-2AP Construct

The loop A-2AP construct contained the substitution, U+2→2AP, in loop A (Fig. 5.6). Like the loop B-2AP construct, docking of the loop A-2AP construct with a U+2→2AP substrate analog was induced by increasing the $MgCl_2$ concentration to 12 mM. Docking was accompanied by an approximately 1.3-fold increase in peak 2AP fluorescence intensity compared with the Mg^{2+}-free control samples under ambient conditions (Fig. 5.11 (a)). This was consistent with previous reports of the sensitivity of U+2→2AP to docking [152]. This sample showed no unusual pressure-dependence up to 200 MPa (Fig. 5.11 (b)), suggesting that hairpin ribozyme remains docked in this pressure range.

Surprisingly, an even larger fluorescence increase of approximately 1.7-fold compared with the Mg^{2+}-free control samples was observed for the same construct docked with the U+2→2AP substrate, i.e. the non-cleavage-protected 13-mer (Fig. 5.11 (a)). This sample showed a strong pressure-dependent behavior below 100 MPa (Fig. 5.11 (b)). Increasing the pressure 0.1 to 100 MPa reduced the fluorescent intensity of this sample to the levels of the loop A-2AP construct docked with the cleavage-protected substrate analog. This pressure effect was reversible.

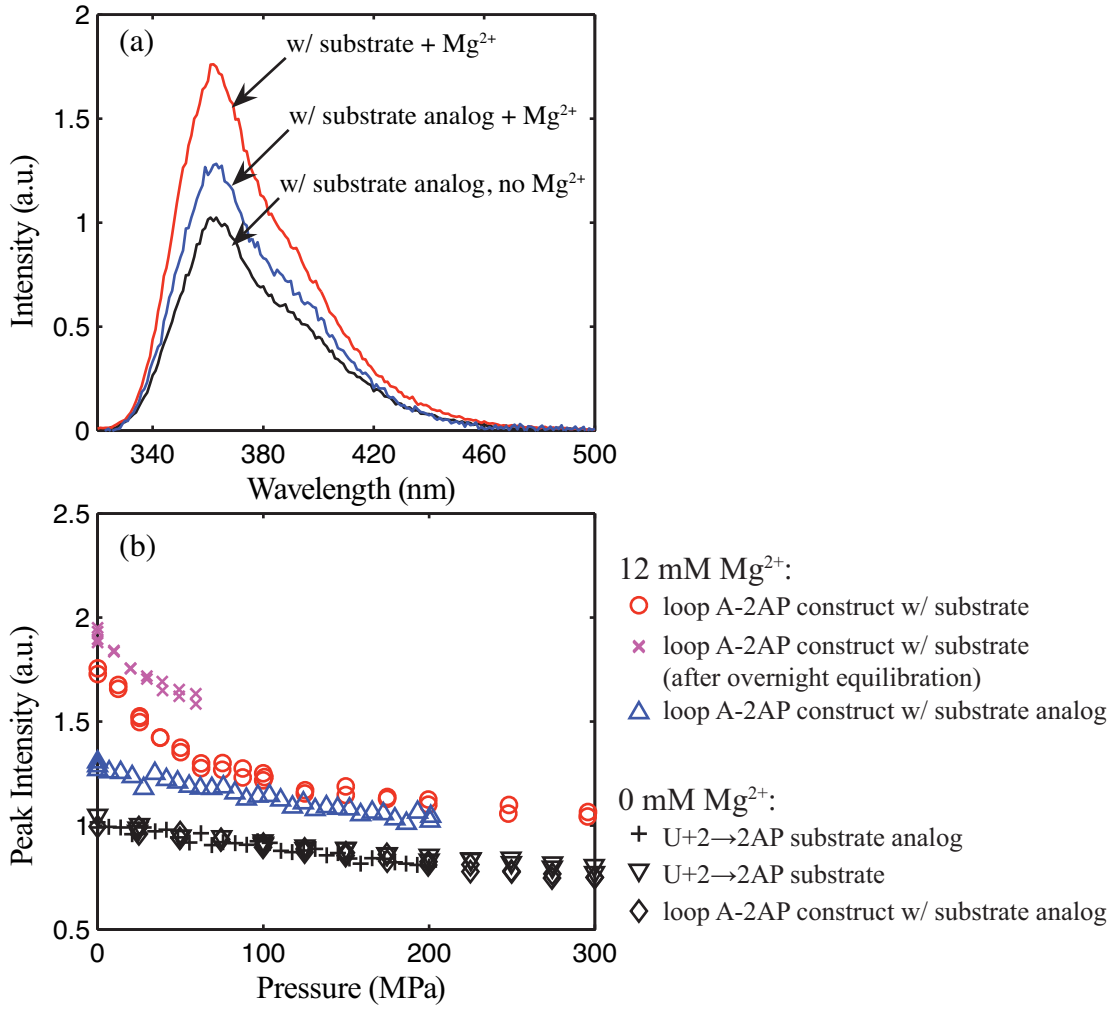

Figure 5.11: Pressure effects on the loop A-2AP construct. (a) Fluorescence spectra under ambient conditions of the loop A-2AP construct with: U+2→2AP substrate analog at 0 mM $MgCl_2$ (black), U+2→2AP substrate analog at 12 mM $MgCl_2$ (blue), and U+2→2AP substrate at 12 mM $MgCl_2$ (red). (b) The pressure dependence of the peak fluorescence intensity.

5.3 Discussion

5.3.1 2AP Fluorescence Quenching Due to Compression of Bases

Although the peak fluorescence intensity of 6 μM free 2AP in solution was pressure-independent, incorporation of 2AP into an RNA strand resulted in a pressure-dependent reduction in its intensity. This reduction in fluorescence intensity is explained by increased quenching due to compressed base-base distances. The structure of an A-form DNA helix at high pressure by Girard *et al.* [45] shows that both the base-stacking and base-pairing distances decrease under compression. A similar pressure-induced compression can be expected for the hairpin ribozyme constructs presented here. The linear pressure-dependence of the Mg^{2+}-free control samples (Fig. 5.8 (b)) was therefore used as a reference for this compression effect.

5.3.2 Single Strand Coil Size Dependence on Mg^{2+} Concentration

Increasing the ionic strength of solutions containing isolated 2AP-labeled RNA strands by addition of $MgCl_2$ caused a decrease in 2AP fluorescence intensity (Fig. 5.8 (b)). As RNA is highly negatively-charged, the presence of Mg^{2+} counter ions can be expected to increase the effective RNA chain flexibility or reduce its coil size [49], thus reducing base-base distances and increasing the quenching effects on 2AP. Similarly, increasing the temperature of an isolated 2AP-incorporated strand in the presence of $MgCl_2$ first caused a fluorescence increase, possibly as a result of thermal expansion of the coil size, followed by a decrease in fluorescence intensity due to thermal quenching (Fig. 5.9).

5.3.3 Secondary and Tertiary Structure Formation with Mg^{2+}

In the absence of Mg^{2+}, the similarity in fluorescence behavior of multiple strand mixtures of the constructs to that of the single 2AP-incorporated strand suggests that the strands act independently and are therefore dissociated (Fig. 5.8 (b)). A decrease in fluorescence intensity was observed when Mg^{2+} was added to a solution containing isolated 2AP-labeled strands. In contrast, a large fluorescence increase accompanied the addition of Mg^{2+} to multiple strand mixtures of both the loop B-2AP (Fig. 5.10 (a)) and the loop A-2AP (Fig. 5.11 (a)) constructs.

At 12 mM $MgCl_2$, docking of the ribozyme and its substrate (or substrate analog) was expected to occur for samples with all three strands [83]. The 2AP fluorescence intensity increase observed with the docking of the loop A-2AP construct can be attributed to a specific change in the local environment of U+2→2AP [151]. The crystal structure of the hinged construct docked with a substrate analog (PDB code 2NPY) shows that the G+1 base is pulled from loop A into the G-binding pocket of loop B and is consequently unstacked from the adjacent base at U+2 (Fig. 5.13) [83]. As the binding of G+1 in the G-binding pocket appears to be an important conformation for catalysis [116], we expect the same to occur for a U+2→2AP construct. Our results are consistent with a fluorescence increase due to the unstacking of 2AP at U+2 from G+1 caused by the docking of loops A and B.

The similar response of the loop B-2AP construct to Mg^{2+} with and without the substrate analog suggests that there is a structural change in the local environment of A38→2AP that cannot be attributed to docking. This is consistent with a recently solved structure of the loop B-2AP construct (PDB code 3BBI). Although this construct was able to dock, it did not form the proper conformation at the active site (Fig. 5.13) [82]. In particular, although 2AP is an adenine analog, at the A38 site, 2AP was sterically

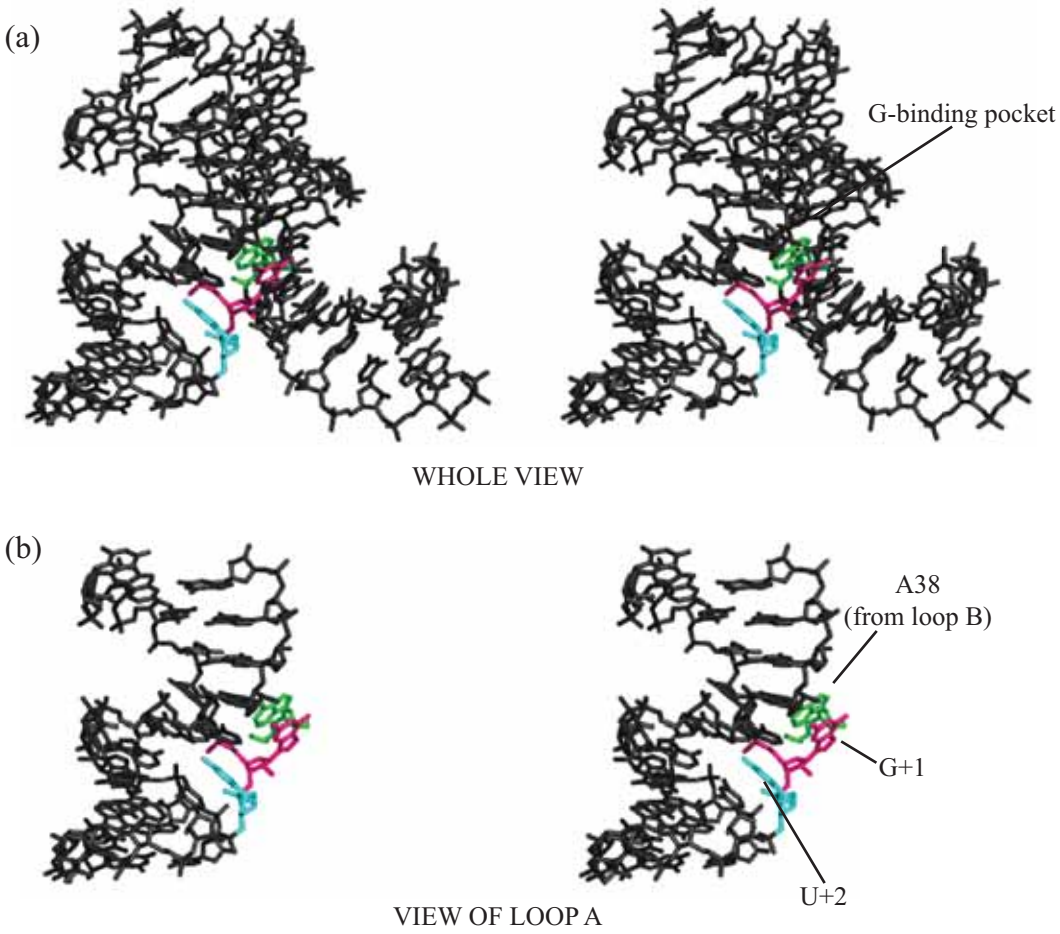

Figure 5.12: Stereo pairs of crystal structure of wild-type (no 2AP incorporation) construct (PDB code 2NPY). (a) Whole view of construct. (b) Cut-out view of loop A. G+1 is pulled into the G-binding pocket and stacks below A38 from loop B. U+2 is unstacked from G+1 as a result.

hindered from forming the native hydrogen bonds. The different positions of the hydrogen bonding NH_2 group on the bases (Fig. 3.5) prevent proper anchoring when 2AP is substituted at the A38 site. As a result, 2AP at the A38 site is unable to properly align the reactive phosphate (between G+1 and A-1).

We therefore speculate that the fluorescence increase seen with the addition of Mg^{2+} to the loop B-2AP construct is due to secondary structure formation. This is supported

by the solution NMR structure of the isolated loop B (the sample does not have the loop A region) solved in the presence of 50 mM NaCl [19]. The loop B strands are able to form a helix without docking, which requires both loops A and B. This is reasonable as strand association may be favored when the cation–modulated inter-chain charge repulsion becomes weaker than inter-chain hydrogen bonding. Crystal structures of substrate-less constructs have been grown, although they were not of sufficient diffraction quality (Joseph E. Wedekind, private communication). We note that the secondary structure of the isolated loop B solution structure displays dramatic differences compared with that seen in crystal structures of hairpin ribozyme constructs, leading to speculation that a large rearrangement of the secondary structure accompanies docking [116, 40]. According to these structures, the bases adjacent to A38 (at positions 37 and 39) becomes unstacked from the helix upon docking. In the docked conformation, these stacking interactions are replaced by A40 and G+1 from loop A (Fig. 5.13). This replacement of base stacking interactions may explain why the docked (with substrate analog) and undocked (no substrate analog) states could not be distinguished by 2AP fluorescence in the loop B-2AP construct.

The pressure-dependence of the 2AP fluorescence emitted by the loop A-2AP construct docked with a U+2→2AP substrate analog was similar to that of the Mg^{2+}-free controls (Fig. 5.11 (b)). This indicates that the U+2 site on loop A in the docked state has a similar local compressibility to that of single strands. By comparison, the loop B-2AP construct in the presence of $MgCl_2$ was highly sensitive to pressure. (Fig. 5.10 (b)). The intensity decrease with pressure was steeper than that of the Mg^{2+}-free controls. This may reflect the fact that the nucleotide base at position 39 (adjacent to A38) does not have a hydrogen bonding partner in either the docked or undocked states [19, 83].

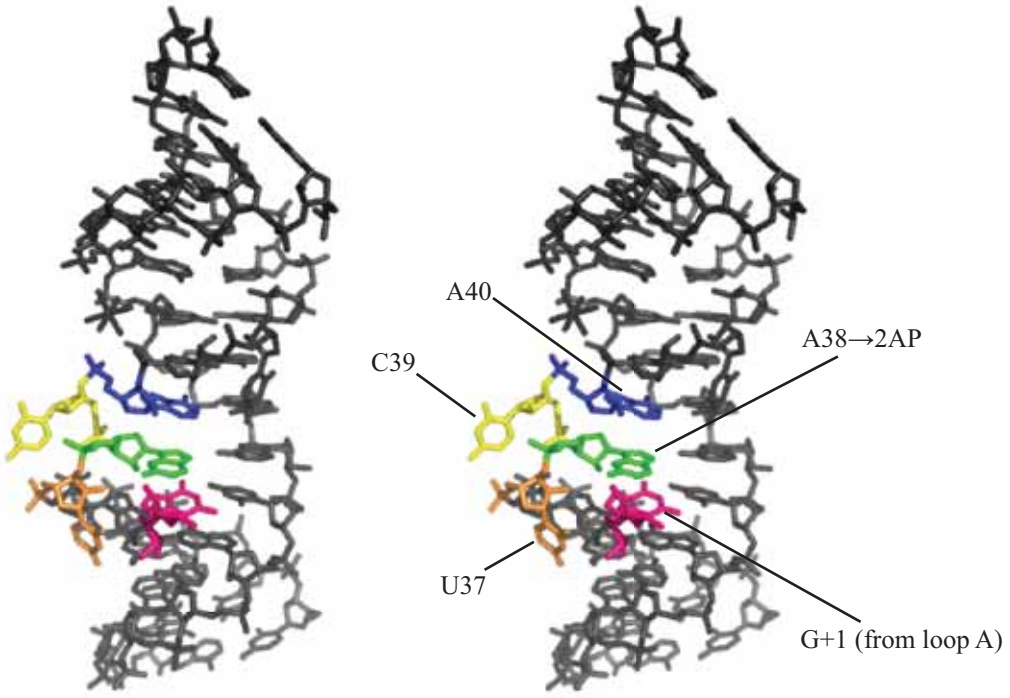

Figure 5.13: Stereo pair of crystal structure of loop B-2AP construct (PDB code 3BBI). Cut-out view of loop B. A38→2AP is unstacked from the adjacent bases, C39 and U37, and stacked over G+1 from loop A.

5.3.4 Pressure Effects on Tertiary Structure

Studies by Maurel and co-workers on a 2WJ hairpin riboyzme construct derived from TRSV (Fig. 5.4 (b)) demonstrated a large reduction in cleavage activity at pressures up to 200 MPa [55, 137]. According to these studies, a positive volume change of approximately 46 $Å^3$ is associated with the docking of loops A and B. As pressure favors a negative volume change, this conclusion suggests that the two loops must undock at high pressure. However, the loop A-2AP construct docked with the substrate analog (cleavage-protected 13-mer) showed no pressure dependence up to 200 MPa other than the compression effect also observed in the control samples (Fig. 5.11 (b)). This result suggests that the docked state remains stable in this pressure range.

We consider two possible reasons for the differing results. 2WJ constructs are generally very unstable compared with the a construct that preserves the 4-way helical junction found in nature. At 12 mM $MgCl_2$, where > 90% of 4WJ constructs are docked, only approximately 65% of 2WJ constructs are docked [151]. Unlike the 2WJ construct, the hinged S9 linker construct used in this thesis (Fig. 5.4 (c)) is a fairly stable construct. At this $MgCl_2$ concentration, roughly 80% of the hinged S9 linker constructs are docked [83], and therefore, the hinged construct used in this thesis is more stable than the 2WJ construct used by Maurel, *et al.* It is possible that the hinged S9 linker and 2WJ constructs do not undock within the same pressure range.

However, in the studies by Maurel and co-workers, it was inferred that undocking of the loops A and B was occurring based on the observed reduction of cleavage products [55, 137]. No direct evidence of structural change was provided. Therefore, it can not be ruled out that undocking did not occur. Undocking can only be favored under pressure if the undocked state is either smaller in volume to the docked state. We thus consider possible sources for negative volume changes in the hairpin ribozyme. As mentioned earlier, the docked state is stabilized by the tertiary contacts in a ribose zipper. As hydrogen bonds are generally thought to be stable under high pressure due to reduced bond lengths [92, 78], we do not expect a negative volume change associated with the dissociation of the ribose zipper stabilizing the docking interface.

In the case of proteins, the hydration of internal cavities (solvent-excluded packing defects) and electrostriction around exposed charged groups are known to contribute significantly to the negative volume change associated with pressure denaturation [115, 44, 4]. The molecular surface tracing program MSMS [119] was used with a 1.2 Å radius rolling probe to identify cavities in the crystal structures of the wild-type (no 2AP incorporation) construct (PDB accession code 2NPY) and the loop B-2AP

construct (3BBI). A large buried cavity was detected in the loop B-2AP construct. The same cavity exists in the structure of the wild-type, but the walls intersect with the external surface of the ribozyme. A higher resolution structure of a junction-less hairpin ribozyme construct (PDB code 2OUE) shows that this cavity is occupied by 5 internal waters: W45, W55, W54, W52, and W86 [118]. As these waters are hydrogen-bonded with the RNA in the active site, they may be considered essential for catalysis and therefore conserved in docked forms of all hairpin ribozyme constructs. This is a reasonable assumption as the cavity is shaped to accommodate the solvent-binding sites of these waters and this shape is conserved in the three structures discussed here (2NPY, 3BBI, 2OUE). The 5 waters in the 2OUE structure reduce the effective cavity size from roughly 144 to 13 $Å^3$. Assuming the cavity is buried in the solution structure of hairpin ribozyme, we can consider it nearly fully occupied and therefore not a major source of a negative volume change by undocking. As RNA is highly charged, the crystal structures were closely examined for solvent-inaccessible phosphate groups. Exposure of a buried charged group leads to an increase in density of the hydration waters and consequently results in a negative volume change. However, no solvent-inaccessible phosphate groups were observed in the crystal structure (2NPY) that represents the docked state. Thus, electrostriction is also not expected to promote pressure-inducing undocking.

5.3.5 Pressure Effects on Cleavage Activity

The 2AP fluorescence intensity from the loop A-2AP construct docked with a cleavable substrate showed strong reversible pressure dependence. In contrast, the loop A-2AP construct docked with the non-cleavable substrate analog showed no pressure dependence.

The 2AP fluorescence intensity at ambient pressure was greater for the substrate than for the substrate analog. We attribute this difference in fluorescence intensity to cleavage of the substrate. As cleavage is rapid at ambient pressure [83], fluorescence measurements were made within 10 minutes of adding $MgCl_2$. Nonetheless, we expect roughly 80% of the non-protected substrates to be cleaved at ambient pressure within this time. The enhanced increase in fluorescence may reflect cleavage due to the proximity of U+2→2AP to the cleavage site [66]. Rapidly raising the pressure to 100 MPa reversibly reduced the fluorescence intensity of the loop A-2AP construct docked with the substrate to the intensity level of the same construct docked with the cleavage-protected substrate analog. After overnight equilibration of the loop A-2AP construct docked with the substrate under ambient conditions, the fluorescence intensity became less sensitive to pressure (Fig. 5.11 (b)). A possible explanation is that pressure promotes the re-docking of hairpin ribozyme with the cleaved substrate, and the first experiment was performed before the cleaved substrate could be fully dissociated. This would imply that the undocked state is smaller in volume than the docked state. Meanwhile, dissociation of cleaved substrates can be expected to complete after overnight equilibration. This is reasonable as the dissociation of cleaved products is slow, particularly under conditions where there are no excess substrates (Law of Mass-Action).

Based on our results, we can consider two possible mechanisms for the reduction in catalytic activity observed by Maurel, *et al.* [55, 137]. The first possible mechanism is that the effective cleavage activity is reduced because pressure promotes the docked state, which prevents release of cleaved substrates and binding of new substrates. However, we consider this mechanism unlikely. In the experiments by Maurel, *et al.*, aliquots subjected to pressure for various durations were removed, and the cleaved products were quantified by denaturing PAGE. If the substrates had cleaved but were not released under pressure, they would be released during denaturing PAGE. Also, as the hairpin ribozyme

construct studied by Maurel, *et al.* was a 2WJ construct made of a single strand (Figure 3 (b)), the substrate was not available in excess as separate strands. Therefore, it was not possible that the cleavage activity was reduced because new substrates could not be bound by the ribozyme under pressure.

The second possible mechanism for the reduction in catalytic activity is that in the pressure-induced docked state, the cleavage reaction is itself affected. The hairpin ribozyme readily performs ligation, the reverse reaction of cleavage, under ambient conditions [53, 54]. As the docked form of hairpin ribozyme is stable at high pressure in the presence of Mg^{2+} it is possible that pressure causes small structural changes to the active site of the docked state that are responsible for changing the catalytic activity of the ribozyme, possibly by preventing cleavage or promoting ligation.

5.4 Conclusions

Although hydrostatic pressure was investigated as a method for selective measurement of the tertiary structure stability of hairpin ribozyme, no measurement was possible as undocking was not observed under pressure. Our results suggest that the docked state is preferred at high pressure, contrary to conclusions reported by Maurel and co-workers on another hairpin ribozyme construct [55, 137]. A high-pressure solution SAXS study is recommended for direct observation of large conformational changes that may be caused by pressure, Mg^{2+}, and substrate binding.

High pressure appeared to have an effect on the catalytic site of the docked hairpin ribozyme. This is reasonable as small structural changes caused by mutations in the catalytic site can have a large effect on the activity of hairpin ribozyme [82]. It was recently shown that small structural changes in the native structure of a protein captured by high-

pressure crystallography can be correlated with a change in function [9]. We speculate that similar structural studies of hairpin ribozyme under high pressure may offer further insight into the catalytic mechanism of hairpin ribozyme. Such an experiment will be discussed and outlined in Chapter 6.

CHAPTER 6

CONCLUSIONS

6.1 Conclusions and Future Directions

In this thesis, the relationship between the structure and thermodynamic stability of biomolecules was investigated as a function of pressure. The classical thermodynamic model of protein denaturation describes thermal denaturation as the transfer of hydrophobic residues from the protein core to the surrounding aqueous environment. However, this model, which is based on the thermal behavior of oil solubility in water, cannot be applied to protein denaturation under pressure. In particular, this model predicts a volume change accompanying pressure denaturation that is strongly pressure dependent [69], yet studies have determined that actual volume changes are smaller in magnitude than predicted and largely constant with pressure [162, 115]. Recent studies had suggested that pressure denaturation is distinct from thermal denaturation in that it involves the penetration of water into the protein core and the hydration of internal cavities rather than the transfer of core hydrophobic residues to water. To investigate water penetration and the volume change associated with pressure denaturation, the protein, T4 lysozyme, and several of its mutants were characterized by high-pressure SAXS and fluorescence spectroscopy.

Four T4 lysozyme mutants with different cavity volumes were characterized at low and neutral pH at pressures up to 400 MPa. The mutants contained six to nine cavities with various volumes between 5 - 223 $Å^3$, resulting in total unoccupied cavity volumes ranging from 125 to 328 $Å^3$ per mutant. It was demonstrated that the negative volume changes associated with the pressure denaturation of T4 lysozyme is contributed by the filling of unoccupied cavities with water and the electrostriction around exposed

charged groups. At low pH, the volume change upon denaturation correlated well with the total cavity volume, indicating that all of the molecule's major cavities are hydrated with pressure. SAXS measurements demonstrated that the pressure-denatured state is extended but not fully unfolded. At neutral pH, the pressure-denatured state was more compact than at low pH, and the small volume changes associated with denaturation suggest that the preferential filling of large cavities is responsible for the compactness of the pressure-denatured state. These results suggest that the degree of internal hydration correlates with the compactness of the denatured state, supporting the water penetration model of pressure denaturation. The relatively small magnitudes of volume changes observed with the pressure denaturation of proteins has been attributed to a positive volume change contribution by the hydration of exposed hydrophobic groups [115]. While the volume changes associated with hydrophobic groups could not be determined in this thesis, preferential cavity filling offers an alternative or additional mechanism to explain the small volume changes.

The catalytic RNA, hairpin ribozyme, offers unique insight into the problem of pressure-induced conformational changes as it does not have a hydrophobic core. Due to the difficulties reported in interpreting the docking thermodynamics of hairpin ribozyme [70], pressure was also explored as a means to selectively measure the stability of the tertiary contacts involved in the docking of hairpin ribozyme. Hinged hairpin ribozyme constructs with 2-aminopurine (2AP) substitutions were investigated with high-pressure fluorescence spectroscopy. However, the docked conformation of hairpin ribozyme remained stable up to pressures of 300 MPa. This result suggested that, contrary to a previously reported hypothesis [137, 55], undocking is not associated with a large and negative volume change. This can be explained purely by the lack of hydration mechanisms that cause negative volume changes. According to crystal structures of the docked hairpin ribozyme (PDB: 2NPY, 2OUE), all of the negatively charged phosphate groups

are oriented towards the solvent, indicating that reduction in volume of the hydration waters around charged groups cannot be expected with undocking. Likewise, while the docked hairpin ribozyme contains a large solvent-sequesterd cavity of approximately 150 $Å^3$ in volume (comparable in size to the cavities in engineered cavity mutants of T4 lysozyme), it was recently shown in a high resolution (2.05 Å) crystal structure (PDB: 2OUE) that this cavity is already occupied at ambient pressure by 5 water molecules that are interacting with catalytic groups in the active site [118]. These results support the view that negative volume changes associated with pressure-induced conformational changes require unoccupied spaces or buried charged groups and are consistent with the conclusions drawn from our work on T4 lysozyme.

Several experiments have been suggested in Chapters 4 and 5 to further understand the pressure denaturation of proteins and effect of pressure on hairpin ribozyme. Two specific experiments are outlined in the following sections. Additionally, improvements to the high-pressure apparatus are suggested.

6.1.1 Effect of Ligand Binding on Various T4 Lysozyme Mutants

The T4 lysozyme mutants with enlarged cavities, L99A and L99G/E108V, have been shown to bind a number of hydrophobic ligands, such as benzene, toluene, and indole (Fig. 6.1) [91]. The smallest of these ligands, benzene, is 147 $Å^3$ in size. As a result, the ligands are selectively bound in the large hydrophobic cavity (Fig. 6.1, cavity 6) and not in smaller hydrophobic cavities. In Chapter 4, it was shown that benzene-binding caused a significant reduction in volume change of L99G/E108V pressure denaturation, supporting our conclusion that the hydration of internal cavities contributes significantly to the volume change associated with the pressure denaturation of proteins. Due to the

slow kinetics, however, it was not possible to accurately quantify the reduction in the volume change.

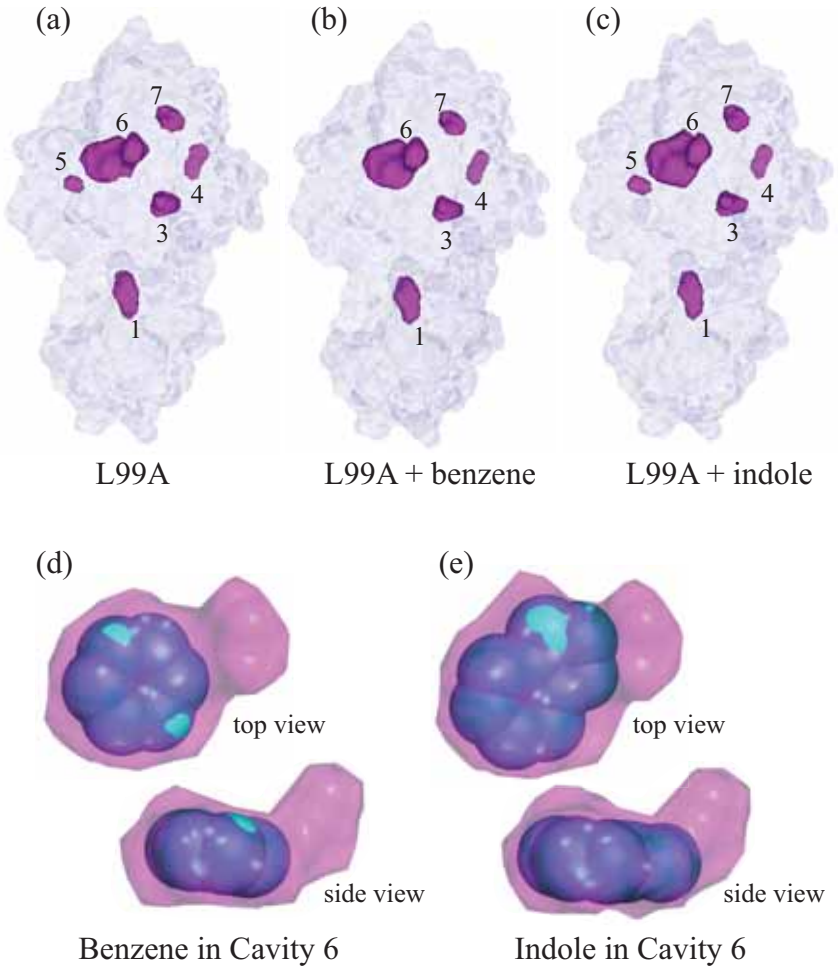

Figure 6.1: The effect of ligand binding on L99A T4 lysozyme. The internal cavities of L99A (shown in magenta; internal solvent and ligands not shown): (a) without ligand (PDB: 1L90) and bound with (b) benzene (1L83) and (d) indole (185L). Binding ligands has a small effect on cavity shape and size. Note that cavity 5 could not be detected in L99A bound with benzene. This is likely due to the slight expansion of the nearby cavity 6 caused by benzene. Top and side views of cavity 6 bound with: (f) benzene and (e) indole. The space-filling models of the ligands overlap slightly with the detected cavity surface.

In a future repetition of this experiment, two questions should be answered: What is the reduction in the volume change of pressure denaturation caused by ligand-binding in T4 lysozyme? Does ligand-binding only affect the denaturation volume change of mutants with large cavities?

If cavity hydration occurs with pressure denaturation, we expect to make the following observations. As a result of ligand binding, L99A and L99G/E108V, is expected to display a reduction in the denaturation volume change that is nearly equivalent to the volume of the ligand. Small structural changes caused by ligand binding must be accounted for in accurately predicting the reduction in volume change (Table 6.1). In the case of L99A, cavity 6 (Fig. 6.1, Table 6.1) expands slightly to accommodate benzene or indole. Mutants with small cavities, A98L and V149G, also serve as valuable controls. As a large hydrophobic cavity is required for ligand biding, we expect that the presence of benzene or indole in solution would have no effect on the denaturation volume change of the mutants A98L and V149G. Such an observation would also verify that the ligands do not affect denaturation thermodynamics by interacting with the protein exterior.

As a variety of ligands have been shown to bind with L99A [91], it will be beneficial to consider the choice of ligand in future studies. Benzene was chosen over toluene in this thesis as it was found that the fluorescence from aqueous benzene overlapped less with that of tryptophan, which was used to probe protein conformation. In this sense, the use of indole as a ligand is not appropriate as distinguishing tryptophan and indole fluorescence may not be possible. However, we mention indole because it is highly sensitive to the polarity of its local environment (Section 3.1.3). In future studies, it will be useful to probe not only the conformational change of the protein, but also the partition of ligand in the protein and in solvent. The latter may be quantified by the use of a environment-sensitive ligand.

Table 6.1: Cavity Volumes (Å^3) of L99A T4 lysozyme Bound with Ligands.

#	L99A (1L90)	+Benzene (1L83)	+Indole (185L)	Comments
0	21103.3	21012.9	21042.1	External Surface
1	51.9 (0)	49.9 (0)	51.8 (0)	WAT 171, 179
2	-	-	-	
3	27.6 (0)	25.1 (0)	27.0 (0)	WAT 208, Trp138
4	26.7 (0)	22.2 (0)	24.7 (0)	WAT 175
5	9.2	-	13.0	
6	161.1	179.3 (34.2)	202.7 (23.9)	
7	28.9	27.0	27.6	Trp126

Volumes of molecular surfaces found with crystallographic solvent molecules removed from structures using a 1.2 Å probe in he program MSMS [119]. In parentheses: volumes of solvent-containing cavities determined with crystallographic internal solvent molecules and ligands kept in structures.

The proposed experiments would benefit from a few improvements to the apparatus. The chemical compatibility of the ligand with the material used for the cap of the internal sample cell should be checked. As ligand binding is expected to increase the pressure stability and reduce the denaturation volume change, the ability to consistently reach high pressure will be critical. The high-pressure reservoir, which is the least robust element of the pressure network, should be re-designed with a more reliable and robust closure seal. This improvement will enable reliable pressurization to 400 MPa, the pressure limit of the apparatus. In the event that pressures exceeding 400 MPa are necessary, the use of a diamond (or sapphire) anvil cell should be considered. Excitation of and fluorescence collection from concentrated samples may be possible with the use of our home-built crystal fluorescence apparatus (similar in design to [16]) in a backscattering geometry. Technically, the use of an anvil cell for fluorescence experiments should be

feasible, as ruby fluorescence is routinely measured in diamond anvil cells for pressure calibration. The use of an anvil cell for fluorescence measurements will also minimize sample volume and eliminate the use of a pressure medium.

6.1.2 High Pressure Structures of Hairpin Ribozyme

As undocking of hairpin ribozyme could not be observed with pressure, selective measurement of the tertiary contact stability was not possible. However, hairpin ribozymes docked with genuine substrates demonstrated a reversible pressure effect (Chapter 5). In agreement with previous reports [137, 55], pressure appeared to have a reversible effect on the cleavage activity. While the exact mechanism is unknown, we speculate that small structural changes in the active site of the docked state caused by pressure are responsible for this. A high-pressure crystallography experiment is currently being planned to further investigate this.

The hairpin ribozyme is able to catalyze cleavage of a phosphodiester bond at a specific site being the G+1 and A-1 nucleotides (Fig. 6.2). This cleavage site is called the scissile phosphate. The products of this reaction are two fragments, one with a 2',3'-cyclic phosphate terminus and the other with a 2'-hydroxyl terminus. The reaction is thought to be a S_2N nucleophilic substitution where the 2'-oxygen of A-1 acts as the nucleophile, the phosphorus of the scissile phosphate is the electrophile, and the 5'-oxygen of G+1 is the leaving group. This is supported by a comparison of the NMR solution structure of the isolated loop A domain and crystal structures of the docked ribozyme (Fig. 6.3 (a)-(b)) [116, 21]. Upon docking, the G+1 base is pulled from the loop A domain into the active site formed at the docking interface of the loops A and B. The rotation of the G+1 base with respect to A-1 brings the 2'-oxygen of A-1, the phospho-

rus, and the 5'-oxygen of G+1 into a near in-line geometry, which is required for a S_2N nucleophilic substitution.

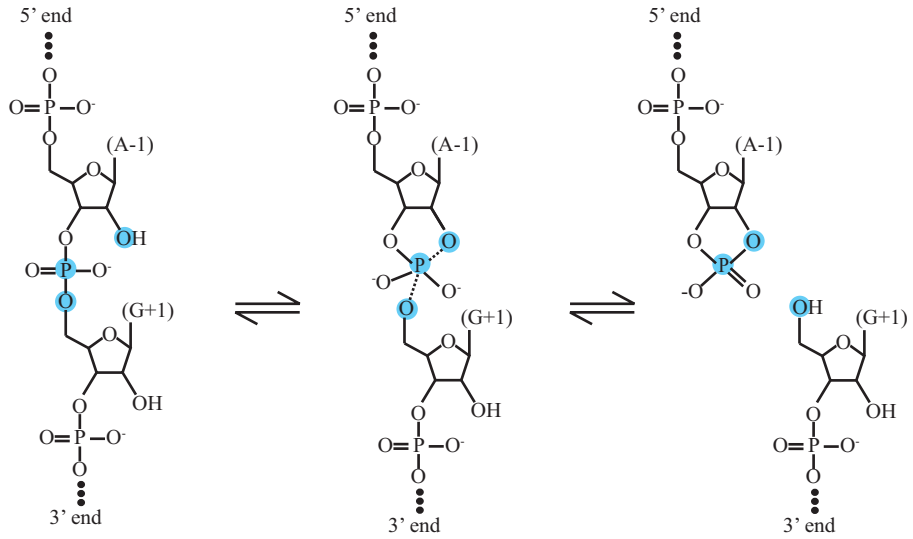

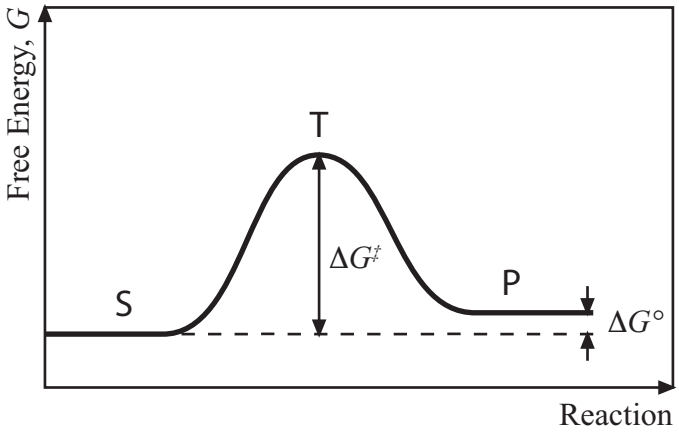

Figure 6.2: Reaction catalyzed by hairpin ribozyme. The reaction is thought to be an S_2N nucleophilic substitution [39]. The ribozyme catalyzes the reaction by reducing the activation energy, $\Delta G^{\ddagger}$ (shown is that of the forward reaction). Hairpin ribozyme is also a very good ligase [38, 51]. Hence the free energy difference between the substrate and product, ΔG°, is very small.

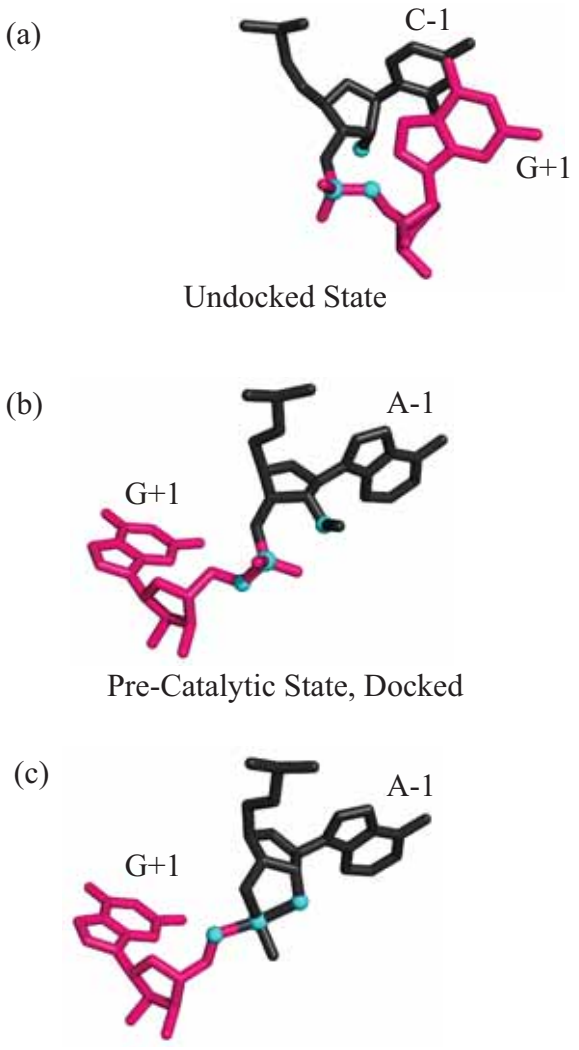

Figure 6.3: Rotation of scissile phosphate upon docking. The 2'-oxygen, phosphor, and 5'-oxygen involved in the cleavage reaction (shown in cyan) approach a nearly co-linear alignment with the rotation of the G+1 base with respect to A-1. (a) Undocked state (solution NMR of isolated domain A). (b) Pre-catalytic state with substrate analog (a sub-state within the docked conformation) (PDB: 2OUE) (c) Transition state mimic (another sub-state). (PDB: 2P7E).

An S_2N nucleophilic substitution implies that there is a single transition state. In the transition state, bond formation and breakage is not complete, and thus the phosphorus must coordinate five oxygens in a trigonal-bipyramidal geometry (Fig. 6.2) [117, 138]. As hairpin ribozyme is also efficient at performing the reverse reaction, ligation, we can deduce that the stabilization of the transitions state, i.e. reduction of the activation energy, is the significant factor in the catalysis by this ribozyme. However, the exact mechanism by which hairpin ribozyme achieves this is not yet fully understood. It is thought that a combination of various factors contribute [39, 138, 118]: (1) by docking, the hairpin ribozyme is able to distort the substrate into a reactive conformation, (2) nearby bases and internal water may stabilize the transition state electrostatically, and (3) nearby bases and internal water may participate in general acid-base catalysis.

Crystallographic endeavors to understand the catalytic mechanism have thus far relied heavily on the use of a substrate analog (Fig.6.4 (a)) and transition state mimic (Fig.6.4 (b)). Only one crystal structure of hairpin ribozyme docked with a genuine substrate has been reported (Fig.6.4 (c)) [117]. An equilibrium mixture of cleaved products and uncleaved substrates was observed in the electron density map of this sample. As the cleaved state was found to predominate in the crystal form of hairpin ribozyme (PDB: 1M5V), the use of a substrate analog has been essential to understanding the pre-catalytic conformation of hairpin ribozyme. However, it remains unknown how the methyl group that blocks the nucleophilic 2'-oxygen in the substrate analog may distort the active site. As direct observations of the transition state is not possible, the structure of this state has been deduced with the use of a pentavalent vanadium oxide bound at the cleavage site [117, 138], but whether this structure fully represents the actual transition state structure remains unknown [138]. Crystallographic studies of hairpin ribozyme have also been limited by the diffraction resolution. Most available structures have been solved to 2 - 3 Å resolution. Internal water molecules interacting with the active site

of hairpin ribozyme were only resolved recently in 2006 by Wedekind and co-workers [118, 138]. According to these structures (PDB: 2OUE, 2NPE), in the transition state, one of the water molecules is pushed out by the rotation of the scissile phosphate (Fig.6.4 (b)).

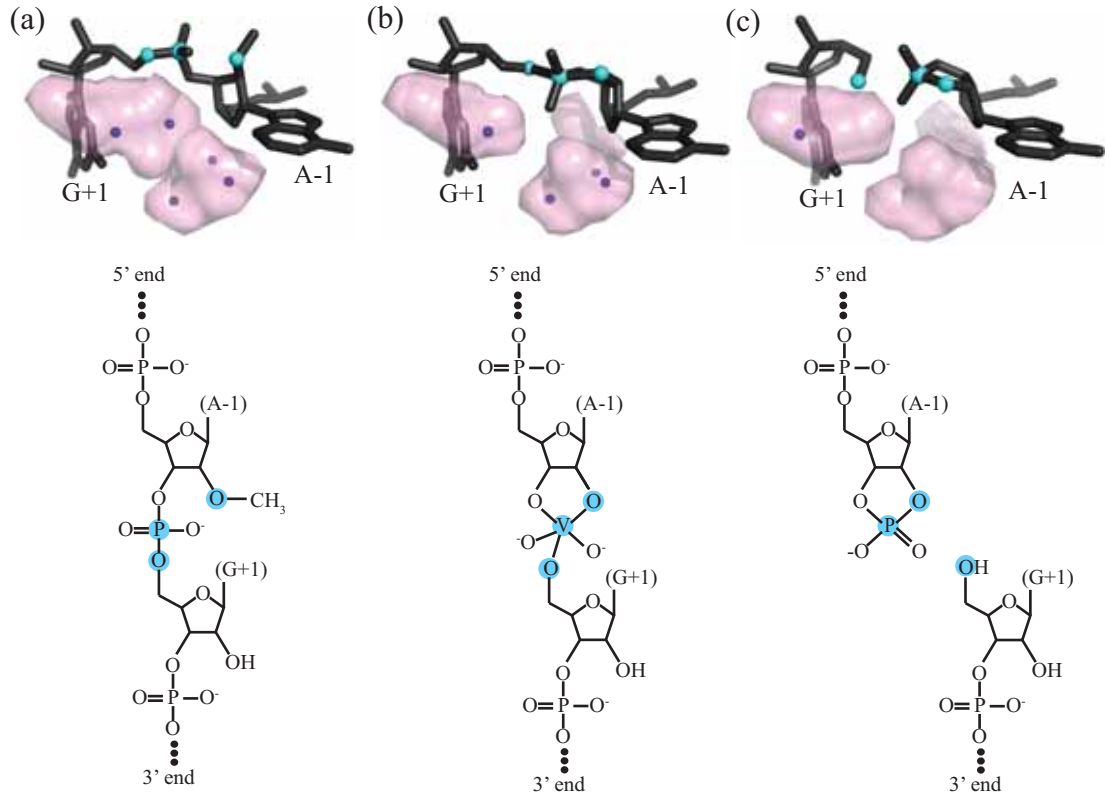

Figure 6.4: Sub-states of the docked hairpin ribozyme. The cavities at the active site are shown in pink. Waters that have thus far been resolved in these cavities are shown as dots.(a) The pre-catalytic conformation is represented by a substrate analog. Five water molecules were observed in the active site (PDB: 2OUE). (b) The transition state conformation is represented by crystal structures solved with a bound vanadium oxide. A water molecule is pushed out by the rotation of the scissile phosphate (PDB: 2P7E). (c) The cleaved product can be observed with crystals grown with a genuine substrate (PDB: 1M5V).

In the planned high-pressure crystallography experiment, crystals of the hinged hairpin ribozyme construct docked with a genuine U+2→2AP substrate (described in Chapter 5) will be studied in collaboration with Prof. Joseph Wedekind and co-workers (Univ. of Rochester). A preliminary experiment demonstrated that these crystals can be grown and that the diffraction quality (2.5 Å resolution at ambient-pressure) is comparable to those of other existing hairpin ribozyme structures. As a control, crystals of the loop A-2AP construct docked with a U+2→2AP substrate analog (cleavage protected by a 2'O-methyl group at A-1) will also be studied.

The goal of this experiment is two-fold. First, we hope to see if high-pressure structures can explain the high-pressure fluorescence results obtained for the loop A-2AP hinged construct. Secondly, we would like to know if and how pressure may affect the free energy landscape of hairpin ribozyme in the docked conformation (Fig. 6.2) and how pressure-induced changes provide further insight into the mechanism of hairpin ribozyme catalysis. Specifically, we ask: Is there a change in substrate-product ratio with pressure? Is there a change in structure or internal hydration with pressure? How well does the substrate analog represent the structure of the pre-catalytic state?

Due to the resolution limit, the hydration state of the cavity at the active site remains unclear [117]. Therefore, it is difficult to predict whether pressure will favor cleavage or ligation, based solely on the differences in the cavity volume and hydration of the reaction sub-states (Fig. 6.4). The effect of pressure on the overall structure of hairpin ribozyme must also be considered. A recent high-pressure crystallography study on the protein citrine reported that pressure-induced deformation of the "active site" (chromophore) was transmitted by structural changes in the scaffold [9]. Nonetheless, we expect that this experiment will provide, at the very least, high resolution structures of hairpin ribozyme; the crystals will be prepared by the high-pressure cryocooling tech-

nique, which has been shown to improve diffraction qualities [65]. Further insight into the mechanism of hairpin ribozyme catalysis can thus be expected.

6.1.3 Upgrading the High-Pressure SAXS Cell

In Chapters 2 and 4, we demonstrated the successful collection of solution SAXS from T4 lysozyme under high pressure with our custom-designed high-pressure SAXS cell. A variety of analyses were possible on the collected data, providing crucial insight into protein structural changes caused by pressure. Due to the limited time available during synchrotron experiments and the complexity of high-pressure experiments, we required an apparatus that is reliable and easy to use at biologically relevant experimental conditions. The use of disposable internal sample cells greatly facilitated this. We found that only one or two persons are necessary to perform perform a typical synchrotron experiment. While the internal sample cells were designed for protein solution samples, they would also be suitable for a variety of other samples [154]. Where necessary, the material choices can be modified for greater compatibility. For very large macromolecules, the scattering at lower q must be recorded. The primary limitation of the current cell is the low angle scattering from the diamond windows. Different sources of diamond windows are being investigated for a possible reduction in the scattering at low q in collaboration with Prof. Russell Hemley and co-workers (Carnegie Institution of Washington). Note that because the diamonds are transparent to a wide spectrum of light, this apparatus can be used with probes other than X-rays with small modifications or additions. This cell has been successfully used to observed pressurized protein crystals and other biological materials under the microscope (unpublished).

To extend the maximum operating pressure above 400 MPa, the design must be

re-optimized. The elastic limit of the body of the high-pressure cell is a function of the yield strength of the material and the dimensions (Eqn. (2.15)). Because Inconel 725 in the age-hardened state features tensile properties that are difficult to surpass, the dimensions must be changed to increase the elastic limit. Although the elastic limit is not the absolute pressure limit of our cell, we do not exceed this pressure in order to extend its lifetime. The windows will also require modifications to withstand higher pressure. The diamond thickness must be increased or the aperture size must be reduced. Such changes, however, affect other properties such as the resolution limit of the high-pressure cell.

Finally, as with other X-ray techniques, radiation damage is ultimately the limiting factor in solution SAXS studies of biological materials. The extent of radiation damage depends upon the sample and the experimental conditions. We have seen that radiation damage induced aggregation of a highly charged protein depended upon the presence of counter ions. We have also observed that multiple short exposures can be less damaging than one long exposure and that pauses between exposures can in some cases recover the undamaged scattering profile. This may be related to the diffusion rate of the aggregates. Radiation damage can be suppressed to a certain extent by the choice of X-ray energy. By tuning beam transmission through the samples, we can optimize the balance between radiation damage and the scattering signal from the proteins. With our samples, we are generally limited to total exposure times on order of 10 to 100 seconds at 10^{12} photons/s before radiation damage irreversibly distorts the scattering profile. In a high-pressure study where one wishes to take measurements from the same sample at multiple pressures, the exposure limit poses a problem. Samples must be changed fairly frequently. A next-generation high-pressure SAXS cell may incorporate a flow cell mechanism to overcome this problem.

APPENDIX A

SCHEMATICS

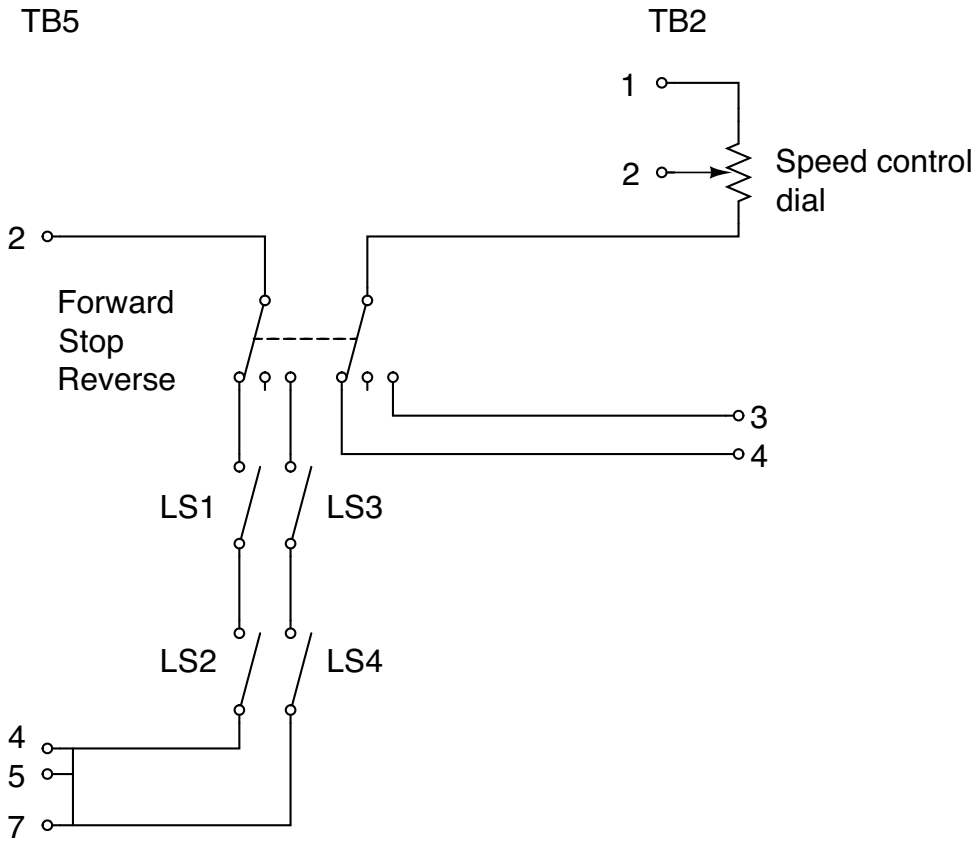

Figure A.1: Motor control circuit for high-pressure pump (Model 37-5.75-60, High Pressure Equipment Co.). The motor (Model C4D17FZ23B DC Gear Motor, Leeson) is controlled by a single-phase adjustable speed regenerative DC motor controller (RGA-RG, Boston Gear) with a control board (Model 106737301, Boston Gear) and a contactor board (Model 106242801). Terminal block 2 (TB2) is on the control board, and TB5 is on the contactor board. The on-off-on switch (double-pole, double throw, center-off) stops or determines the direction of the pump piston movement (forward, reverse). A pair of normally-closed limit switches are installed at each end of the pump housing; the limit switches are activated when the piston reaches either end of the housing. The speed of the piston is controlled continuously by the speed control dial

Figure A.2: Schematic of SAXS3.

A. Inconel 725HS high-pressure SAXS cell body
B. acrylic inner sample cell
C. brass anti-extrusion ring
D. 113 75D Viton O-ring
E. Inconel 725HS window cap
F. natural diamond (0.5 mm thick, 3.3 mm diameter)
G. Inconel 725HS window plug
H. brass jam washer
I. stainless steel 304 closure nut

Notes and Instructions: Inner sample cells were fabricated by ALine, Inc. (Redondo Beach, CA). They are laser-cut cast acrylic laminates composed of two .020" outer layers, a .040" middle layer, and .002" thick pressure-sensitive adhesive (467MP, 3M). Thin film X-ray windows (such as 7.5 micron Kapton) are later glued on outer surfaces (Super Glue Brush-On, Loctite). Inconel 725HS was provided by Special Metals Corp. Parts were machined from annealed material, then age-hardened to increase yield-strength. Break all sharp edges. Diamond-mating surface on window plug is polished. Finish with 0.5 micron diamond lapping film (Precision Surfaces International, Houston, TX). The required torque on the closure nuts is 90 ft-lb.

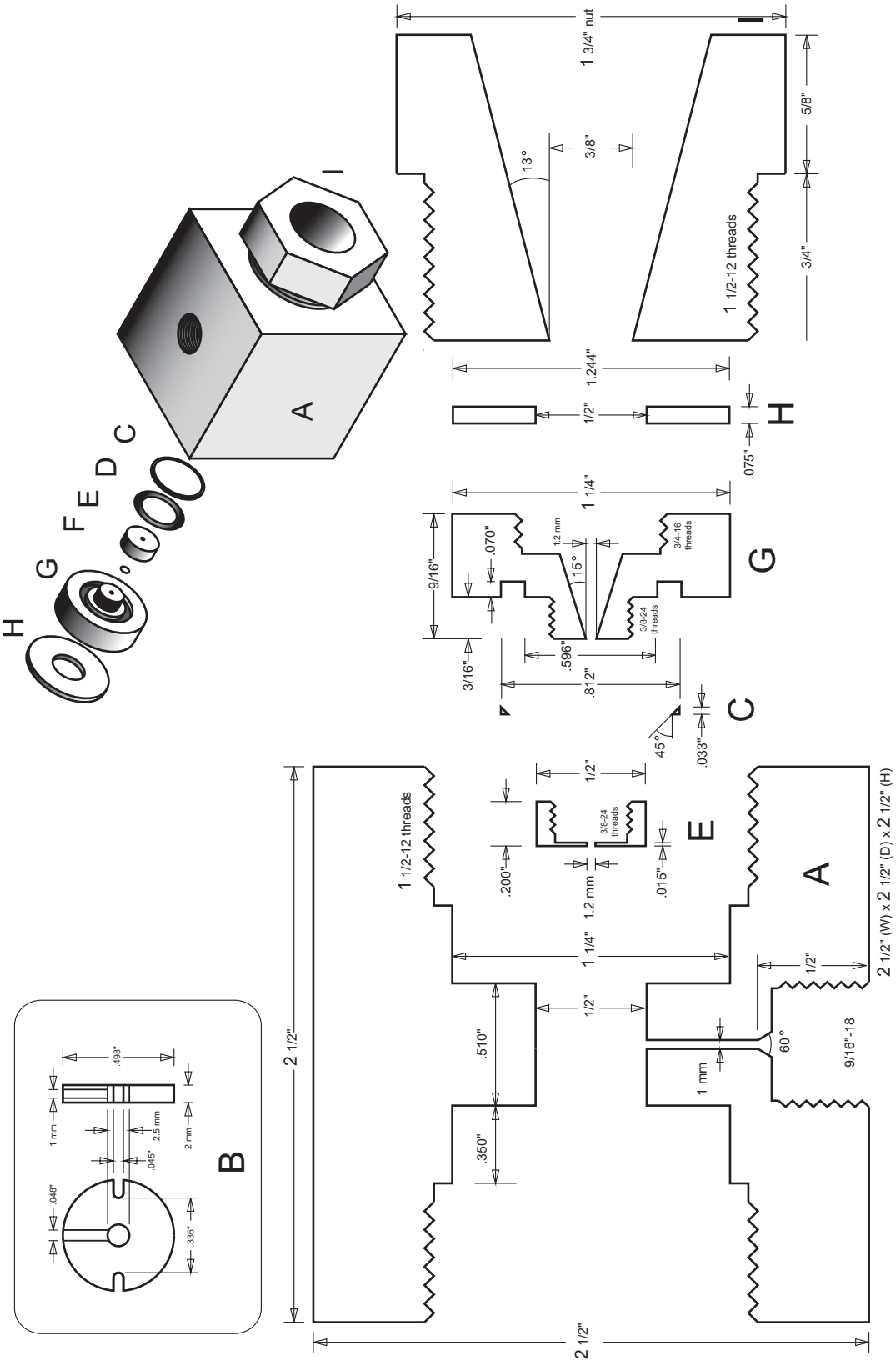
A
B
C
D
E
F
G
H
I
1 3/4" nut
13 °
3/8"
5/8"
3/4"
1 1/2-12 threads
1.244"
1/2"
.075"
1 1/4"
9/16"
.070"
1.2 mm
15 °
3/4-16 threads
3/8-24 threads
3/16"
.596"
.812"
45 °
.033"
.200"
.015"
.510"
.350"
1 mm
60 °
9/16"-18
2 1/2" (W) x 2 1/2" (D) x 2 1/2" (H)
2 1/2"
.498"
.048"
.045"
2.5 mm
2 mm
.336"

Figure A.2:

Figure A.3: Schematic of high-pressure reservoir

The top side of the reservoir body connects to the high-pressure cell via a standard 1/4" pressure connection. Before filling the reservoir, vacuum grease is applied to the inner wall using the brass piston as an applicator. The piston can be handled by screwing in a rod with 1/4"-20 threads at one end. The brass piston is fitted with two 114 75D Viton O-rings and vacuum greased before it is inserted into the filled reservoir. Molybdenum grease is applied to the closure nut threads. A 211 75D Buna-N O-ring and a brass anti-extrustion ring is fitted before the closure nut is tightened to 110 ft-lb. The bottom connection in the closure nut is connected to the pressure pump network via a standard 1/4" pressure connection.

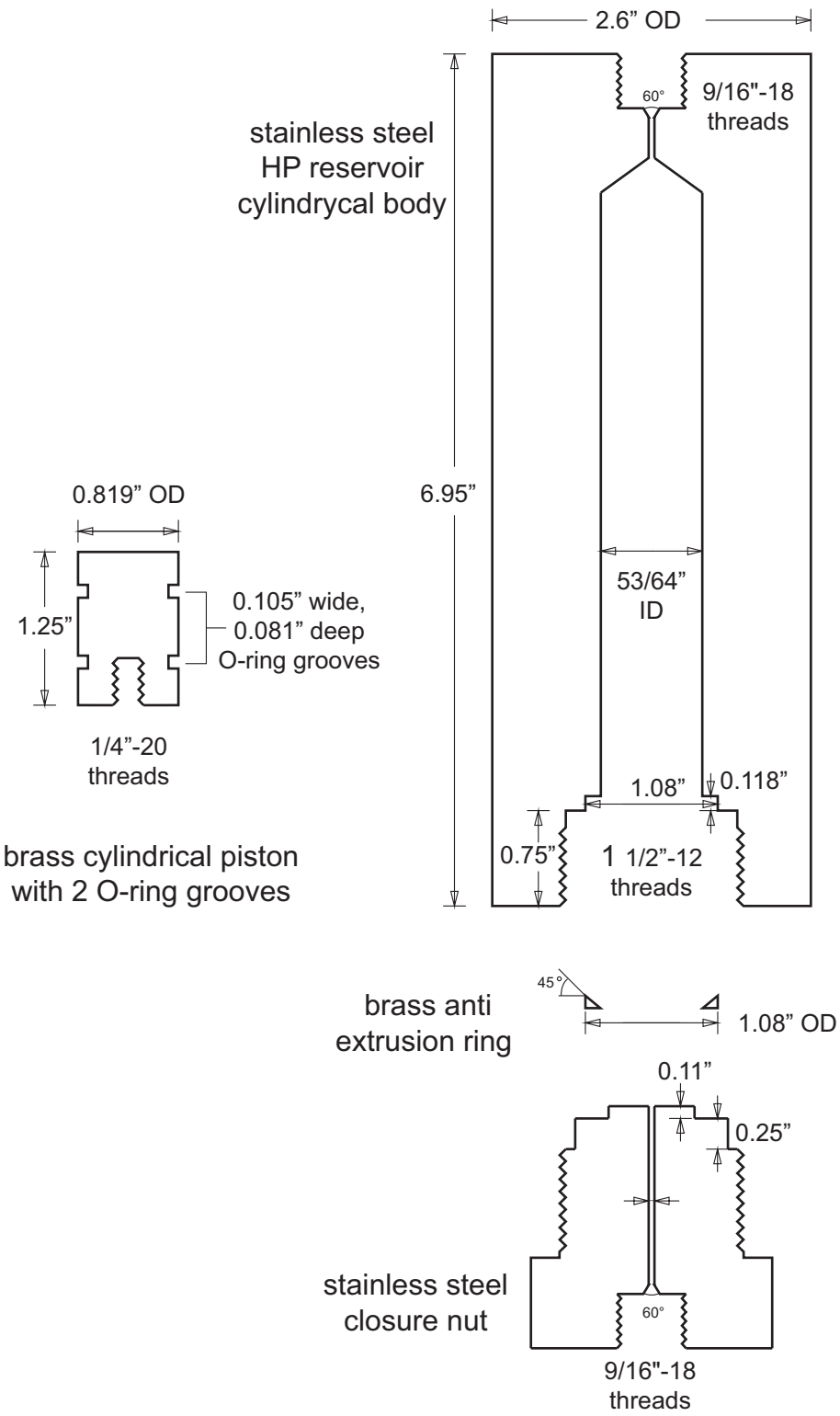
2.6” OD
60°
9/16"-18
threads
stainless steel
HP reservoir
cylindrycal body
6.95”
53/64”
ID
0.819” OD
1.25”
0.105” wide,
0.081” deep
O-ring grooves
1/4”-20
threads
1.08”
0.118”
0.75”
1 1/2”-12
threads
brass cylindrical piston
with 2 O-ring grooves
45°
brass anti
extrusion ring
1.08” OD
0.11”
0.25”
stainless steel
closure nut
60°
9/16"-18
threads

Figure A.3:

BIBLIOGRAPHY

[1] G. N. Agrios, editor. *Plant Pathology*. Academic Press, Amsterdram, 4th edition, 2005.

[2] S. Alam, V. Grum-Tokars, J. Krucinska, M. Kundracik, and J. E. Wedekind. Conformational heterogeneity at position U37 of an all-RNA hairpin ribozyme with implications for metal binding and the catalytic structure of the S-turn. *Biochemistry*, 2005.

[3] R. A. Alberty and R. J. Silbey. *Physical Chemistry*. John Wiley & Sons, Inc., New York, 2nd edition, 1997.

[4] N. Ando, B. Barstow, W. A. Baase, A. Fields, B. W. Matthews, and S. M. Gruner. Structural and thermodynamic characterization of T4 lysozyme mutants and the contribution of internal cavities to pressure denaturation. *Biochemistry*, 47:11097–11109, 2008.

[5] N. Ando, P. Chenevier, M. Novak, M. W. Tate, and S. M. Gruner. High hydrostatic pressure small-angle X-ray scattering cell for protein solution studies featuring diamond windows and disposable sample cells. *J. Appl. Cryst.*, 41:167–175, 2008.

[6] C. B. Anfinsen and E. Haber. Studies on the reduction and re-formation of protein disulfide bonds. *J. Biol. Chem.*, 236:1361–1363, 1961.

[7] M. Arai, K. Ito, T. Inobe, M. Nakao, K. Maki, K. Kamagata, H. Kihara, Y. Amemiya, and K. Kuwajima. Fast compaction of alpha-lactalbumin during folding studied by stopped-flow X-ray scattering. *J. Mol. Biol.*, 321:121–132, 2002.

[8] S. L. Barna, M. W. Tate, S. M. Gruner, and E. F. Eikenberry. Calibration procedures for charge-coupled device X-ray detectors. *Rev. Sci. Instr.*, 70:2927–2934, 1999.

[9] B. Barstow, N. Ando, C. U. Kim, and S. M. Gruner. Alteration of citrine structure by hydrostatic pressure explains the accompanying spectral shift. *Proc. Natl. Acad. Sci. USA*, 105:13362–13366, 2008.

[10] W. Becktel and W. Baase. Thermal denaturation of bacteriophage T4 lysozyme at neutral pH. *Biopolymers*, 26:619–623, 1987.

[11] J. A. Bell, K. P. Wilson, X. J. Zhang, H. R. Faber, H. Nicholson, and B. W. Matthews. Comparison of the crystal structure of bacteriophage T4 lysozyme at low, medium, and high ionic strengths. *Proteins*, 10:10–21, 1991.

[12] P. Bernadó, L. Blanchard, P. Timmins, D. Marion, R. W. H. Ruigrok, and M. Blackledge. A structural model for unfolded proteins from residual dipolar couplings and small-angle X-ray scattering. *Proc. Natl. Acad. Sci. USA*, 102:17002–17007, 2005.

[13] P. Bernadó, E. Mylonas, M. V. Petoukhov, M. Blackledge, and D. I. Svergun. Structural characterization of flexible proteins using small-angle X-ray scattering. *J. Am. Chem. Soc.*, 129:5656–5664, 2007.

[14] A. Berzal-Herranz, S. Joseph, B. Chowrira, S. E. Butcher, and J. M. Burke. Essential nucleotide sequences and secondary structure elements of the hairpin ribozyme. *EMBO J.*, 12:2567–2573, 1993.

[15] T. Blanton, T. Huang, H Toraya, C. Hubbard, S. Robie, D Louer, H. Gobel, G Will, R Gilles, and T Raftery. JCPDS—international centre for diffraction data round robin study of silver behenate. A possible low-angle X-ray diffraction calibration standard. *Powder Diffr.*, 10:91–95, 1995.

[16] D. Bourgeois, X. Vernede, V. Adam, E. Fioravanti, and T. Ursby. A microspectrophotometer for UV-visible absorption and fluorescence studies of protein crystals. *J. Appl. Cryst.*, 35:319–326, 2002.

[17] P. Bridgman. The coagulation of egg albumen by pressure. *J. Biol. Chem.*, 19:511–512, 1914.

[18] L. Brun, D. G. Isom, P. Velu, B. García-Moreno, and C. A. Royer. Hydration of the folding transition state ensemble of a protein. *Biochemistry*, 45:3473–3480, 2006.

[19] S. E. Butcher, F. H. Allain, and J. Feigon. Solution structure of the loop B domain from the hairpin ribozyme. *Nat. Struct. Biol.*, 6:212–216, 1999.

[20] J. Buzayan, W. Gerlach, and G. Bruening. Satellite tobacco ringspot virus RNA: A subset of the RNA sequence is sufficient for autolytic processing. *Proc. Natl. Acad. Sci. USA*, 83:8859–8862, 1986.

[21] Z. Cai and I. Tinoco. Solution structure of loop a from the hairpin ribozyme from tobacco ringspot virus satellite. *Biochemistry*, 35:6026–6036, 1996.

[22] P. R. Callis. 1La and 1Lb transitions of tryptophan: Applications of theory and experimental observations to fluorescence of proteins. *Meth. Enzymol.*, 278:113–150, 1997.

[23] L. Chen, G. Wildegger, T. Kiefhaber, K. O. Hodgson, and S. Doniach. Kinetics of lysozyme refolding: Structural characterization of a non-specifically collapsed state using time-resolved X-ray scattering. *J. Mol. Biol.*, 276:225–237, 1998.

[24] M. D. Collins. *High-Pressure X-ray Crystallography and Core Hydrophobicity of T4 Lysozyme*. PhD thesis, Cornell University, 2006.

[25] M. D. Collins, G. Hummer, M. L. Quillin, B. W. Matthews, and S. M. Gruner. Cooperative water filling of a nonpolar protein cavity observed by high-pressure crystallography and simulation. *Proc. Natl. Acad. Sci. USA*, 102(46):16668–16671, Nov 2005.

[26] R. Day and A. E. García. Water penetration in the low and high pressure native states of ubiquitin. *Proteins*, 70:1175–1184, 2008.

[27] P. Debye. Zerstreuung von Röntgenstrahlen. *Annalen der Physik*, 351:809–823, 1914.

[28] K. A. Dill. Dominant forces in protein folding. *Biochemistry*, 29:7133–7155, 1990.

[29] K. A. Dill and D. Shortle. Denatured states of proteins. *Annual Review of Biochemistry*, 60:795–825, 1991.

[30] D. N. Dubins, A. Lee, R. B. Macgregor, and T. V. Chalikian. On the stability of double stranded nucleic acids. *J .Am. Chem. Soc.*, 123:9254–9259, 2001.

[31] M. L. Elwell and J. A. Schellman. Phage T4 lysozyme. Physical properties and reversible unfolding. *Biochim. Biophys. Acta*, 386:309–323, 1975.

[32] M. L. Elwell and J. A. Schellman. Stability of phage T4 lysozymes. I. Native properties and thermal stability of wild type and two mutant lysozymes. *Biochim. Biophys. Acta*, 494:367–383, 1977.

[33] J. Erbes, R. Winter, and G. Rapp. Rate of transformations between mesophases of the 1:2 lechitin/fatty acid mixtures DMPC/MA and DPPC/PA: A time-resolved synchtrotron X-ray diffraction study. *Ber. Bensenges. Phys. Chem.*, 100:1713–1722, 1996.

[34] M. Eremets. *High Pressure Experimental Methods*. Oxford University Press, Oxford, 1996.

[35] A. E. Eriksson, W. A. Baase, and B. W. Matthews. Similar hydrophobic replacements of Leu99 and Phe153 within the core of T4 lysozyme have different structural and thermodynamic consequences. *J. Mol. Biol.*, 229:747–769, 1993.

[36] A. E. Eriksson, W. A. Baase, J. A. Wozniak, and B. W. Matthews. A cavity-containing mutant of T4 lysozyme is stabilized by buried benzene. *Nature*, 355:371–373, 1992.

[37] A. E. Eriksson, W. A. Baase, X. J. Zhang, D. W. Heinz, M. Blaber, E. P. Baldwin, and B. W. Matthews. Response of a protein structure to cavity-creating mutations and its relation to the hydrophobic effect. *Science*, 255:178–183, 1992.

[38] M. J. Fedor. Tertiary structure stabilization promotes hairpin ribozyme ligation. *Biochemistry*, 38:11040–11050, 1999.

[39] A. R. Ferré-D'Amaré. The hairpin ribozyme. *Biopolymers*, 73:71–78, 2004.

[40] A. R. Ferré-D'amaré and P. B. Rupert. The hairpin ribozyme: from crystal structure to function. *Biochem. Soc. Trans.*, 30:1105–1109, 2002.

[41] J. E. Field. *The Properties of Diamond*. Academic Press, London, 1979.

[42] A. Finkelstein and O. G. Ptitsyn. *Protein Physics*. Academic Press, London, 2002.

[43] R. Fourme, I. Ascone, R. Kahn, M. Mezouar, P. Bouvier, E. Girard, T. Lin, and J. E. Johnson. Opening the high-pressure domain beyond 2 kbar to protein and virus crystallography–technical advance. *Structure*, 10:1409–1414, 2002.

[44] K. J. Frye and C. A. Royer. Probing the contribution of internal cavities to the volume change of protein unfolding under pressure. *Protein .Sci.*, 7:2217–2222, 1998.

[45] E. Girard, T. Prangé, A.-C. Dhaussy, E. Migianu-Griffoni, M. Lecouvey, J.-C. Chervin, M. Mezouar, R. Kahn, and R. Fourme. Adaptation of the base-paired double-helix molecular architecture to extreme pressure. *Nucleic Acids Res.*, 35:4800–4808, 2007.

[46] O. Glatter and O. Kratky, editors. *Small Angle X-ray Scattering*. Academic Press, New York, 1982.

[47] Y. Goto, L. J. Calciano, and A. L. Fink. Acid-induced folding of proteins. *Proc. Natl. Acad. Sci. USA*, 87:573–577, 1990.

[48] Y. V. Griko, P. L. Privalov, J. M. Sturtevant, and S. Y. Venyaminov. Cold denaturation of staphylococcal nuclease. *Proc. Natl. Acad. Sci. USA*, 85:3343–3347, 1988.

[49] M. Hara, editor. *Polyelectrolytes: Science and Technology*, pages 301–302. CRC Press, New York, 1992.

[50] Y. Harpaz, M. Gerstein, and C. Chothia. Volume changes on protein folding. *Structure*, 2:641–649, 1994.

[51] L. A. Hegg and M. J. Fedor. Kinetics and thermodynamics of intermolecular catalysis by hairpin ribozymes. *Biochemistry*, 34:15813–15828, 1995.

[52] K. Heremans and L. Smeller. Protein structure and dynamics at high pressure. *Biochim. Biophys. Acta.*, 1386:353–370, 1998.

[53] K. J. Hertel, D. Herschlag, and O. C. Uhlenbeck. A kinetic and thermodynamic framework for the hammerhead ribozyme reaction. *Biochemistry*, 33:3374–3385, 1994.

[54] K. J. Hertel and O. C. Uhlenbeck. The internal equilibrium of the hammerhead ribozyme reaction. *Biochemistry*, 34:1744–1749, 1995.

[55] G. Hervé, S. Tobé, T. Heams, J. Vergne, and M.-C. Maurel. Hydrostatic and osmotic pressure study of the hairpin ribozyme. *Biochim. Biophys. Acta*, 1764:573–577, 2006.

[56] A. Hodel, S. Kim, and A. Brunger. Model bias in macromolecular crystal structures. *Acta Cryst.*, A48:851–858, 1992.

[57] W. B. Holzapfel and N. S. Isaacs, editors. *High-pressure techniques in chemistry and physics: A practical approach*. Oxford University Press, Oxford, 1997.

[58] B. Honig. Protein folding: from the levinthal paradox to structure prediction. *Journal of Molecular Biology*, 293:283–293., 1999.

[59] T. Huang, H Toraya, T. Blanton, and Y Wu. X-ray powder diffraction analysis of silver behenate, a possible low-angle diffraction standard. *J. Appl. Cryst.*, 26:180–184, 1993.

[60] G. Hummer, S. Garde, A. E. García, M. E. Paulaitis, and L. R Pratt. The pressure dependence of hydrophobic interactions is consistent with the observed pressure denaturation of proteins. *Proc. Natl. Acad. Sci. USA*, 95:1552–1555, 1998.

[61] W. Kauzmann. *The Mechanism of Enzyme Action (McElroy, W. D. & Glass, B., Eds.)*, page 70. Johns Hopkins Press, 1954.

[62] W. Kauzmann. Some factors in the interpretation of protein denaturation. *Adv. Protein Chem.*, 14:1–63, 1959.

[63] W. Kauzmann, A. Bodanszky, and J. Rasper. Volume changes in protein reactions. II. Comparison of ionization reactions in proteins and small molecules. *J. Am. Chem. Soc.*, 84:1777–1788, 1962.

[64] J. C. Kendrew, R. E. Dickerson, B. E. Strandberg, R. G. Hart, D. R. Davies, D. C. Phillips, and V. C. Shore. Structure of myoglobin: A three-dimensional Fourier synthesis at 2 Å resolution. *Nature*, 185:422–427, 1960.

[65] C. U. Kim, R. Kapfer, and S. M. Gruner. High pressure cooling of protein crystals without cryoprotectants. *Acta Cryst.*, D61:881–890, 2005.

[66] S. R. Kirk, N. W. Luedtke, and Y. Tor. 2-Aminopurine as a real-time probe of enzymatic cleavage and inhibition of hammerhead ribozymes. *Bioorg. Med. Chem.*, 9:2295–2301, 2001.

[67] D. B. Kitchen, L. H. Reed, and R. M. Levy. Molecular dynamics simulation of solvated protein at high pressure. *Biochemistry*, 31:10083–10093, 1992.

[68] M. H. Klapper. On the nature of the protein interior. *Biochim. Biophys. Acta*, 229:557–566, 1971.

[69] H. L. Kliman. *The Solubility of 4-Octonone in Water: A Model Compound Study of Hydrophobic Interactions at High-Pressure*. PhD thesis, Princeton University, 1970.

[70] D. Klostermeier and D. P. Millar. Helical junctions as determinants for RNA folding: Origin of tertiary structure stability of the hairpin ribozyme. *Biochemistry*, 39:12970–12978, 2000.

[71] J. Kohn, I. Millett, J. Jacob, B. Zagrovic, and et al. Correction for Kohn et al., Random-coil behavior and the dimensions of chemically unfolded proteins. *Proc. Natl. Acad. Sci. USA*, 102:14475, 2004.

[72] J. E. Kohn, I. S. Millett, J. Jacob, B. Zagrovic, T. M. Dillon, N. Cingel, R. S. Dothager, S. Seifert, P. Thiyagarajan, T. R. Sosnick, M. Z. Hasan, V. S. Pande, I. Ruczinski, S. Doniach, and K. W. Plaxco. Random-coil behavior and the dimensions of chemically unfolded proteins. *Proc. Natl. Acad. Sci. USA*, 101:12491–12496, 2004.

[73] P. Konarev, V. Volkov, A. Sokolova, M. Koch, and D. I. Svergun. PRIMUS: a Windows PC-based system for small-angle scattering data analysis. *J. Appl. Cryst.*, 36:1277–1282, 2003.

[74] C. E. Kundrot and F. M. Richards. Crystal structure of hen egg-white lysozyme at a hydrostatic pressure of 1000 atmospheres. *J. Mol. Biol.*, 193:157–170, 1987.

[75] J. R. Lakowicz. *Principles of Fluorescence Spectroscopy*. Springer, New York, third edition, 2006.

[76] M. W. Lassalle, H. Yamada, and K. Akasaka. The pressure-temperature free energy-landscape of staphylococcal nuclease monitored by (1)H NMR. *J. Mol. Biol.*, 298:293–302, 2000.

[77] B. Lee. Solvent reorganization contribution to the transfer thermodynamics of small nonpolar molecules. *Biopolymers*, 31:993–1008, 1991.

[78] H. Li, H. Yamada, and K. Akasaka. Effect of pressure on individual hydrogen bonds in proteins. Basic pancreatic trypsin inhibitor. *Biochemistry*, 37:1167–1173, 1998.

[79] J. Lipfert and S. Doniach. Small-angle X-ray scattering from RNA, proteins, and protein complexes. *Annual Review of Biophysics and Biomolecular Structure*, 36:307–327, 2007.

[80] R. Liu, W. A. Baase, and B. W. Matthews. The introduction of strain and its effects on the structure and stability of T4 lysozyme. *J. Mol. Biol.*, 295:127–145, 2000.

[81] R. Lumry and R. Biltonen. Validity of the "two-state" hypothesis for conformational transitions of proteins. *Biopolymers*, 4:917–944, 1966.

[82] C. MacElrevey, J. D. Salter, J. Krucinska, and J. E. Wedekind. Structural effects of nucleobase variations at key active site residue Ade38 in the hairpin ribozyme. *RNA*, 14:1600–1616, 2008.

[83] C. MacElrevey, R. C. Spitale, J. Krucinska, and J. E. Wedekind. A posteriori design of crystal contacts to improve the X-ray diffraction properties of a small RNA enzyme. *Acta Cryst.*, D63:812–825, 2007.

[84] R. B. Macgregor. The interactions of nucleic acids at elevated hydrostatic pressure. *Biochim. Biophys. Acta*, 1595:266–276, 2002.

[85] G. I. Makhatadze and P. L. Privalov. Hydration effects in protein unfolding. *Biophys. Chem.*, 51:291–304, 1994.

[86] M. Matsumura, J. Becktel W, M. Levitt, and B. W. Matthews. Stabilization of phage T4 lysozyme by engineered disulfide bonds. *Proc. Natl. Acad. Sci. U.S.A.*, 86:6562–6566, 1989.

[87] B. W. Matthews. Structural and genetic analysis of protein stability. *Annual Review of Biochemistry*, 62:139–160, 1993.

[88] B. W. Matthews and S. J. Remington. The three dimensional structure of the lysozyme from bacteriophage T4. *Proc. Natl. Acad. Sci. USA*, 71:4178–4182, 1974.

[89] F. Meersman, C. M. Dobson, and K. Heremans. Protein unfolding, amyloid fibril formation and configurational energy landscapes under high pressure conditions. *Chemical Society Reviews*, 35:908–917, 2006.

[90] M.Martick and W. G. Scott. Tertiary contacts distant from the active site prime a ribozyme for catalysis. *Cell*, 126:309–320, 2006.

[91] A. Morton, W. A .Baase, and B. W. Matthews. Energetic origins of specificity of ligand binding in an interior nonpolar cavity of T4 lysozyme. *Biochemistry*, 34:8564–8575, 1995.

[92] V. V. Mozhaev, K. Heremans, J. Frank, P. Masson, and C. Balny. High pressure effects on protein structure and function. *Proteins*, 24:81–91, 1996.

[93] D. C. Muchmore, L. P. McIntosh, C. B. Russell, D. E. Anderson, and F. W. Dahlquist. Expression and nitrogen-15 labeling of proteins for proton and nitrogen-15 nuclear magnetic resonance. *Meth. Enzymol.*, 177:44–73, 1989.

[94] K. Murphy, P. L. Privalov, and S. Gill. Common features of protein unfolding and dissolution of hydrophobic compounds. *Science*, 247:559–561, 1990.

[95] R. Neuman Jr., W. Kauzmann, and A. Zipp. Pressure dependence of weak acid ionization in aqueous buffers. *J. Phys. Chem.*, 77:2687–2691, 1973.

[96] Y. Nishikawa, T. Fujisawa, Y. Inoko, and M. Moritoki. Improvement of a high pressure cell with diamond windows for solution X-ray scattering of proteins. *Nuclear Instruments and Methods in Physics Research A*, 467-468:1384–1387, 2001.

[97] A. A. Paladini and G. Weber. Absolute measurements of fluorescence polarization at high pressures. *Rev. Sci. Instr.*, 52:419–427, 1981.

[98] A. A. Paladini and G. Weber. Pressure-induced reversible dissociation of enolase. *Biochemistry*, 20:2587–2593, 1981.

[99] A. Paliwal, D. Asthagiri, D. P. Bossev, and M. E. Paulaitis. Pressure denaturation of staphylococcal nuclease studied by neutron small-angle scattering and molecular simulation. *Biophys. J.*, 87:3479–3492, 2004.

[100] G. Panick, R. Malessa, and R. Winter. Differences between the pressure- and temperature-induced denaturation and aggregation of beta-lactoglobulin A, B, and AB monitored by FT-IR spectroscopy and small-angle X-ray scattering. *Biochemistry*, 38:6512–6519, 1999.

[101] G. Panick, R. Malessa, R. Winter, G. Rapp, K. J. Frye, and C. A. Royer. Structural characterization of the pressure-denatured state and unfolding/refolding kinetics of staphylococcal nuclease by synchrotron small-angle X-ray scattering and Fourier-transform infrared spectroscopy. *J. Mol. Biol.*, 275:389–402, 1998.

[102] Q. Peng and H. Li. Atomic force microscopy reveals parallel mechanical unfolding pathways of T4 lysozyme: Evidence for a kinetic partitioning mechanism. *Proc. Natl. Acad. Sci. USA*, 105:1885–1890, 2008.

[103] M. F. Perutz, M. G. Rossmann, A. F. Cullis, H. Muirhead, G. Will, and A. C. T. North. Structure of hæmoglobin: A three-dimensional Fourier synthesis at 5.5-Å resolution, obtained by X-ray analysis. *Nature*, 185:416–422, 1960.

[104] L. Pollack, M. W. Tate, N. C. Darnton, J. B. Knight, S. M. Gruner, W. A. Eatons, and R. H. Austin. Compactness of the denatured state of a fast-folding protein

measured by submillisecond small-angle X-ray scattering. *Proc. Natl. Acad. Sci. USA*, 96:10115–10117, 1999.

[105] L. Pollack, M. W. Tate, A. C. Finnefrock, C. Kalidas, S. Trotter, N. C. Darnton, L. Lurio, R. H. Austin, C. A. Batt, S. M. Gruner, and S. G. Mochrie. Time resolved collapse of a folding protein observed with small angle X-ray scattering. *Phys. Rev. Lett.*, 86:4962–4965, 2001.

[106] A. R. Poteete, D. P. Sun, H. Nicholson, and B. W. Matthews. Second-site revertants of an inactive T4 lysozyme mutant restore activity by restructuring the active site cleft. *Biochemistry*, 30:1425–1432, 1991.

[107] T. C. Poulter. Apparatus for optical studies at high pressure. *Physical Review*, 40:861–871, 1932.

[108] K. E. Prehoda, E. S. Mooberry, and J. L. Markley. Pressure denaturation of proteins: Evaluation of compressibility effects. *Biochemistry*, 37:5785–5790, 1998.

[109] K. Pressl, M. Kriechbaum, M. Steinhart, and P. Laggner. High pressure cell for small- and wide-angle X-ray scattering. *Rev. Sci. Instr.*, 68:4588–4592, 1996.

[110] P. L. Privalov, Y. Griko, S. Venyaminov, and V. P. Kutyshenko. Cold denaturation of myoglobin. *J. Mol. Biol.*, 190:487–498, 1986.

[111] S. W. Provencher and J. Glöckner. Estimation of globular protein secondary structure from circular dichroism. *Biochemistry*, 20:33–37, 1981.

[112] H. Reiss. *Methods of Thermodynamics*. Blaisdell Publishing Company, New York, 1996.

[113] F. M. Richards. The interpretation of protein structures: Total volume, group volume distributions and packing density. *J. Mol. Biol.*, 82:1–14, 1974.

[114] M. J. Roossinck, D. Sleat, and P. Palukaitis. Satellite RNAs of plant viruses: Structures and biological effects. *Microbiol. Rev.*, 56:265–279, 1992.

[115] C. A. Royer. Revisiting volume changes in pressure-induced protein unfolding. *Biochim. Biophys. Acta*, 1595:201–209, 2002.

[116] P. B. Rupert and A. R. Ferré-D'Amaré. Crystal structure of a hairpin ribozyme-inhibitor complex with implications for catalysis. *Nature*, 410:780–786, 2001.

[117] P. B. Rupert, A. P. Massey, S. T. Sigurdsson, and A. R Ferré-D'Amaré. Transition state stabilization by a catalytic RNA. *Science*, 298(5597):1421–1424, Nov 2002.

[118] J. Salter, J. Krucinska, S. Alam, V. Grum-Tokars, and J. E. Wedekind. Water in the active site of an all-RNA hairpin ribozyme and effects of Gua8 base variants on the geometry of phosphoryl transfer. *Biochemistry*, 45:686–700, 2006.

[119] M. Sanner, A. Olson, and J.-C. Spehner. Reduced surface: An efficient way to compute molecular surfaces. *Biopolymers*, 38:305–320, 1996.

[120] J. Schellman. The thermodynamic stability of proteins. *Annual Review of Biophysics and Biomolecular Structure*, 16:115–137, 1987.

[121] S. G. Schulman. *Fluorescence an Phosphorescence Spectroscopy: Physiochemical Principles and Practice*. Pergamon Press, Oxford, first edition, 1977.

[122] H. Seemann, R. Winter, and C. A. Royer. Volume, expansivity and isothermal compressibility changes associated with temperature and pressure unfolding of staphylococcal nuclease. *J. Mol. Biol.*, 307:1091–1102, 2001.

[123] W. F. Sherman and A. A. Stadtmuller. *Experimental Techniques in High Pressure Research*. Wiley, Chichester, 1987.

[124] A. A. Shiryaev, K. Dembo, Y. A. Klyuev, A. M. Naletov, and B. N. Feigelson. Small-angle X-ray scattering of extended defects in diamonds. *J. Appl. Cryst.*, 36:420–424, 2003.

[125] A. A. Shiryaev, Y. A. Klyuev, A. M. Naletov, A. T. Dembo, and B. N. Feigelson. Small-angle X-ray scattering in type Ia diamonds. *Diam. Relat. Mater.*, 9:1494–1499, 2000.

[126] J. L. Silva, D. Foguel, A. T. Poian, and P. E. Prevelige. The use of hydrostatic pressure as a tool to study viruses and other macromolecular assemblages. *Curr. Opin. Struct. Biol.*, 6:166–175, 1996.

[127] L. Smeller. Pressure-temperature phase diagrams of biomolecules. *Biochim. Biophys. Acta*, 1595:11–29, 2002.

[128] N. Southall, K. A. Dill, and A. Haymet. A view of the hydrophobic effect. *J. Phys. Chem. B*, 106:521–533, 2002.

[129] I. L. Spain and J. Paauwe. *High Pressure Technology*. Marcel Dekker Inc., NY, 1977.

[130] G. Strang. *Introduction to Linear Algebra*. Wellesley-Cambridge Press, MA, second edition edition, 1998.

[131] D. I. Svergun and M. H. J. Koch. Advances in structure analysis using small-angle scattering in solution. *Curr. Opin. Struct. Biol.*, 12:654–660, 2002.

[132] D. I. Svergun and M. H. J. Koch. Small-angle scattering studies of biological macromolecules in solution. *Reports on Progress in Physics*, 66:1735–1782, 2003.

[133] R. H. Symons. Plant pathogenic RNAs and RNA catalysis. *Nucleic Acids Res.*, 25:2683–2689, 1997.

[134] A. Tardieu, A. Le Verge, M. Malfois, F. Bonnete, S. Finet, M. Ries-Kautt, and L. Belloni. Proteins in solution: From X-ray scattering intensities to interaction potentials. *J. Crystal Growth*, 196:193–203, 1999.

[135] M. W. Tate, E. F. Eikenberry, S. L. Barna, M. E. Wall, J. L. Lowrance, and S. M. Gruner. A large-format high-resolution area X-ray detector based on a fiber-optically bonded charge-coupled device (CCD). *J. Appl. Cryst.*, 28:196–205, 1995.

[136] N. Taulier and T. V. Chalikian. Compressibility of protein transitions. *Biochim. Biophys. Acta*, 1595:48–70, 2002.

[137] S. Tobé, T. Heams, J. Vergne, G. Hervé, and M.-C. Maurel. The catalytic mechanism of hairpin ribozyme studied by hydrostatic pressure. *Nucleic Acids Res.*, 33:2557–2564, 2005.

[138] A. T. Torelli, J. Krucinska, and J. E. Wedekind. A comparison of vanadate to a 2'-5' linkage at the active site of a small ribozyme suggests a role for water in transition-state stabilization. *RNA*, 13:1052–1070, 2007.

[139] J. Torrent, J. P. Connelly, M. G. Coll, M. Ribó, R. Lange, and M. Vilanova. Pressure versus heat-induced unfolding of ribonuclease A: The case of hydrophobic interactions within a chain-folding initiation site. *Biochemistry*, 38:15952–15961, 2000.

[140] R. Y. Tsien. The green fluorescent protein. *Annual Review of Biochemistry*, 67:509–544, 1998.

[141] S. E. Tsutakawa, G. L. Hura, K. A. Frankel, P. K. Cooper, and J. A. Tainer. Structural analysis of flexible proteins in solution by small angle X-ray scattering combined with crystallography. *J. Struct. Biol.*, 158:214–223, 2007.

[142] N. J. Turro. *Molecular Photochemistry*. W. A. Benjamin, Inc., London, 1965.

[143] N. J. Turro. *Modern Molecular Photochemistry*. University Science Books, California, 1991.

[144] P. Urayama, E. W. Frey, and M. J. Eldridge. A fluid handling system with finger-tightened connectors for biological studies at kiloatmosphere pressures. *Rev. Sci. Instr.*, 79:046103, 2008.

[145] P. Urayama, G. N. Phillips, and S. M. Gruner. Probing substates in sperm whale myoglobin using high-pressure crystallography. *Structure*, 10:51–60, 2002.

[146] V. N. Uversky. Natively unfolded proteins: A point where biology waits for physics. *Protein Sci.*, 11:739–756, 2002.

[147] G. D. Van Duyne, R. F. Standaert, P. A. Karplus, S. L. Schreiber, and J. Clardy. Atomic structures of the human immunophilin FKBP-12 complexes with FK506 and rapamycin. *J. Mol. Biol.*, 229:105–124, 1993.

[148] I. R. Vetter, W. A. Baase, D. W. Heinz, J. P. Xiong, S. Snow, and B. W. Matthews. Protein structural plasticity exemplified by insertion and deletion mutants in T4 lysozyme. *Protein Sci.*, 5:2399–23415, 1996.

[149] G. J. Vidugiris, D. M. Truckses, J. L. Markley, and C. A. Royer. High-pressure denaturation of staphylococcal nuclease proline-to-glycine substitution mutants. *Biochemistry*, 35:3857–3864, 1996.

[150] J. T. Vivian and P. R. Callis. Mechanisms of tryptophan fluorescence shifts in proteins. *Biophys. J.*, 80:2093–2109, 2001.

[151] N. G. Walter, J. M. Burke, and D. P. Millar. Stability of hairpin ribozyme tertiary structure is governed by the interdomain junction. *Nat. Struct. Biol.*, 6:544–549, 1999.

[152] N. G. Walter, P. Chan, K. Hampel, D. Millar, and J. M. Burke. A base change in the catalytic core of the hairpin ribozyme perturbs function but not domain docking. *Biochemistry*, 40:2580–2587, 2001.

[153] D. C. Ward, E. Reich, and L. Stryer. Fluorescence studies of nucleotides and polynucleotides. I. Formycin, 2-aminopurine riboside, 2,6-diaminopurine riboside, and their derivatives. *J. Biol. Chem.*, 244:1228–1237, 1969.

[154] J. E. Wedekind, R. Gillilan, A. Janda, J. Krucinska, J. D. Salter, R. P. Bennett, J. Raina, and H. C. Smith. Nanostructures of APOBEC3G support a hierarchical assembly model of high molecular mass ribonucleoprotein particles from dimeric subunits. *J. Biol. Chem.*, 281:38122–38126, 2006.

[155] J. E. Wedekind and D. B. McKay. Purification, crystallization, and X-ray diffraction analysis of small ribozymes. *Meth. Enzymol.*, 317:149–168, 2000.

[156] J. Woenckhaus, R. Köhling, P. Thiyagarajan, K. C. Littrell, S. Seifert, C. A. Royer, and R. Winter. Pressure-jump small-angle X-ray scattering detected kinetics of staphylococcal nuclease folding. *Biophys. J.*, 80:1518–1523, 2001.

[157] J. Woenckhaus, R. Köhling, R. Winter, P. Thiyagarajan, and S. Finet. High pressure-jump apparatus for kinetic studies of protein folding reactions using the small-angle synchrotron X-ray scattering technique. *Rev. Sci. Instr.*, 71:3895–3899, 2000.

[158] J. W. Wray, W. A. Baase, J. D. Lindstrom, L. H. Weaver, A. R. Poteete, and B. W. Matthews. Structural analysis of a non-contiguous second-site revertant in T4 lysozyme shows that increasing the rigidity of a protein can enhance its stability. *J. Mol. Biol.*, 292:1111–1120, 1999.

[159] J. Xu, W. A. Baase, M. L. Quillin, E. P. Baldwin, and B. W. Matthews. Structural and thermodynamic analysis of the binding of solvent at internal sites in T4 lysozyme. *Protein Sci.*, 10:1067–1078, 2001.

[160] T. Yuan, A. Weljie, and H. Vogel. Tryptophan fluorescence quenching by methionine and selenomethionine residues of calmodulin: Orientation of peptide and protein binding. *Biochemistry*, 37:3187–3195, 1998.

[161] X. J. Zhang and B. W. Matthews. Conservation of solvent-binding sites in 10 crystal forms of T4 lysozyme. *Protein Sci.*, 3:1031–1039, 1994.

[162] A. Zipp and W. Kauzmann. Pressure denaturation of metmyoglobin. *Biochemistry*, 12:4217–4228, 1973.

[163] A. P. Zipp. *The Effects of Solvents and Pressure on the Spectra of Some Chemical and Biological Systems*. PhD thesis, Princeton University, 1973.